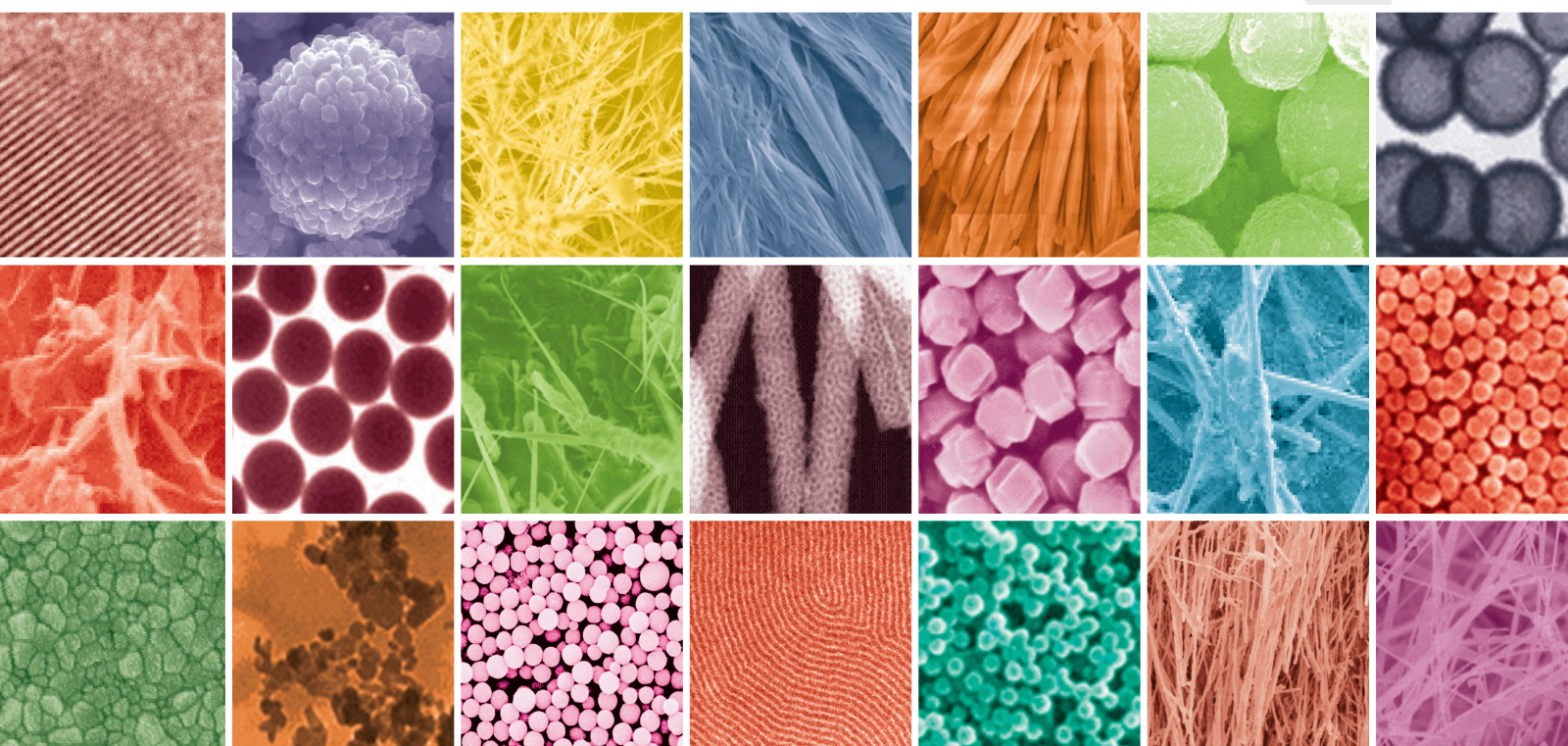


Hydrothermal Synthesis of Nanomaterials

Lead Guest Editor: Yong X. Gan

Guest Editors: Ahalapitiya H. Jayatissa, Zhen Yu, Xi Chen, and Mingheng Li





Hydrothermal Synthesis of Nanomaterials

Journal of Nanomaterials

Hydrothermal Synthesis of Nanomaterials

Lead Guest Editor: Yong X. Gan

Guest Editors: Ahalapitiya H. Jayatissa, Zhen Yu, Xi Chen,
and Mingheng Li



Copyright © 2020 Hindawi Limited. All rights reserved.

This is a special issue published in "Journal of Nanomaterials." All articles are open access articles distributed under the Creative Commons Attribution License, which permits unrestricted use, distribution, and reproduction in any medium, provided the original work is properly cited.

Editorial Board

Domenico Acierno, Italy
Katerina Aifantis, USA
Nageh K. Allam, USA
Margarida Amaral, Portugal
Martin Andersson, Sweden
Raul Arenal, Spain
Ilaria Armentano, Italy
Hassan Azzazy, Egypt
Vincenzo Baglio, Italy
Lavinia Balan, France
Thierry Baron, France
Andrew R. Barron, USA
Stefano Bellucci, Italy
Enrico Bergamaschi, Italy
Debes Bhattacharyya, New Zealand
Sergio Bietti, Italy
Giovanni Bongiovanni, Italy
Mohamed Bououdina, Bahrain
Victor M. Castaño, Mexico
Albano Cavaleiro, Portugal
Bhanu P. S. Chauhan, USA
Shafiul Chowdhury, USA
Yu-Lun Chueh, Taiwan
Elisabetta Comini, Italy
Giuseppe Compagnini, Italy
David Cornu, France
Miguel A. Correa-Duarte, Spain
P. Davide Cozzoli, Italy
Anuja Datta, USA
Loretta L. Del Mercato, Italy
Yong Ding, USA
Yu Dong, Australia
Zehra Durmus, Turkey
Joydeep Dutta, Oman
Ovidiu Ersen, France
Ana Espinosa, France
Claude Estournès, France
Giuliana Faggio, Italy
Andrea Falqui, Saudi Arabia
Matteo Ferroni, Italy
Ilaria Fratoddi, Italy
Siddhartha Ghosh, Singapore
Filippo Giubileo, Italy
Fabien Grasset, Japan
Jean M. Greneche, France
Kimberly Hamad-Schifferli, USA
Simo-Pekka Hannula, Finland
Michael Harris, USA
Yasuhiko Hayashi, Japan
Michael Z. Hu, USA
Nay Ming Huang, Malaysia
Zafar Iqbal, USA
Balachandran Jeyadevan, Japan
Jeong-won Kang, Republic of Korea
Hassan Karimi-Maleh, Iran
Antonios Kelarakis, United Kingdom
Alireza Khataee, Iran
Ali Khorsand Zak, Iran
Philippe Knauth, France
Prashant Kumar, United Kingdom
Eric Le Bourhis, France
Jun Li, Singapore
Shijun Liao, China
Meiyong Liao, Japan
Silvia Licoccia, Italy
Nathan C. Lindquist, USA
Zainovia Lockman, Malaysia
Jim Low, Australia
Gaurav Mago, USA
Muhamamd A. Malik, United Kingdom
Ivan Marri, Italy
Laura Martinez Maestro, United Kingdom
Sanjay R. Mathur, Germany
Tony McNally, United Kingdom
Yogendra Mishra, Germany
Paulo Cesar Morais, Brazil
Paul Munroe, Australia
Jae-Min Myoung, Republic of Korea
Rajesh R. Naik, USA
Albert Nasibulin, Russia
Toshiaki Natsuki, Japan
Hiromasa Nishikiori, Japan
Sherine Obare, USA
Won-Chun Oh, Republic of Korea

Abdelwahab Omri, Canada
Ungyu Paik, Republic of Korea
Dillip K. Panda, USA
Edward A. Payzant, USA
Alessandro Pegoretti, Italy
Oscar Perales-Pérez, Puerto Rico
Jorge Pérez-Juste, Spain
Alexey P. Popov, Finland
Thathan Premkumar, Republic of Korea
Helena Prima-García, Spain
Alexander Pyatenko, Japan
Haisheng Qian, China
You Qiang, USA
Philip D. Rack, USA
Mohammad Rahimi-Gorji, Belgium
Peter Reiss, France
Ilker S. Bayer, Italy
Lucien Saviot, France
Sudipta Seal, USA
Shu Seki, Japan
Donglu Shi, USA
Bhanu P. Singh, India
Surinder Singh, USA
Vladimir Sivakov, Germany
Adolfo Speghini, Italy
Kishore Sridharan, India
Marinella Striccoli, Italy
Andreas Stylianou, Cyprus
Fengqiang Sun, China
Ashok K. Sundramoorthy, India
Angelo Taglietti, Italy
Bo Tan, Canada
Leander Tapfer, Italy
Valeri P. Tolstoy, Russia
Muhammet S. Toprak, Sweden
R. Torrecillas, Spain
Achim Trampert, Germany
Takuya Tsuzuki, Australia
Tamer Uyar, USA
Luca Valentini, Italy
Antonio Vassallo, Italy
Ester Vazquez, Spain
Ajayan Vinu, Australia
Shiren Wang, USA
Yong Wang, USA
Ruibing Wang, Macau
Magnus Willander, Sweden

Ping Xiao, United Kingdom
Zhi Li Xiao, USA
Yingchao Yang, USA
Yoke K. Yap, USA
Dong Kee Yi, Republic of Korea
Jianbo Yin, China
William Yu, USA
Michele Zappalorto, Italy
Renyun Zhang, Sweden

Contents

Hydrothermal Synthesis of Nanomaterials

Yong X. Gan , Ahalapitiya H. Jayatissa, Zhen Yu, Xi Chen , and Mingheng Li
Editorial (3 pages), Article ID 8917013, Volume 2020 (2020)

Negative Surface Energies of Nickel Ferrite Nanoparticles under Hydrothermal Conditions

Zs. Rák  and D. W. Brenner
Research Article (6 pages), Article ID 5268415, Volume 2019 (2019)

Optimization of a Hydrothermal Growth Process for Low Resistance 1D Fluorine-Doped Zinc Oxide Nanostructures

Muhammad L. M. Napi , S. M. Sultan , Razali Ismail , Mohd K. Ahmad, and G. M. T. Chai
Research Article (10 pages), Article ID 4574507, Volume 2019 (2019)

Stable Electrochemical Measurements of Platinum Screen-Printed Electrodes Modified with Vertical ZnO Nanorods for Bacterial Detection

Thi Hong Phuoc Nguyen, Matteo Tonezzer, Thi Thanh Le Dang , Quang Khue Vu, Quang Huy Tran , Duc Hoa Nguyen , and Van Hieu Nguyen
Research Article (9 pages), Article ID 2341268, Volume 2019 (2019)

Preparation of Three-Layer Graphene Sheets from Asphaltenes Using a Montmorillonite Template

Xiaolong Wu , Bojing Ma, Yisheng Xu, Jun Xu, Haowei Zhai, Zechen Xiong, Xiangbiao Liao, Xiaoyang Shi, and Xi Chen 
Research Article (6 pages), Article ID 2094723, Volume 2019 (2019)

Waste Utilization of Synthetic Carbon Quantum Dots Based on Tea and Peanut Shell

Jing Zhu, Fengyuan Zhu, Xiaona Yue, Peirong Chen, Yue Sun, Liang Zhang, Dongdong Mu , and Fei Ke 
Research Article (7 pages), Article ID 7965756, Volume 2019 (2019)

Continuous-Flow Synthesis of Thermochromic M-Phase VO₂ Particles via Rapid One-Step Hydrothermal Reaction: Effect of Mixers

Xiaojie Yan , William Trevillyan, Ioannina Castano, Yugang Sun, Ralph Muehleisen, and Jie Li
Research Article (10 pages), Article ID 2570698, Volume 2019 (2019)

Optimization of Tb³⁺/Gd³⁺ Molar Ratio for Rapid Detection of Naja Atracobra Venom by Immunoglobulin G-Conjugated GdPO₄·nH₂O : Tb³⁺ Nanorods

Pham Thi Lien, Nguyen Thanh Huong , Tran Thu Huong, Hoang Thi Khuyen, Nguyen Thi Ngoc Anh, Nguyen Duc Van, Nguyen Ngoc Tuan, Vu Xuan Nghia, and Le Quoc Minh
Research Article (8 pages), Article ID 3858439, Volume 2019 (2019)

Synthesis and Photocatalytic Properties of Co-Doped Zn_{1-x}CoxMn₂O Hollow Nanospheres

Long Ma, Zhiqiang Wei , Xueliang Zhu, Jiahao Liang, and Xudong Zhang
Research Article (9 pages), Article ID 4257270, Volume 2019 (2019)

Template-Free Preparation and Photocatalytic and Photoluminescent Properties of Brookite TiO₂ Hollow Spheres

Yunjian Wang  and Yuchan Li

Research Article (7 pages), Article ID 3605976, Volume 2019 (2019)

One-Pot Synthesis of Titanate Nanotubes Decorated with Anatase Nanoparticles Using a Microwave-Assisted Hydrothermal Reaction

Suziete B. S. Gusmão, Anupama Ghosh , Thalles M. F. Marques, Odair P. Ferreira , Anderson O. Lobo, Josy A. O. Osajima, Cleanio Luz-Lima, Romulo R. M. Sousa, Jose M. E. Matos, and Bartolomeu C. Viana 

Research Article (10 pages), Article ID 4825432, Volume 2019 (2019)

Synthesis and Characterization of ZnO-ZrO₂ Nanocomposites for Photocatalytic Degradation and Mineralization of Phenol

M. C. Uribe López, M. A. Alvarez Lemus , M. C. Hidalgo, R. López González , P. Quintana Owen, S. Oros-Ruiz, S. A. Uribe López, and J. Acosta

Research Article (12 pages), Article ID 1015876, Volume 2019 (2019)

Editorial

Hydrothermal Synthesis of Nanomaterials

Yong X. Gan ¹, **Ahalapitiya H. Jayatissa**,² **Zhen Yu**,³ **Xi Chen** ⁴, and **Mingheng Li**⁵

¹*Department of Mechanical Engineering, California State Polytechnic University Pomona, 3801 W. Temple Avenue, Pomona, CA 91768, USA*

²*Department of Mechanical, Industrial and Manufacturing Engineering, University of Toledo, 2801 W. Bancroft Street, Toledo, OH 43606, USA*

³*Department of Electrical and Computer Engineering, California State Polytechnic University Pomona, 3801 W. Temple Avenue, Pomona, CA 91768, USA*

⁴*Department of Earth and Environmental Engineering, Columbia University, 500 W. 120th Street, New York, NY 10027, USA*

⁵*Department of Chemical and Materials Engineering, California State Polytechnic University Pomona, 3801 W. Temple Avenue, Pomona, CA 91768, USA*

Correspondence should be addressed to Yong X. Gan; yxgan@cpp.edu

Received 21 January 2020; Accepted 22 January 2020; Published 30 January 2020

Copyright © 2020 Yong X. Gan et al. This is an open access article distributed under the Creative Commons Attribution License, which permits unrestricted use, distribution, and reproduction in any medium, provided the original work is properly cited.

Hydrothermal synthesis is one of the most commonly used methods for preparation of nanomaterials. It is basically a solution reaction-based approach. In hydrothermal synthesis, the formation of nanomaterials can happen in a wide temperature range from room temperature to very high temperatures. To control the morphology of the materials to be prepared, either low-pressure or high-pressure conditions can be used depending on the vapor pressure of the main composition in the reaction. Many types of nanomaterials have been successfully synthesized by the use of this approach. There are significant advantages of hydrothermal synthesis method over others. Hydrothermal synthesis can generate nanomaterials which are not stable at elevated temperatures. Nanomaterials with high vapor pressures can be produced by the hydrothermal method with minimum loss of materials. The compositions of nanomaterials to be synthesized can be well controlled in hydrothermal synthesis through liquid phase or multiphase chemical reactions. This special issue serves as a forum presenting the recent research results of hydrothermal synthesis of nanomaterials. Several papers on hydrothermal synthesis of nanoparticles, nanorods, nanotubes, hollow nanospheres, and graphene nanosheets have been published in this special issue. New synthesis methods, for example, microwave-assisted hydrothermal synthesis and template-free self-assembling catalytic synthesis, are reported

in this special issue. Research work on optimization of the synthesis conditions is included as well. Nanomaterials for applications such as energy harvesting and biosensing are also studied in the papers published in this special issue. In addition, hydrothermal synthesis using waste materials to achieve environment protection was studied in one of the papers. A brief summary of all the eleven accepted papers is presented as follows.

The paper by Z. Rák and D. W. Brenner presents the fundamental work on the formation of nickel ferrite (NiFe_2O_4) nanoparticles under hydrothermal conditions. A model was established via a method that combines results of first-principle calculations, elements of aqueous thermochemistry, and experimental free energies of formation. Based on calculations using the model, negative formation energies for the (111) surfaces and positive free energies for the formation of bulk nickel ferrite were predicted. The combination of the negative surface and positive bulk energies yields thermodynamically stable nickel ferrite nanoparticles with sizes between 30 and 150 nm in the temperature range of 300 to 400 K under alkaline conditions. The effect of processing condition on the stability of the nickel ferrite nanoparticle was discussed.

The work by M. L. M. Napi et al. deals with hydrothermal synthesis condition parameter optimization. Design

of Experiment (DOE) was used to determine the processing parameters for hydrothermal growth of one-dimensional fluorine-doped zinc oxide (1D-FZO) using Au nanoparticles as the catalyst. The DOE includes three design points on each of the parameter. The selected parameters are the gold sputtering time (10 s, 15 s, and 20 s), hydrothermal reaction time (3 hours, 6.5 hours, and 10 hours), and hydrothermal temperature (50°C, 75°C, and 100°C). The effects of these parameters on the quality of 1D-FZO produced are analyzed statistically. It is found that the sputtering time of the Au nanoparticles has significant effect on the morphology and electrical property of the 1D-FZO. The lowest resistance value of 22.57 Ω was achieved for the 1D-FZO grown with the longest Au sputtering time. The hydrothermal growth temperature below 100°C was suggested.

The work performed by T. H. P. Nguyen et al. investigated the stability of electrochemical and biosensing properties of ZnO nanorod-based platinum screen-printed electrodes (SPEs) applied for detection of bacterial pathogens. The ZnO nanorods (NRs) were grown on the platinum working electrode using the hydrothermal method. The standard photolithography and lift-off process were used to fabricate the patterned platinum SPEs on a silicon wafer. For sensor property characterization, Salmonella polyclonal antibodies were immobilized at the ZnO NR surface through crosslinking. Morphological and structural analysis of the ZnO NRs by scanning electron microscopy (SEM), transmission electron microscopy (TEM), and X-ray diffraction (XRD) shows that the ZnO NRs were grown vertically on platinum electrodes with a diameter around 20-200 nm and a length of 5-7 μm . These modified electrodes were applied for detecting Salmonella enteritidis at a concentration of 103 cfu/mL. Electrochemical measurements including cyclic voltammetry (CV) and electrochemical impedance spectroscopy (EIS) reveal that the ZnO NR-modified platinum electrodes could detect Salmonella bacteria well with signal to noise ratio much higher than 3:1. This indicates that the ZnO NR-modified platinum SPEs have potential for the development of biochips for electrochemical detection of bacterial pathogens.

The paper by X. Wu et al. reported the findings on synthesis of graphene sheets with high quality by calcinating composites intercalated with montmorillonite (MMT) and asphaltene. The graphene sample obtained is continuous and as long as 10.79 μm . The surface is smooth with little defects. By analyzing the XRD patterns of graphene/MMT composites at different conditions, the graphene formation mechanism is proposed and the optimal calcination conditions are suggested. This work provides important insights into how to make low-cost graphene using asphaltene extracted from heavy crude oil.

In the paper by J. Zhu et al., carbon quantum dots (CQDs) with high quantum yield and good stability were synthesized from waste tea leaves and peanut shells by a one-step hydrothermal method. This work introduced the concept of waste utilization and environmental protection while making useful nanomaterials from sustainable sources. The synthesis conditions, structures, and optical properties of CQDs were researched. Their unique characteristics of

emitting strong and steady blue fluorescence under excitation of ultraviolet light were found due to the existence of plenty of hydrophilic groups at the surface of the CQDs. It is concluded that the CQDs have potentials for analytical detection and for application as biomarkers.

The paper by X. Yan et al. shows that the continuous-flow hydrothermal processes have advantages for synthesizing VO₂ particles over the traditional batch reaction systems. Specifically, the role of mixers in continuous-flow synthesis of thermochromic VO₂ particles via rapid one-step hydrothermal reaction was studied. In this work, a Center T-Mixer and a Collision Cross-Mixer are developed and implemented in a hot water fluidized suspension reaction (HWFSR) system. The influence of the resident time on the particle phase and size was examined, and properties of particles derived from systems equipped with differing mixers were compared. The resulting particles were characterized using techniques of X-ray powder diffraction (XRD) analysis, scanning electron microscopy (SEM), and differential scanning calorimetry (DSC). The results confirm the crucial role of mixers in particle fabrication in continuous-flow systems. When compared with the Center T-Mixer, the Collision Cross-Mixer has better control regarding the morphology and size distribution of resulting particles while improving the transition temperatures of the as-synthesized materials. HWFSR systems containing novel mixer designs are capable of producing pure M-phase VO₂ particles in a single step contrary to the current reactor design that uses a second post heat treatment step, and they are capable of synthesizing many other nanoparticle species, especially those requiring high temperature and pressure reaction conditions. The synthesized VO₂ particles are promising materials for thermochromic smart windows that reduce building energy loss.

The paper by P. T. Lien et al. reported synthesis of GdPO₄·nH₂O and Tb³⁺-doped GdPO₄·nH₂O nanorods@silica-NH₂ conjugated with IgG antibody by hydrothermal, sol-gel, and coprecipitation methods. The effect of Tb³⁺/Gd³⁺ molar ratio on the size, morphology, and luminescence of the synthesized samples was investigated. It is found that under optimized conditions, the GdPO₄·nH₂O:Tb³⁺ as uniform nanorods sizing from 10 to 30 nm in diameter and from 200 to 300 nm in length shows the strongest luminescence in green color with narrow bands under the UV excitation (325 nm). After being coated with silica-NH₂ and conjugated with IgG antibody, all luminescence characteristic peaks of GdPO₄·nH₂O:Tb³⁺ corresponding to the process of energy transfer from Gd³⁺ to Tb³⁺ and then the emission from ⁵D₄ → ⁷F_J (J = 6, 5, 4, 3) of Tb³⁺ can still be observed. The application of the Tb³⁺-doped GdPO₄·nH₂O nanorods@silica-NH₂ conjugated with IgG antibody for rapid selective detection of Naja atra cobra venom was also shown.

L. Ma et al. published their work on hydrothermal synthesis of various Co-doped Zn_{1-x}Co_xMn₂O nanocrystals with a spinel structure. The nanocrystals form hollow nanospheres. The influence of Co doping concentration on the structure, morphology, elemental composition, and optical and photocatalytic properties of the samples was studied. It is found that Co²⁺ ions replaced some of the lattice sites of

Zn^{2+} in the ZnMn_2O_4 nanocrystals. The crystalline size decreased with the increase of Co doping. The band gap of $\text{Zn}_{1-x}\text{Co}_x\text{Mn}_2\text{O}_4$ is smaller than that of pure ZnMn_2O_4 and red shifted was found for the doped sample. It is also found that the photocatalytic activity of the Co-doped sample is higher than that of the undoped sample during the photodegradation of methyl orange (MO) under visible light irradiation. The results indicate that Co-doped spinel ZnMn_2O_4 nanocrystals are effective in photocatalytic degradation of the pollutants.

Y. Wang and Y. Li reported their research on hydrothermal synthesizing titanium dioxide hollow nanospheres for photoluminescence and catalysis. As known, there exists challenge in preparing high-purity brookite TiO_2 with some unique structure. In this work, high-purity brookite TiO_2 hollow spheres were hydrothermally synthesized by employing titanium sulfate as the titanium source and chloroacetic acid and sodium hydroxide as the pH regulator. The structure, morphology, and optical properties were characterized by X-ray diffraction (XRD), scanning electron microscopy (SEM), transmission electron microscopy (TEM), X-ray photoelectron spectroscopy (XPS), and UV-Vis diffuse reflectance spectroscopy (UV-Vis DRS). The results showed that the as-prepared brookite TiO_2 hollow spheres in a size of about 1.0 micrometer had a direct band gap of 3.13 eV. Thermal analysis in combination with infrared spectroscopy showed that the as-prepared brookite TiO_2 was surface capped with water and organic molecules. The photocatalytic and photoluminescence properties of brookite TiO_2 were shown.

The paper by S. B. S. Gusmão et al. focuses on the microwave-assisted hydrothermal reaction method. One-pot synthesis of titanate nanotubes decorated with anatase nanoparticles was demonstrated for the first time. This nano-heterostructure of titanate nanotubes decorated with anatase nanoparticles (TiNT@AnNP) was characterized by various methods including X-ray diffraction, Raman spectroscopy, scanning electron microscopy (SEM), energy-dispersive X-ray spectroscopy (EDXS), high-resolution transmission electron microscopy (HRTEM), selected-area electron diffraction, and X-ray photoelectron spectroscopy (XPS). The results showed that the TiNT@AnNP nanomaterial is highly crystalline and in nanometer size. The synthesized TiNT@AnNP degraded an anionic dye (Remazol blue) more efficiently under UV-visible light (380–780 nm) than a commercial anatase- TiO_2 precursor. This increased efficiency of photodegradation is due to the large surface area and the effective separation of the photon induced electron-hole pairs. The benefit of microwave-assisted hydrothermal synthesis in the production of TiNT@AnNP for environmental applications was discussed as well.

In the paper by M. C. Uribe López et al., synthesis of ZnO-ZrO₂ nanocomposites was introduced. Characterization of the nanomaterials for photocatalytic degradation and mineralization of phenol was also presented. Zinc (II) acetylacetonate was used as the source materials for generating different ZnO contents (13, 25, 50, and 75% mol) in the nanocomposites. The synthesized ZnO-ZrO₂ nanomaterials showed both the tetragonal crystalline structure of zirconia

and the hexagonal one of ZnO. The morphology was observed, and the size of the nanomaterials was analyzed by electron microscopy. The formation of ZnO nanorods with the size ranging from 50 nm to 300 nm and zirconia particles with the size smaller than 50 nm was revealed. The advantage of using the nanocomposites for photocatalytic degradation of phenol was demonstrated. The mineralization degree of the 75ZnO-25ZrO₂ nanocomposite has higher mineralization degree than pure ZnO. The nanocomposite can also inhibit the generation of undesirable intermediates.

Conflicts of Interest

The editors declare that they have no conflicts of interest regarding the publication of this special issue.

Acknowledgments

We would like to express our gratitude to all authors who made this special issue possible. We hope this collection of articles will be useful to the scientific community.

Yong X. Gan
Ahalapitiya H. Jayatissa
Zhen Yu
Xi Chen
Mingheng Li

Research Article

Negative Surface Energies of Nickel Ferrite Nanoparticles under Hydrothermal Conditions

Zs. Rák  and D. W. Brenner

Department of Materials Science and Engineering, North Carolina State University, Raleigh, NC 27695, USA

Correspondence should be addressed to Zs. Rák; zrak@ncsu.edu

Received 31 January 2019; Revised 30 August 2019; Accepted 9 September 2019; Published 7 October 2019

Guest Editor: Zhen Yu

Copyright © 2019 Zs. Rák and D. W. Brenner. This is an open access article distributed under the Creative Commons Attribution License, which permits unrestricted use, distribution, and reproduction in any medium, provided the original work is properly cited.

The formation of nickel ferrite (NiFe_2O_4) nanoparticles under hydrothermal conditions has been modeled using a method that combines results of first-principle calculations, elements of aqueous thermochemistry, and experimental free energies of formation. The calculations predict negative formation energies for the (111) surfaces and positive free energies for the formation of bulk nickel ferrite. Based on classical nucleation theory, the combination of the negative surface and positive bulk energies yields thermodynamically stable nickel ferrite nanoparticles with sizes between 30 and 150 nm in the temperature range of 300 to 400 K under alkaline conditions. The surface and bulk energetics as well as the stability of the nickel ferrite nanoparticle as a function of temperature and pH are discussed.

1. Introduction

Nanostructured materials can display physical properties that are very different from what they exhibit on the macro-scale. This is because at nanoscale quantum effects become dominant, affecting the electrical, optical, and magnetic behavior of matter [1]. Furthermore, the reduction in particle size leads to a larger relative surface area, and this can alter the chemical reactivity and strength of the material. These characteristics make nanostructured materials to be of great scientific and technological interests [1–3]. Among nanostructured materials, magnetic nanoparticles have been the focus of intense research because of their potential use in numerous technological areas, for example, in catalysis, data storage, nanofluids, microwave devices, and defect sensors [4–8]. Nanosized nickel ferrite (NiFe_2O_4) has received considerable scientific attention due to its magnetic characteristics that depend sensitively on the size, shape, purity, and thermal history of the samples [9, 10]. Nickel ferrite nanoparticles have been synthesized through conventional techniques including solid-state reaction, sol-gel combustion, coprecipitation, and hydrothermal methods [9–17]. Among

these methods, hydrothermal synthesis appears to be a promising technique to produce highly crystallized, weekly agglomerated powder, where particle size, morphology, and other characteristics can be controlled by adjustment of temperature, time, and pH value [18, 19].

Nickel ferrite is known to be present in the coolant of pressurized water reactors (PWR), and it is also a major component in the porous oxide deposits that accumulate on fuel rods during reactor operation. In previous work, we carried out first-principle-based thermodynamic modeling to describe the processes of formation and deposition of nickel ferrite particles in PWRs [20–24]. We combined results of density functional theory (DFT) calculations with experimental Gibbs free energies of formation to evaluate the surface energies of nickel ferrite as a function of temperature. To mimic the conditions of pressure, ionic concentrations, and pH in operating PWRs, we also incorporated elements of aqueous chemistry into the model [20, 21]. Unexpectedly, it was found that several reconstructed nickel ferrite surfaces had negative formation energies, while the enthalpy of formation of the bulk material was positive. The combination of negative surface and positive bulk free

energies predicts thermodynamically stable nickel ferrite nanoparticles in the PWR coolant.

In this paper, we use the first-principle informed thermodynamics method developed earlier [20, 21], to model the nucleation and formation of nickel ferrite nanoparticles from solvated ionic species under hydrothermal conditions.

2. Theoretical Method

Details of the DFT-informed thermodynamics scheme as well as details of the atomic structures used for the modeling of bulk and surfaces of nickel ferrite are described in our previous work [20, 21]. Here, we only present a summary of the method. To determine the surface energies as a function of temperature, a set of temperature-dependent effective chemical potentials (ECP) are calculated based on the following system of linear equations:

$$\Delta_f G_{A_x B_y O_z}(T, P) = E_{A_x B_y O_z} - x\mu_A^0(T) - y\mu_B^0(T) - \frac{z}{2}\mu_{O_2}^0(T), \quad (1)$$

where the change in free energies, $\Delta_f G_{A_x B_y O_z}(T, P)$, are taken from the experiment [25, 26], $E_{A_x B_y O_z}$ are the total DFT energies of various binary and ternary oxides, and μ_i^0 are the ECPs that are determined by solving the system of linear equations (1) by the least squares method. Similar to the ECPs determined by equation (1), the chemical potentials for the solvated cations, $\mu_{M^{z+},aq}^0$, are calculated using

$$\Delta_f G_{M^{z+},aq}^0(T, P) = \mu_{M^{z+},aq}^0(T, P) - \mu_M^0(T) + \frac{z}{2}\mu_{H_2}^0(T) - z\mu_{H^+}^0(T). \quad (2)$$

The Gibbs energies of formation of the aqueous species, $\Delta_f G_{M^{z+},aq}^0(T, P)$, used in equation (2) are taken from the SUPCRT database [27, 28]. The chemical potential for the solvated proton is evaluated in terms of the pH value as

$$\mu_{H^+}(T) = \mu_{H^+}^0(T_r) + RT \ln(10^{-\text{pH}}). \quad (3)$$

Using the ECPs determined by equations (1) and (2), combined with DFT total energies calculated for the slab geometries, and assuming that the dissolved Fe and Ni are in 3+ and 2+ oxidation states, respectively, the temperature-dependent surface energies of nickel ferrite are calculated through

$$\gamma(T, P) = \frac{1}{2A} \left[\left(G_{\text{slab}} - \Gamma_{\text{Fe}}\mu_{\text{Fe}^{3+}} - \Gamma_{\text{Ni}}\mu_{\text{Ni}^{2+}} - \Gamma_{\text{NiFe}_2\text{O}_4}g_{\text{NiFe}_2\text{O}_4} - n_{\text{H}_2}\mu_{\text{H}_2\text{O}} \right) - \left(\frac{3}{2}\Gamma_{\text{Fe}} + \Gamma_{\text{Ni}} \right) \left(2\mu_{\text{H}^+} - \mu_{\text{H}_2} + \Delta_f G(\text{H}_{2,\text{aq}}) \right) \right]. \quad (4)$$

In equation (4), G_{slab} and $g_{\text{NiFe}_2\text{O}_4}$ represent the DFT total energies of the surface slab and the bulk, $\mu_{i^{z+}}$ are the environment-dependent chemical potentials, and Γ_i represent the surface excess quantities that are related to the number of atoms used in the reconstruction of the nonstoichiometric surfaces considered in the calculations. They are given by

$$\begin{aligned} \Gamma_{\text{Fe}} &= n_{\text{Fe}} - n_{\text{O}_2} + \frac{n_{\text{H}_2}}{2}, \\ \Gamma_{\text{Ni}} &= n_{\text{Ni}} - \frac{n_{\text{O}_2}}{2} + \frac{n_{\text{H}_2}}{4}, \\ \Gamma_{\text{NiFe}_2\text{O}_4} &= \frac{n_{\text{O}_2}}{2} - \frac{n_{\text{H}_2}}{4}. \end{aligned} \quad (5)$$

In the case of nonstoichiometric surfaces, the free energies are dependent on the environment *via* the chemical potentials. These are related to ECPs through the molal concentrations by the relation:

$$\mu_{i^{z+}} = \mu_{i^{z+}}^0(T, P) + RT \ln [i^{z+}]. \quad (6)$$

The DFT calculations have been carried out using the VASP package [29, 30] with the GGA-PBE exchange correlation functional [31]. The on-site Coulomb interactions were added to the *d*-states of Ni and Fe in the Dudarev formulation [32], with the values of 6.0 and 4.5 eV, respectively.

In addition to characterizing nickel ferrite nanoparticles, the first-principle informed thermodynamics scheme, briefly described above, has been successfully used to investigate other processes that take place under operating PWRs, such as boron uptake by nickel ferrite [33] and formation of bonaccordite (Ni_2FeBO_5) on nuclear fuel rods [34].

3. Nucleation: Theory and Experiment

Classical homogeneous nucleation theory gives the change in free energy ΔG^T as phase transformation proceeds as a sum of two terms. The first term is an interfacial energy per unit area, γ , times the area between the two phases. The second term is the difference in free energy of the two phases, ΔG , times the volume of the transformed material. Therefore, the free energy change as the transformation progresses is given by

$$\Delta G^T = (\text{surface area}) \cdot \gamma + (\text{volume}) \cdot \Delta G, \quad (7)$$

where a combination of positive surface energy and a negative ΔG yields a free energy barrier for the nucleation process. In general, the magnitude of ΔG increases as the temperature is lowered below that of the phase transition, which produces both a smaller nucleation barrier and critical cluster radius. For direction-dependent γ values, a Wulff construction can be used to determine appropriate volume and surface energies for a given nanoparticle size.

Nanocrystalline nickel ferrite has been synthesized through hydrothermal reaction and characterized in numerous experimental studies [11–17]. In hydrothermal processes, Fe is usually in a 3+ oxidation state originating from

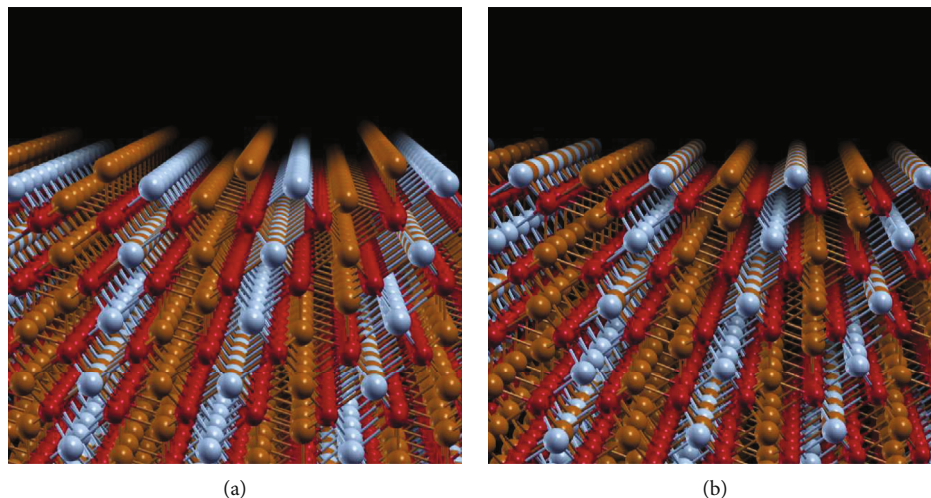


FIGURE 1: Slab models with the lowest (111) surface formation energies. The most stable surfaces expose (a) tetrahedral and (b) octahedral Ni/Fe cations. The red balls represent O atoms, and the grey and brown are Ni and Fe, respectively.

precursors such as $\text{FeO}(\text{OH})$, $\text{Fe}(\text{NO})_3$, and FeCl_3 and the typical mole ratio of Fe:Ni is close to 2:1. To simulate these conditions, the molal concentrations of Fe^{3+} and Ni^{2+} were set to 2×10^{-21} and 1×10^{-21} mol/kg. Furthermore, because higher alkalinity of the solution enhances the crystallization of nickel ferrite [11], the simulations were carried out for pH values ranging from 7 to 8.

4. Results and Discussions

The surface free energies of nickel ferrite with 12 different terminations along the low index surfaces have been calculated. To explore the effect of the water chemisorption on surface stability, in addition to the bare surface configurations, the calculations were also carried out with OH groups attached to the surface metal ions and H attached to the surface oxygens. On several surface orientations, we also investigated the effect of OH and H adsorptions separately.

The energy of a stoichiometric surface, which is always positive, can be lowered by adsorbates or by surface reconstruction. Depending on the chemical potentials of the adsorbed species or the species participating in the surface reconstruction, the surface energies can become negative [35–37]. In our modeling, under hydrothermal conditions, several of the nickel ferrite surfaces have negative formation energies. This can be related to the reference chemical potentials of the aqueous species used in the calculations that depend on temperature, pressure, and pH value.

Under conditions of hydrothermal synthesis, the most stable surfaces of nickel ferrite are predicted to be along the (111) orientation. This is in agreement with earlier DFT simulations carried out on nickel ferrite surfaces [38]. Out of the six nonequivalent surface terminations examined along the (111) direction, the ones that expose the most metal cations are the most stable. As illustrated in Figures 1(a) and 1(b), these surfaces consist of metallic layers of tetrahedral and octahedral Ni/Fe cations, respectively. Even though these surfaces create more broken bonds than other cuts along the

(111) direction, they are the most stable because the simulations were carried out under oxygen-poor conditions. Therefore, surfaces that expose more metal cations are more stable. The calculated energies associated with these two terminations are nearly the same: they differ by only 0.014 J/m^2 , with the termination illustrated in Figure 1(a) being more stable. This difference in the surface energies is related to the DFT slab energies, and therefore, it is independent of temperature, pH, or ion concentrations. The surfaces can be further stabilized through the adsorption of dissociated H_2O , by capping the exposed metal sites with OH groups and placing the H atoms above O atoms in the subsurface layer.

Plotted in Figure 2(a) are the free energies of formation of the most stable nickel ferrite surface (represented in Figure 1(a)) with and without H_2O termination, as a function of temperature, for three different pH values. As mentioned earlier, the surfaces are stabilized by the adsorption of H_2O . At 300 K, for instance, the presence of H_2O lowers the surface formation energy by $\sim 7 \text{ J/m}^2$. However, as apparent in Figure 2(a), the exothermicity of the adsorption process decreases with temperature, such that around 600 K (not shown), the surface becomes denuded. This trend is consistent with the IR powder spectroscopy measurements that revealed water desorption from nickel ferrite surfaces at temperature above 400 K [11].

Using the conditions of temperature, pH, and concentration of aqueous species specified above, the free energy for the formation of bulk nickel ferrite is evaluated through the reaction:



As illustrated in Figure 2(b), the bulk free energy of formation, calculated by equation (8), decreases with temperature and pH but remains mostly positive for the entire range of 300–400 K. As visible in Figures 2(a) and 2(b) as the values of temperature and pH increase, the surfaces become less stable while the bulk becomes more stable.

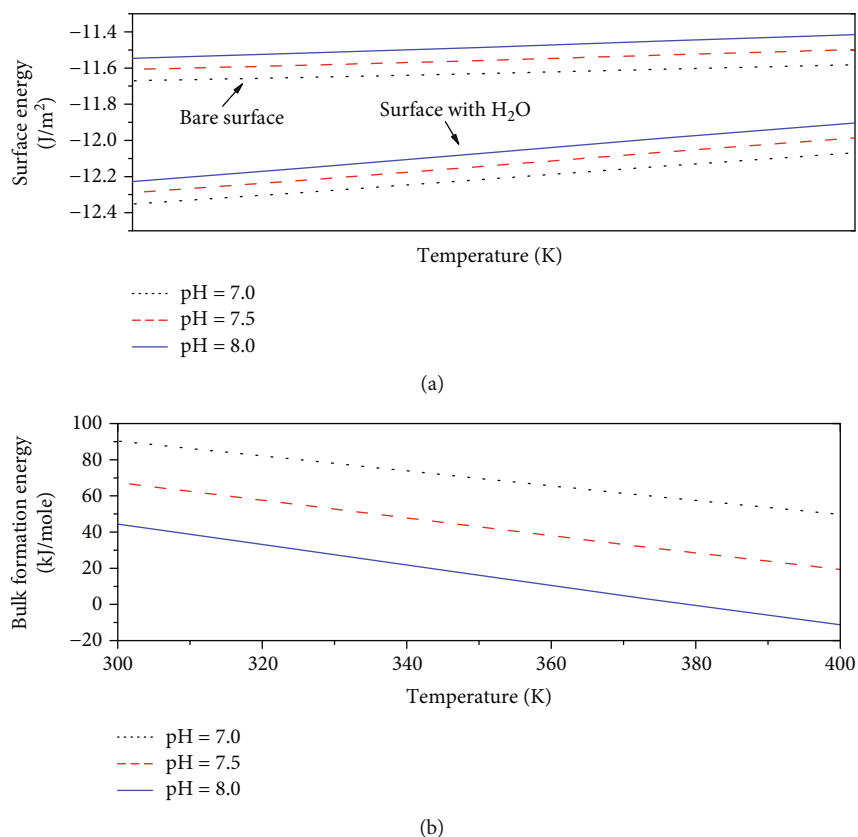


FIGURE 2: (a) Surface formation energies for the bare and hydroxylated nickel ferrite (111) surfaces as a function of temperature and pH value. The exothermicity of the H_2O adsorption process decreases with temperature. (b) Free energy of formation for bulk nickel ferrite as a function of temperature and pH. As the temperature and pH increase, the bulk becomes more stable.

At temperatures above 400 K and/or pH values above 8, the free energy of formation of the bulk becomes negative (Figure 2(b)), causing the crystallization of bulk nickel ferrite.

A Wulff construction based on the surface energies described above predicts that nickel ferrite particles only expose their (111) surfaces, producing particles with octahedral morphology. This is consistent with the observation of the octahedral nickel ferrite particles ranging from 60 to 100 nm in size generated through hydrothermal reactions [11, 12].

To evaluate the thermodynamic stability of the nickel ferrite particles under hydrothermal conditions, the free energy associated with the formation of an octahedral particle is calculated as a function of size. This is done by adding the product of the negative (111) surface energy and the total surface area of the octahedral particle to the product of the positive formation energy of bulk nickel ferrite and the volume of the particle. The change in free energy for the formation of nickel ferrite particles as a function of particle size is plotted in Figure 3(a) for different temperatures. Interestingly, instead of the energy barriers expected from the classical nucleation theory, the calculated free energy curves in Figure 3 display energy wells, where the nickel ferrite clusters are predicted to be thermodynamically stable. This atypical behavior of the nucleation curve occurs because in our simulation, the surface energies of nickel ferrite are negative while the bulk formation energies are positive. As specified in the

previous paragraph, the free energy for particle formation is the sum of a surface term and a volume term. Because the volume term varies more rapidly with size than the surface term, at small sizes, the surface term dominates and the free energy is negative. At larger particle sizes, the volume term takes over, and the free energy is dominated by the positive formation energy of bulk nickel ferrite. This is illustrated in Figure 3(a), where for temperatures ranging from 300 to 400 K and pH = 7, the free energy curves have minima corresponding to particle sizes of 30 to 60 nm. As visible in Figure 3(b), the depth of the energy wells and the sizes of nickel ferrite particles associated with the wells depend sensitively on the pH. As the alkalinity of the solution increases, the clusters become larger; for instance, at 350 K and pH = 8, the side length of the nickel ferrite octahedron is predicted to be around 150 nm. This trend as well as the predicted cluster sizes appears to be in good agreement with experimental results [11, 12].

5. Conclusion

This study combines results of first-principle DFT calculations with experimental data and elements of aqueous chemistry to evaluate the energetics of nickel ferrite synthesis in hydrothermal environments. Based on solid-liquid equilibrium conditions, the formation energies of the bare and

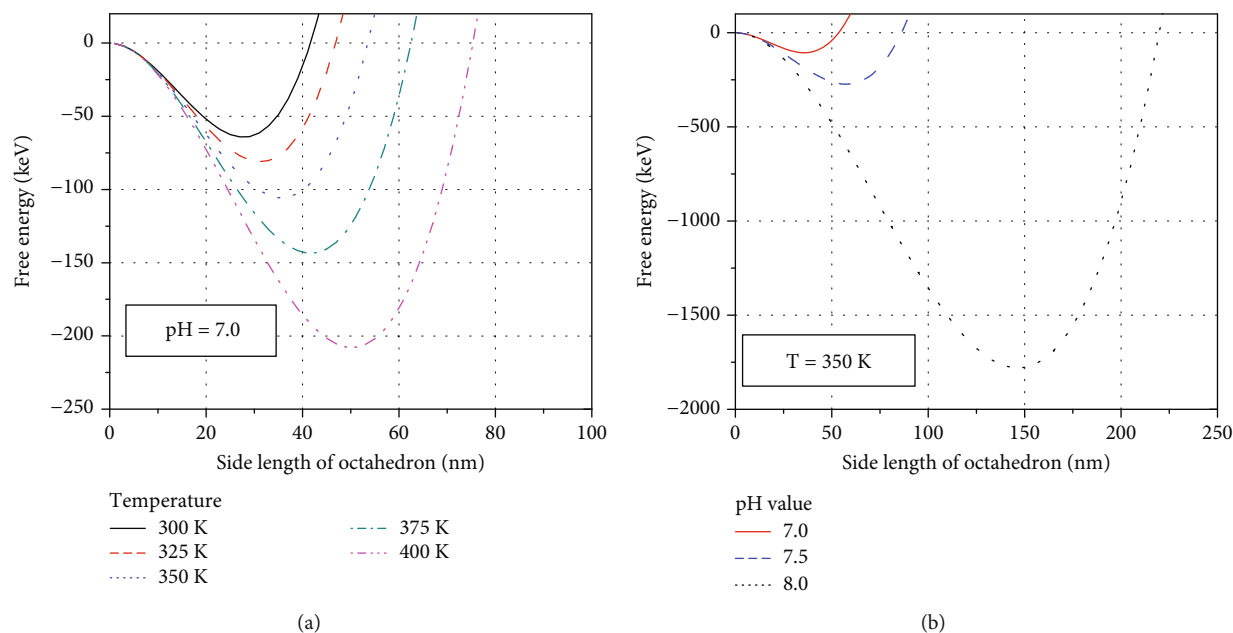


FIGURE 3: Free energies of formation of an octahedral nickel ferrite particle as a function of particle size for various (a) temperature and (b) pH values. The size of the nickel ferrite clusters associated with the free energy minima depends sensitively on temperature and pH.

hydroxylated nickel ferrite surfaces have been calculated. The lowest formation energy belongs to the (111) surface formed by tetrahedral cation terminations. As a general trend, under conditions of temperature, ion concentration, and pH characteristic to hydrothermal reactions, surfaces that expose a larger number of metal cations are the most stable. These surfaces are further stabilized by the adsorption of dissociated water molecules. At temperatures above 400 K, however, the water-induced stabilization decreases and the surfaces become denuded.

An important aspect of this study is related to the fact that the formation energy of the most stable (111) surface is negative, while the free energy of formation of the bulk material, under identical thermodynamic conditions, is positive. When creating a nickel ferrite particle, the energy cost associated with the formation of the bulk material is counterbalanced by the energy gained through the formation of the interface between the bulk and its aqueous surrounding. In terms of nucleation theory, the negative surface and positive bulk energies produce energy wells, with minima (and corresponding particle sizes) that depend sensitively on temperature, pH, and ion concentration. The general trend regarding the phase stability and predicted nanoparticle size and morphology as a function of thermodynamic conditions agrees well with the experiment.

Data Availability

Data are available in thermochemical databases and previous publications cited in this article.

Conflicts of Interest

The authors declare that they have no conflicts of interest.

Acknowledgments

This research was supported by the Consortium for Advanced Simulation of Light Water Reactors (<https://www.casl.gov>), an Energy Innovation Hub (<https://www.energy.gov/hubs>) for Modeling and Simulation of Nuclear Reactors under U.S. Department of Energy Contract No. DE-AC05-00OR22725.

References

- [1] P. Moriarty, *Reports on Progress in Physics*, vol. 64, no. 3, pp. 297–381, 2001.
- [2] H. Gleiter, “Tuning the electronic structure of solids by means of nanometer-sized microstructures,” *Scripta Materialia*, vol. 44, no. 8–9, pp. 1161–1168, 2001.
- [3] H. Gleiter, “Nanostructured materials: basic concepts and microstructure,” *Acta Materialia*, vol. 48, no. 1, pp. 1–29, 2000.
- [4] J. T. Hu, L. S. Li, W. D. Yang, L. Manna, L. W. Wang, and A. P. Alivisatos, “Linearly polarized emission from colloidal semiconductor quantum rods,” *Science*, vol. 292, no. 5524, pp. 2060–2063, 2001.
- [5] S. Komarneni, M. Tsuji, Y. Wada, and Y. Tamaura, “Nanophase ferrites for CO₂ greenhouse gas decomposition,” *Journal of Materials Chemistry*, vol. 7, no. 12, pp. 2339–2340, 1997.
- [6] E. Hasmonay, J. Depuyrot, M. H. Sousa, F. A. Tourinho, J. C. Bacri, and R. Perzynski, “Optical properties of nickel ferrite ferrofluids,” *Journal of Magnetism and Magnetic Materials*, vol. 201, no. 1–3, pp. 195–199, 1999.
- [7] D. Wirtz and M. Fermigier, “One-dimensional patterns and wavelength selection in magnetic fluids,” *Physical Review Letters*, vol. 72, no. 14, pp. 2294–2297, 1994.
- [8] D. E. Spiliotis, “Magnetic recording beyond the first 100 years,” *Journal of Magnetism and Magnetic Materials*, vol. 193, no. 1–3, pp. 29–35, 1999.

- [9] K. Maaz, A. Mumtaz, S. K. Hasanain, and M. F. Bertino, "Temperature dependent coercivity and magnetization of nickel ferrite nanoparticles," *Journal of Magnetism and Magnetic Materials*, vol. 322, no. 15, pp. 2199–2202, 2010.
- [10] K. Maaz, S. Karim, A. Mumtaz, S. K. Hasanain, J. Liu, and J. L. Duan, "Synthesis and magnetic characterization of nickel ferrite nanoparticles prepared by co-precipitation route," *Journal of Magnetism and Magnetic Materials*, vol. 321, no. 12, pp. 1838–1842, 2009.
- [11] D. Chen, D. Chen, X. Jiao, Y. Zhao, and M. He, "Hydrothermal synthesis and characterization of octahedral nickel ferrite particles," *Powder Technology*, vol. 133, no. 1-3, pp. 247–250, 2003.
- [12] Y. Cheng, Y. Zheng, Y. Wang, F. Bao, and Y. Qin, "Synthesis and magnetic properties of nickel ferrite nano-octahedra," *Journal of Solid State Chemistry*, vol. 178, no. 7, pp. 2394–2397, 2005.
- [13] M. M. Bučko and K. Haberko, "Hydrothermal synthesis of nickel ferrite powders, their properties and sintering," *Journal of the European Ceramic Society*, vol. 27, no. 2-3, pp. 723–727, 2007.
- [14] J. Huo and M. Wei, "Characterization and magnetic properties of nanocrystalline nickel ferrite synthesized by hydrothermal method," *Materials Letters*, vol. 63, no. 13-14, pp. 1183–1184, 2009.
- [15] M. Salavati-Niasari, F. Davar, and T. Mahmoudi, "A simple route to synthesize nanocrystalline nickel ferrite (NiFe_2O_4) in the presence of octanoic acid as a surfactant," *Polyhedron*, vol. 28, no. 8, pp. 1455–1458, 2009.
- [16] K. Sue, M. Aoki, T. Sato et al., "Continuous hydrothermal synthesis of nickel ferrite nanoparticles using a central collision-type micromixer: effects of temperature, residence time, metal salt molality, and NaOH addition on conversion, particle size, and crystal phase," *Industrial & Engineering Chemistry Research*, vol. 50, no. 16, pp. 9625–9631, 2011.
- [17] K. Nejati and R. Zabihi, "Preparation and magnetic properties of nano size nickel ferrite particles using hydrothermal method," *Chemistry Central Journal*, vol. 6, no. 1, p. 23, 2012.
- [18] D. Chen, X. Jiao, and G. Cheng, "Hydrothermal synthesis of zinc oxide powders with different morphologies," *Solid State Communications*, vol. 113, no. 6, pp. 363–366, 1999.
- [19] R. S. Sapiezko and E. Matijević, "Preparation of well-defined colloidal particles by thermal decomposition of metal chelates. I. Iron oxides," *Journal of Colloid and Interface Science*, vol. 74, no. 2, pp. 405–422, 1980.
- [20] C. J. O'Brien, Z. Rák, and D. W. Brenner, "Free energies of (Co, Fe, Ni, Zn) Fe_2O_4 spinels and oxides in water at high temperatures and pressure from density functional theory: results for stoichiometric NiO and NiFe_2O_4 surfaces," *Journal of Physics: Condensed Matter*, vol. 25, no. 44, article 445008, 2013.
- [21] C. J. O'Brien, Z. Rák, and D. W. Brenner, "Calculated stability and structure of nickel ferrite crystal surfaces in hydrothermal environments," *Journal of Physical Chemistry C*, vol. 118, no. 10, pp. 5414–5423, 2014.
- [22] C. J. O'Brien, Z. Rák, E. W. Bucholz, and D. W. Brenner, "First principles calculations predict stable 50 nm nickel ferrite particles in PWR coolant," *Journal of Nuclear Materials*, vol. 454, no. 1-3, pp. 77–80, 2014.
- [23] D. W. Brenner, S. Lu, C. J. O'Brien, E. W. Bucholz, and Z. Rak, "A particle assembly/constrained expansion (PACE) model for the formation and structure of porous metal oxide deposits on nuclear fuel rods in pressurized light water reactors," *Journal of Nuclear Materials*, vol. 457, pp. 209–212, 2015.
- [24] Z. Rak, C. J. O'Brien, D. W. Brenner, D. A. Andersson, and C. R. Stanek, *JOM*, vol. 68, no. 11, pp. 2912–2921, 2016.
- [25] O. Kubaschewski, C. B. Alcock, and P. J. Spencer, *Materials Thermochemistry*, Pergamon Press, New York, NY, USA, 6th edition, 1993.
- [26] M. W. Chase Jr, J. L. Curnutt, J. R. Downey Jr., R. A. McDonald, A. N. Syverud, and E. A. Valenzuela, "JANAF thermochemical tables, 1982 supplement," *Journal of Physical and Chemical Reference Data*, vol. 11, no. 3, pp. 695–940, 1982.
- [27] T. Windman and E. Shock, "A web-based interactive version of SUPCRT92," *Geochimica et Cosmochimica Acta*, vol. 72, article A1027, 2008.
- [28] J. W. Johnson, E. H. Oelkers, and H. C. Helgeson, "SUPCRT92: a software package for calculating the standard molal thermodynamic properties of minerals, gases, aqueous species, and reactions from 1 to 5000 bar and 0 to 1000°C," *Computers & Geosciences*, vol. 18, no. 7, pp. 899–947, 1992.
- [29] G. Kresse and J. Furthmüller, "Efficient iterative schemes for *ab initio* total-energy calculations using a plane-wave basis set," *Physical Review B*, vol. 54, no. 16, pp. 11169–11186, 1996.
- [30] G. Kresse and J. Furthmüller, "Efficiency of *ab-initio* total energy calculations for metals and semiconductors using a plane-wave basis set," *Computational Materials Science*, vol. 6, no. 1, pp. 15–50, 1996.
- [31] J. P. Perdew, K. Burke, and M. Ernzerhof, "Generalized gradient approximation made simple," *Physical Review Letters*, vol. 77, no. 18, pp. 3865–3868, 1996.
- [32] S. L. Dudarev, G. A. Botton, S. Y. Savrasov, C. J. Humphreys, and A. P. Sutton, "Electron-energy-loss spectra and the structural stability of nickel oxide: an LSDA+U study," *Physical Review B*, vol. 57, no. 3, pp. 1505–1509, 1998.
- [33] Z. Rák, E. W. Bucholz, and D. W. Brenner, "Defect formation in aqueous environment: theoretical assessment of boron incorporation in nickel ferrite under conditions of an operating pressurized-water nuclear reactor (PWR)," *Journal of Nuclear Materials*, vol. 461, pp. 350–356, 2015.
- [34] Z. Rak, C. J. O'Brien, D. Shin, A. D. Andersson, C. R. Stanek, and D. W. Brenner, "Theoretical assessment of bonaccordite formation in pressurized water reactors," *Journal of Nuclear Materials*, vol. 474, pp. 62–64, 2016.
- [35] Z. Lodziana, N. Y. Topsoe, and J. K. Norskov, "A negative surface energy for alumina," *Nature Materials*, vol. 3, no. 5, pp. 289–293, 2004.
- [36] Z. Rak, R. C. Ewing, and U. Becker, "Hydroxylation-induced surface stability of AnO_2 (An=U, Np, Pu) from first-principles," *Surface Science*, vol. 608, pp. 180–187, 2013.
- [37] Y. J. Siao, P. L. Liu, and Y. T. Wu, "*Ab initio* study of atomic hydrogen on ZnO surfaces," *Applied Physics Express*, vol. 4, no. 12, article 125601, 2011.
- [38] P. V. Kumar, M. P. Short, S. Yip, B. Yildiz, and J. C. Grossman, "High surface reactivity and water adsorption on NiFe_2O_4 (111) surfaces," *Journal of Physical Chemistry C*, vol. 117, no. 11, pp. 5678–5683, 2013.

Research Article

Optimization of a Hydrothermal Growth Process for Low Resistance 1D Fluorine-Doped Zinc Oxide Nanostructures

Muhammad L. M. Napi ¹, S. M. Sultan ¹, Razali Ismail ¹, Mohd K. Ahmad,²
and G. M. T. Chai³

¹Computational Nanoelectronics Research Lab, School of Electrical Engineering, Universiti Teknologi Malaysia Johor Bahru, 81310 Skudai, Johor, Malaysia

²Microelectronics and Nanotechnology-Shamsuddin Research Centre, Universiti Tun Hussein Onn Malaysia, 86400 Parit Raja, Johor, Malaysia

³University of Southampton Malaysia Campus, Johor, Malaysia

Correspondence should be addressed to S. M. Sultan; suhanasultan@utm.my

Received 1 February 2019; Revised 2 June 2019; Accepted 27 June 2019; Published 14 August 2019

Guest Editor: Yong X. Gan

Copyright © 2019 Muhammad L. M. Napi et al. This is an open access article distributed under the Creative Commons Attribution License, which permits unrestricted use, distribution, and reproduction in any medium, provided the original work is properly cited.

Design of Experiment (DOE) has been used for the optimization of a hydrothermal growth process of one-dimensional fluorine-doped zinc oxide (1D-FZO). Box-Behnken design was used in the DOE which includes three design points on each of the synthesis condition parameters. The condition parameters were the gold sputtering time (10 s, 15 s, and 20 s), hydrothermal reaction time (3 hours, 6.5 hours, and 10 hours), and hydrothermal temperature (50°C, 75°C, and 100°C). This statistical method of DOE was used to study the effects of these hydrothermal conditions on the quality of 1D-FZO produced. Au nanoparticles were used as the catalyst to enable the growth of the 1D-FZO. The XRD and EDX analysis confirmed the formation of polycrystalline FZO with the presence of fluorine, zinc, and oxygen elements. SEM observations indicated that the sputtering time of the Au nanoparticles has significant effect on the morphology and growth process of 1D-FZO. The lowest resistance value of 22.57 Ω was achieved for 1D-FZO grown with the longest Au sputtering time at growth temperature below 100°C.

1. Introduction

Nanostructured zinc oxide (ZnO) has been attracting a lot of attention due to its capability of working in a variety of applications such as dye-sensitised solar cells [1], biosensors [2], gas sensors [3], and organic light-emitting diodes [4]. This n-type semiconductor has demonstrated experimentally that it has fast electron transfer kinetic, high isoelectric point, and wide band gap of 3.37 eV at ambient condition [5, 6]. Furthermore, its unique morphology especially one-dimensional structures (nanorod) made it as one of the promising nanomaterials. In fact, 1D-ZnO can provide a stable and direct electron transfer [7]. In addition, the presence of the dopant element in the ZnO system can affect its electrical properties. Previously, influence of nitrogen, copper, aluminium, and fluorine dopant on ZnO was extensively studied [8–11]. Among them, the fluorine element is the most effective dopant for the ZnO matrix as it could avoid

the lattice distortion and produce an efficient charge carrier without an electron trap [12]. Since 1948, the demand of low-cost and environment-friendly fabrication processes for nanostructures leads to the development of a hydrothermal process [13]. This method plays an important role in producing crystalline 1D-ZnO on various substrates including glass, silicon, and polymer [14, 15]. Furthermore, the nanostructures' properties can be tuned by varying different parameters of a hydrothermal process such as the reaction time, temperature, concentration of a precursor, and the pH value of the solutions. Boubenia et al. [16] focused on the best concentration of ammonia (as an additive) for producing a high aspect ratio of ZnO nanowires. Meanwhile, the experiment conducted by Jiao et al. [17] found that the growth duration of ZnO nanorods influenced their structural size and electrical properties. Wahid et al. used gold nanoparticles (Au-np) as a nucleation site for the hydrothermal growth of 1D-ZnO and at the same time improved the adhesive surface

layer of the substrate [18]. From their results, Au nanoparticles could promote the growth of 1D-ZnO in shorter time [18]. However, they disregarded to optimize the amount of Au-np on the substrate. The high concentration of Au-np may lead to excess of impurities and can become the dominant layer which is able to influence the electrical performance of the device. It was found that the previous work only focused on one parameter at one time. Although, this optimization approach improved performance of the nanostructures, it limits to a fixed (certain) condition.

The Response of Surface Methodology (RSM) has been used to indicate the unknown relationship between the independent variables (input factor) and the process response. This method actually a combination of statistical and mathematical techniques to analyze, model, and optimize processes [19]. Initially, the observations are made to fit either a linear function also known as a first-order model or a second-order model which is suitable to be used based on the results produced [20]. Choosing the best experimental design significantly influences the efficiency of the response analysis. Therefore, Box-Behnken and Central Composite Design (CCD) are the most favourable class of design to fit response surfaces. To optimize the quality of ZnO film deposition, Sultan et al. [21] applied the Box-Behnken design in their study to determine the impact of remote plasma parameters on the film deposited.

Similarly, Design of Experiment (surface response methodology) is used in this study to identify the impact of hydrothermal conditions (reaction time and temperature) and Au sputtering time to produce a good quality 1D-FZO. However, CCD design is not compatible since there is a concern regarding the process of constraints to test each factor at extreme levels. As a result, the Box-Behnken technique was selected to design the experiment, since its factorial combinations do not include any points at the vertices of the cubic region and the resulting design is still rotatable as shown in Figure 1. The electrical, structural, elemental, and morphological properties of 1D-FZO produced were examined using a semiconductor parameter analyzer, X-ray diffractometer (XRD), energy dispersive X-ray spectroscopy (EDX), and a variable-pressure scanning electron microscope (VPSEM), respectively.

2. Experimental Method

2.1. Synthesis. 1D-FZO nanostructures were fabricated on a glass substrate via hydrothermal process. For optimization, the Box-Behnken design was used which includes three design points to correspond to each synthesis condition parameter. There were three design factors or condition parameters considered in this work which were the gold sputtering time (10 s, 15 s, and 20 s), hydrothermal reaction time (3 hours, 6.5 hours, and 10 hours), and hydrothermal temperature (50°C, 75°C, and 100°C). Unblocked Box-Behnken design for three factors was chosen with 15 experiments to run. The precursors used for FZO were zinc nitrate (alfa aesar, 99%), hexamethylenetetramine (alfa aesar, 99 +%), and ammonium fluoride (R&M) with equimolar of 0.01 M in DI water. The precursor solutions were stirred for

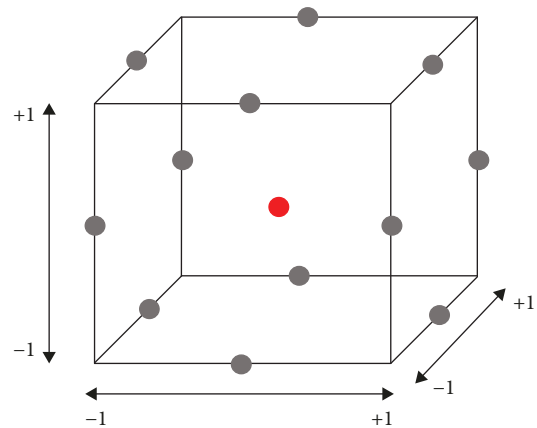


FIGURE 1: Surface response methodology (Box-Behnken design) for three factors.

1 hour at ambient temperature. At the same time, 2×2 cm glass substrates were immersed in 2-propanol and ethanol solution inside an ultrasonic cleaner for 15 minutes. Next, the substrates were coated with gold nanoparticles by sputter coating at constant current (60 mA) with three different sputtering times to enhance its adhesiveness on the surface layer. Then, the substrates were rinsed with 2-propanol solution before drying in an oven under 100°C for 15 minutes to remove any moist on its surface. The cleaned substrates were placed inside the autoclave by facing downwards as illustrated in Figure 2(a). Finally, the precursor solution was poured gently into the autoclave for the subsequent growth process in the oven. After growing, an aluminium contact was deposited on FZO as a metal contact. The distance between the two metal contacts was fixed at 1 cm as shown in Figure 2(b).

2.2. Characterization. The electrical characteristics were measured using a B1500 Semiconductor Parameter Analyzer. The current response was recorded between -1 V and 1 V. The surface morphology of 1D-FZO synthesized with different parameters was studied in a scanning electron microscope (VPSEM) (JEOL JSM-IT300LV). The element composition was examined by using an energy dispersive X-ray spectroscopy (EDX) which is attached with the SEM system. For structural analysis, measurements were conducted by X-ray diffraction (XRD) (Rigaku SmartLab).

3. Results and Discussion

3.1. Optimization of Hydrothermal Growth. To determine the optimal growth parameters, a series of preliminary hydrothermal growth experiments were conducted. These initial experiments were conducted to determine the effect of different process parameters during the growth towards the electrical properties of FZO. In this experiment, the concentration of $\text{Zn}(\text{NO}_3)_2 \cdot 6\text{H}_2\text{O}$, HMT, and NH_4F were fixed at 0.01 M. The Au sputtering time, hydrothermal reaction time, and hydrothermal temperature were varied systematically based on Box-Behnken design. After each synthesis, the FZO sample was measured for its resistance using the

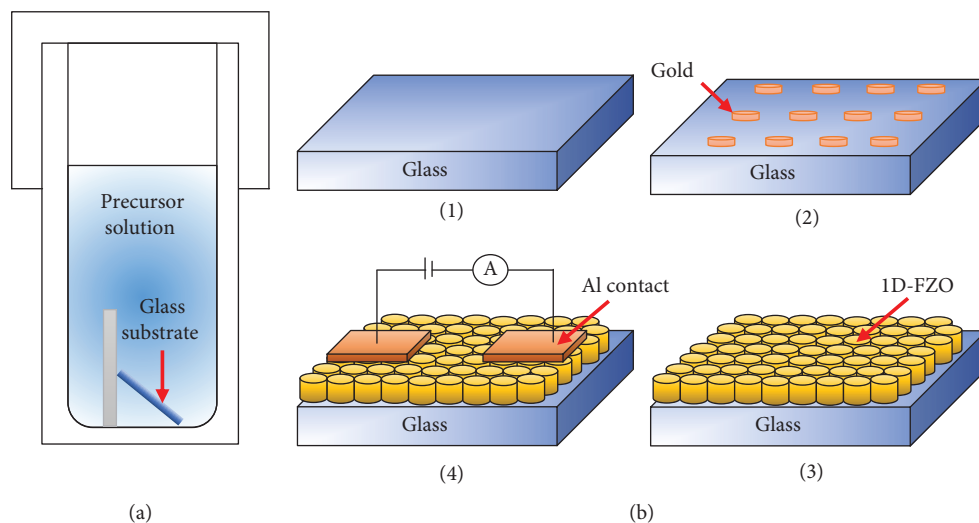


FIGURE 2: (a) A schematic diagram of substrate in an autoclave, top surface of glass was facing down. (b) A process flow for 1D-FZO fabrication: (1) 2×2 cm of glass substrate, (2) gold nanoparticles were coated on a glass by sputter coating, (3) hydrothermal growth of 1D-FZO, and (4) aluminium was deposited on 1D-FZO to perform the electrical measurement.

parameter analyzer. Table 1 shows the DOE parameters generated with its corresponding resistance values measured for each sample. The lowest resistance values measured for the sample grown with Au sputtering time of 10 s, 15 s, and 20 s were 571.43 Ω , 94.42 Ω , and 22.57 Ω , respectively. As Au nanoparticles have contributed to the electrical properties, three contour plots were produced separately based on three sputtering times, 10 s, 15 s, and 20 s as shown in Figures 3(a) and 3(b), respectively. The x -axis and y -axis represent the hydrothermal reaction time and the hydrothermal temperature, respectively. Samples with 10 s of Au sputtering time showed that low-resistance-nanostructured material can be produced at a temperature $> 60^\circ\text{C}$. Samples with 15 s of Au sputtering time showed that low reaction times are required to produce low-resistance-nanostructured material at a wider temperature range.

Interestingly, from Figure 3(b), it only needs 3 hours of reaction time in order to obtain the lowest resistance value. In contrast, for samples with 20 s of Au sputtering time, the lowest resistance was achieved at 7 hours~10 hours of reaction time as shown in Figure 3(c).

Figure 4(a) shows the three main effects plot towards the resistance of the samples produced. The Au sputtering time shows a significant effect on the electrical resistance values of the FZO nanostructures. This indicates that Au sputtering time plays an important role to tune the electrical properties of the samples. Initially, the resistance decreases with increasing sputtering times. However, at 20 s of sputtering time, the resistance increases slightly forming an arch. The initial measurements on substrate with Au nanoparticles before the FZO growth process exhibit no electrical response. Figure 4(b) shows the effect of resistance against the sputtering time with three different temperatures. When the hydrothermal temperature increases, the resistance of the FZO nanostructures also reduces.

Based on the main effect plot in Figure 4(a), the range of the optimized conditions to obtain the lowest resistance

TABLE 1: Design matrix for I-V measurements.

Standard order	Sputtering time (s)	Temperature ($^\circ\text{C}$)	Reaction time (h)	Resistance (Ω)
1	10	50	6.5	571.43
2	20	50	6.5	28.06
3	10	100	6.5	4074.98
4	20	100	6.5	29.98
5	10	75	3.0	3130.87
6	20	75	3.0	22.57
7	10	75	10.0	2119.09
8	20	75	10.0	64.81
9	15	50	3.0	149.47
10	15	100	3.0	303.95
11	15	50	10.0	94.52
12	15	100	10.0	94.42
13	15	75	6.5	267.38
14	15	75	6.5	240.38
15	15	75	6.5	286.53

nanostructures is as follows: sputtering time of 15~20 s, hydrothermal reaction time of 3 hours, and the hydrothermal temperature of 75~100 $^\circ\text{C}$.

To study in detail the effect of Au sputtering time and hydrothermal temperature on the produced FZO nanostructures, further characterizations were executed such as their morphological, structural, and elemental properties.

3.2. Structural and Elemental Analysis. The XRD analysis was carried out in order to investigate the crystal structure of fabricated 1D-FZO. An X-ray source operated at 40 kV and 30 mA was used. The diffraction patterns were collected over 0° - 100° with a step width 0.1° and scan speed of 10.0619 $^\circ$ /min. Figure 5 depicts XRD spectrum for FZO

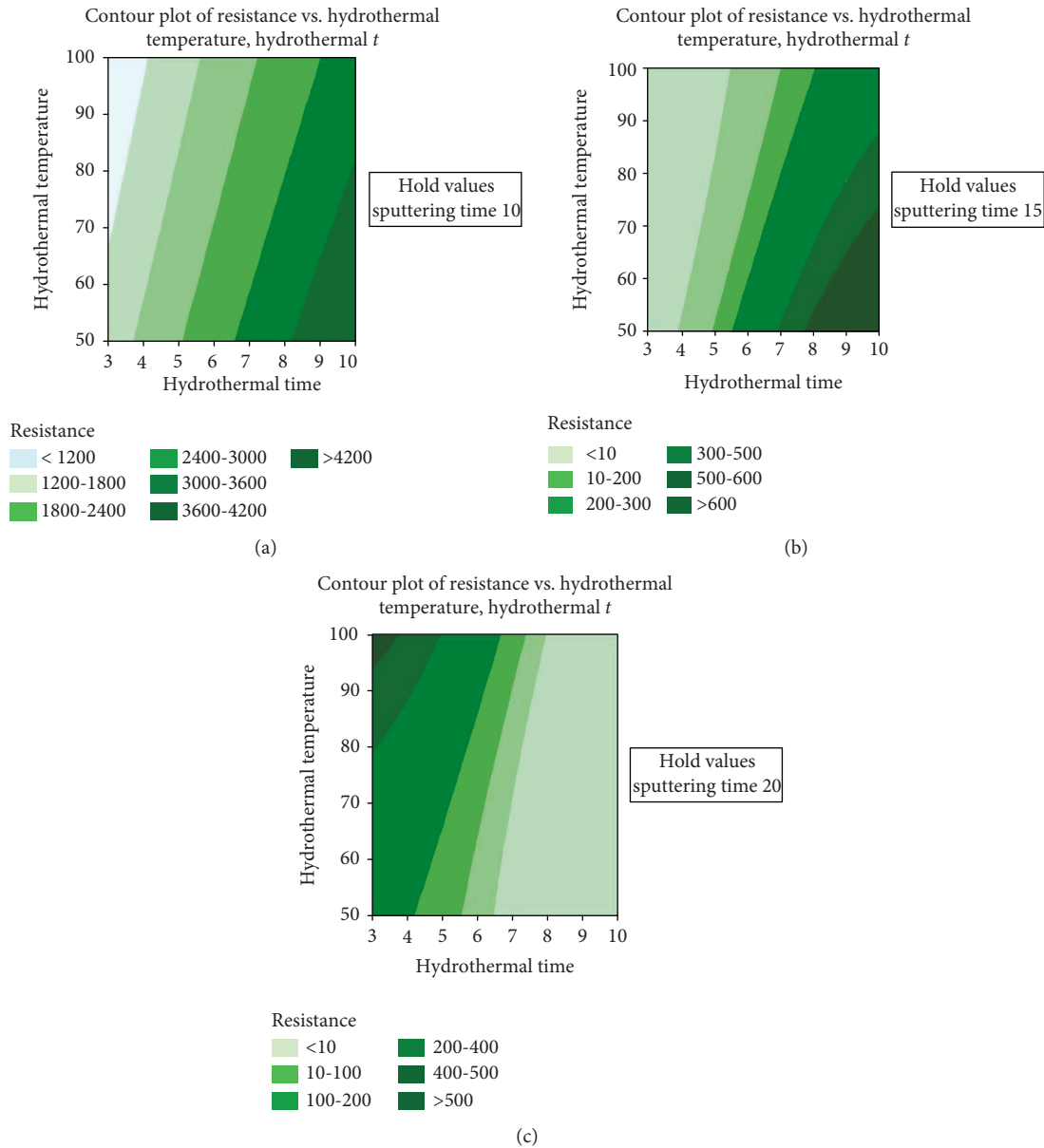


FIGURE 3: Generated contour plot of measured resistance (Ω) when reaction time (in hours) and temperature (in $^{\circ}\text{C}$) were varied for (a) 10 s, (b) 15 s, and (c) 20 s of Au sputtering time.

fabricated on 15 s of Au sputtering time, 100°C of hydrothermal temperature for 10 hours of reaction time. As can be seen, the major XRD peaks were detected with diffraction of (100), (002), and (101) planes and all the peaks are indexed to hexagonal wurtzite ZnO according to the 01-082-3143 ICDD file. From the observation of the XRD spectrum, the peaks only showed the presence of the ZnO phase without the fluorine phase. A similar result was found in FTO film structure because the fluorine phase overlapped with the SnO_2 peaks [22]. This is due to the level of fluorine doping which is relatively small with respect to the host lattice. However, the existence of the fluorine element can be detected using EDX analysis.

The EDX spectrum of fabricated FZO with three different Au sputtering times is presented in Figures 6(a)–6(c). All

samples show the presence of fluorine (F), zinc (Zn), and oxygen (O) elements as main composition in FZO. Furthermore, weight percentage of the Au material was decreased when Au nanoparticles were sputtered at longer time. This confirmed that samples prepared consist of polycrystalline FZO as supported by XRD result.

3.3. Surface Morphology. The Au nanoparticles improve the adhesiveness of the surface layer thus promoting nanostructure growth. Since sputtering time significantly impacted to the initial growth process as reported in [23], the surface morphology presented in this section focused on three different Au sputtering times: 10 s, 15 s, and 20 s (Figures 7(a)–7(c)). The samples shown in Figures 7(a)–7(c) exhibited the lowest resistance based on the contour plot shown earlier

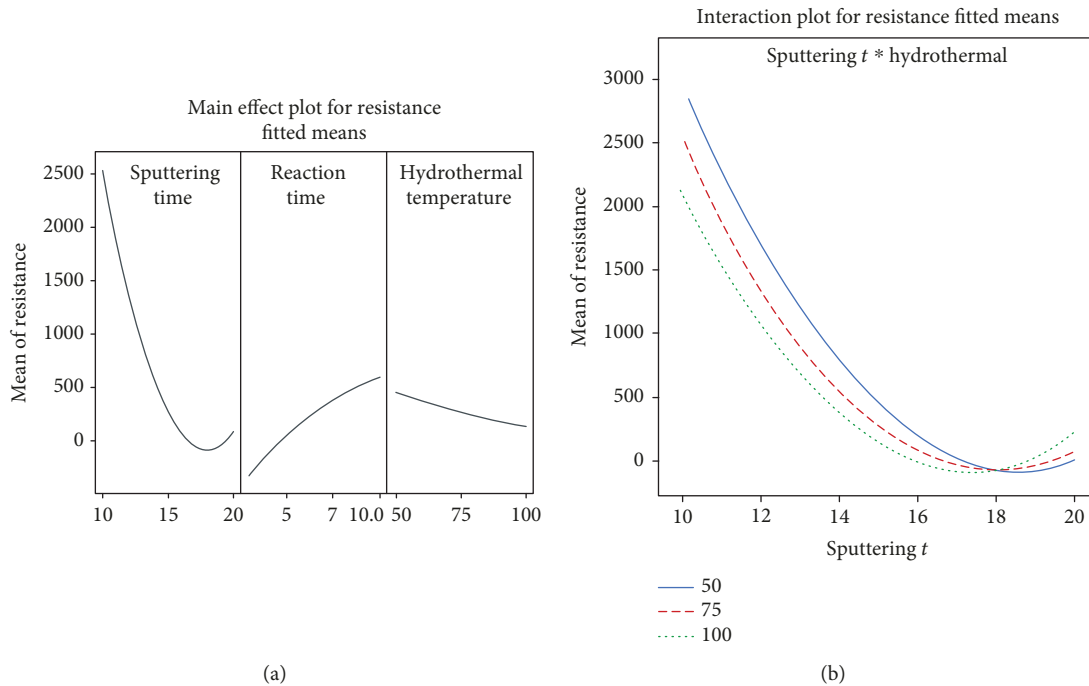


FIGURE 4: (a) Generated main effect plot of measured resistance (Ω) against sputtering times in seconds (s), hydrothermal reaction times in hours, hydrothermal temperatures in $^{\circ}\text{C}$. (b) Interaction plot of resistance with sputtering times and hydrothermal temperatures.

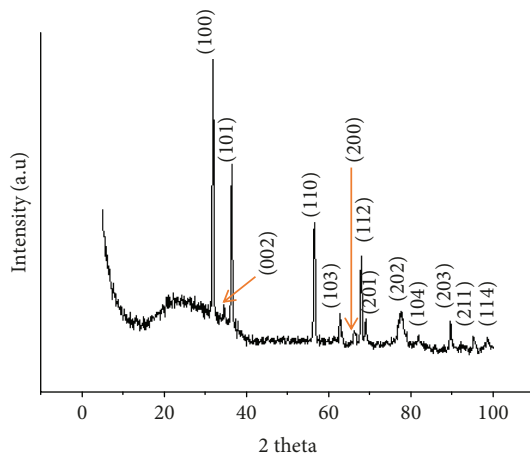


FIGURE 5: XRD spectrum of 1D-FZO grown with 15 s of sputtering time under 100°C for 10 hours of reaction time.

for different sputtering times of the Au nanoparticles. Therefore, the growth process conditions for the three samples were not the same. Figure 7(a) shows the formation of FZO nanoparticles for shortest Au sputtering time, 10 s. Meanwhile, 15 s of sputtering time indicated that FZO nanostructures starting to grow into 1D formation. However, the lengths of the nanostructures formed were not uniform (Figure 7(b)). The size of the FZO increased when the substrate was coated with Au nanoparticles at 20 s. In this sample, it only needs low temperature and low reaction time to grow 1D-FZO compared to the other samples produced with shorter sputtering time.

The growing process for FZO nanostructures using the hydrothermal method is based on reactant species and the crystallographic orientation of hexagonal wurtzite FZO. HMT was used to maintain the neutral behaviour of solution at pH 7 and provided a hydroxyl group for ZnO formation [24]. First, formaldehyde ($6\text{CH}_2\text{O}$) was formed when HMT solution was heated. Then, ammonia (NH_3) continues to hydrolyze and produce ammonium (NH_4^+) and hydroxyl ions (OH^-) [25]. The chemical reaction can be described as equations (1) and (2) [26].

HMT decomposition reaction

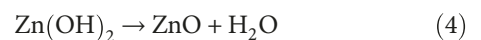


As the concentration of these Zn^{2+} and OH^- ions exceeds a critical value, the precipitation of ZnO nuclei starts. The $\text{Zn}(\text{OH})_2$ was transformed into ZnO crystals via these simple chemical reactions.

Formation of complex compound of $\text{Zn}(\text{OH})_2$



Dehydration



Meanwhile, the decomposition of NH_4F took place simultaneously according to equation (5) [27].

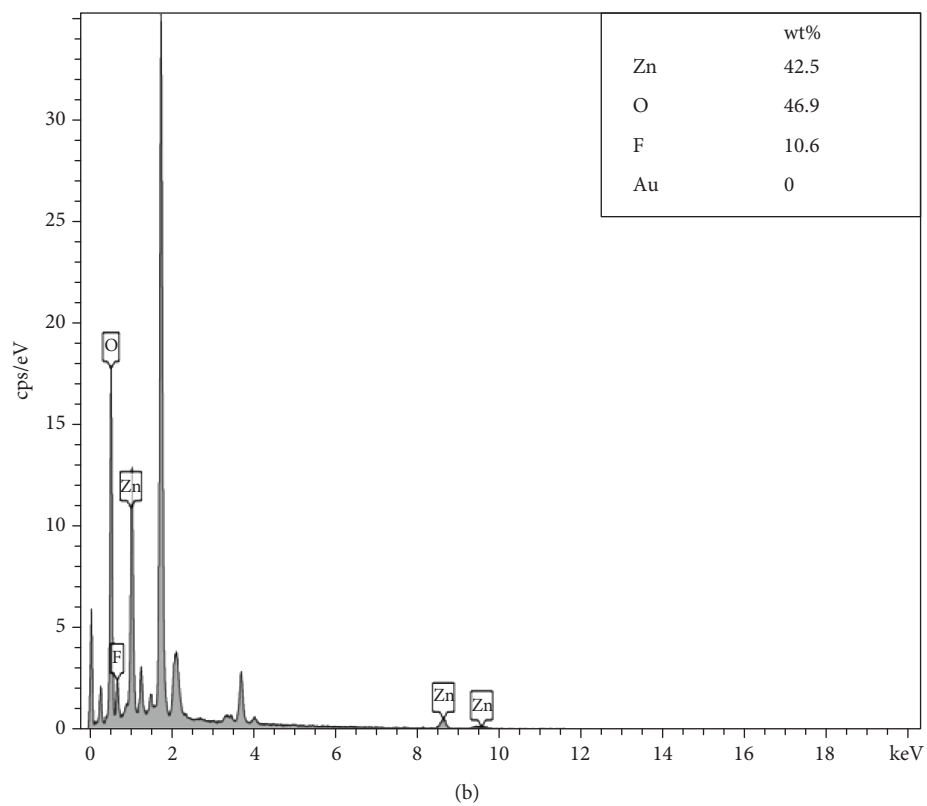
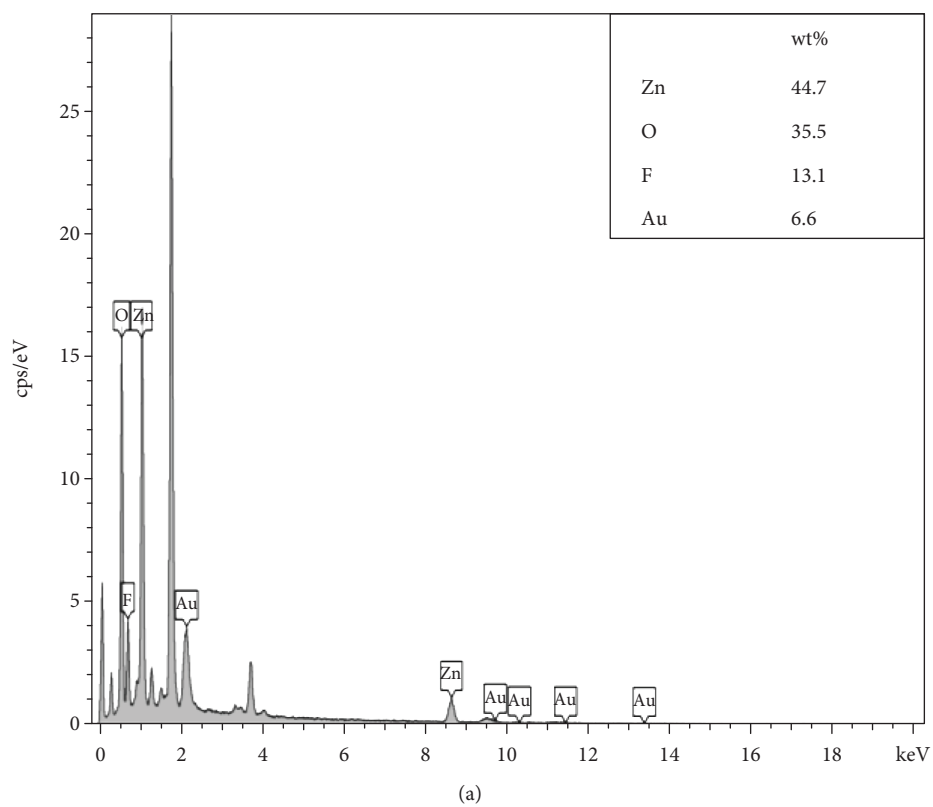


FIGURE 6: Continued.

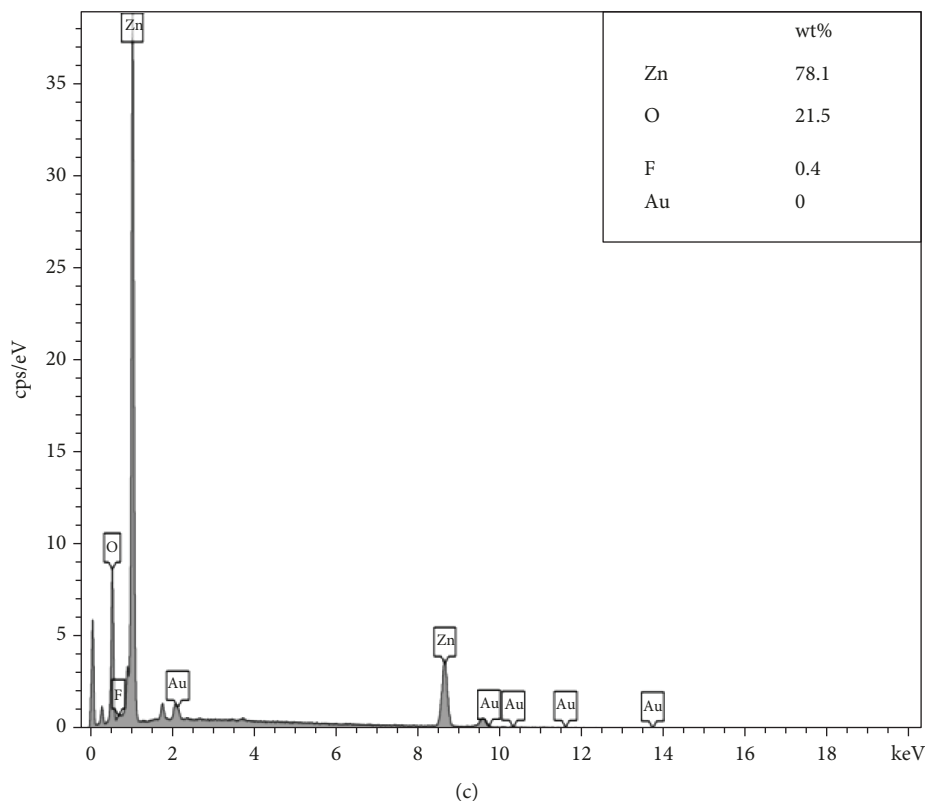


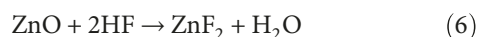
FIGURE 6: EDX spectrum of FZO deposited on three different Au sputtering times (a) 10 s, (b) 15 s, and (c) 20 s.

Formation of halo acid



The chemical reaction between the growing ZnO and the halo acid leads to equation (6).

Doped process



3.4. Growth Mechanism. A possible growth formation of FZO on three different Au sputtering times is proposed. Au nanoparticles have a function similar to that of seed layers which is to promote the further growth of 1D structures [23]. It also acted as nucleus site for initial growth after the nucleation process [16]. As stated by Demes et al. [28], the nucleation process can occur at two possible conditions which are on seed layer surface or at their grain boundaries [25]. Au nanoparticles were sputter coated on the glass substrate at three different times to produce three different samples. It was believed that, after a shorter time, the Au nanoparticles deposited would not be distributed uniformly on the substrate surface.

The growth mechanisms of FZO are illustrated in Figures 8(a)–8(c). During the early stage of a hydrothermal process, there were two types of processes occurred which were physisorption (adsorb) and surface diffusion. Physisorbed species could move at finite distances on the substrate [29]. Since the glass substrate has high activation energy, the surface diffusion process was difficult to achieve. As a result,

physisorbed species has high tendency to desorb. Here, Au nanoparticles functioned as large nuclei attracting physisorbed species by forming chemical bonds. Through coalesces with nearby nuclei, a thin first layer is formed [29]. The increase of FZO thickness was achieved by increasing the hydrothermal temperature which promote a nucleation process as shown in Figure 8(a). At this stage, the nucleation rate was higher and grains were easier to coalesce [30]. A similar mechanism for substrate with 15 s of Au sputtering time. However, the coating process for this sample took longer than the previous sample. Therefore, there is a high chance for more nucleus sites deposited on the substrate. As a result, the growth species assembled each other into 1D formation. Some parts on the substrate surface only produced nanoparticles illustrated in Figure 8(b). This phenomenon is clearly observed in the SEM image in Figure 7(b). The 1D nanostructures were grown with different lengths and sizes. Interestingly, after 20 s of Au sputtering time, the 1D-FZO with lowest resistance was achieved in 3 hours at 75°C as shown in the SEM image (Figure 7(c)). This suggested that, after the longer times (coating process), Au nanoparticles were well distributed along the substrate surface (Figure 8(c)). As a result, 1D-FZO was easier to grow even with shorter reaction time. Then, as the temperature increased, their size were also increased and this finding is similar to the results of a previous study by Heinonen et al. [31].

3.5. Effect of 1D-FZO Morphology towards Electrical Properties. One of the factors that affect the resistance values of the FZO is the grain boundary. It presents a discontinuity

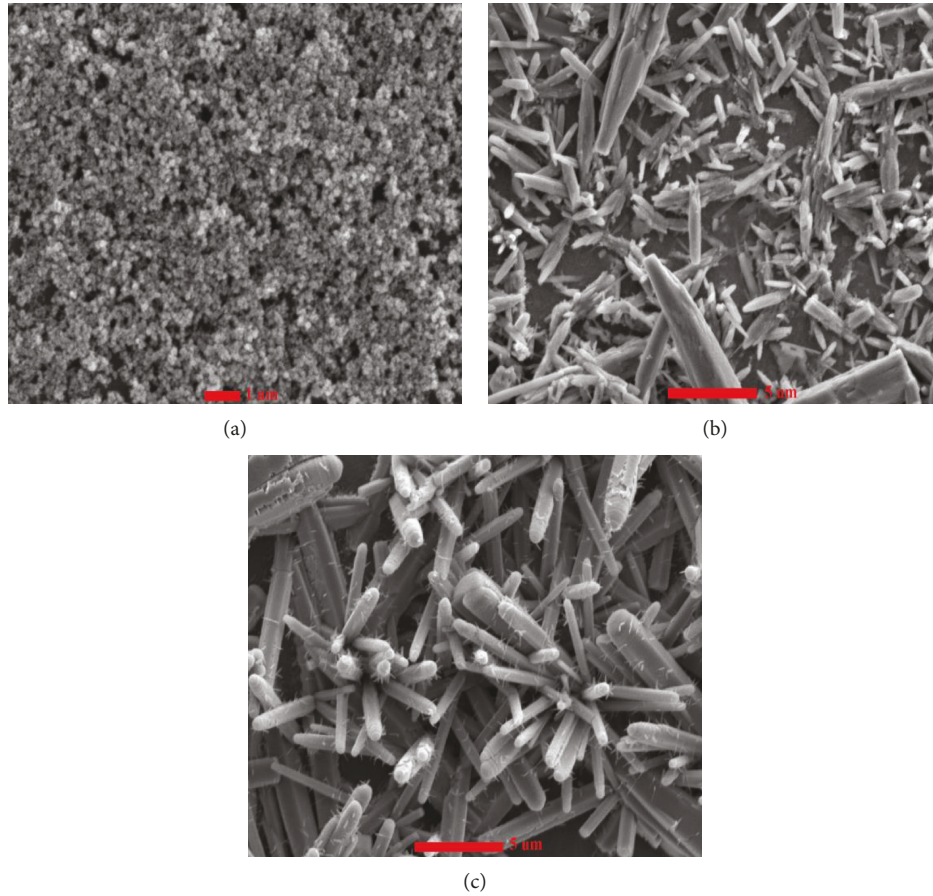


FIGURE 7: SEM images of FZO deposited at different sputtering times, temperatures and reaction times: (a) 10 s, 50°C, 6.5 hours; (b) 15 s, 100°C, 10 hours, and (c) 20 s, 75°C, 3 hours, respectively.

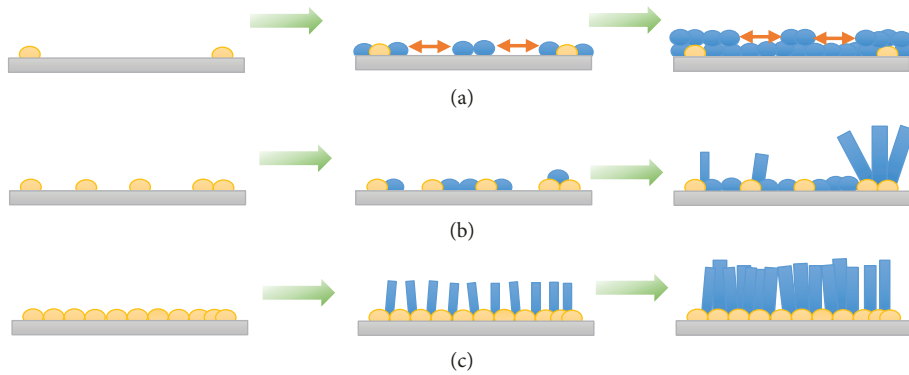


FIGURE 8: Illustration of the growth mechanism of FZO at different Au sputtering times (a) 10 s, (b) 15 s, and (c) 20 s.

in the crystalline of the FZO. Between the grain boundaries, a space charge region formed resulting in a potential barrier scattering of the electrons and reducing their mobility [32]. This condition can occur for samples coated with Au nanoparticles at 10 s and 15 s of sputtering time. As the temperature increased, the grain size with improvement in crystallinity contributed to the increase of carrier mobility as well. The total interfacial grain boundary was reduced when the grain size increases [30]. These findings agree with

the results of the previous studies conducted by Kim et al. [33] and Napi et al. [34]. For substrate coated with Au nanoparticles at longest sputtering time, the nanostructures grown are more uniform but nanoneedle structure attached on nanorods as clearly seen in Figure 7(c). In fact, the 1D-FZO can provide a stable and direct electron transfer than the ZnO nanoparticles [7]. However, the nanoneedles which were attached on nanorods affected their resistance. Furthermore, the increase in temperature increased the number of

nanoneedles. Consequently, the resistance of the FZO also increased. This is verified from the contour plot (Figure 3(c)) which indicated that at low temperature, the measured resistance values were low. Subsequently, the resistance values recorded increased as the temperature increased.

4. Conclusion

From the Design of Experiment analysis, the Au sputtering time showed a significant effect on the resistance of 1D-FZO nanostructures compared to the other two parameters which are hydrothermal reaction time and temperatures. From the main effect plots and the contour plots, the optimized grow low resistance 1D-FZO are with sputtering time of 15~20 s, hydrothermal reaction time of 3 hours, and at temperature range of 75~100°C. It was evident from the SEM observations that by increasing the sputtering time, the 1D-FZO nanostructures are easier to grow with less reaction time (3 hours) and at lower temperature (75°C). This can be due to the increase density of the Au nanoparticles when the sputtering time increases. Samples coated with Au nanoparticles with less sputtering time form many grain boundaries which form a potential barrier for the electrons, hence reducing the mobility. However, the increase in temperature increased the grain size with improvement in crystallinity which contributed to the decrease of the nanostructure resistance. From the growth mechanism proposed, Au nanoparticles form nucleus sites to promote growth species to assemble each other into 1D formation. Longer Au sputter time caused the Au nanoparticles to be well distributed along substrate surface. As a result, 1D-FZO was easier to grow even with shorter reaction time. This discovery could facilitate the fabrication of various 1D-FZO nanomaterial-based devices such as transparent conducting oxide, biosensor, and optical detector.

Data Availability

All data obtained from characterization technique used to support this study are available from the corresponding author upon request.

Conflicts of Interest

The authors declare that they have no conflicts of interest.

Acknowledgments

This work was supported by the Ministry of Education Malaysia through Fundamental Research Grant Scheme (FRGS) vot 5F053, Research University grant of Universiti Teknologi Malaysia GUP Tier 1, vot no. 19H33, and UoSM 2018/18 seed fund. The authors would like to acknowledge the fabrication and experimental support from the Micro-Nano Systems Engineering, School of Electrical Engineering, Universiti Teknologi Malaysia, and University-Industry Research Lab of UTM. The authors also acknowledge the support from the UTM Research Management Centre.

References

- [1] A. Hezam, K. Namratha, Q. A. Drmoseh et al., "Electronically semitransparent ZnO nanorods with superior electron transport ability for DSSCs and solar photocatalysis," *Ceramics International*, vol. 44, no. 6, pp. 7202–7208, 2018.
- [2] S. M. Sultan, M. R. R. de Planque, P. Ashburn, and H. M. H. Chong, "Effect of phosphate buffered saline solutions on top-down fabricated ZnO nanowire field effect transistor," *Journal of Nanomaterials*, vol. 2017, Article ID 5413705, 7 pages, 2017.
- [3] W. Khoo and S. M. Sultan, "A study on the gas sensing effect on current-voltage characteristics of ZnO nanostructures," in *IEEE International Conference on Semiconductor Electronics (ICSE2014)*, pp. 221–224, 2014.
- [4] D. Dong, Y. Wang, L. Lian, D. Feng, H. Wang, and G. He, "Novel solution-processed ZnO-based electron injection layer for organic light-emitting diodes," *Physica Status Solidi (a)*, vol. 214, no. 12, 2017.
- [5] F. Zhou, W. Jing, P. Liu, D. Han, Z. Jiang, and Z. Wei, "Doping Ag in ZnO nanorods to improve the performance of related enzymatic glucose sensors," *Sensors*, vol. 17, no. 10, p. 2214, 2017.
- [6] N. Izyumskaya, A. Tahira, Z. H. Ibupoto et al., "Review—Electrochemical Biosensors Based on ZnO Nanostructures," *ECSE Journal of Solid State Science and Technology*, vol. 6, no. 8, pp. Q84–Q100, 2017.
- [7] N. Wei, H. Cui, X. Wang et al., "Hierarchical assembly of In₂O₃ nanoparticles on ZnO hollow nanotubes using carbon fibers as templates: enhanced photocatalytic and gas-sensing properties," *Journal of Colloid and Interface Science*, vol. 498, pp. 263–270, 2017.
- [8] K. Jindal, M. Tomar, and V. Gupta, "Nitrogen-doped zinc oxide thin films biosensor for determination of uric acid," *Analyst*, vol. 138, no. 15, pp. 4353–4362, 2013.
- [9] M. G. Nair, M. Nirmala, K. Rekha, and A. Anukaliani, "Structural, optical, photo catalytic and antibacterial activity of ZnO and Co doped ZnO nanoparticles," *Materials Letters*, vol. 65, no. 12, pp. 1797–1800, 2011.
- [10] M. W. Kadi, D. McKinney, R. M. Mohamed, I. A. Mkhallid, and W. Sigmund, "Fluorine doped zinc oxide nanowires: enhanced photocatalysts degrade malachite green dye under visible light conditions," *Ceramics International*, vol. 42, no. 4, pp. 4672–4678, 2016.
- [11] S. O. El hamali, W. M. Cranton, N. Kalfagiannis, X. Hou, R. Ranson, and D. C. Koutsogeorgis, "Enhanced electrical and optical properties of room temperature deposited Aluminium doped Zinc Oxide (AZO) thin films by excimer laser annealing," *Optics and Lasers in Engineering*, vol. 80, pp. 45–51, 2016.
- [12] J. Chang, Z. Lin, M. Lin, C. Zhu, J. Zhang, and J. Wu, "Solution processed F doped ZnO (ZnO:F) for thin film transistors and improved stability through co-doping with alkali metals," *Journal of Materials Chemistry C*, vol. 3, no. 8, pp. 1787–1793, 2015.
- [13] M. Shandilya, R. Rai, and J. Singh, "Review: hydrothermal technology for smart materials," *Advances in Applied Ceramics*, vol. 115, no. 6, pp. 354–376, 2016.
- [14] Z. Yu, H. Li, Y. Qiu et al., "Size-controllable growth of ZnO nanorods on Si substrate," *Superlattices and Microstructures*, vol. 101, pp. 469–479, 2017.
- [15] A. Hassanpour, N. Bogdan, J. A. Capobianco, and P. Bianucci, "Hydrothermal selective growth of low aspect ratio isolated

- ZnO nanorods,” *Materials & Design*, vol. 119, pp. 464–469, 2017.
- [16] S. Boubenia, A. S. Dahiya, G. Poulin-Vittrant, F. Morini, K. Nadaud, and D. Alquier, “A facile hydrothermal approach for the density tunable growth of ZnO nanowires and their electrical characterizations,” *Scientific Reports*, vol. 7, no. 1, p. 15187, 2017.
- [17] M. Jiao, N. V. Chien, N. V. Duy et al., “On-chip hydrothermal growth of ZnO nanorods at low temperature for highly selective NO₂ gas sensor,” *Materials Letters*, vol. 169, pp. 231–235, 2016.
- [18] K. A. Wahid, W. Y. Lee, H. W. Lee, A. S. Teh, D. C. S. Bien, and I. A. Azid, “Effect of seed annealing temperature and growth duration on hydrothermal ZnO nanorod structures and their electrical characteristics,” *Applied Surface Science*, vol. 283, pp. 629–635, 2013.
- [19] K. Kandananond, “Using the response surface method to optimize the turning process of AISI 12L14 steel,” *Advances in Mechanical Engineering*, vol. 2, 2015.
- [20] S. Shafiei, A. Nourbakhsh, B. Ganjipour, M. Zahedifar, and G. Vakili-Nezhaad, “Diameter optimization of VLS-synthesized ZnO nanowires using statistical design of experiment,” *Nanotechnology*, vol. 18, no. 35, p. 355708, 2007.
- [21] S. M. Sultan, O. D. Clark, T. B. Masaud et al., “Remote plasma enhanced atomic layer deposition of ZnO for thin film electronic applications,” *Microelectronic Engineering*, vol. 97, pp. 162–165, 2012.
- [22] W. Z. Samad, M. M. Salleh, A. Shafiee, and M. A. Yarmo, “Structural, optical and electrical properties of fluorine doped tin oxide thin films deposited using inkjet printing technique,” *Sains Malaysiana*, vol. 40, no. 3, pp. 251–257, 2011.
- [23] H. Nguyen, C. T. Quy, N. D. Hoa et al., “Controllable growth of ZnO nanowires grown on discrete islands of Au catalyst for realization of planar-type micro gas sensors,” *Sensors and Actuators B: Chemical*, vol. 193, pp. 888–894, 2014.
- [24] S. Öztürk, N. Kılınç, and Z. Z. Öztürk, “Fabrication of ZnO nanorods for NO₂ sensor applications: effect of dimensions and electrode position,” *Journal of Alloys and Compounds*, vol. 581, pp. 196–201, 2013.
- [25] J. F. Tang, H. H. Su, Y. M. Lu, and S. Y. Chu, “Controlled growth of ZnO nanoflowers on nanowall and nanorod networks via a hydrothermal method,” *CrystEngComm*, vol. 17, no. 3, pp. 592–597, 2015.
- [26] S. A. Azzez, Z. Hassan, J. J. Hassan, M. S. Mukhlif, M. S. Mahdi, and M. Bououdina, “Effect of temperature on hydrothermally grown high-quality single-crystals Mg-doped ZnO nanorods for light-emitting diode application,” *Journal of Luminescence*, vol. 192, pp. 634–643, 2017.
- [27] A. V. Moholkar, S. M. Pawar, K. Y. Rajpure, C. H. Bhosale, and J. H. Kim, “Effect of fluorine doping on highly transparent conductive spray deposited nanocrystalline tin oxide thin films,” *Applied Surface Science*, vol. 255, no. 23, pp. 9358–9364, 2009.
- [28] T. Demes, C. Ternon, F. Morisot et al., “Mechanisms involved in the hydrothermal growth of ultra-thin and high aspect ratio ZnO nanowires,” *Applied Surface Science*, vol. 410, pp. 423–431, 2017.
- [29] N. A. Jayah, H. Yahaya, M. R. Mahmood, T. Terasako, K. Yasui, and A. M. Hashim, “High electron mobility and low carrier concentration of hydrothermally grown ZnO thin films on seeded a-plane sapphire at low temperature,” *Nano-scale Research Letters*, vol. 10, no. 1, 2015.
- [30] S. Chen, M. E. A. Warwick, and R. Binions, “Effects of film thickness and thermal treatment on the structural and optoelectronic properties of Ga-doped ZnO films deposited by sol-gel method,” *Solar Energy Materials and Solar Cells*, vol. 137, pp. 202–209, 2015.
- [31] S. Heinonen, J. P. Nikkanen, H. Hakola et al., “Effect of temperature and concentration of precursors on morphology and photocatalytic activity of zinc oxide thin films prepared by hydrothermal route,” *IOP Conference Series: Materials Science and Engineering*, vol. 123, p. 012030, 2016.
- [32] J. T. Wang, X. L. Shi, W. W. Liu et al., “Influence of preferred orientation on the electrical conductivity of fluorine-doped tin oxide films,” *Scientific reports*, vol. 4, no. 1, 2015.
- [33] H. Kim, J. S. Horwitz, G. Kushto et al., “Effect of film thickness on the properties of indium tin oxide thin films,” *Journal of Applied Physics*, vol. 88, no. 10, pp. 6021–6025, 2000.
- [34] M. M. Napi, N. Nayan, M. K. Ahmad, F. I. M. Fazlee, N. K. A. Hamed, and N. S. Khalid, “Fabrication of fluorine doped tin oxide with different volume of solvents on FTO seed layer by hydrothermal method,” *Sains Malaysiana*, vol. 45, no. 8, pp. 1207–1211, 2016.

Research Article

Stable Electrochemical Measurements of Platinum Screen-Printed Electrodes Modified with Vertical ZnO Nanorods for Bacterial Detection

Thi Hong Phuoc Nguyen,¹ Matteo Tonzzer,¹ Thi Thanh Le Dang¹,¹ Quang Khue Vu,² Quang Huy Tran¹,³ Duc Hoa Nguyen¹,¹ and Van Hieu Nguyen^{4,5}

¹International Training Institute of Materials Science (ITIMS), Hanoi University of Science and Technology (HUST), 1-Dai Co Viet Road, Hanoi, Vietnam

²AIST, Hanoi University of Science and Technology (HUST), 1-Dai Co Viet Road, Hanoi, Vietnam

³National Institute of Hygiene and Epidemiology, 1 Yersin Street, Hanoi, Vietnam

⁴Faculty of Electrical and Electronic Engineering, Phenikaa Institute for Advanced Study (PIAS), Phenikaa University, Yen Nghia, Ha Dong District, Hanoi, Vietnam

⁵Phenikaa Research and Technology Institute (PRATI), A&A Green Phoenix Group, 167 Hoang Ngan, Hanoi, Vietnam

Correspondence should be addressed to Thi Thanh Le Dang; thanhle@itims.edu.vn and Quang Huy Tran; tqh@nihe.org.vn

Received 25 February 2019; Revised 24 May 2019; Accepted 19 June 2019; Published 1 August 2019

Guest Editor: Zhen Yu

Copyright © 2019 Thi Hong Phuoc Nguyen et al. This is an open access article distributed under the Creative Commons Attribution License, which permits unrestricted use, distribution, and reproduction in any medium, provided the original work is properly cited.

The study is aimed at investigating the stability of electrochemical and biosensing properties of ZnO nanorod-based platinum screen-printed electrodes (SPEs) applied for detection of bacterial pathogens. The platinum SPEs were designed and patterned according to standard photolithography and lift-off process on a silicon wafer. ZnO nanorods (NRs) were grown on the platinum working electrode by the hydrothermal method, whereas *Salmonella* polyclonal antibodies were selected and immobilized onto ZnO NR surface via a crosslinking process. Morphological and structural characteristics of ZnO NRs were investigated by scanning electron microscopy (SEM), transmission electron microscopy (TEM), and X-ray diffraction (XRD). The results showed that the ZnO NRs were grown vertically on platinum electrodes with a diameter around 20–200 nm and a length of 5–7 μm . These modified electrodes were applied for detection of *Salmonella enteritidis* at a concentration of 10^3 cfu/mL by electrochemical measurements including cyclic voltammetry (CV) and electrochemical impedance spectroscopy (EIS). The ZnO NR-modified platinum electrodes could detect *Salmonella* bacteria well with stable measurements, and the signal to noise ratio was much higher than that of 3 : 1. This study indicated that ZnO NR-modified platinum SPEs could be potential for the development of biochips for electrochemical detection of bacterial pathogens.

1. Introduction

Electrochemical biosensors have recently attracted much attention because of their potential applications in food safety, environmental pollution monitoring, pharmaceutical chemistry, and clinical diagnostics [1–3]. The electrochemical biosensors have many advantages such as easy operation, low cost, high sensitivity, a simple instrument, and suitability for portable devices [4]. However, these platforms require a stable surface over time for specific applications; it will help

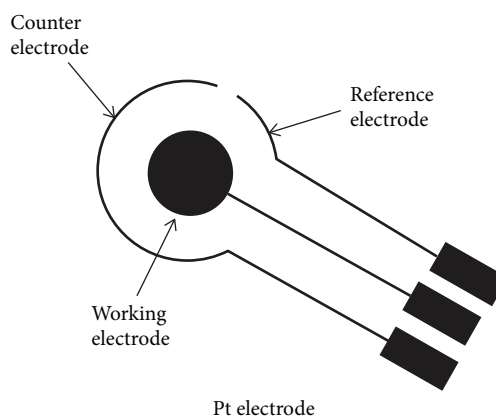
the system to improve the electron transfer between electrolytic solution and electrode and minimize the loss of biological molecules during the electrochemical process. Carbon screen-printed electrodes (SPEs) are normally used for detection of biological molecules, but they seem more preferable for enzyme-based biosensors with enzymatic redox reactions than for deoxyribonucleic acid (DNA) or immuno-based biosensors [5, 6]. Platinum SPEs are also developed for various purposes. Thanks to their electronic properties and a narrow area of the working electrode, the

electron transfer would occur easily [7]. However, it also leads to a limitation of the contact space with targets and the existence of biological molecules on the surface of electrodes during the electrochemical process. Some advanced nanomaterials have been proposed to solve the problem and also enhance the sensor performance [8, 9].

Nanostructured metal oxides are quite attractive for biosensor applications thanks to their biocompatibility and advanced physical and chemical properties [10]. The advantages of nanostructured metal oxides involve the surface-charged depletion and efficient charge-transfer catalytic properties which enable them to become a useful solid support for antibody immobilization in biosensors [11]. Among others, zinc oxide (ZnO), a nontoxic *n*-type semiconductor with wide band gap (3.37 eV), high chemical stability, good electrical properties, high isoelectric point (pH 9–9.5), and high electron transfer capability, is one of the most interesting metal oxides used for biosensors [12–14]. Recently, ZnO nanorods (NRs) have also revealed advantages in biosensors, such as good reproducibility, high sensitivity, and cost-effective fabrication techniques as well as portability [15]. There are several ways reported to deposit ZnO nanorods on substrates such as dielectrophoresis [16], focused-ion-beam [17], or chemical vapour deposition [18]. This material can be easily synthesized in the nanorod shape by the fast, low temperature, and inexpensive hydrothermal route [19, 20]. Besides, the hydrothermal route can be performed at low temperature to grow ZnO NRs on-chip [21]. However, most reports of ZnO NR electrochemical-based biosensor rely on the traditional three-electrode system involving separated platinum wire counter electrode, ZnO NR working electrode, and a reference electrode. The use of traditionally separated electrodes suffers from a complex configuration of the sensor measurement system and consumes a large number of bioreceptors [22].

In the strategy of developing a new type of electrochemical biochips for quick and accurate detection of bacterial pathogens, ZnO NR-modified platinum SPEs have been developed, and *Salmonella* bacteria is selected for testing the stability of electrochemical and biosensing properties of single-modified electrodes. Recently, *Salmonella* species infection has posed a serious threat to public health, especially in developing countries, where people use poultry meats and food-producing animals without control measures [14, 19, 20]. In Vietnam, it is reported that *Salmonella*, a bacterial pathogen, is present in most animal-origin foods including poultry, ovines, porcines, fish, and seafood and their food products [23]. Furthermore, some *Salmonella*-contaminated fruits and fresh vegetables are also reported to be associated with the *Salmonellosis* [24–26]. However, detecting *Salmonella* is time-consuming and labour-intensive, because the conventional methods require isolation, pre-enrichment, or genome amplification [27]. Development of a rapid and reliable method, especially biochip for electrochemical detection of the presence of these pathogens at a low concentration, is also a very important mission for point-of-care applications.

In this study, we designed and fabricated the ZnO NR-modified platinum (Pt) compact electrodes by integration



SCHEME 1: Design of a platinum based on the SPE.

of counter, working, and pseudoreference electrodes on a chip. In the design, Pt is used as both counter and pseudoreference electrodes, whereas vertically grown ZnO NRs act as working electrode. We also investigated the stability of the electrochemical signal of the ZnO NR-modified Pt SPEs before and after antibody immobilization and the detection of *Salmonella* bacteria. The success of the study will help fabricate multimodified sensors on a biochip for further direct detection of bacterial pathogens.

2. Experimental

2.1. Reagents and Materials. Rabbit anti-*Salmonella* IgG polyclonal antibody, *Salmonella enteritidis* (ATCC 13076), and *Escherichia coli* (ATCC 25923) (10^6 cfu/mL, each) were provided by the Department of Bacteriology, National Institute of Hygiene and Epidemiology, Vietnam. Phosphate-buffered saline (PBS) buffer, bovine serum albumin (BSA), (3-mercaptopropyl)trimethoxysilane (MTS), N-(γ -maleimidobutyryloxy)-sulphosuccinimide ester (GMBS), zinc nitrate hexahydrate ($Zn(NO_3)_2 \cdot 6H_2O$), and hexamethylenetetramine (HMTA) were from Sigma-Aldrich. All chemicals were of analytical grade and used without any further purification. Deionized (DI) water ($>18 M\Omega$) obtained from the Milli-Q purifying system was used in this study.

2.2. Fabrication of ZnO Nanorod Matrix/Electrode. The platinum SPEs were designed and patterned according to standard photolithography and lift-off process on a 4-inch silicon wafer. The design of platinum SPE is shown in Scheme 1, which includes Cr/Pt counter, working, and pseudoreference electrodes. The double layer of Cr/Pt (20/150 nm thickness) was deposited on a Si wafer covered with 300 nm of SiO_2 using a sputtering system. The thin Cr layer promotes adhesion of the Pt layer. The circular working electrode has a diameter of 4 mm, and the area covered by the electrodes is 12.56 mm^2 , as in our previous publication [28]. A 20 nm of Zn seed layer was deposited by direct current (DC) sputtering on the Pt layer of the circular working electrode in order to grow the ZnO NRs thanks to our experience published previously [29, 30] (Figure 1(a)).

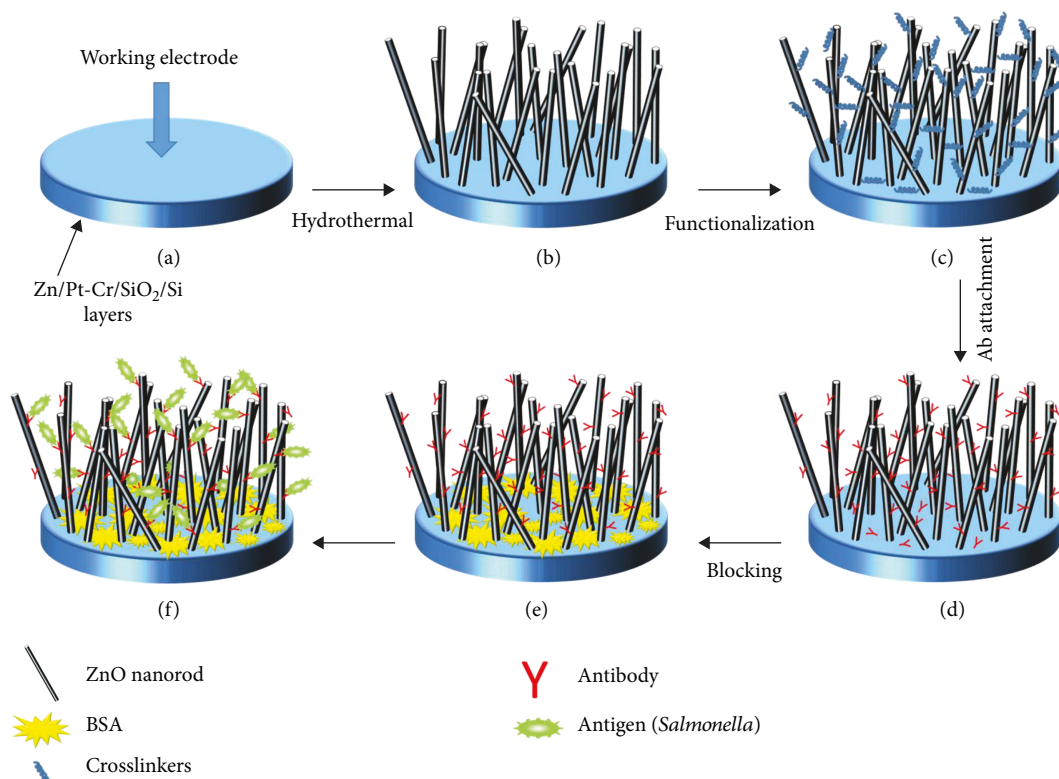


FIGURE 1: The schematic outline of the fabrication of on-chip electrochemical electrodes based on ZnO NRs: (a) deposition of Zn/Pt electrode on the silicon substrate, (b) growth of ZnO NRs, (c) functionalization of ZnO NRs with silane and GMBS, (d) antibody immobilization, (e) blocking the unspecific ZnO NR sites by using BSA, and (f) binding of bacterial antigens on the surface of the working electrode via specific antibodies immobilized in advance.

Figure 1 describes the whole preparation of ZnO NR-modified Pt SPEs for electrochemical detection of bacterial pathogens. After the growth of ZnO NRs on the Pt working electrode, they were functionalized by crosslinkers to provide active sites for antibody immobilization. Then, nonspecific binding sites were blocked by BSA. Finally, bacterial pathogens were added on the working electrode for testing by using electrochemical measurements.

ZnO NRs were vertically grown by a hydrothermal method, as reported elsewhere [15]. Briefly, an aqueous solution of 0.02 M zinc nitrate hexahydrate ($\text{Zn}(\text{NO}_3)_2 \cdot 6\text{H}_2\text{O}$) and 0.02 M hexamethylenetetramine (HMTA) was prepared in deionized water (Mili-Q). After vigorously stirring (700 rpm) the mixture solution for 2 h at 25°C, the microelectrodes were loaded upside down in the solution, and then, the temperature was increased to 80°C. After 24 h of deposition, the ZnO-coated electrodes were washed in deionized water and dried with an N_2 jet (Figure 1(b)).

2.3. Functionalization. Rabbit anti-*Salmonella* IgG polyclonal antibodies were immobilized onto the surface of ZnO NRs by crosslinking with N-[gamma-maleimidobutyryloxy] succinimide (GMBS). This heterobifunctional crosslinker contains N-hydroxysuccinimide (NHS) ester and maleimide groups that allow covalent conjugation with amino acid side chains presenting amine and sulfhydryl groups. The immobilization process includes silanization and crosslinking, as shown in Figure 2.

In the silanization step (Figure 2(a)), the ZnO NR electrode was submerged in a 2% solution of (3-mercaptopropyl)trimethoxysilane (MTS)/ethanol for 1 h. To remove the unbounded MTS, the silanized ZnO NRs were then washed in the solvent and finally dried with an N_2 jet. Attachment of the MTS molecules to the ZnO NR surface was reported to be predominantly through the silane groups with the sulfhydryl groups molecularly oriented away from the surface [31]. As metal oxides have hydroxyl groups on their surfaces, the interaction with silanes (MTS) leads to the formation of covalent -O-Si- groups between the surface and the crosslinking agent, as shown in Figure 2(a). MTS is a feasible option for functionalizing ZnO-based biosensors because it is a commercially available chemical and provides high antibody surface coverage with good uniformity [32, 33]. Therefore, this stage makes sulfhydryl (-SH) groups available at the surface of the ZnO NRs for further linking to the maleimide region of the secondary crosslinker GMBS in an organic solvent [34]. In the crosslinking step (Figure 2(b)), 5 μL of the GMBS was spread over the silanized ZnO NRs and left to incubate for 1 h at room temperature. During this process, the maleimide region of the conjugate GMBS binds to the sulfhydryl groups present on the silanized surface of the ZnO. Covalent conjugation is possible by the attachment of the NHS ester groups of the GMBS to the amine groups of the antibody (Figure 2(c)). At the end, the prepared sensors were washed in PBS solution and dried with N_2 jet (Figure 1(c)).

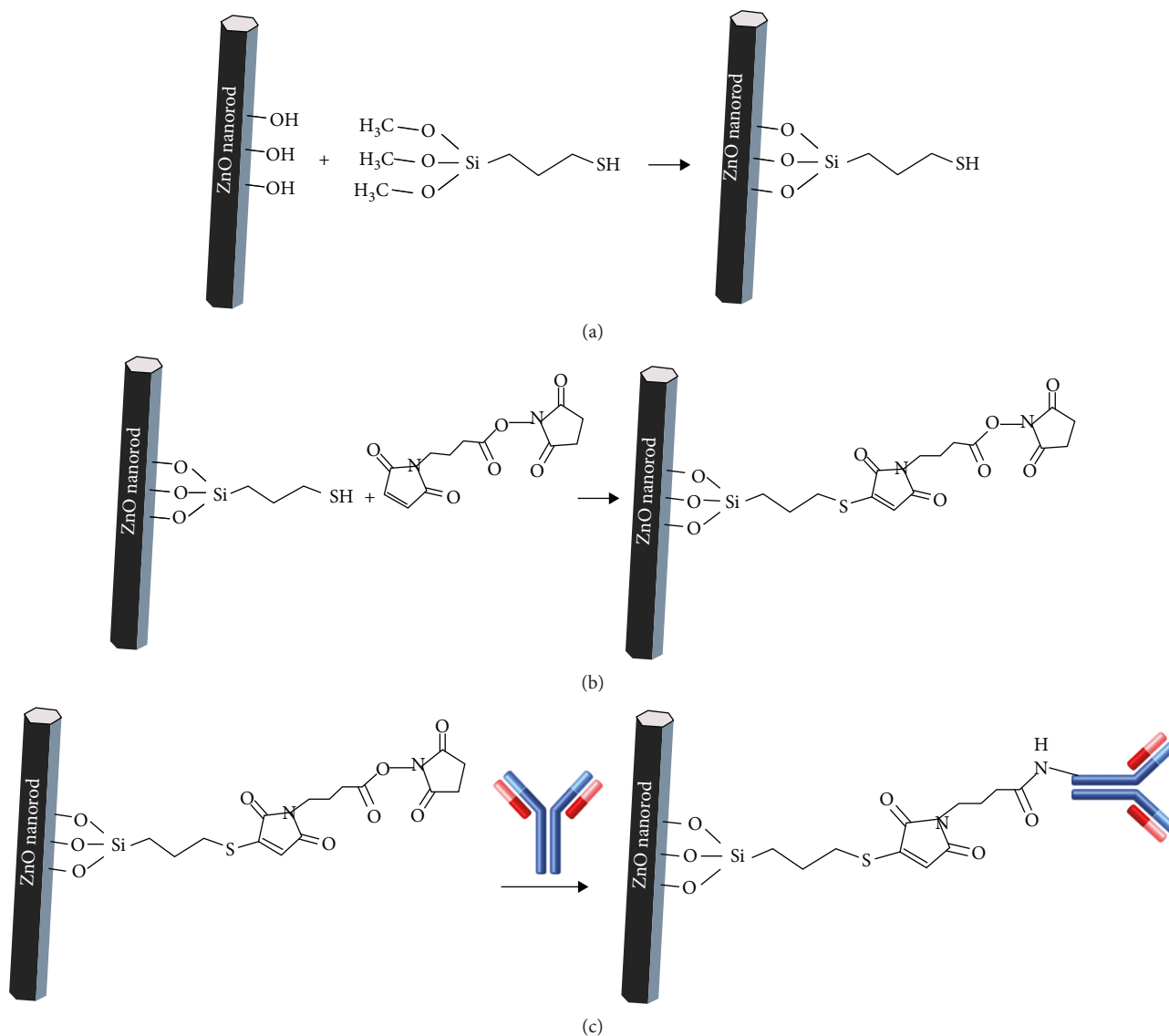


FIGURE 2: Antibody immobilization on ZnO NRs via GMBS crosslinker: (a) silanization the surface of the ZnO NRs, (b) conjugation of the crosslinker GMBS to the silanized ZnO NRs, and (c) conjugation of the antibody with the crosslinking moiety.

2.4. Preparation of the Electrochemical Biosensor Based on ZnO NR-Modified Pt SPEs. All reagents and vials were stored at 4°C during preparation and were left at room temperature just before analysis. In order to immobilize the antibody on the ZnO NR matrix electrode, the antibody solution was prepared by dilution in a 0.01 M phosphate-buffered saline (PBS) solution (pH 7.4). In order to investigate electrochemical and biosensing properties of ZnO NR-modified Pt SPEs, a fixed concentration of 2 µg/mL of anti-*Salmonella* IgG polyclonal antibody has been selected for capturing the working electrode [32, 33]. The antibody was dropped onto the functionalized ZnO NR matrix working electrodes and incubated for 60 min at room temperature to maximize the binding of antibody to ZnO NRs (Figure 1(d)). Following the antibody immobilization, a 5 µL 0.2% BSA/PBS (0.01 M, pH 7.4) was dropped onto the surface of the working electrodes in order to block the blank space (Figure 1(e)) and also

cover nonspecific binding sites, then left them in incubation for further 60 min [4]. The electrodes were washed twice in PBS to remove loosely bound antibodies. Afterwards, 5 µL of *Salmonella* bacteria diluted in PBS (0.01 M, pH 7.4) at a concentration of 10³ cfu/mL was dropped onto the modified working electrode and incubated for 30 min at room temperature, then washed in PBS (0.01 M, pH 7.4) to remove unbound components (Figure 1(f)). Similarly, positive and negative controls were performed with *E. coli* at a concentration of 10⁶ cfu/mL and 0.2% BSA/PBS (0.01 M, pH 7.4), respectively. After drying the electrodes under gentle N₂ flow, they were analyzed by electrochemical measurements. Expectedly, during incubation, antigens of *Salmonella* would bind specifically to antibodies on the surface of electrodes, forming an insulating immune complex between *Salmonella* antibody and antigens, which inhibits electron transfer from the electrolytic solution to the electrode and

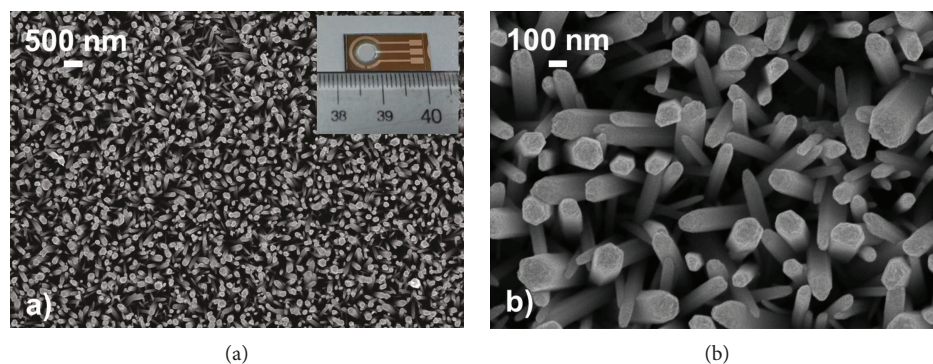


FIGURE 3: SEM images of ZnO NRs on the Pt working electrode at different magnifications: (a) low magnification; (b) high magnification. Inset: a picture of a sensor chip.

further changes in the electron transfer resistance. All electrochemical measurements and testing were repeated with five sensors which have similar electrochemical properties.

2.5. Characterization and Electrochemical Measurements. Morphology and structure of ZnO NRs were studied by field effect scanning electron microscopy (FESEM, S4800; Hitachi) and high-resolution transmission electron microscopy (HRTEM, JEM 2100, JEOL). The crystalline structure was analyzed by XRD (Rigaku Smart Lab®System) with Cu $K\alpha$ radiation operating at 40 kV and 40 mA. Electrochemical measurements were performed by a PalmSens3 (Netherlands). Cyclic voltammetry (CV) and electrochemical impedance spectra (EIS) were recorded in a 5 mM $K_3[Fe(CN)_6]/K_4[Fe(CN)_6]$ solution. For CV, the potential was cycled between -0.6 V and +0.6 V at a scan rate of 100 mV/s. The EIS measurements were performed in the frequency range from 50 mHz to 20 kHz around the open-circuit potential using an alternating-current probe with amplitude of 10 mV.

3. Results and Discussion

3.1. Characterization of ZnO Nanorods. The morphology of the ZnO NR matrix on the Pt SPEs was investigated by FESEM, as shown in Figure 3. The inset of Figure 3(a) is a picture of the sensor chip based on ZnO NR-modified Pt SPEs, which involves the Pt counter electrode, the Pt pseudoreference electrode, and the ZnO NR working electrode. Vertical ZnO NRs were successfully grown on the patterned Pt working electrode. Figure 3(b) shows a higher magnification top-view of the grown ZnO NR matrix. The as-prepared ZnO NRs have a clear hexagonal cross section with a diameter and a length of around 20–200 nm and 5–7 μm , respectively. The NRs were firmly grown and uniformly distributed over the entire circular working electrode substrate. The growth mechanism of ZnO NRs has been discussed in detail in references [35, 36].

The crystal structure of the ZnO NRs grown on Pt electrode was analyzed by XRD, and the result is shown in Figure 4.

The diffraction peaks of the ZnO NRs can be indexed to the standard profile of the wurtzite ZnO (JCPDS 36-1451)

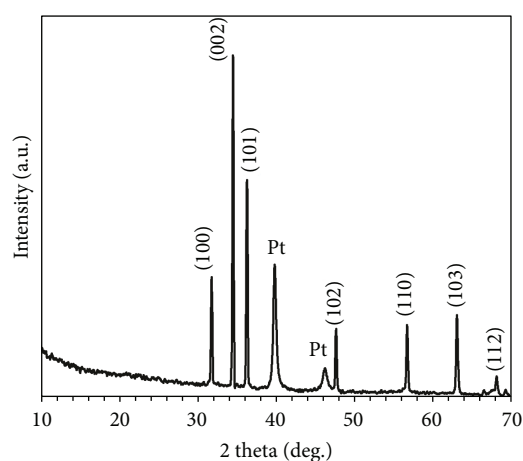


FIGURE 4: XRD pattern of hydrothermally grown ZnO NRs.

[13]. Two extra peaks at $2\theta = 40^\circ$ and 46.5° were indexed to the Pt layer coated over the silicon substrate. No other peaks are present, signifying the absence of any impurity or intermediate formation during growth. Sharp and intense diffraction peaks confirm a high degree of crystallization of ZnO NRs.

Morphology and crystalline structure of the ZnO NRs were confirmed by HRTEM analysis, as shown in Figure 5. Figure 5(a) illustrates a low magnification TEM image of ZnO NRs with diameters around 30 nm. The lattice fringes of about 2.38 Å are visible in Figure 5(b), confirming the good monocrystallinity of the NRs. The lattice fringes are consistent with the [0001] direction of hexagonal ZnO [12].

3.2. Electrochemical Measurements. To study the influence of the substrate modification on the performance of the sensing device, two kinds of electrodes including bare platinum SPEs and ZnO NR-modified platinum SPEs were investigated. The antibody (anti-*Salmonella* Ab) was immobilized on a self-assembled monolayer (SAM) on electrodes using the same synthesis protocol as described in Section 2.4.

Cyclic voltammetry (CV) in a solution containing 5 mM $[Fe(CN)_6]^{3-/4-}$ at 100 mV/s scan rate gives a typical sigmoid curve with steady state diffusion limited currents, as shown in

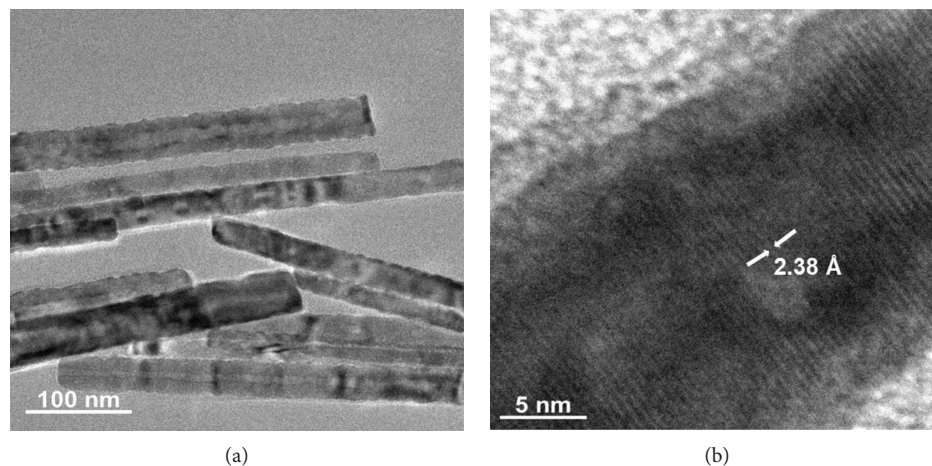


FIGURE 5: HRTEM images of ZnO NRs at (a) low and (b) high magnification.

Figure 6. The CV plot from the ZnO NR-modified working electrode (Figure 6, the red curve) shows lower redox peaks than those from the bare Pt electrode (Figure 6, the black curve), indicating a larger resistance associated with the ZnO NR modification. After the antibody immobilization onto the surface of ZnO NR-modified Pt SPEs, the peak currents of $[\text{Fe}(\text{CN})_6]^{3-/4-}$ decreased (Figure 6, the blue curve). This can be explained by the formation of a monolayer of antibodies on the surface of electrodes that could hinder the charge transfer to a certain extent. After incubation with the sample solution, this layer could be thicker based on the specific reaction of antigen-antibody on the electrode surface; indeed, the redox peak currents further decreased (Figure 6, the dark-cyan curve). This might be attributed to the negatively charged antibody, which obstructed the transfer of charges. The redox peak currents of antibody-immobilized ZnO NR-Pt SPEs were stable after 20 cycles of CV scanning. This confirmed the significant bond strength between ZnO NR-antibody via the crosslinkers. After the *Salmonella* bacteria was incubated on the working electrode surface for 30 min, the redox peak currents steeply decreased (Figure 6, the dark-cyan curve). This might be attributed to the thick layer of antibody-*Salmonella* bacteria binding which inhibited the electron transfer from the electrolytic solution to the electrode.

To explain more clearly the phenomenon on the surface of electrodes, electrochemical impedance spectroscopy (EIS) was investigated. Thus, the impedimetric measurements of ZnO NR-modified Pt SPEs have been performed before and after antibody immobilization and also after the incubation of bacterial antigens, as shown in Figure 7. Nyquist plots were used to investigate the change in the electron transfer resistance at the interface between working electrodes and electrolytic solution after each modification step.

The semicircle diameter at higher frequencies was related to the charge transfer resistance (R_{ct}) that controls the charge transfer kinetics of the redox probe at the electrode interface. As can be seen from Figure 7, the bare Pt SPEs exhibited a small semicircle due to the fast charge transfer process (Figure 7, the black curve, which was presented in the inset).

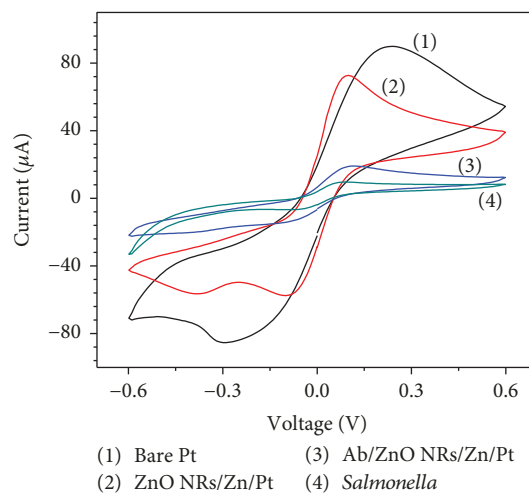


FIGURE 6: The CV of ZnO NR-modified Pt SPEs in response to 10^3 cfu/mL of *Salmonella* bacteria incubated for 30 min and measured in a solution containing 5 mM $[\text{Fe}(\text{CN})_6]^{3-/4-}$ at a scan rate of 100 mV/s, with 20 cycles.

It is the EIS of the bare platinum SPEs zoomed in; the Nyquist plots did not come from the point of origin between Z' and Z'' axes (real and imaginary parts). They started from the values of around 200 ohm of the Z' axis because of the solution resistance. In fact, Pt is a metal with a high electrical conductivity. After the modification of the Pt electrode surface with ZnO NRs, the charge transfer resistance R_{ct} of the device became higher (Figure 7, the red curve), indicating that ZnO NRs could detain the charge transfer as a semiconductor material. When the antibody was immobilized on the working electrodes' surface, the resistance value significantly increased, implying that the antibody hindered the charge transfer to the electrode as an additional barrier (Figure 7, the blue curve). Subsequently, after the reaction of bacterial antigen-antibody, the layer at the electrode surface becomes thicker and the resistance steeply rose even after 5 cycles of CV scanning (Figure 7, the dark-cyan curve). The Randles

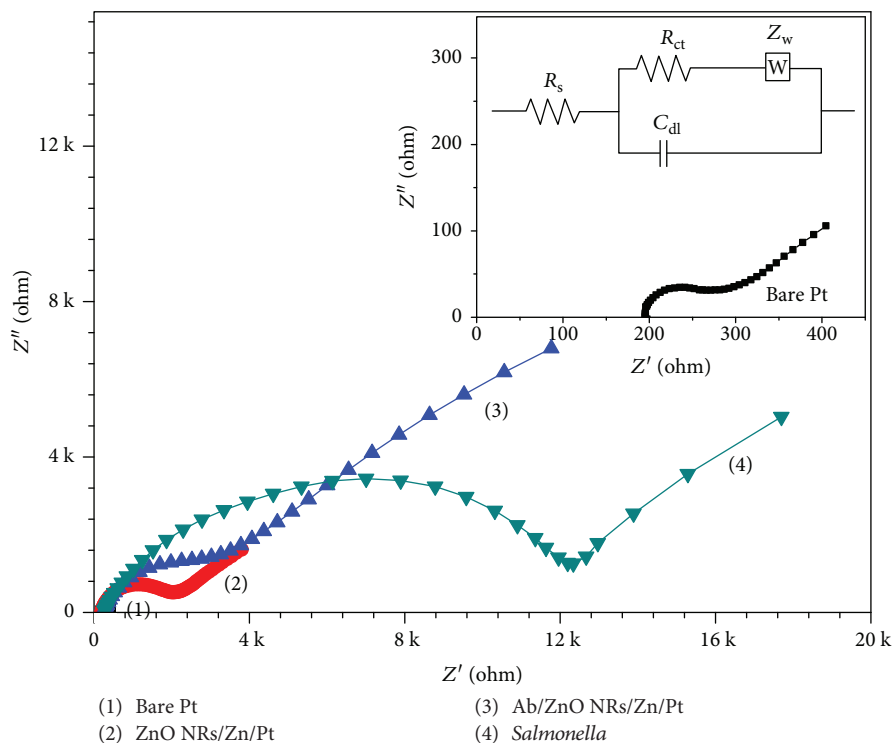


FIGURE 7: The Nyquist plot of ZnO NR-modified Pt electrode exposed to 10^3 cfu/mL *Salmonella*, measured in a solution containing 5 mM $[\text{Fe}(\text{CN})_6]^{3-/4-}$. Inset: the Nyquist plot of the bare Pt SPEs; the equivalent Randles circuit: R_s : electrolytic solution resistance, R_{ct} : charge transfer resistance, and Z_w : Warburg impedance.

equivalent circuit of the modified SPEs is also provided in Figure 7.

For ZnO NR-modified Pt SPEs, factors such as high antibody binding and electron transfer rate play a major role. In this work, all the experiments were performed at pH of 7.4 to retain its bioactivity but also accelerate charge transfer communication between antigen and the electrode to a large extent [9].

The respective semicircle diameter corresponds to the charge transfer resistance (R_{ct}), the values of which are calculated using the fitting program IviumSoft (developed by Ivium Technologies, Netherlands) (Table 1). After antibody immobilization of the ZnO NR-modified Pt SPE surface, the mean R_{ct} value was calculated as about $2,536 \Omega$ after 5 cycles of CV scanning, which is 1.56-fold higher than the $1,621 \Omega$ obtained with the ZnO NR-modified Pt SPEs. This indicates a clear verification that antibodies have been successfully immobilized onto the platinum surface and remained during the electrochemical process. The higher R_{ct} value can best be explained by reduced efficiency of the redox couple, $[\text{Fe}(\text{CN})_6]^{3-/4-}$, to reach the electrode surface in the presence of antibody, presumably due to charge repulsion between the negatively charged antibody and $[\text{Fe}(\text{CN})_6]^{3-/4-}$ [37]. After the *Salmonella* bacteria interacted on the electrode surface, the mean R_{ct} quickly increased, reaching $9,158 \Omega$ after 5 cycles of CV scanning. This might be attributed to the thicker layer of bacteria-antibody formed, which obstructed the transfer of charges, as discussed above. These results were consistent with the results obtained from CV. After the same scan cycles of CV, the mean R_{ct} values

TABLE 1: The R_{ct} values varied according to the changes on the surface of modified SPEs.

Sample	R_{ct} (ohm)
Pt SPEs	76.66 ± 0.42
ZnO NR-modified Pt SPEs	$1,621.00 \pm 81.05$
Ab/ZnO NR-modified Pt SPEs	$2,536.00 \pm 177.52$
<i>Salmonella</i> -Ab/ZnO NR-modified Pt SPEs	$9,158.00 \pm 457.90$
BSA-Ab/ZnO NR-modified Pt SPEs	$2,791.00 \pm 167.46$
<i>E. coli</i> -Ab/ZnO NR-modified Pt SPEs	$3,016.00 \pm 211.12$

of ZnO NR-modified Pt SPEs after antibody immobilization and *E. coli* incubation were much lower, $2,791 \Omega$ and $3,016 \Omega$, respectively. It is reasonable to suppose that most unspecific elements have been removed from the electrodes during washing steps and CV scanning as well. However, there are still some elements bounded on the electrodes due to the space obstruction. It also confirms that ZnO NR-modified Pt SPEs were successfully used for the detection of *Salmonella* bacteria at the concentration of 10^3 cfu/mL and could be optimized for the further development of biochips for electrochemical detection of other pathogens.

4. Conclusions

This study revealed that potential biosensors which could be developed from Pt SPEs modified with vertical ZnO NRs on

the working electrode for electrochemical detection of bacterial pathogens. The morphological and structural investigation showed that the ZnO NR matrix was well-patterned and firmly grown on the Pt working electrode without impurities. CV and EIS measurements proved the stability in the detection of *Salmonella* bacteria at the concentration of 10^3 cfu/mL. The study opens opportunities for further development of electrochemical biochips based on ZnO NR-modified Pt SPEs for the expansion of rapid and accurate detection systems for highly pathogenic bacteria.

Data Availability

The data used to support the findings of this study are available from the corresponding authors upon request.

Conflicts of Interest

The authors declare that there is no conflict of interests regarding the publication of this paper.

Acknowledgments

This research is funded by Vietnam National Foundation for Science and Technology Development (NAFOSTED) under grant number 103.02-2015.43.

References

- [1] P. B. Lippa, L. J. Sokoll, and D. W. Chan, "Immunosensors—principles and applications to clinical chemistry," *Clinica Chimica Acta*, vol. 314, no. 1-2, pp. 1–26, 2001.
- [2] E. Katz and I. Willner, "Probing biomolecular interactions at conductive and semiconductive surfaces by impedance spectroscopy: routes to impedimetric immunosensors, DNA-sensors, and enzyme biosensors," *Electroanalysis*, vol. 15, no. 11, pp. 913–947, 2003.
- [3] M. Pumera, S. Sánchez, I. Ichinose, and J. Tang, "Electrochemical nanobiosensors," *Sensors and Actuators B: Chemical*, vol. 123, no. 2, pp. 1195–1205, 2007.
- [4] A. Tereshchenko, M. Bechelany, R. Viter et al., "Optical biosensors based on ZnO nanostructures: advantages and perspectives. A review," *Sensors and Actuators B: Chemical*, vol. 229, pp. 664–677, 2016.
- [5] M. Dequaire and A. Heller, "Screen printing of nucleic acid detecting carbon electrodes," *Analytical Chemistry*, vol. 74, no. 17, pp. 4370–4377, 2002.
- [6] Y.-H. Lin, S.-H. Chen, Y.-C. Chuang et al., "Disposable amperometric immunosensing strips fabricated by Au nanoparticles-modified screen-printed carbon electrodes for the detection of foodborne pathogen *Escherichia coli* O157:H7," *Biosensors & Bioelectronics*, vol. 23, no. 12, pp. 1832–1837, 2008.
- [7] L. Falcicola, V. Pifferi, and E. Mascheroni, "Platinum-based and carbon-based screen printed electrodes for the determination of benzidine by differential pulse voltammetry," *Electroanalysis*, vol. 24, no. 4, pp. 767–775, 2012.
- [8] S. K. Arya, S. Saha, J. E. Ramirez-Vick, V. Gupta, S. Bhansali, and S. P. Singh, "Recent advances in ZnO nanostructures and thin films for biosensor applications: review," *Analytica Chimica Acta*, vol. 737, pp. 1–21, 2012.
- [9] A. A. Ansari, A. Kaushik, P. R. Solanki, and B. D. Malhotra, "Nanostructured zinc oxide platform for mycotoxin detection," *Bioelectrochemistry*, vol. 77, no. 2, pp. 75–81, 2010.
- [10] P. R. Solanki, A. Kaushik, V. V. Agrawal, and B. D. Malhotra, "Nanostructured metal oxide-based biosensors," *NPG Asia Materials*, vol. 3, no. 1, pp. 17–24, 2011.
- [11] P. Pashazadeh, A. Mokhtarzadeh, M. Hasanzadeh, M. Hejazi, M. Hashemi, and M. de la Guardia, "Nano-materials for use in sensing of salmonella infections: recent advances," *Biosensors & Bioelectronics*, vol. 87, pp. 1050–1064, 2017.
- [12] M. Tonezzer, T. T. L. Dang, N. Bazzanella, V. H. Nguyen, and S. Iannotta, "Comparative gas-sensing performance of 1D and 2D ZnO nanostructures," *Sensors and Actuators B: Chemical*, vol. 220, pp. 1152–1160, 2015.
- [13] L. Vayssieres, "Growth of arrayed nanorods and nanowires of ZnO from aqueous solutions," *Advanced Materials*, vol. 15, no. 5, pp. 464–466, 2003.
- [14] N. Phu Huong Lan, T. Le Thi Phuong, H. Nguyen Huu et al., "Invasive non-typhoidal *Salmonella* infections in Asia: clinical observations, disease outcome and dominant serovars from an infectious disease hospital in Vietnam," *PLoS Neglected Tropical Diseases*, vol. 10, no. 8, article e0004857, 2016.
- [15] M. Jiao, N. V. Chien, N. V. Duy et al., "On-chip hydrothermal growth of ZnO nanorods at low temperature for highly selective NO₂ gas sensor," *Materials Letters*, vol. 169, pp. 231–235, 2016.
- [16] Z. Yang, M. Wang, Q. Zhao et al., "Dielectrophoretic-assembled single and parallel-aligned Ag nanowire–ZnO-branched nanorod heteronanowire ultraviolet photodetectors," *ACS Applied Materials & Interfaces*, vol. 9, no. 27, pp. 22837–22845, 2017.
- [17] O. Lupan, L. Chow, G. Chai, L. Chernyak, O. Lopatiuk-Tirpak, and H. Heinrich, "Focused-ion-beam fabrication of ZnO nanorod-based UV photodetector using the in-situ lift-off technique," *Physica Status Solidi*, vol. 205, no. 11, pp. 2673–2678, 2008.
- [18] T. Van Dang, N. Duc Hoa, N. Van Duy, and N. Van Hieu, "Chlorine gas sensing performance of on-chip grown ZnO, WO₃, and SnO₂ nanowire sensors," *ACS Applied Materials & Interfaces*, vol. 8, no. 7, pp. 4828–4837, 2016.
- [19] L. Q. Toan, H. Nguyen-Viet, and B. M. Huong, "Risk assessment of *Salmonella* in pork in Hanoi, Vietnam," *Vietnamese Journal of Preventive Medicine*, vol. 23, no. 4, pp. 10–17, 2013.
- [20] L. Q. Huong, F. Reinhard, P. Padungtod et al., "Prevalence of *Salmonella* in retail chicken meat in Hanoi, Vietnam," *Annals of the New York Academy of Sciences*, vol. 1081, no. 1, pp. 257–261, 2006.
- [21] T. T. Le Dang, M. Tonezzer, and V. H. Nguyen, "Hydrothermal growth and hydrogen selective sensing of nickel oxide nanowires," *Journal of Nanomaterials*, vol. 2015, Article ID 785856, 8 pages, 2015.
- [22] G. Fiaschi, S. Cosentino, R. Pandey et al., "A novel gas-phase mono and bimetallic clusters decorated ZnO nanorods electrochemical sensor for 4-aminophenol detection," *Journal of Electroanalytical Chemistry*, vol. 811, pp. 89–95, 2018.
- [23] D. T. A. Nguyen, M. Kanki, P. D. Nguyen et al., "Prevalence, antibiotic resistance, and extended-spectrum and AmpC β -lactamase productivity of *Salmonella* isolates from raw meat and seafood samples in Ho Chi Minh City, Vietnam," *International Journal of Food Microbiology*, vol. 236, pp. 115–122, 2016.

- [24] S. Park, B. Szonyi, R. Gautam, K. Nightingale, J. Anciso, and R. Ivanek, "Risk factors for microbial contamination in fruits and vegetables at the preharvest level: a systematic review," *Journal of Food Protection*, vol. 75, no. 11, pp. 2055–2081, 2012.
- [25] J. Guard-Petter, "The chicken, the egg and Salmonella enteritidis," *Environmental Microbiology*, vol. 3, no. 7, pp. 421–430, 2001.
- [26] V. Nandakumar, J. T. La Belle, J. Reed et al., "A methodology for rapid detection of Salmonella typhimurium using label-free electrochemical impedance spectroscopy," *Biosensors & Bioelectronics*, vol. 24, no. 4, pp. 1039–1042, 2008.
- [27] S. Cinti, G. Volpe, S. Piermarini, E. Delibato, and G. Palleschi, "Electrochemical biosensors for rapid detection of foodborne Salmonella: a critical overview," *Sensors*, vol. 17, no. 8, p. 1910, 2017.
- [28] D. T. T. Le, N. V. Hoang, N. V. Hieu, V. Q. Khue, and T. Q. Huy, "Fabrication of electrochemical electrodes based on platinum and ZnO nanofibers for biosensing applications," *Communications on Physics*, vol. 27, no. 3, pp. 221–231, 2017.
- [29] M. Jiao, N. Van Duy, D. D. Trung et al., "Comparison of NO₂ gas-sensing properties of three different ZnO nanostructures synthesized by on-chip low-temperature hydrothermal growth," *Journal of Electronic Materials*, vol. 47, no. 1, pp. 785–793, 2018.
- [30] V. T. Duoc, D. T. T. Le, N. D. Hoa et al., "New design of ZnO nanorod- and nanowire-based NO₂ room-temperature sensors prepared by hydrothermal method," *Journal of Nanomaterials*, vol. 2019, Article ID 6821937, 9 pages, 2019.
- [31] R. M. Petoral Jr., G. R. Yazdi, A. Lloyd Spetz, R. Yakimova, and K. Uvdal, "Organosilane-functionalized wide band gap semiconductor surfaces," *Applied Physics Letters*, vol. 90, no. 22, article 223904, 2007.
- [32] C. D. Corso, A. Dickherber, and W. D. Hunt, "An investigation of antibody immobilization methods employing organosilanes on planar ZnO surfaces for biosensor applications," *Biosensors & Bioelectronics*, vol. 24, no. 4, pp. 805–811, 2008.
- [33] S. K. Bhatia, L. C. Shriver-Lake, K. J. Prior et al., "Use of thiol-terminal silanes and heterobifunctional crosslinkers for immobilization of antibodies on silica surfaces," *Analytical Biochemistry*, vol. 178, no. 2, pp. 408–413, 1989.
- [34] P. Sanguino, T. Monteiro, S. R. Bhattacharyya, C. J. Dias, R. Igreja, and R. Franco, "ZnO nanorods as immobilization layers for interdigitated capacitive immunosensors," *Sensors and Actuators B: Chemical*, vol. 204, pp. 211–217, 2014.
- [35] S. Baruah and J. Dutta, "Hydrothermal growth of ZnO nanostructures," *Science and Technology of Advanced Materials*, vol. 10, no. 1, article 13001, 2016.
- [36] T. R. Chetia, M. S. Ansari, and M. Qureshi, "Graphitic carbon nitride as a photovoltaic booster in quantum dot sensitized solar cells: a synergistic approach for enhanced charge separation and injection," *Journal of Materials Chemistry A*, vol. 4, no. 15, pp. 5528–5541, 2016.
- [37] F. Rohrbach, H. Karadeniz, A. Erdem, M. Famulok, and G. Mayer, "Label-free impedimetric aptasensor for lysozyme detection based on carbon nanotube-modified screen-printed electrodes," *Analytical Biochemistry*, vol. 421, no. 2, pp. 454–459, 2012.

Research Article

Preparation of Three-Layer Graphene Sheets from Asphaltenes Using a Montmorillonite Template

Xiaolong Wu ^{1,2}, Bojing Ma,² Yisheng Xu,² Jun Xu,² Haowei Zhai,³ Zechen Xiong,¹ Xiangbiao Liao,¹ Xiaoyang Shi,¹ and Xi Chen ^{1,4}

¹Yonghong Zhang Family Center for Advanced Materials for Energy and Environment, Department of Earth and Environmental Engineering, Columbia University, New York, NY 10027, USA

²State Key Laboratory of Chemical Engineering, East China University of Science and Technology, Shanghai 200237, China

³Department of Applied Physics and Applied Mathematics, Columbia University, New York, NY 10025, USA

⁴School of Chemical Engineering, Northwest University, Xi'an 710069, China

Correspondence should be addressed to Xi Chen; xichen@columbia.edu

Received 15 January 2019; Revised 16 May 2019; Accepted 10 June 2019; Published 9 July 2019

Academic Editor: Paulo Cesar Morais

Copyright © 2019 Xiaolong Wu et al. This is an open access article distributed under the Creative Commons Attribution License, which permits unrestricted use, distribution, and reproduction in any medium, provided the original work is properly cited.

We propose a novel approach to synthesize graphene sheets with fine quality by calcinating the composites intercalated with montmorillonite (MMT) and asphaltene. The graphene sample thus fabricated could reach 10.79 μm long, with smooth and continuous morphology and with little defects. By analyzing the XRD patterns of graphene/MMT composites at different conditions, the graphene formation mechanism is elucidated and the optimal calcination conditions are researched. This study may provide useful insights for low-cost and scalable fabrication of graphene from asphaltene extracted from heavy crude oil.

1. Introduction

Since discovered in 2004, graphene has been shown to have prominent physical and electronic properties. Many strategies are developed to prepare graphene, such as oxidation-reduction process, and chemical vapor deposition [1, 2]. However, those methods are high-energy consumptive and the fabrication cost can also be high.

Recently, the fabrication of graphene by converting the low-cost asphalt into carbon nanomaterials provides an alternative approach to take advantage of the byproduct of heavy crude oil [1]. The fundamental aromatic rings of asphaltene can be regarded as fragments of graphene, and the molecular diameter of asphaltene is 1.5~5.0 nm, which provides an ideal template for graphene formation. Through the calcination process, the aromatic moieties of asphaltene recombine to become graphene.

The 8-10 layers of graphene sheets fabricated from the previous study [1], however, do not testify the prominent properties of graphene. A new method needs to be developed so that single-layer graphene or low-layer graphene may be

fabricated by limiting the growth of graphene along the vertical direction. Although the synthesis of graphene along the vertical direction remains very hard to control, one could apply a template so that the synthesis takes place within a confined volume. For that matter, the montmorillonite (MMT) emerges as an ideal confinement thanks to its 1 nm natural interlamellar spacing structure. And the main purpose of this paper is to fabricate large-dimension single- or low-layer graphene through intercalation with MMT.

In practice, however, the 1 nm interlamellar spacing may be too limited for the growth of graphene, and modification of the MMT is required. STAB is chosen for MMT modification, through which the lamellar spacing of MMT can be expanded from 1 nm to 2.1 nm [3, 4], which may provide adequate spacing for asphaltene adsorption. By adjusting different combined calcination conditions including temperature and time, the calcination process is optimized in this work, and large-dimension graphene sheets are prepared by acid treatment. The prepared graphene is examined by XRD, Raman, AFM, SEM, and TEM, and optimum fabrication condition is proposed. The work may inspire low-cost

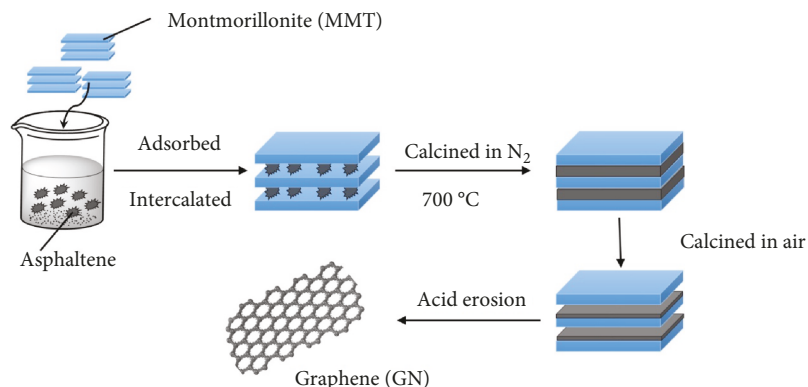


FIGURE 1: Schematic of preparation of large-dimension graphene sheets based on asphaltenes.

and scalable production of graphene through engineered MMT and calcination process.

2. Experimental

2.1. Materials. Asphaltenes are extracted from Tahe heavy crude oil. MMT is pretreated following the procedure reported elsewhere [3, 5]: 50.0 g MMT is mixed with 4.0 g Na₂CO₃ and stirred for 30 min every 3 h for 24 h. After that, MMT is filtrated by suction filtration from the solution and dried in an oven at 80 °C in vacuum for 6 h. Next, 3.0 CEC STAB is fed slowly into 5.0 wt.% MMT solution under stir at 80 °C for 4 h, followed by filtration and washing until no Br⁻ is detected. Finally, the modified MMT is grinded and then sieved by a 325-mesh sieve.

2.2. Preparation of Graphene. The procedure for graphene synthesis is illustrated in Figure 1. Firstly, 1.0 g asphaltene and 20 ml toluene are mixed and subjected to ultrasonication for 1 h. Next, 10.0 g treated MMT is slowly fed in and stirred for 1 h. Asphaltene/MMT composites are collected after filtration and dried at 100 °C in vacuum. The composite is then pyrolyzed in N₂ for 2 h at 700 °C [1] and calcined in air for 15 min at 700 °C in muffle. During this step, graphene is synthesized between the layers of MMT. Finally, the graphene/MMT composite is etched in the solution of 10 wt.% HF and 10 wt.% HCl under stirring. The graphene is filtrated and dried until the color of filtrate became transparent. After acid wash, the absolute asphaltene could be scooped up from the supernatant liquid.

3. Results and Discussion

3.1. Structural Characterization of Graphene. X-ray power diffraction (XRD; Bruker) is used to examine the structure of graphene [6]. Samples prepared from asphaltene/MMT composites calcined in air with different conditions are examined, so that an optimal process may be identified. Figures 2(c) and 2(d) show the comparison of XRD diffraction patterns of GN/MMT samples calcined in air at different times ranging from 15 min to 2 h, at 600 °C and 700 °C, respectively. According to the Bragg equation ($2d \cdot \sin \theta = n \cdot \lambda$), the characteristic peak at $2\theta = 23.15^\circ$ corresponds to the interpla-

nar spacing value of 0.38 nm. The characteristic peak at $2\theta = 23.15^\circ$ exists in all conditions except for 2 h calcinations regardless of the temperature used.

In Figure 2(a), the weak peak at around 23.1° is nearly 0, which indicates that there is no characteristic peak similar to graphene. The weak peaks at around 23.1° for 2 h calcination at both 600 °C and 700 °C (Figures 2(c) and 2(d)) indicate that most of the graphene are burnt out, and the montmorillonite is decomposed under such high temperature so that there are no characteristic peaks of montmorillonite in Figures 2(c) and 2(d). For other calcination conditions, the detailed information including peak height, full-width at half-maximum (FWHM), and crystallinity of GN/MMT in XRD patterns is presented in Table 1. The crystallinity is calculated by using MDI Jade 6. The higher value of peak height in XRD indicates the larger amount. The results indicate that more graphene with lower crystallinity is obtained at 600 °C, while the sample with the highest crystallinity is obtained at 700 °C.

Owing to the high crystallinity being positively correlated with fine quality, the condition of 15 min calcination at 700 °C is regarded as the optimal calcination condition in the present study. The purified graphene is obtained after acid erosion and wash. The XRD pattern of the purified graphene at 23.09° (Figure 2(b)) shows that purification improves the crystallinity of graphene to 81.90% at the optimal condition mentioned above. In addition, the peaks around $15^\circ\sim 17^\circ$ indicate the existence of some unconfirmed impurities.

Raman spectroscopy is useful for confirming the presence of sp² phase in graphene [7], and in Figure 2(e), two typical bands are shown at 1596 cm^{-1} (G band) corresponding to the E_{2g} phonon at the Brillouin zone and at 1346 cm^{-1} (D band), indicating a disordered structure or the edge of the sample associated with structural defects [2, 8–12]. The intensity of D band is 125, and the intensity of G band is 152.5, thus the I_D/I_G intensity ratio (0.82) is much smaller than the graphene similarly prepared from asphaltene by Xu et al. [1], reflecting better quality with fewer vacancies or disorder defects [13]. Since the adsorption spacing of modified MMT is just about half of the spacing of modified vermiculite [1], it provides more appropriate spacing for graphene synthesis and facilitates the fabrication of low-layer graphene sheets. Owing to the smaller spacing for graphene synthesis, the pyrolysis time in N₂ can be increased from

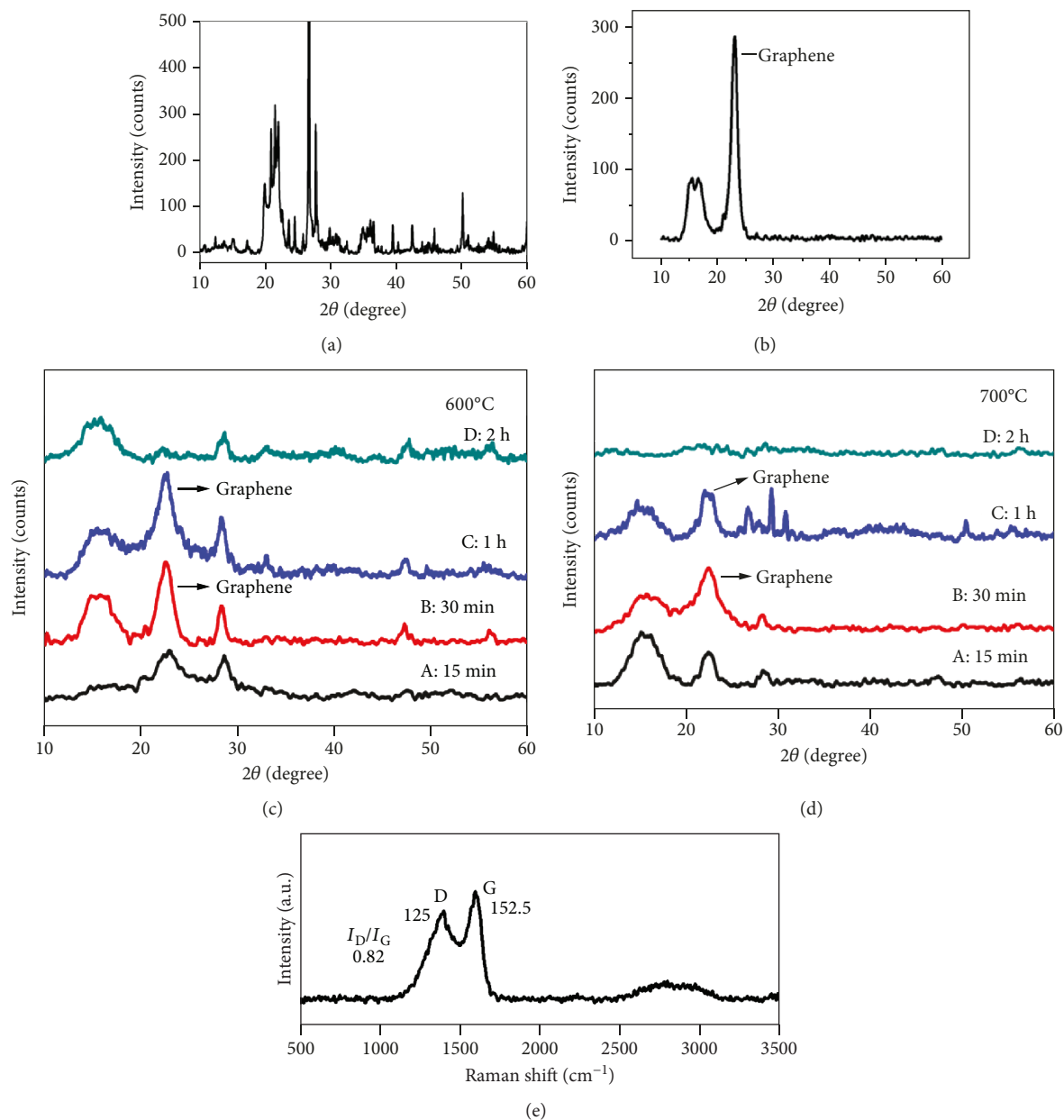


FIGURE 2: XRD patterns of modified montmorillonite (a) and purified graphene sheets (b) and different calcining time of graphene/MMT samples at 600°C (c) and 700°C (d) without erosion treatment and the Raman spectrum (e) of the prepared graphene with I_D/I_G 0.82 at around 23.1°.

TABLE 1: Results of XRD analysis of graphene/MMT samples at six conditions.

Temperature	Time (min)	2θ (°)	Peak height	FWHM (°)	Crystallinity (%)
600°C	15	23.11	21	2.317	50.84
	30	23.09	97	1.913	45.19
	60	23.12	97	2.449	54.43
700°C	15	23.09	33	1.620	78.63
	30	22.92	67	2.635	33.93
	60	23.12	33	1.762	59.90

1 h to 2 h to ensure the adequate carbonization of asphaltene molecules intercalated into MMT, and the I_D/I_G intensity ratio is reduced consequently. And the step of calcination in air removes the allotropes of graphene. These results are consistent with the high crystallinity without allotropes from XRD analysis.

3.2. Topographical Analysis of Graphene. Graphene sheet prepared under the condition of 700°C for 15 min is under investigation in the section. The topography and the thickness of prepared graphene are examined by atomic force microscope (AFM; Veeco). Figure 3(a) shows that the graphene is coherent with little defects, attaining a length of

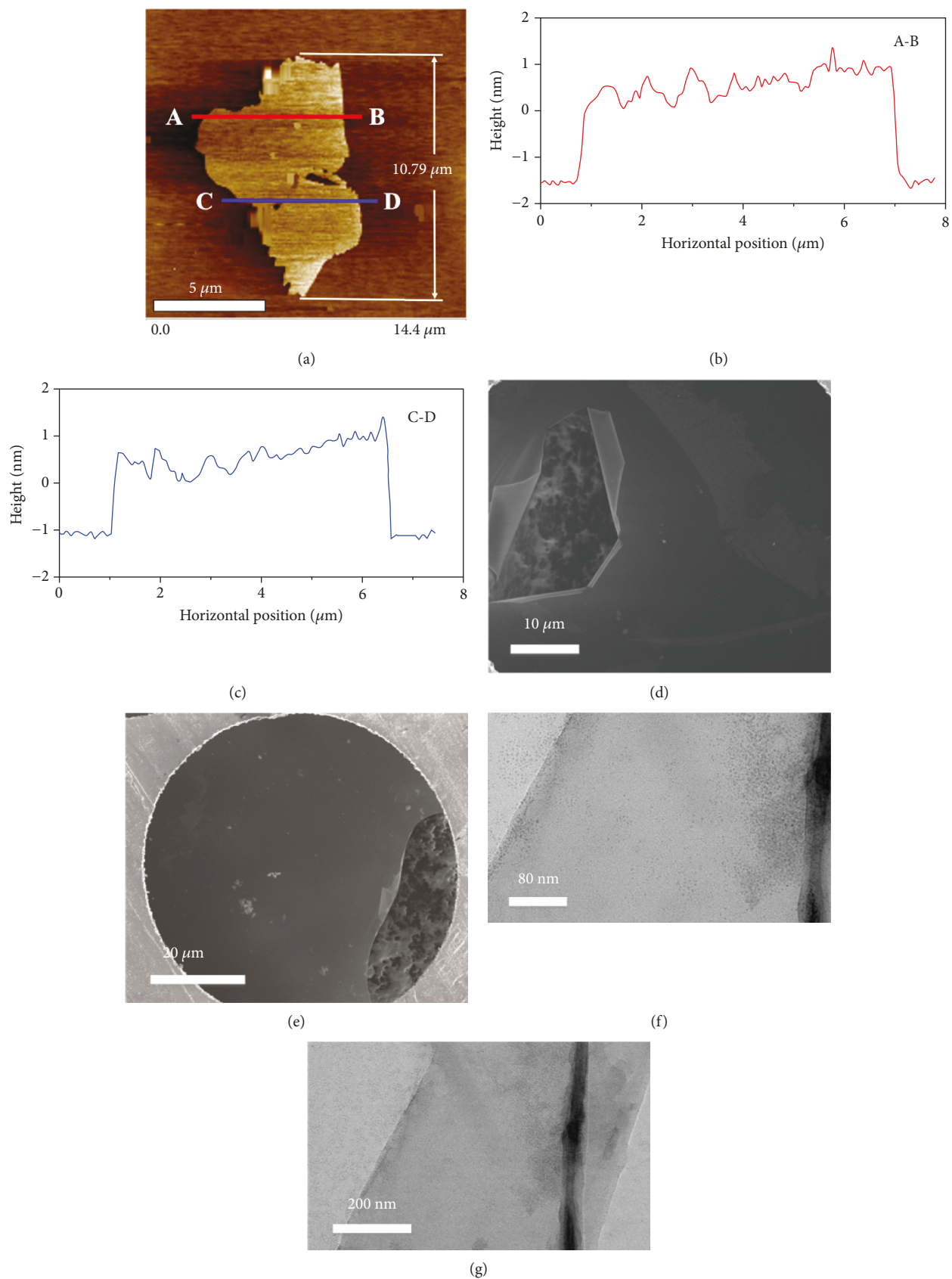


FIGURE 3: AFM image (a) and height profiles (b, c) of the asphaltene-derived graphene sheet. SEM (d, e) and TEM (f, g) images of the asphaltene-derived graphene sheets.

10.79 μm and with a width of 6–7 μm . AFM analysis (Figures 3(b) and 3(c), along lines AB and CD, respectively) indicates a flat feature with a consistent thickness of ~ 1.81 nm. Since the thickness of ideal single-layer graphene is approximately 0.34 nm [14], the present graphene sheet may represent three layers of graphene according to the three-layer graphene with height ~ 1.9 nm by Li et al. [15]. Furthermore, the RMS (root mean square) roughness estimated with AFM data is 0.31 nm over a 60 μm^2 area [16], reflecting an overall smooth surface of the graphene plane [17].

The morphology of the graphene samples is investigated using a scanning electron microscope (SEM; FEI NOVA Nano SEM 450) and high-resolution transmission electron microscopy (HRTEM; JEOL JEM-2100). Figures 3(d) and 3(e) show the scanning image of asphalt-derived graphene sheet attached to a copper sheet. The graphene sheet is quite smooth with little defects. In addition, a graphene sheet with the size up to 600 μm can be obtained by using the current method. According to the HRTEM images (Figures 3(f) and 3(g)), the asphaltene-derived graphene sheet is fairly smooth and transparent, which is in close agreement with the observations in AFM.

According to relevant studies [18–20], double-layered graphene sheet may become very attractive. To obtain even fewer layers of graphene, the MMT may be modified from hydrophilicity to lipophilicity without the expansion of interlamellar spacing of MMT, so that double-layered graphene might be possibly generated within the interlamellar spacing of around 1.5 nm. Moreover, recarbonization may lead to a larger scale of graphene sheets. These studies will be carried out in the future.

4. Conclusions

A novel low-cost approach to prepare low-layer graphene is presented by intercalation of asphaltene and MMT. Thanks to the appropriate interlamellar spacing provided by modified MMT, which blocks the crispation of asphaltene molecules to forming carbon nanotubes but only graphene sheets. The intercalation degree of asphaltene by thermogravimetric analysis (TGA) and recycle of unreacted asphaltene should be investigated in future works to get the optimal strategy to maximize the yield. The longer pyrolysis time in N_2 atmosphere reduces the I_D/I_G intensity ratio and defect, which improves the quality of the obtained graphene sheets. In addition, the calcination process in air removes the allotropes of graphene to approach high crystallinity. By using low-cost raw chemicals from the heavy oil and calcined at optimal conditions (15 min at 700°C), three-layer graphene sheets with large dimension and high quality (with high crystallinity and low defect ratio) are successfully obtained. Microscopy examination confirmed the integrity of the prepared graphene. The proposed methodology has the advantage over other chemical pathways, such as oxidation-reduction, which may preserve the pristine structure and maintain the integrity of graphene. The present work may inspire further study of scalable production of low-layer graphene sheets.

Data Availability

The data used to support the findings of this study are included within the article.

Conflicts of Interest

There is no conflict of interests in this article.

Acknowledgments

Financial support by the National Natural Science Foundation of China (51003028, 21004021, 21306049, and 51273063), the Fundamental Research Funds for the Central Universities, the Higher School Specialized Research Fund for the Doctoral Program (20110074110003), and the 111 Project grant (B08021) is gratefully acknowledged. The authors also thank Petrochina Liaohe Oilfield Company for yielding oil samples and technological supports.

References

- [1] C. Xu, G. Ning, X. Zhu et al., “Synthesis of graphene from asphaltene molecules adsorbed on vermiculite layers,” *Carbon*, vol. 62, pp. 213–221, 2013.
- [2] Z. Tu, Z. Liu, Y. Li et al., “Controllable growth of 1–7 layers of graphene by chemical vapour deposition,” *Carbon*, vol. 73, pp. 252–258, 2014.
- [3] H. A. Essawy, A. S. Badran, A. M. Youssef, and A. E. F. A. Abdel-Hakim, “Polystyrene/montmorillonite nanocomposites prepared by in situ intercalative polymerization: influence of the surfactant type,” *Macromolecular Chemistry and Physics*, vol. 205, no. 17, pp. 2366–2370, 2004.
- [4] L. Wang and A. Wang, “Adsorption properties of Congo red from aqueous solution onto surfactant-modified montmorillonite,” *Journal of Hazardous Materials*, vol. 160, no. 1, pp. 173–180, 2008.
- [5] X. Feng, G. Hu, X. Meng, Y. Ding, S. Zhang, and M. Yang, “Influence of ethanol addition on the modification of montmorillonite by hexadecyl trimethylammonium bromide,” *Applied Clay Science*, vol. 45, no. 4, pp. 239–243, 2009.
- [6] R. K. Jammula, A. Tumuluri, N. K. Rotte, K. C. James Raju, and V. V. S. S. Srikanth, “Cupric oxide decked few-layered graphene: synthesis and dielectric behaviour,” *Carbon*, vol. 78, pp. 374–383, 2014.
- [7] M. A. Pimenta, G. Dresselhaus, M. S. Dresselhaus, L. G. Cançado, A. Jorio, and R. Saito, “Studying disorder in graphite-based systems by Raman spectroscopy,” *Physical Chemistry Chemical Physics*, vol. 9, no. 11, pp. 1276–1290, 2007.
- [8] S. M. Clark, K. J. Jeon, J. Y. Chen, and C. S. Yoo, “Few-layer graphene under high pressure: Raman and X-ray diffraction studies,” *Solid State Communications*, vol. 154, pp. 15–18, 2013.
- [9] L. M. Malard, M. A. Pimenta, G. Dresselhaus, and M. S. Dresselhaus, “Raman spectroscopy in graphene,” *Physics Reports*, vol. 473, no. 5–6, pp. 51–87, 2009.
- [10] L. G. Cançado, A. Jorio, E. H. M. Ferreira et al., “Quantifying defects in graphene via Raman spectroscopy at different excitation energies,” *Nano Letters*, vol. 11, no. 8, pp. 3190–3196, 2011.

- [11] S. Lu, M. Yao, X. Yang et al., "High pressure transformation of graphene nanoplates: a Raman study," *Chemical Physics Letters*, vol. 585, pp. 101–106, 2013.
- [12] M. J. Allen, V. C. Tung, and R. B. Kaner, "Honeycomb carbon: a review of graphene," *Chemical Reviews*, vol. 110, no. 1, pp. 132–145, 2010.
- [13] A. Eckmann, A. Felten, A. Mishchenko et al., "Probing the nature of defects in graphene by Raman spectroscopy," *Nano Letters*, vol. 12, no. 8, pp. 3925–3930, 2012.
- [14] X. Li, J. Li, X. Zhou et al., "Silver nanoparticles protected by monolayer graphene as a stabilized substrate for surface enhanced Raman spectroscopy," *Carbon*, vol. 66, pp. 713–719, 2014.
- [15] X. Li, X. Wang, L. Zhang, S. Lee, and H. Dai, "Chemically derived, ultrasmooth graphene nanoribbon semiconductors," *Science*, vol. 319, no. 5867, pp. 1229–1232, 2008.
- [16] Y. Yao and C.-p. Wong, "Monolayer graphene growth using additional etching process in atmospheric pressure chemical vapor deposition," *Carbon*, vol. 50, no. 14, pp. 5203–5209, 2012.
- [17] I. F. Cheng, Y. Xie, R. Allen Gonzales et al., "Synthesis of graphene paper from pyrolyzed asphalt," *Carbon*, vol. 49, no. 8, pp. 2852–2861, 2011.
- [18] X. Fan, K. Elgammal, A. D. Smith et al., "Humidity and CO₂ gas sensing properties of double-layer graphene," *Carbon*, vol. 127, pp. 576–587, 2018.
- [19] M. Liu, X. Yin, and X. Zhang, "Double-layer graphene optical modulator," *Nano Letters*, vol. 12, no. 3, pp. 1482–1485, 2012.
- [20] L. Thirugnanam and R. Sundara, "Few layer graphene wrapped mixed phase TiO₂ nanofiber as a potential electrode material for high performance supercapacitor applications," *Applied Surface Science*, vol. 444, pp. 414–422, 2018.

Research Article

Waste Utilization of Synthetic Carbon Quantum Dots Based on Tea and Peanut Shell

Jing Zhu,¹ Fengyuan Zhu,² Xiaona Yue,¹ Peirong Chen,¹ Yue Sun,¹ Liang Zhang,¹ Dongdong Mu ^{1,3} and Fei Ke ¹

¹Department of Applied Chemistry & State Key Laboratory of Tea Plant Biology and Utilization, Anhui Agricultural University, Hefei, 230036 Anhui, China

²Key Laboratory of Organic Synthesis of Jiangsu Province, College of Chemistry, Chemical Engineering and Materials Science & Collaborative Innovation Center of Suzhou Nano Science and Technology, Soochow University, Suzhou, 215123 Jiangsu, China

³School of Food Science and Engineering, Key Laboratory for Agricultural Products Processing of Anhui Province, Hefei University of Technology, Hefei 230009, China

Correspondence should be addressed to Dongdong Mu; d.mu@hfut.edu.cn and Fei Ke; kfeifei@ahau.edu.cn

Received 28 February 2019; Revised 27 April 2019; Accepted 30 May 2019; Published 8 July 2019

Guest Editor: Mingheng Li

Copyright © 2019 Jing Zhu et al. This is an open access article distributed under the Creative Commons Attribution License, which permits unrestricted use, distribution, and reproduction in any medium, provided the original work is properly cited.

According to the concept of waste utilization and environmental protection, carbon quantum dots (CQDs) with high quantum yield and good stability were synthesized from waste tea leaves and peanut shells by a one-step hydrothermal method. In this study, we explored the synthetic conditions, structures, and optical properties of CQDs. Their unique characteristics of emitting strong and steady blue fluorescence under excitation of ultraviolet light and possessing of plenty of hydrophilic groups on a surface conferred CQD potentials in the field of biomarkers and analytical detection.

1. Introduction

Carbon quantum dots (CQDs) are quasisize-zero-dimensional carbon nanoparticles with an average particle size of less than 10 nm, and the surfaces of CQDs contain many organic functional groups. The synthesis of the CQD process is simple, and the raw materials are low-cost. Due to their low toxicity, good biocompatibility, high chemical stability, and good light stability, CQDs have potential applications in many fields such as biomarkers [1], ion detection, and photocatalysis [2–6]. Meanwhile, a CQD preparation method has many advantages, such as abundant carbon sources, simple reaction equipment, and high fluorescent efficiency. The synthetic CQDs are soluble in water. 0.2 mL tea soup and 0.1 mL CQD solution were added into the tube, and the solution was mixed [7–11]. To date, there are many ways to synthesize carbon quantum dots: for example, electrochemistry, combustion, ultrasonic, pyrolysis, and microwave. But most of the methods

are complex, costly, and toxic. The toxic substances used in the experiment have always been the problem that researchers are eager to solve. Therefore, it is very important for us to explore a simple, low-cost, and low-toxic synthesis method. [12] In addition to the reagents purified in laboratory, household waste which provides a rich carbon source can also be used as raw materials to synthesize CQDs [13–17]. In countries where people like drinking tea, such as East Asia and UK, large amounts of discarded tea leaves are produced every year. The same neglected situation also occurred on the peanut shell. The number of peanut shells discarded each year is also very large, and the shell is difficult to recycle. The reuse of wastes has become one of the hottest scientific research topics nowadays. In this study, a hydrothermal synthesis method for preparing CQDs from abandoned tea leaves and peanuts shell was created (Figure 1), by which the generated CQDs become soluble in water properly and gain excellent fluorescence characteristics and good stability.



FIGURE 1: Process routing of CQDs.

2. Experimental Section

2.1. Apparatus and Reagents. Ethanol and acetic acid were purchased from Sinopharm Chemical Reagent Co. Ltd. All reagents used were of analytical grade without further treatment. The water used throughout was ultrapure water. Dianhong black tea samples were collected from Yunnan Dianhong Black Tea Group Co. Ltd. Abandoned Tieguanyin Tea (purchased on Taobao) was soaked in hot water at 100°C for 5 times and dried in an oven to get the discarded tea. Peanut shell was washed with pure water and dried in an oven at 100°C, then grinded into powder by a crusher, packed in a sealed bag, and kept at 4°C.

A Cary Eclipse fluorescence spectrophotometer (Agilent Technologies, America) and a UV-2100 ultraviolet spectrophotometer (Shimadzu Corporation, Japan) were used to record fluorescence spectra and absorption spectra of CQDs, respectively. A HT-7700 transmission electron microscope (TEM) was used to observe the size and morphology.

2.2. Synthesis of Tea CQDs. The preparation process of CQDs is shown in Figure 1. Firstly, ground tea powder was dissolved in 30 mL 3% acetic acid solution and sonicated for 15 min. Then, the mixture was poured into a 50 mL PPL reactor to react at 200°C for 4 h and cooled down to room temperature after the reaction finished. The obtained yellow liquid was filtered twice by a 0.22 μm microfiltration membrane and dialyzed in a dialysis bag for 24 h to obtain CQD solution; the pure water was changed every 6 hours. A light yellow CQD powder was obtained after vacuum drying.

2.3. Synthesis of Peanut Shell CQDs. Firstly, peanut shell powder was dissolved in 30 mL 3% acetic acid solution and sonicated for 15 min. Then, the mixture was poured into the 50 mL PPL reactor to react at 200°C for 4 h and cooled down to room temperature after the reaction finished. The obtained yellow liquid was filtered twice by a 0.22 μm microfiltration membrane and dialyzed in a dialysis bag for 24 h to obtain a CQD solution.

2.4. Characterization of CQDs. The luminescence properties of samples were determined by a fluorescence spectrophotometer and an ultraviolet spectrophotometer. The morphology and size of the samples were observed and determined using a TEM.

2.5. Application of Quantum Dots in Detection. The purchased black tea had been divided into 8 experimental grades

(Super, First, Second, Third, Fourth, Fifth, Sixth, and Outside) based on its quality. Three samples (0.1 g per sample) were taken from each tea grade, yielding a total of 24 samples. 100 mg of each tea samples was soaked in water at 90°C for 3 min. After adding 3 mL of water to a 5 mL centrifuge tube, 0.2 mL of tea soup and 0.1 mL of quantum dot solution were added and the mixture was shaken. The sample was subjected to fluorescence detection, and the data was saved for analysis.

3. Results and Discussion

3.1. The Effect of Carbon Source Dosage on CQD Preparation. When using tea as a carbon source, we weighed 0.25 g, 0.50 g, 0.75 g, 1.00 g, 1.25 g, and 1.50 g of tea to get reactions separately. Through the fluorescence spectrum (Figure 2(a)), the fluorescence intensity did not change anymore when the amount of the tea reaches 1 g. It showed that the optimal reaction of tea CQDs is 1 g, and the best ratio of waste Tieguanyin tea powder quality to 3% acetic acid solution is 0.033 g/mL. As shown in Figure 2(b), 0.25 g, 0.50 g, 0.75 g, 1.00 g, 1.25 g, 1.50 g, 1.75 g, 2.00 g, and 2.25 g of peanut shell were used to get reactions separately. Different from tea, when the amount of peanut shell exceeds 1.5 g, the fluorescence intensity showed a significant decrease indicating the optimum amount of the peanut shell powder for preparing the CQDs is 1.5 g.

3.2. The Effect of Reaction Time on CQD Preparation. For tea CQDs, we recorded the fluorescence spectrum (Figure 3(a)) of the reaction time in 120, 180, 240, 300, 360, 420, and 480 min, respectively. The results showed the fluorescence intensity did not change after the reaction time reached 300 min, which meant the optimal reaction time of tea carbon quantum dots was 300 min. The fluorescence intensity of the peanut shell is shown in Figure 3(b), the measured fluorescence intensity was the strongest when the reaction time was 300 min. After that, as the reaction time increased, the fluorescence intensity gradually decreased. It showed that the optimal reaction time of peanut shell CQDs was 300 min.

3.3. The Effect of Reaction Temperature on CQD Preparation. The tea reaction solution was reacted at 100°C, 150°C, 180°C, 200°C, 210°C, 220°C, 230°C, 240°C, 250°C, 260°C, and 270°C, for 300 min respectively. As shown in Figure 4(a), as the temperature raised, fluorescence intensity first increased, then decreased, and the intensity reached a maximum at 250°C. Similarly, we also optimized the reaction temperature of peanut shell CQDs. The tests were carried out at 100°C, 150°C,

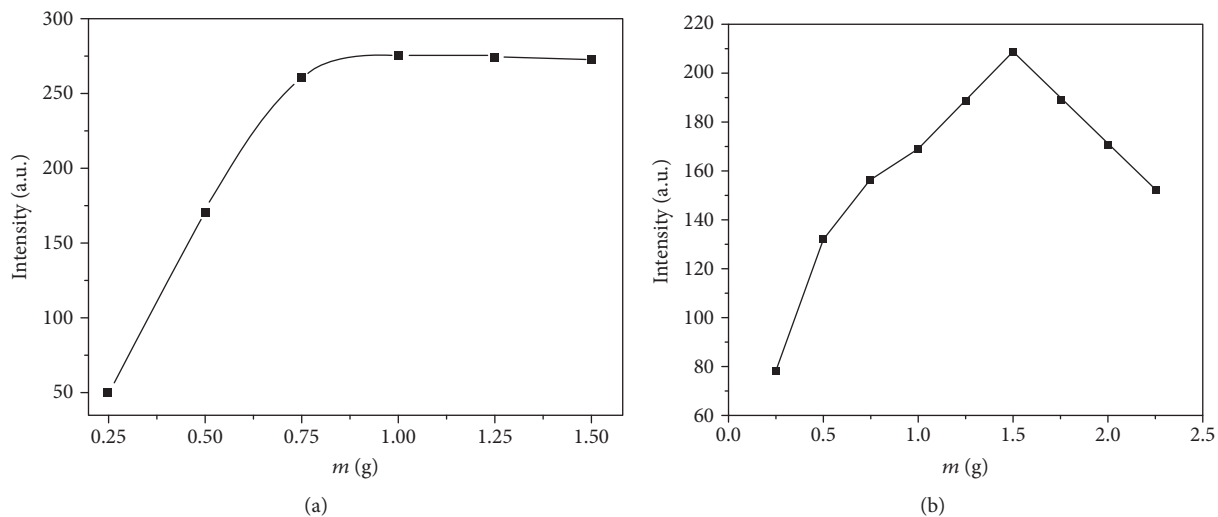


FIGURE 2: Influence of carbon source dosage of (a) tea and (b) peanut shell.

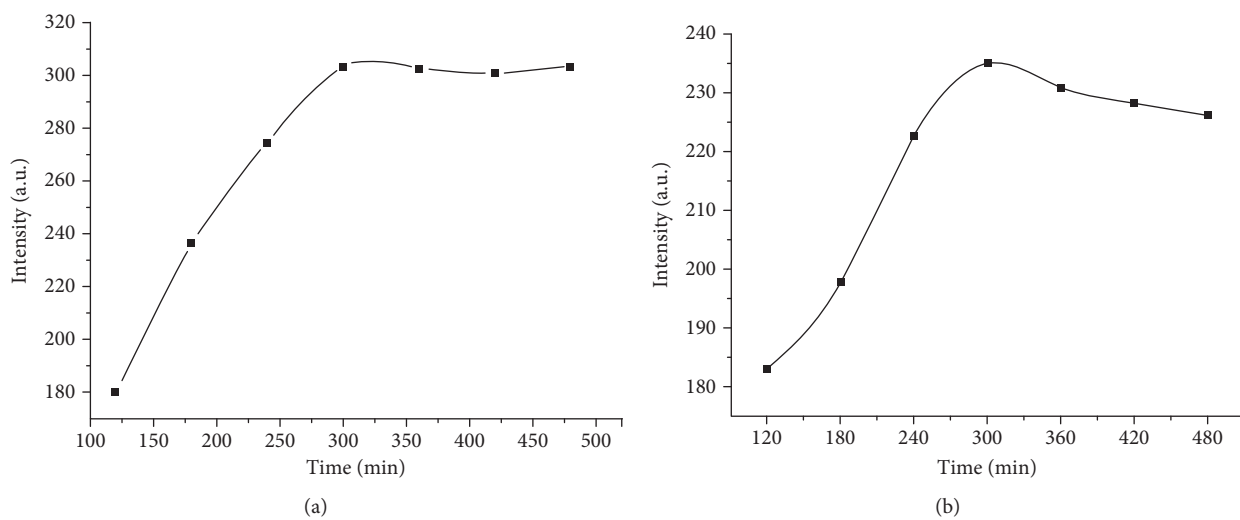


FIGURE 3: Influence of reaction time of (a) tea and (b) peanut shell.

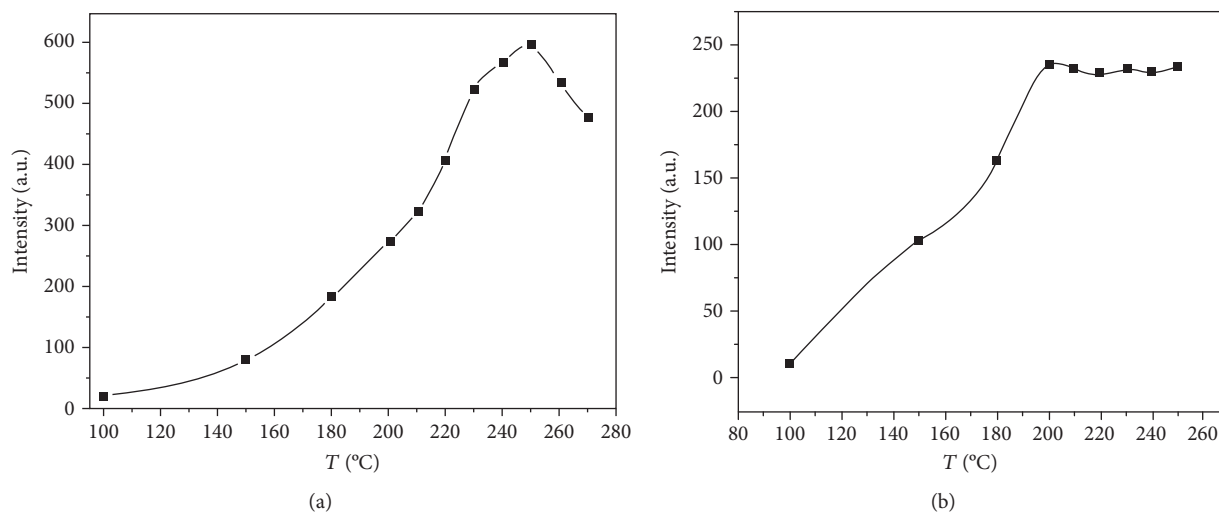


FIGURE 4: Influence of reaction temperature of (a) tea and (b) peanut shell.

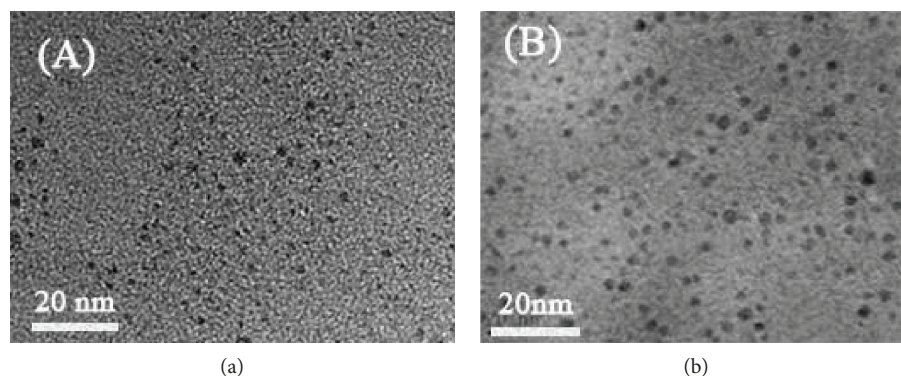


FIGURE 5: Transmission electron microscopy micrograph of CQDs of (a) tea and (b) peanut shell.

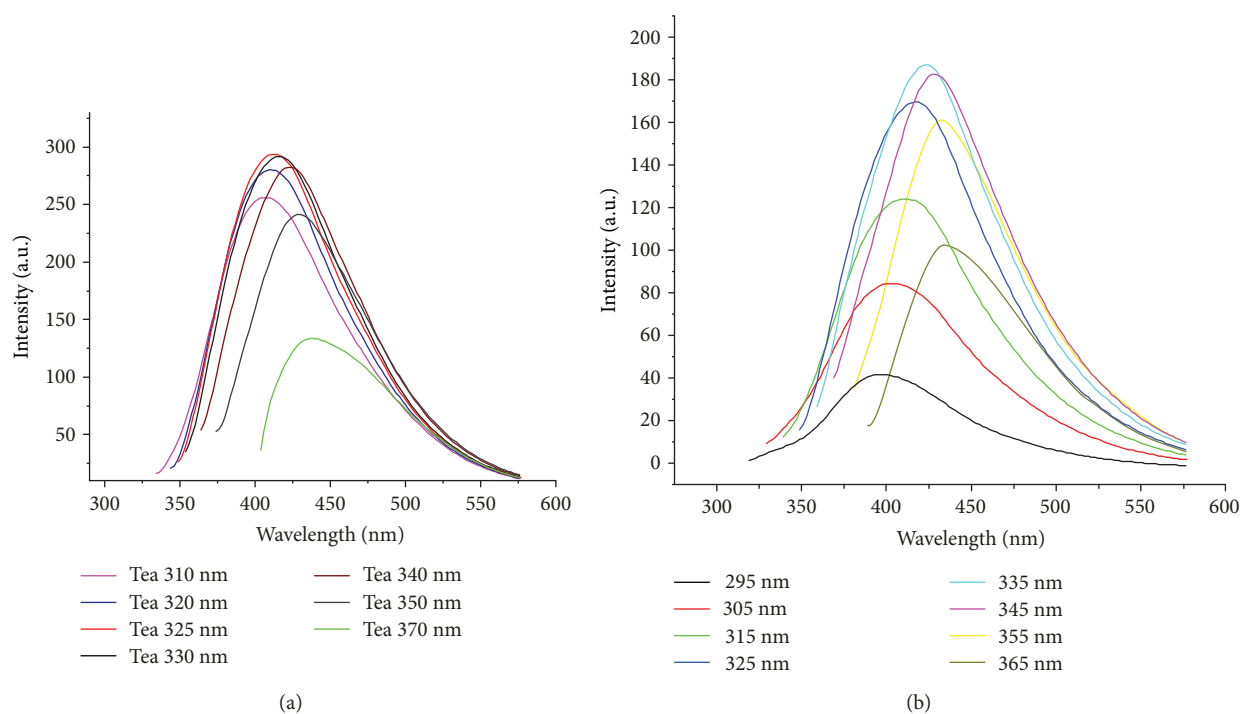


FIGURE 6: Fluorescence spectrum of CQDs of (a) tea and (b) peanut shell.

180°C, 200°C, 210°C, 220°C, 230°C, 240°C, and 250°C. From Figure 4(b), when the holding temperature exceeds 200°C, the measured fluorescence intensity did not change significantly. It showed that the optimal preparation temperature for carbon quantum dots is 200°C.

3.4. Spectral Properties of CQDs. According to the TEM test results (Figure 5), there was no obvious difference in the morphology between tea CQDs and peanut shell CQDs. The diameter was 7-9 nm, its shape was spherical, and the dispersion was uniform, which indicated the tea CQDs and peanut shell CQDs were more stable in water.

The tea CQDs had the strongest fluorescence intensity at 325 nm under different excitation light conditions and emitted blue light fluorescence.

Therefore, the wavelength of the best excitation light was 325 nm; as the wavelength of the excitation light increases, the fluorescence appeared red-shifted. It is shown in Figure 6

that optimum excitation wavelength of peanut shell CQDs was 335 nm and the luminescence was also concentrated in the blue light region.

Through the infrared spectrum (Figure 7), it could be seen that there were some differences in the functional groups between the two carbon quantum dots. Quantum dots using tea as a carbon source had more functional groups on the surface than the others, such as -COOH and -OH, so the water solubility and stability of CDQs were very good.

3.5. Application of CQDs. As we knew, many substances could cause the quenching of quantum dots. The content of tea was very rich, and tea soup could cause the quenching of CQDs. There were differences in the ingredients contained in different grades of tea. However, such a difference was relatively subtle and had high requirements for the accuracy of the test instrument. This high sensitivity of carbon quantum could be used to identify such subtle differences. We took

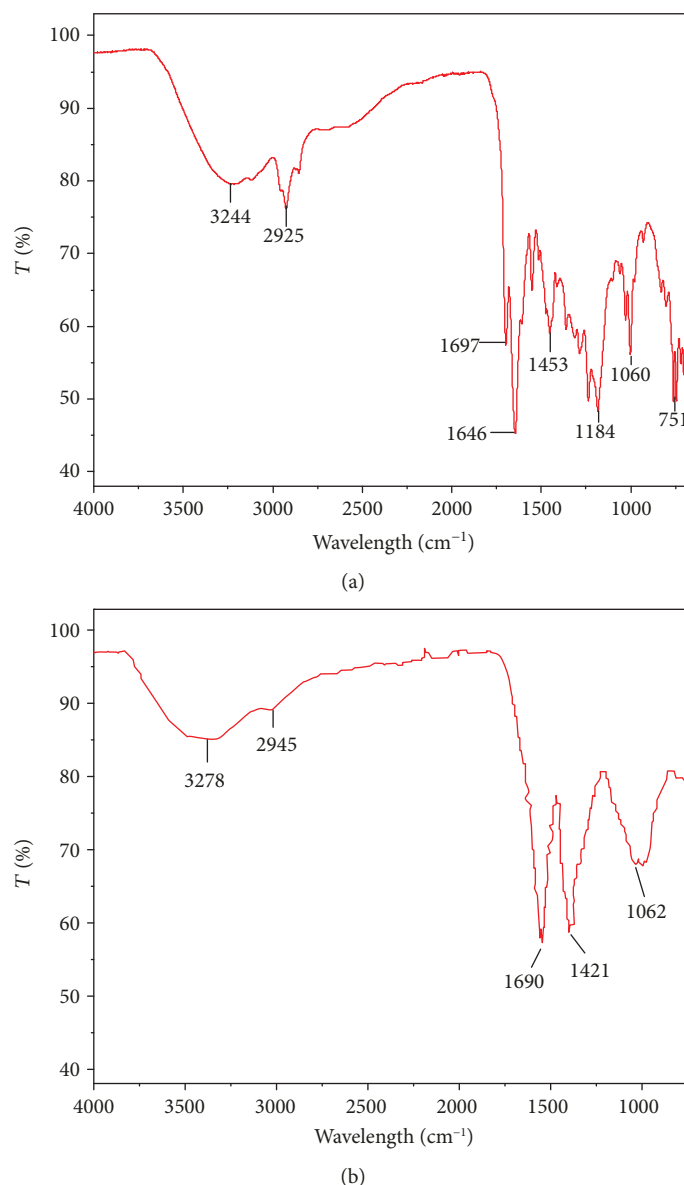


FIGURE 7: Infrared spectrum of CQDs of (a) tea and (b) peanut shell as carbon source.

black tea as an experimental sample and divided it into eight grades (Super, First, Second, Third, Fourth, Fifth, Sixth, and Outside). For each grade, three tea samples were taken for experiment. We used SPSS software to perform principal component analysis on the quantum dot fluorescence curve (Figure 8(a)) after black tea annihilation. The cumulative contribution rate of the first principal component and the second principal component is 99.15%, which was sufficient to indicate that the two data could sufficiently represent the information of the sample. We constructed the two-dimensional image by taking the first principal component and the second principal component data as the x -axis and the y -axis, respectively. It could be seen from Figure 8(b) that each grade of tea sample had a certain regional distribution. This provided an idea for using quantum dots to discriminate tea grades or food quality in the future.

4. Conclusions

We used waste tea leaves and peanut shells as carbon sources to synthesize CQDs. This method has advantages of extremely low cost and easy manipulation. The synthesized light yellow CQD solution emitted strong blue fluorescence under the irradiation of ultraviolet light with a wavelength of 365 nm. After the optimization of preparing conditions and characterization of CQDs, we found the best preparation condition is 200°C. It is known that the CQDs are 7~9 nm in size, spherical in shape, and homogenous in water. The surface contains a large number of hydrophilic groups. Furthermore, we used CQDs to discriminate tea grades with high accuracy. The results obtained in this work provided a way to reduce costs for the practical application of carbon quantum dots in the future.

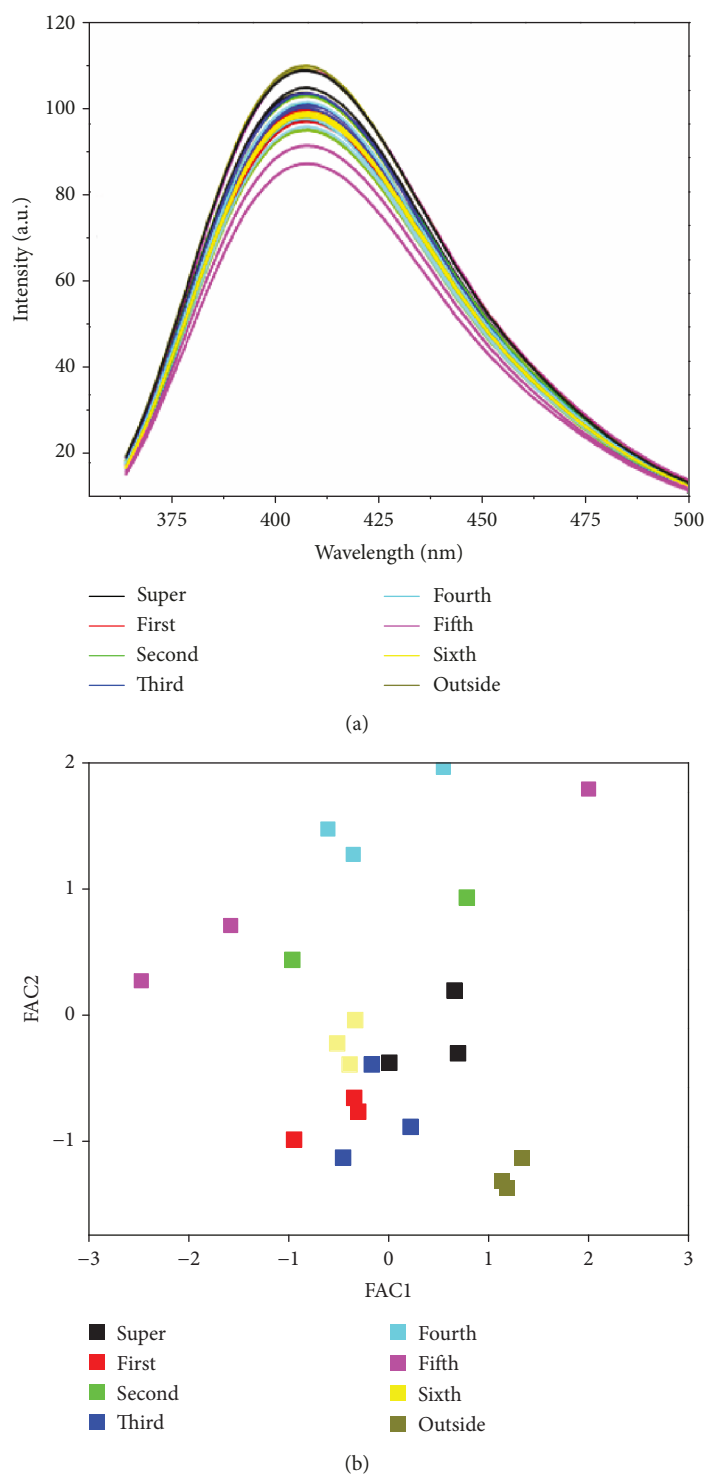


FIGURE 8: Tea grades of (a) fluorescence spectra and (b) distribution map based on principal component.

Data Availability

The data used to support the findings of this study are available from the corresponding authors upon request.

Conflicts of Interest

The authors declare no conflict of interest.

Authors' Contributions

Jing Zhu and Fengyuan Zhu contributed equally to this work.

Acknowledgments

This study was financially supported by the National Natural Science Foundation of China (NSFC, 51702004), the

Scientific Research Foundation of Anhui Agricultural University (Grant No. yj2017-06), the Youth Research Foundation of Anhui Agricultural University (2016ZR003), the Natural Science Foundation of Anhui Province (1808085QE158), and the Open Fund of State Key Laboratory of Tea Plant Biology and Utilization (SKLTOF20180107).

References

- [1] K. M. Tripathi, A. Sachan, M. Castro, V. Choudhary, S. K. Sonkar, and J. F. Feller, "Green carbon nanostructured quantum resistive sensors to detect volatile biomarkers," *Sustainable Materials and Technologies*, vol. 16, pp. 1–11, 2018.
- [2] S. C. Ray, A. Saha, N. R. Jana, and R. Sarkar, "Fluorescent carbon nanoparticles: synthesis, characterization, and bioimaging application," *The Journal of Physical Chemistry C*, vol. 113, no. 43, pp. 18546–18551, 2009.
- [3] F. Zhu, J. Zhu, and Z. Zhang, "Selective detection of glufosinate using CuInS₂ quantum dots as a fluorescence probe," *RSC Advances*, vol. 7, no. 76, pp. 48077–48082, 2017.
- [4] Y. Yang, J. Cui, M. Zheng et al., "One-step synthesis of amino-functionalized fluorescent carbon nanoparticles by hydrothermal carbonization of chitosan," *Chemical Communications*, vol. 48, no. 3, pp. 380–382, 2012.
- [5] F. Yan, D. Kong, Y. Luo et al., "Carbon dots serve as an effective probe for the quantitative determination and for intracellular imaging of mercury(II)," *Microchimica Acta*, vol. 183, no. 5, pp. 1611–1618, 2016.
- [6] A. Cayuela, C. Carrillo-Carrión, M. L. Soriano, W. J. Parak, and M. Valcárcel, "One-step synthesis and characterization of N-doped carbon nanodots for sensing in organic media," *Analytical Chemistry*, vol. 88, no. 6, pp. 3178–3185, 2016.
- [7] S. Sahu, B. Behera, T. K. Maiti, and S. Mohapatra, "Simple one-step synthesis of highly luminescent carbon dots from orange juice: application as excellent bio-imaging agents," *Chemical Communications*, vol. 48, no. 70, pp. 8835–8837, 2012.
- [8] T. Lai, E. Zheng, L. Chen et al., "Hybrid carbon source for producing nitrogen-doped polymer nanodots: one-pot hydrothermal synthesis, fluorescence enhancement and highly selective detection of Fe(III)," *Nanoscale*, vol. 5, no. 17, pp. 8015–8021, 2013.
- [9] S. Zhu, Y. Song, X. Zhao, J. Shao, J. Zhang, and B. Yang, "The photoluminescence mechanism in carbon dots (graphene quantum dots, carbon nanodots, and polymer dots): current state and future perspective," *Nano Research*, vol. 8, no. 2, pp. 355–381, 2015.
- [10] S. Panda, A. Jadav, N. Panda, and S. Mohapatra, "A novel carbon quantum dot-based fluorescent nanosensor for selective detection of flumioxazin in real samples," *New Journal of Chemistry*, vol. 42, no. 3, pp. 2074–2080, 2018.
- [11] Y. Wang and A. Hu, "Carbon quantum dots: synthesis, properties and applications," *Journal of Materials Chemistry C*, vol. 2, no. 34, pp. 6921–6939, 2014.
- [12] A. Tyagi, K. M. Tripathi, N. Singh, S. Choudhary, and R. K. Gupta, "Green synthesis of carbon quantum dots from lemon peel waste: applications in sensing and photocatalysis," *RSC Advances*, vol. 6, no. 76, pp. 72423–72432, 2016.
- [13] L. Wang, J. Hou, H. Li et al., "Facile synthesis of nitrogen-doped carbon dots and its application as sensing probes for serum iron," *Journal of Nanoparticle Research*, vol. 17, no. 11, p. 457, 2015.
- [14] S. Y. Lim, W. Shen, and Z. Gao, "Carbon quantum dots and their applications," *Chemical Society Reviews*, vol. 44, no. 1, pp. 362–381, 2015.
- [15] Y. Zhang, L. Hu, Y. Sun et al., "One-step synthesis of chiral carbon quantum dots and their enantioselective recognition," *RSC Advances*, vol. 6, no. 65, pp. 59956–59960, 2016.
- [16] X. Gao, C. Du, Z. Zhuang, and W. Chen, "Carbon quantum dot-based nanoprobes for metal ion detection," *Journal of Materials Chemistry C*, vol. 4, no. 29, pp. 6927–6945, 2016.
- [17] P. G. Luo, F. Yang, S.-T. Yang et al., "Carbon-based quantum dots for fluorescence imaging of cells and tissues," *RSC Advances*, vol. 4, no. 21, pp. 10791–10807, 2014.

Research Article

Continuous-Flow Synthesis of Thermochromic M-Phase VO₂ Particles via Rapid One-Step Hydrothermal Reaction: Effect of Mixers

Xiaojie Yan ¹, William Trevillyan,² Ioannina Castano,³ Yugang Sun,⁴ Ralph Muehleisen,⁵ and Jie Li¹

¹Applied Materials Division, Argonne National Laboratory, Lemont 60439, USA

²Department of Chemical and Biological Engineering, South Dakota School of Mines and Technology, Rapid City 57701, USA

³Department of Chemistry, University of San Francisco, San Francisco 94117, USA

⁴Department of Chemistry, Temple University, Philadelphia 19122, USA

⁵Energy Systems Division, Argonne National Laboratory, Lemont 60439, USA

Correspondence should be addressed to Xiaojie Yan; alina.yan.2015@gmail.com

Received 6 January 2019; Revised 15 April 2019; Accepted 6 May 2019; Published 10 June 2019

Guest Editor: Mingheng Li

Copyright © 2019 Xiaojie Yan et al. This is an open access article distributed under the Creative Commons Attribution License, which permits unrestricted use, distribution, and reproduction in any medium, provided the original work is properly cited.

VO₂ particles are promising materials for thermochromic smart windows that reduce building energy loss. Continuous-flow hydrothermal processes showcase advantages for synthesizing VO₂ particles compared with traditional batch reaction systems. Mixers play a crucial role in particle fabrication in continuous-flow systems. In this study, a Center T-Mixer and a Collision Cross-Mixer are developed and implemented in a hot water fluidized suspension reaction (HWFSR) system. The influence of the resident time on the particle phase and size was evaluated, and properties of particles derived from systems equipped with differing mixers were compared. The resulting particles were characterized using techniques of X-ray powder diffraction (XRD) analysis, scanning electron microscopy (SEM), and differential scanning calorimetry (DSC). When compared with the Center T-Mixer, results indicate that the Collision Cross-Mixer has better control regarding the morphology and size distribution of resulting particles while improving the transition temperatures of the as-synthesized materials. HWFSR systems containing novel mixer designs are capable of producing pure M-phase VO₂ particles in a single step contrary to the current reactor design that use a second postheat treatment step, and they are capable of synthesizing many other nanoparticle species, especially those requiring high temperature and pressure reaction conditions.

1. Introduction

Thermochromic smart window technologies are attracting tremendous attention due to their ability to regulate infrared heat without noticeable change in visible light transmittance [1]. Vanadium dioxide has shown potential to be utilized as a smart window film material due to its temperature-dependent phase transition behavior in which there are dramatic changes in electrical and optical properties [2]. Among the various existing polymorphs, VO₂ (A), VO₂ (B), VO₂ (M), VO₂ (R) [3], etc., the most suitable polymorph for smart

window applications is VO₂ (M) because of its fully reversible metal insulation transition (MIT) temperature of 68°C, which is significantly lower than the transition temperatures of the other phases [4]. There are several major challenges for current VO₂-based smart window/window films including limitations of the solar transmission modulation (ΔT_{sol}) which is the difference in IR light transmission between the low and high temperature states (usually under 10%), low luminance transmittance (T_{lum}) which is the fraction of visible light transmittance (normally less than 40%), and the high phase transition temperature T_c (about 68°C) [5].

Emerging technologies demonstrate the potential for overcoming these challenges by tuning the particle size, shape, aspect ratio, environment, and doping [6–8].

One of the most convenient routes for VO₂ nanoparticle fabrication is through a hydrothermal reaction [9]. Traditionally, the reaction is performed in an autoclave batch reactor, requiring reaction times of 1–7 days [3] at temperatures and pressures over 220°C and 20 bar, respectively [9], inducing potential explosion hazards. Continuous-flow processing, however, is capable of conducting a hydrothermal reaction more quickly and safely than batch processes with reaction times ranging from a few seconds to few minutes with only a small volume of solution present in the reactor at any one time. In addition, reaction parameters such as temperature, pressure, and resident time are more convenient to control and investigate [10–12] in a continuous-flow process. A two-step route for VO₂ (M) nanoparticle synthesis consisting of a continuous-flow particle production step and a separate postannealing step has been used [13]. However, a postannealing step is not economically efficient for a large-scale production in regard to time and energy consumption. Recently, our group fabricated pure M-phase VO₂ particles using a hot water fluidized suspension reaction (HWFSR) under two minutes [14]. Our novel reaction system uses a traditional T union to mix the hot water solution and reactant which enters through the side. Although the reaction occurring in this system is fast and safe, there is a small deposition of nanoparticles on the metal tubing at the reactor entrance due to a heated stainless steel entrance which initiates particle nucleation early and prior to mixing. In the new HWFSR system, the reactant enters through the bottom of the Center T-Mixer containing a flow distributor and a cooling jacket which prevents the particles from growing on the interior wall of the mixer. This single-step synthesis avoids an additional postannealing treatment step while maintaining the production of pure M-phase VO₂ particles.

Mixing at the entrance is one of the key parameters that trigger instant nucleation and a resulting homogeneous particle size distribution for continuous-flow hydrothermal reaction systems. Unfortunately, a traditional 90° angle T-Mixer is reported to show slower mixing compared with 30°, 50°, and 60° angles or swirling T-Mixers [15, 16]. Other types of passive mixers, including swirling cross mixers [17], micromixers with needle adjustment [18], and center collision mixers [19], are all able to reduce the particle size and increase the uniformity of the particle size distribution but require additional machining and cost.

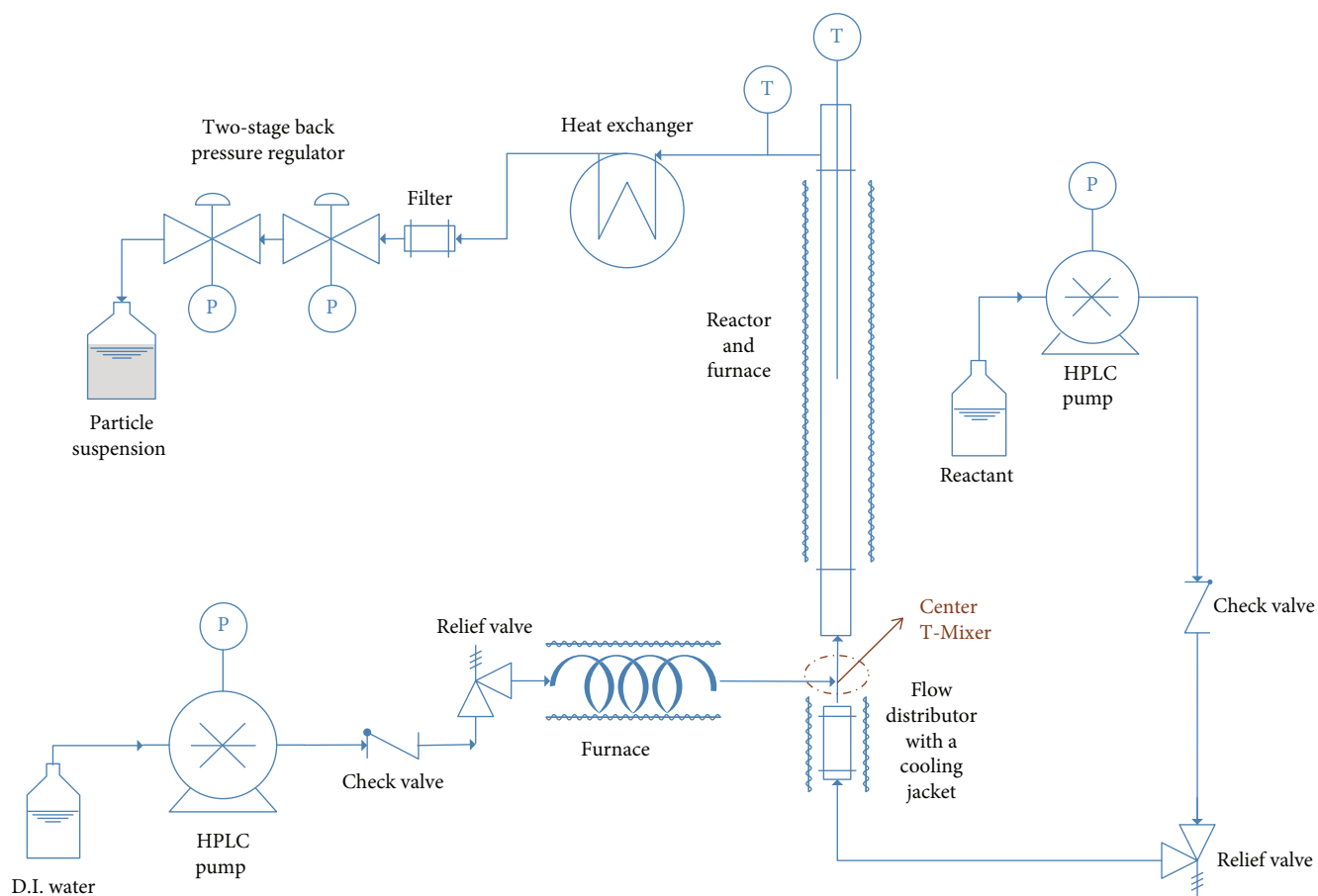
In this research, we continue the development of a hydrothermal continuous-flow process for VO₂ particle synthesis using both a Center T-Mixer and a Collision Cross-Mixer. In the Center T-Mixer, hot water flows out from a small orifice in the center of the T union, before mixing with the reactant solution. The small orifice induces a higher flow rate on the hot water and guarantees a better contact of water with the reactant solution. In the Collision Cross-Mixer, two orifices are used for introducing hot water with a third used for bringing in reactant solution. The collision high flow rate liquid in the center of the cross union creates rapid

mixing of the three groups of flow. VO₂ (M) particles are prepared from the HWFSR system using either a Center T-Mixer or a Collision Cross-Mixer in a single step. Flow rates (resident times) affect VO₂ particle properties. Both mixer styles are compared under various flow rates within the reaction system. When comparing the two styles of mixers, the Collision Cross-Mixer produced smaller VO₂ particles with a narrower particle size distribution. This study also provides a systematic approach and reference for using two differing types of mixers for the hydrothermal continuous fabrication of other nanomaterials.

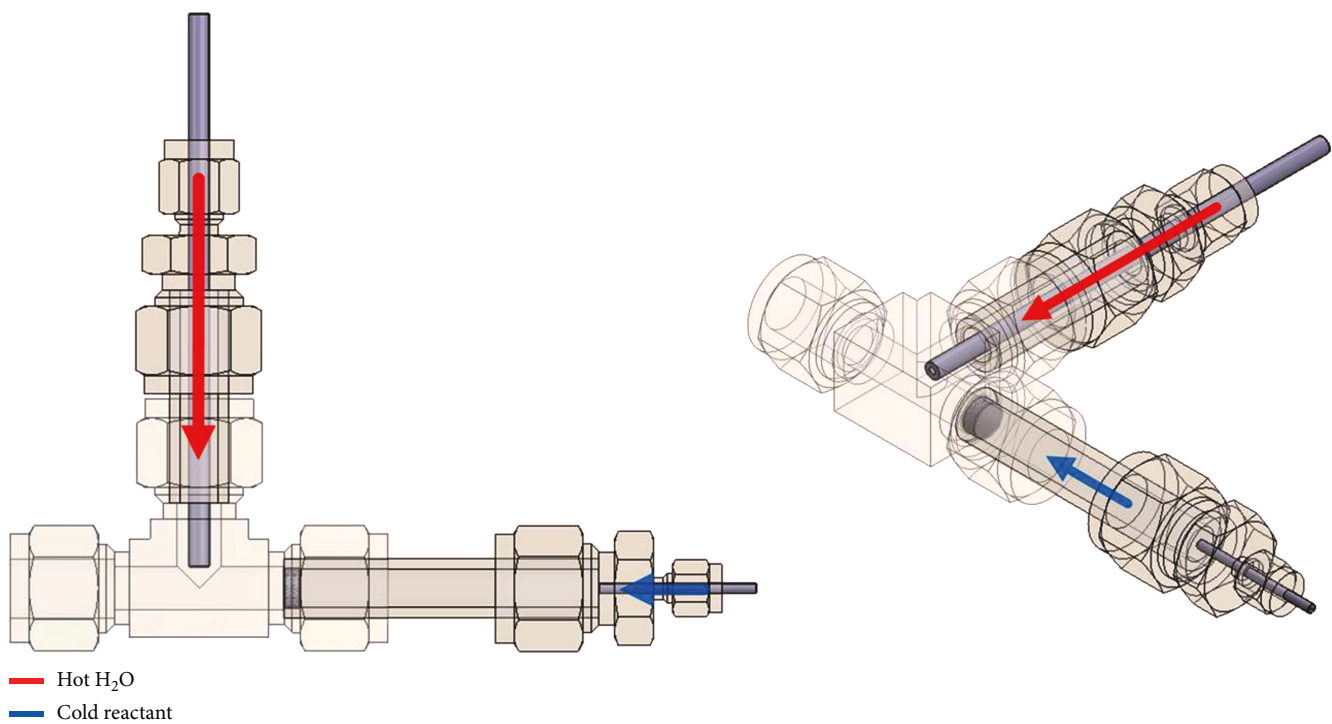
2. Materials and Methods

2.1. Materials, Design of Apparatus, and Procedures. V₂O₅ and C₂H₂O₄·2H₂O (Sigma-Aldrich) are used as starting materials. In a typical synthesis procedure, an appropriate amount of V₂O₅ and C₂H₂O₄·2H₂O (molar ratio 1 : 3) is dissolved in 50 mL, 60 mL, or 70 mL distilled water. The mixture is then left in an ultrasonic bath for 1 hour for thorough mixing and V⁵⁺ reduction. A dark blue solution is thus formed with a V⁴⁺ concentration of 0.0712 mol/L. All the chemicals are used without further purification.

The HWFSR system used a Center T-Mixer for this study, as shown in Figure 1(a). A similar setup with a T union instead of a T-Mixer was used by our group previously and is described elsewhere [14]. The current setup contains two HPLC pumps (BlueShadow 40P and BlueShadow 20P, Knauer Inc.): one for the hot water injection stream and the other for the precursor solution. Two check valves (Swagelok Inc.) are used to prevent the gas generated during the reaction from returning to the pumps, and two relief valves (Swagelok Inc.) are used to relieve the system if pressures exceed 250 bar. Prior to the reaction, hot water (10 mL/min, 5 mL/min, or 4 mL/min) is heated up by a furnace (Applied Test System Inc.) to subcritical conditions, and a precursor solution (5 mL/min, 2.5 mL/min, or 2 mL/min) is kept cool by a cooling jacket. Then, the hot water and precursor streams are sent to the mixer system. Mixed in the mixer, the reactant stream is dispersed by an in-house-built distributor containing an inner porous metal substrate (provided by Mott Co.) while the hot water is expelled from a 1/8" tube within 3/8" T union (Figure 1(b)). Following the mixing, the stream is sent to the tube reactor located within a furnace (Phoenix Flow Reactor™, purchased from Thales-Nano Nanotechnology Inc. to solely use the furnace), which is set to a temperature of 350°C to maintain a reaction temperature of 345°C (which is mainly achieved by the introduction of the hot water stream). In order to cool down the product solution of mostly VO₂ nanoparticles and water after the tube reactor, a heat exchanger (Sentry Equipment & Erectors Inc.) is fixed adjacent to the tube reactor's outlet. Located in series downstream from the heat exchanger, two back pressure regulators (TESCOM, Emerson Electric Manufacturing Co.) maintain a system pressure of 170 bar. An outlet fluid containing VO₂ nanoparticles in the form of a black liquid suspension passes through the back pressure regulators and gets collected by a glass bottle. Then, the suspension is washed seven times using a centrifuge

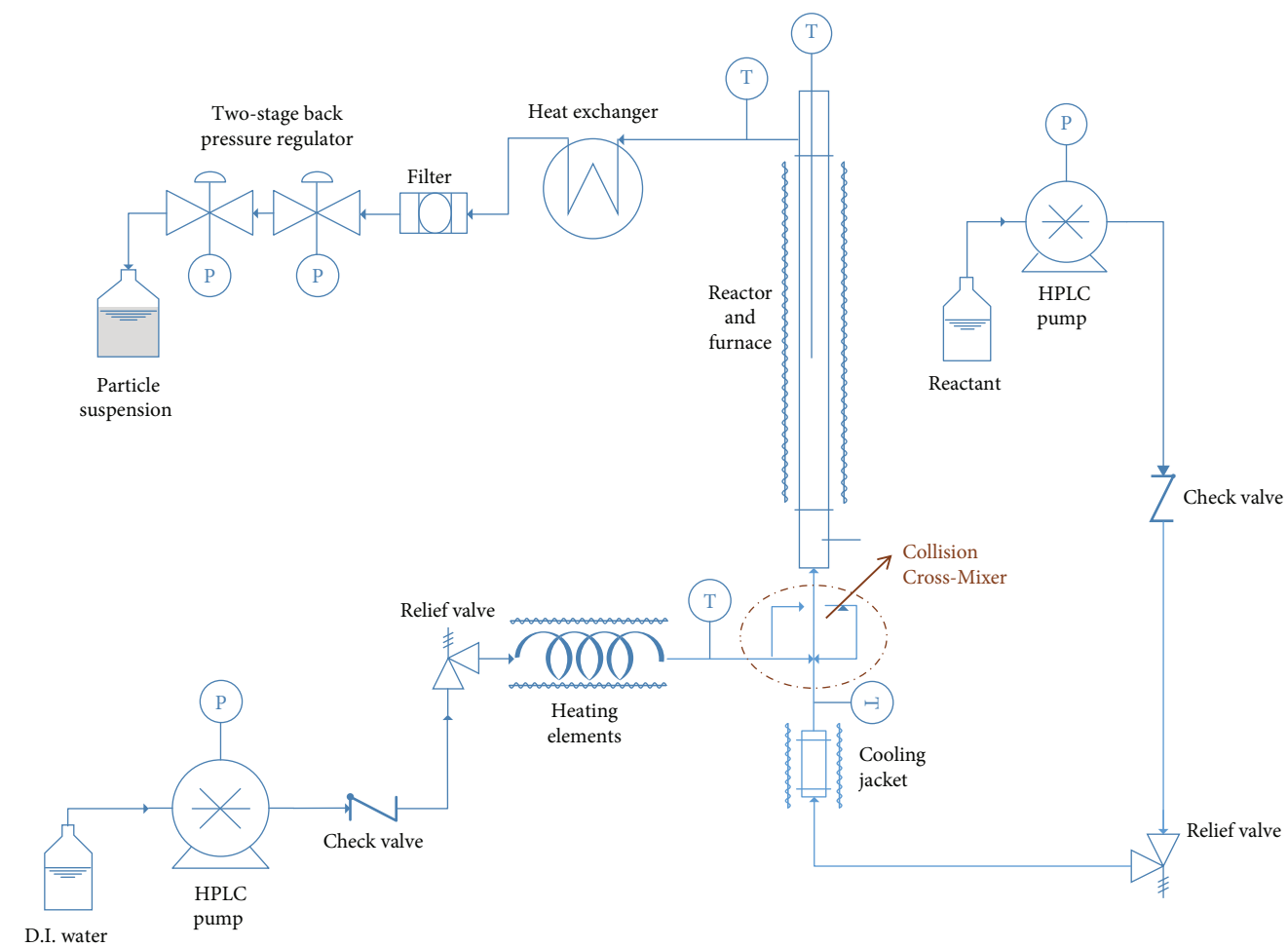


(a)

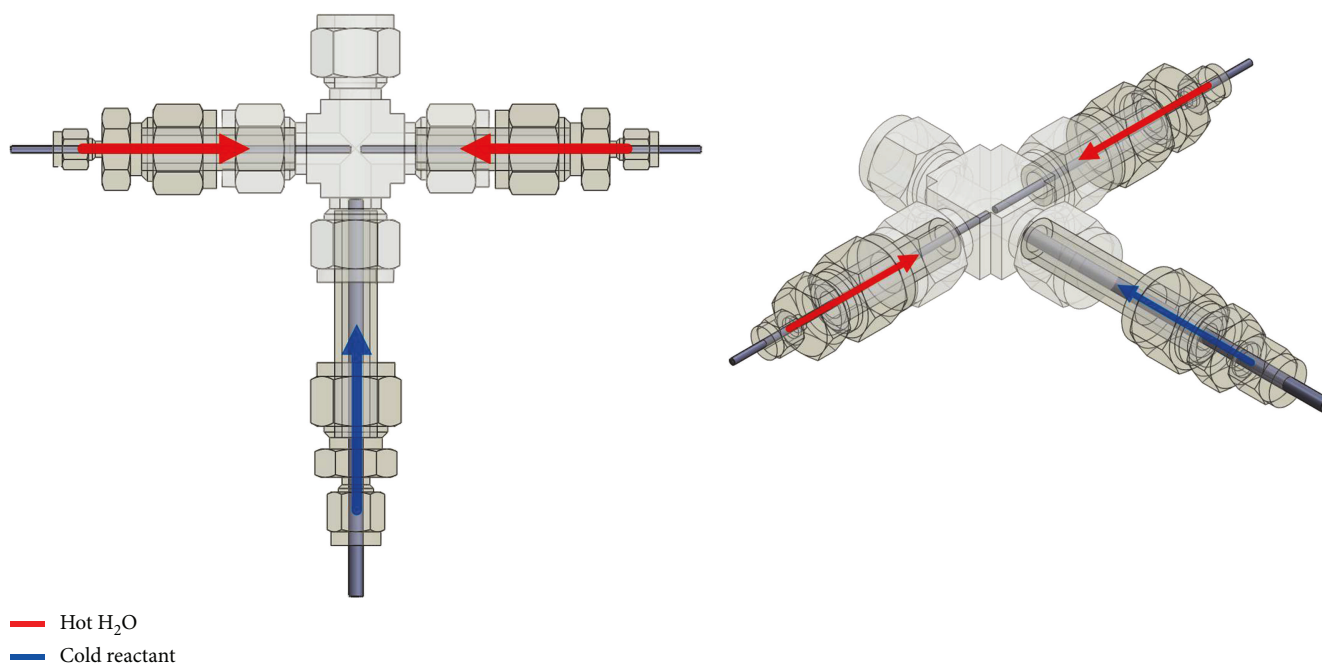


(b)

FIGURE 1: (a) Schematic diagram of the hot water fluidized suspension reaction (HWFSR) system used for VO₂ particle preparation mounted with the Center T-Mixer. (b) A Center T-Mixer.



(a)



(b)

FIGURE 2: (a) Schematic diagram of the HWFSR system used for VO_2 particle preparation mounted with the Collision Cross-Mixer. (b) A Collision Cross-Mixer.

TABLE 1: VO₂ nanoparticle samples prepared via Center T-Mixer and Collision Cross-Mixer mixing systems under various flow rates. (10, 5) represents flow rates of hot water and reactant solution of 10 mL/min and 5 mL/min. All the samples are prepared under reaction temperature of 345°C and a V⁴⁺ concentration of 0.0712 mol/L.

Sample	Mixer type	Flow rate (mL/min)
T1	T	10, 5
T2	T	5, 2.5
T3	T	4, 2
C1	Collision cross	10, 5
C2	Collision cross	5, 2.5
C3	Collision cross	4, 2

(7600 RPM) and ethanol, followed by the collection of the product, a black liquid suspension. Finally, the samples are left in air overnight to dry. All the tubing and fittings for the reaction system were purchased from Swagelok Inc.

Figure 2(a) depicts the HWFSR system using a Collision Cross-Mixer. In this design, the mixer is comprised of a 3/8" cross containing two 1/16" tubes for hot water inlets and a 1/8" tube for a reactant inlet. The hot water enters from both the left and right sides of the cross while the reactant enters from the bottom as shown in Figure 2(b). Every other section of the system is the same as the previously described HWFSR system using a Center T-Mixer Figure 1(a). This new system was designed to enhance mixing between the reactant and hot water, thus leading to more nucleation locations, a more uniform temperature distribution within the reactor, and a more uniform VO₂ nanoparticle size distribution.

2.2. Characterization. The phase purity data is determined by X-ray diffraction (XRD) analysis, which is carried out on a Bruker D2 Phaser using a CuK α 1, a CuK α 2, and a 1% Kbeta line X-ray source and a Lynxeye detector. Scanning was performed over a 2 θ angle ranging from 10° to 70° with a step size of 0.05 units and a rate of 0.1 s/step. The morphology and surface structure of a sample are examined using a scanning electron microscope (SEM) (10 kV acceleration voltage, JEOL 7500) at room temperature. ImageJ software is used to measure the particle diameters. Phase transition properties of the samples are analyzed using differential scanning calorimetry (DSC) (DSC823, Mettler-Toledo International Inc.) with a temperature ranging from 15°C to 90°C, a heating/cooling rate of 2°C/min, and a liquid nitrogen cooling system.

3. Results and Discussion

In this study, six experiments were performed with HWFSR systems, three each using the Center T-Mixer and the Collision Cross-Mixer. Flow rates were 10 mL hot water/min and 5 mL reactant/min (mean residence time: 0.7 min), 5 mL hot water/min and 2.5 mL reactant/min (mean residence time: 1.5 min), and 4 mL hot water/min and 2 mL reactant/min (mean residence time: 1.8 min) as shown in Table 1. These variations in flow rates are used to evaluate the effects

of resident time and the mixer. A reactant temperature of 345°C and a V⁴⁺ concentration of 0.712 mol/L were selected based on former experimental results [14].

Figure 3(a) displays the XRD patterns for samples prepared from a HWFSR system mounted with a Center T-Mixer denoted as T1, T2, and T3. All the samples were shown to be well crystallized, and typical peaks for VO₂ (M), VO₂ (A), and VO₂ (B) phases were detected without phase identification of other possible VO₂ phases. Samples prepared with hot water and reactant flow rates of 10 mL/min and 5 mL/min, respectively, with a mean residence time of 0.7 min produced a mixture of peaks for VO₂ (M), VO₂ (A), and VO₂ (B). As the hot water and reactant flow rates are reduced towards 5 mL/min and 2.5 mL/min, respectively, increasing the mean residence time to 1.5 min, the intensity of XRD peaks for VO₂ (B) phase and VO₂ (A) phase decreases. When the mean residence time is increased further to 1.8 min with corresponding hot water and reactant solution flow rates of 4 mL/min and 2 mL/min, respectively, only peaks corresponding with pure M-phase VO₂ could be identified. The trend indicates that VO₂ (M) particles are more favored with longer resident times. Figure 3(b) shows a similar set of samples fabricated from a HWFSR system mounted with a Collision Cross-Mixer. They exhibit similar phase and crystal indicators as the samples formed from the system mounted with Center T-Mixer.

Morphologies of the particles synthesized from HWFSR systems are displayed in Figure 4. Particles prepared using a Center T-Mixer are shown to have a size distribution ranging from a few nanometers to around 1 μ m in diameter with various rod- and spherical-shaped nanoparticles. When high hot water and reactant solution flow rates of 10 mL/min and 5 mL/min, respectively, were applied, less micron-sized particles were produced, and the portion of large particles became more dominant as the flow rates were lowered (Figure 4(a) T3 and Figure 4(b) T3). As discussed in prior research [14], a longer resident time, while beneficial for producing M-phase particles, results in the aggregation of small particles into larger particles. Additionally, at the entrance of the HWFSR, a differential rate of precursor decomposition and grain growth causes a polarized particle size distribution. Rapid heating and homogeneous nucleation are playing substantial roles in forming smaller and more uniform particles [19]. In this research, the decomposition temperature of the intermediate precursor VOC₂O₄ is 342.9°C [20]. Supersaturation occurs when hot water supplies enough energy to the reactant solution, which then triggers the subsequent nucleation. After the fluid passes the entrance of the mixers, the flow is considered to be laminar with an estimated Reynolds number (Re) between 67 and 168, when total flow rates range from 6 mL/min to 15 mL/min. A nonuniform particle size distribution will trigger differential travelling speeds between larger particles and smaller particles along the reactor, which will increase the probability of particle collision thereby increasing both particle aggregation and elevating the Ostwald ripening. In contrast, if all the particles passing the reactor entrance are of a similar size and shape, the particles tend to not collide with each other under

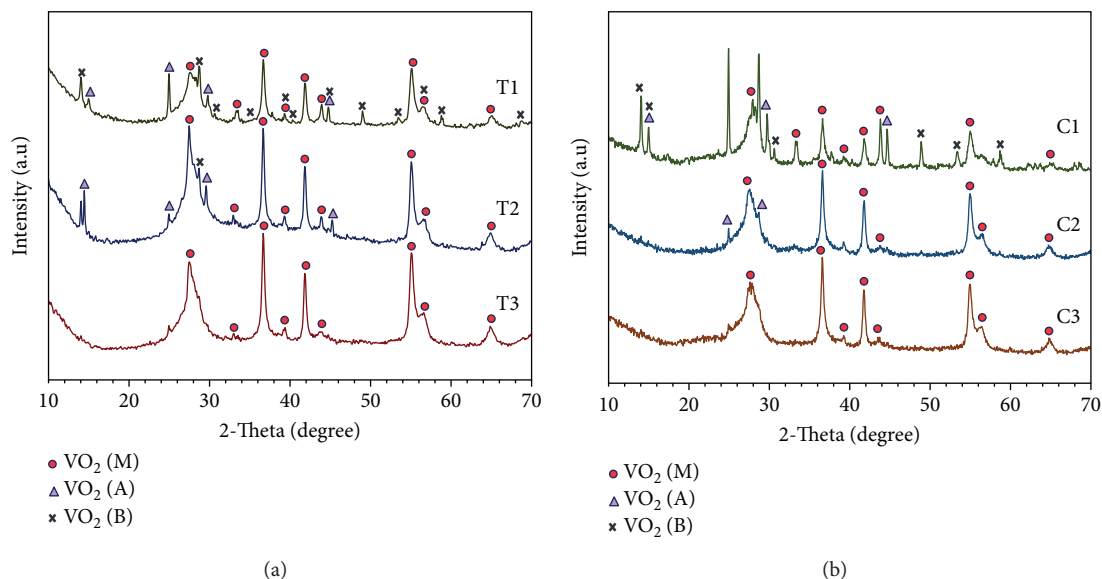


FIGURE 3: The XRD patterns of samples prepared under differing flow rates. (a) Represents samples from a reaction system equipped with the Center T-Mixer, and (b) represents samples from a reaction system equipped with the Collision Cross-Mixer.

moderate concentration and will likely not grow into larger particles before flowing out the reactor. Therefore, choosing the right style of mixer is crucial in regard to both initially and eventually forming monodispersed particles. As observed in Figures 4(a) and 4(b) (C1-C3), the Collision Cross-Mixer (Figure 2(b)) appears to improve mixing when compared to the Center T-Mixer (Figure 1(b)) because it allows entering hot water flow from both sides of the union cross through small orifices rather than only one side. This type of design creates numerous tiny eddies when the two groups of hot fluid from 1/16" tubings meet the reactant solution from a 1/8" tubing. These eddies significantly increase mass and heat transfer between the fluids. Compared with Center T-Mixer, a symmetric mixer design is also beneficial for improving homogeneity of energy dissipation, supersaturation, and the nucleation afterwards. At high hot water and reactant solution flow rates of 10 mL/min and 5 mL/min, respectively, particles formed from the Collision Cross-Mixer mounted system demonstrate better uniformity and sizes up to 400 nm (Figure 4(b)), when comparing them to the nanoparticles formed from the Center T-Mixer mounted system at equivalent flow rates.

When viewing SEM images of samples that were formed utilizing lower flow rates of 4 mL/min and 2 mL/min, the average particle size is larger for both the Collision Cross-Mixer and Center T-Mixer. Longer resident time triggers the aggregation of the particles. However, the undesirable particle growth could be mitigated by applying higher temperature under larger flow rates (shorter resident time) or by utilizing stabilizing agents. In the case of bipolar particle size distribution caused by uneven mixing, longer resident time also assists larger particle growth by consuming smaller particles gradually, which could be explained by the theory of Ostwald ripening. As a matter of fact, microsized VO_2 hollow spheres have been synthesized previously based on this theory in an autoclave reactor [21]. In the same type of

the reactor, the growth of M-phase VO_2 particles was observed by consuming B-phase and A-phase VO_2 particles due to the same reason [3]. In this research, small VO_2 particles are attached on larger ones. The morphologies are identical to microwave-synthesized carbon particles explained by the same Ostwald ripening theory [22]. Nevertheless, due to the fact that only one set of experiments was reported on synthesizing VO_2 via a continuous-flow process prior to this research [13], the direct comparison of Ostwald ripening effect on particle-morphology formation requires more study and is under further investigation by our group. Instantaneous and homogeneous heating alleviates this phenomenon by providing environment for particles to grow uniformly. Particles produced by the Collision Cross-Mixer were much smaller in comparison to those formed using the Center T-Mixer, as well as a narrower particle size distribution (Figures 4(b) and 4(c)). For all of the samples, particles produced using the Collision Cross-Mixer have clear edges in the SEM images, which contrasts the shapeless, blurry particles derived from the Center T-Mixer. A low monomer formation rate versus a high nucleus growth rate may explain this phenomenon. A faster precursor decomposition rate is expected within the Collision Cross-Mixer due to the more efficient instantaneous mixing of hot water and reactant solution compared with the Center T-Mixer. This is in agreement with the fact that particles fabricated under the same reaction conditions (temperature, pressure, residence time, etc.) with different mixers have nonidentical morphologies. A Collision Cross-Mixer can be employed to improve the size, shape, and surface structure of particles while maintaining the requirement of needing pure M-phase VO_2 material.

In order to confirm that the as-prepared M-phase VO_2 particles have thermochromic effects, DSC analysis is conducted as shown in Figure 5. All the samples display MIT temperatures between 29°C and 61°C, which are lower than the reported phase transition temperature of 67-68°C for

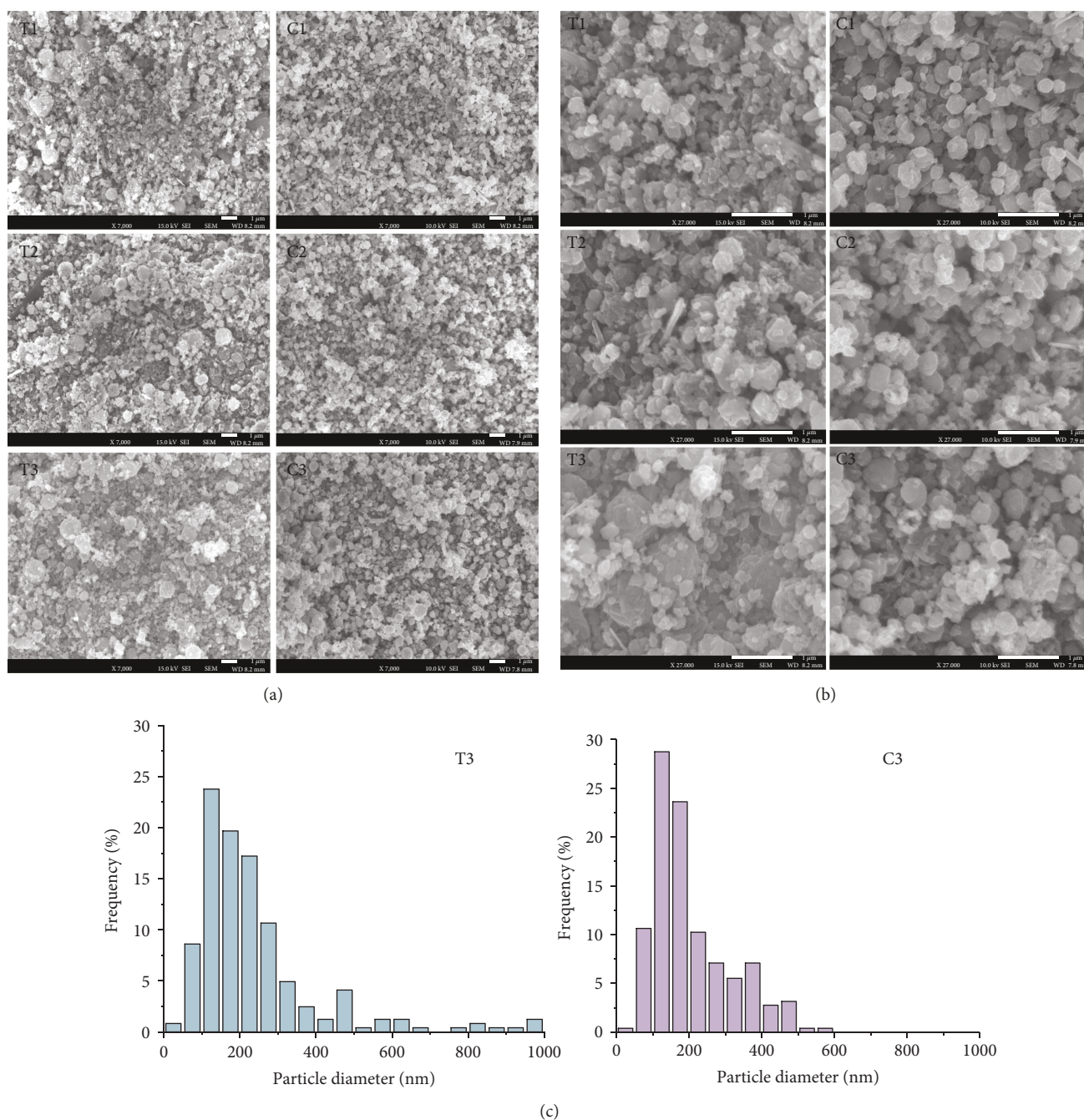


FIGURE 4: (a) The SEM images of samples synthesized under differing flow rates from a system that utilized either a Center T-Mixer or a Collision Cross-Mixer—magnification 7,000. (b) The SEM images of the samples synthesized under differing flow rates from a system that utilized either a Center T-Mixer or a Collision Cross-Mixer—magnification 27,000. (c) Particle size distribution of samples synthesized under flow rates of 4 mL hot water/min and 2 mL reactant solution/min from a system that utilized either a Center T-Mixer or a Collision Cross-Mixer.

bulk VO_2 materials. As discussed in the prior research, many factors could induce a lower MIT temperature, including but not limited to smaller particle sizes [23–25], particle defects, doping [14] (impurities), and film thickness [26]. The reasons are complex, and the transition temperatures of the VO_2 materials differ when applying different synthetic process techniques [27]. The samples synthesized at low hot water and reactant solution flow rates of 4 mL/min and

2 mL/min, respectively, from the Center T-Mixer present MIT temperatures of 54°C when heating ($T_{c\text{-heat}}$) and 39°C upon cooling ($T_{c\text{-cool}}$). Smaller particle size compared with bulk VO_2 might explain the existence of broaden peaks upon heating and cooling from both mixers, which is consistent with the particle size observed from SEM results. However, a narrower peak presents during the cooling process for the material synthesized from the Collision Cross-Mixer.

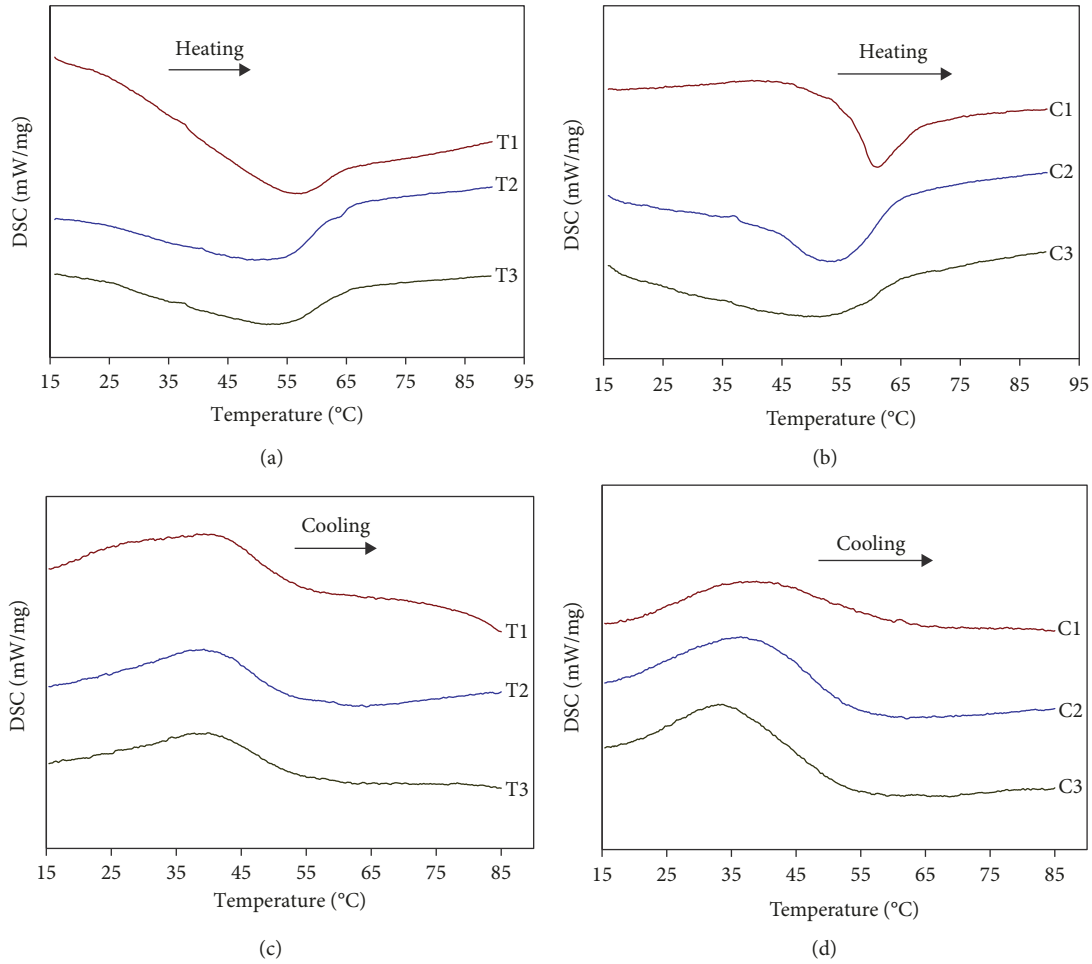


FIGURE 5: The DSC results of VO_2 samples synthesized under differing flow rates from a system that utilized either a Center T-Mixer or a Collision Cross-Mixer: (a, b) heating and (c, d) cooling.

The asymmetric phase transition of VO_2 particles might be explained by the surface defects, which also contributes to the overall change of T_c [1]. Compared with 54°C of $T_{c\text{-heat}}$ from particles produced by using the Center T-Mixer, $T_{c\text{-heat}}$ of particles produced by using the Collision Cross-Mixer has reduced to 51°C . In terms of cooling, $T_{c\text{-cool}}$ has been reduced from 39°C to 34°C by using the Collision Cross-Mixer instead of the Center T-Mixer. This is in agreement with one previous report that smaller particles bring down the $T_{c\text{-heat}}$ temperature [24] but differs from the other reported phenomena on the formation of a $T_{c\text{-heat}}$ temperature higher than 68°C by using smaller VO_2 particles [1, 28]. Despite the complexity of the formation mechanism on an improved $T_{c\text{-heat}}$ and a decreased $T_{c\text{-cool}}$, decreasing T_c from bulk material transition temperature of 68°C without doping is beneficial for VO_2 (M) material synthesis process simplification and process cost reduction for many applications. Additionally, VO_2 particles fabricated by using the Collision Cross-Mixer are more thermally stable compared with those from the Center T-Mixer. DSC analysis (Figure 5) demonstrates a slightly larger latent heat area (Figure 5(d) C3) on particles fabricated from the Collision Cross-Mixer, in contrast to a smaller latent heat area from

particles fabricated under the same condition but with a Center T-Mixer (Figure 5(c) T3). This phenomenon is not significant when dealing with heating curves. Taking into account the potential desired lower switching temperatures from 68°C on VO_2 (M)/ VO_2 (R), DSC results indicate the advantages of producing VO_2 particles by HWFSR mounted with a Collision Cross-Mixer in contrast to that with a Center T-Mixer. It also showcases the potential to decrease T_c by tuning the mixer design and by developing new processes, without introducing extra doping elements. It should be noticed that for samples synthesized with higher flow rates, only a fraction of the VO_2 particles were contributing to the latent heat under 100°C , considering the fact that the MIT of A-phase VO_2 is 162°C [4]. Therefore, samples fabricated with flow rates higher than 4 mL/min and 2 mL/min are purely for reference in this study, indicating that thermochromic effects do exist even for samples with mixed phases.

It is clearly shown that a collision type of the mixing system is capable of improving the morphologies and phase transition temperatures of VO_2 nanoparticles in comparison to the Center T-Mixer, without affecting the phase purity significantly.

4. Conclusions

Continuous-flow hydrothermal syntheses of VO₂ nanoparticles were performed using a hot water fluidized suspension reaction (HWFSR) system mounted with two differing styles of mixers: a Center T-Mixer and a Collision Cross-Mixer. The utilization of a Collision Cross-Mixer resulted in smaller particles with up to 600 nm diameter and a narrower particle size distribution with a shorter mean residence time of 0.7 min when compared to the implementation of a Center T-Mixer that produced a size distribution ranging from a few nanometers to around 1 μm. In addition, pure M-phase particles were obtained from both mixing systems when increasing the mean residence time to 1.8 minutes. Transition temperatures of the as-derived VO₂ particles are also decreased by using the Collision Cross-Mixer. The mixer is cost-effective and convenient for implementation into a microreactor. The reaction procedure is a one-step rapid process without the energy consuming annealing step which is traditionally used to force all A- or B-phase VO₂ particles into pure M-phase material. Furthermore, the safe and fast HWFSR continuous-flow process equipped with designed mixers is applicable for other particle fabrication processes requiring high temperatures and pressures.

Data Availability

The X-ray diffraction analysis and differential scanning calorimetry measurement data on synthesized materials used to support the findings of this study are available from the corresponding author upon request.

Conflicts of Interest

The authors declare that there is no conflict of interest regarding the publication of this paper.

Acknowledgments

This work is funded by the Argonne National Laboratory LDRD (Lab Directed Research & Development) program. Use of the Center for Nanoscale Materials, an Office of the Science User Facility, was supported by the U.S. Department of Energy, Office of Science, Office of Basic Energy Sciences, under Contract No. DE-AC02-06CH11357. We thank Dr. Elena Shevchenko, Dr. Xiao-Min Lin, Dr. Brandon Fisher, and Dr. Christopher Fry from the Center of Nanoscale Materials for the assistance on characterization processes.

References

- [1] Z. Chen, Y. F. Gao, L. T. Kang, C. X. Cao, S. Chen, and H. J. Luo, "Fine crystalline VO₂ nanoparticles: synthesis, abnormal phase transition temperatures and excellent optical properties of a derived VO₂ nanocomposite foil," *Journal of Materials Chemistry A*, vol. 2, no. 8, pp. 2718–2727, 2014.
- [2] L. L. Chen, X. F. Wang, D. Y. Wan et al., "Tuning the phase transition temperature, electrical and optical properties of VO₂ by oxygen nonstoichiometry: insights from first-principles calculations," *RSC Advances*, vol. 6, no. 77, pp. 73070–73082, 2016.
- [3] W. L. Yu, S. Li, and C. Huang, "Phase evolution and crystal growth of VO₂ nanostructures under hydrothermal reactions," *RSC Advances*, vol. 6, no. 9, pp. 7113–7120, 2016.
- [4] Y. F. Zhang, "VO₂(B) conversion to VO₂(A) and VO₂(M) and their oxidation resistance and optical switching properties," *Materials Science-Poland*, vol. 34, no. 1, pp. 169–176, 2016.
- [5] S.-Y. Li, G. A. Niklasson, and C. G. Granqvist, "Thermochromic fenestration with VO₂-based materials: three challenges and how they can be met," *Thin Solid Films*, vol. 520, no. 10, pp. 3823–3828, 2012.
- [6] R. Lopez, T. E. Haynes, L. A. Boatner, L. C. Feldman, and R. F. Haglund, "Temperature-controlled surface plasmon resonance in VO₂ nanorods," *Optics Letters*, vol. 27, no. 15, pp. 1327–1329, 2002.
- [7] Y. Zhou, Y. F. Cai, X. Hu, and Y. Long, "VO₂/hydrogel hybrid nanothermochromic material with ultra-high solar modulation and luminous transmission," *Journal of Materials Chemistry A*, vol. 3, no. 3, pp. 1121–1126, 2015.
- [8] S.-Y. Lia, G. A. Niklasson, and C. G. Granqvist, "Nanothermochromics: calculations for VO₂ nanoparticles in dielectric hosts show much improved luminous transmittance and solar energy transmittance modulation," *Journal of Applied Physics*, vol. 108, no. 6, article 063525, 2010.
- [9] J. Livage, "Hydrothermal synthesis of nanostructured vanadium oxides," *Materials*, vol. 3, no. 8, pp. 4175–4195, 2010.
- [10] S. Marre, J. Y. Baek, J. N. Park, M. G. Bawendi, and K. F. Jensen, "High-pressure/high-temperature microreactors for nanostructure synthesis," *Journal of the Association for Laboratory Automation*, vol. 14, no. 6, pp. 367–373, 2009.
- [11] P. W. Dunne, A. S. Munn, C. L. Starkey, T. A. Huddle, and E. H. Lester, "Continuous-flow hydrothermal synthesis for the production of inorganic nanomaterials," *Philosophical Transactions of the Royal Society A: Mathematical, Physical and Engineering Sciences*, vol. 373, no. 2057, article 20150015, 2015.
- [12] R. I. Gruar, C. J. Tighe, and J. A. Darr, "Scaling-up a confined jet reactor for the continuous hydrothermal manufacture of nanomaterials," *Industrial & Engineering Chemistry Research*, vol. 52, no. 15, pp. 5270–5281, 2013.
- [13] M. J. Powell, P. Marchand, C. J. Denis, J. C. Bear, J. A. Darr, and I. P. Parkin, "Direct and continuous synthesis of VO₂ nanoparticles," *Nanoscale*, vol. 7, no. 44, pp. 18686–18693, 2015.
- [14] X. J. Yan, I. Castano, Y. G. Sun, R. Muehleisen, and J. Li, "Continuous-flow synthesis of thermochromic M-phase VO₂ particles via one-step hydrothermal reaction," *Materials Science and Engineering B*, 2019.
- [15] L. Zhou, S. Z. Wang, D. H. Xu, and Y. Guo, "Impact of mixing for the production of CuO nanoparticles in supercritical hydrothermal synthesis," *Industrial & Engineering Chemistry Research*, vol. 53, no. 1, pp. 481–493, 2014.
- [16] S. A. Hong, S. J. Kim, K. Y. Chung, M. S. Chun, B. G. Lee, and J. H. Kim, "Continuous synthesis of lithium iron phosphate (LiFePO₄) nanoparticles in supercritical water: effect of mixing tee," *The Journal of Supercritical Fluids*, vol. 73, pp. 70–79, 2013.
- [17] Y. Wakashima, A. Suzuki, S. I. Kawasaki, K. Matsui, and Y. Hakuta, "Development of a new swirling micro mixer for continuous hydrothermal synthesis of nano-size particles,"

- Journal of Chemical Engineering of Japan*, vol. 40, no. 8, pp. 622–629, 2007.
- [18] K. Mae, A. Suzuki, T. Maki, Y. Hakuta, H. Sato, and K. Arai, “A new micromixer with needle adjustment for instant mixing and heating under high pressure and high temperature,” *Journal of Chemical Engineering of Japan*, vol. 40, no. 12, pp. 1101–1107, 2007.
- [19] K. Sue, T. Sato, S. Kawasaki et al., “Continuous hydrothermal synthesis of Fe_2O_3 nanoparticles using a central collision-type micromixer for rapid and homogeneous nucleation at 673 K and 30 MPa,” *Industrial & Engineering Chemistry Research*, vol. 49, no. 18, pp. 8841–8846, 2010.
- [20] L. Hua, Z. Jian, and L. Qing, “Preparation and characterization of VO_2 nano powder by thermal decomposing $\text{VOCl}_2 \cdot 2\text{H}_2\text{O}$,” *Iron Steel Vanadium Titanium*, vol. 27, no. 1, pp. 58–63, 2006.
- [21] F. Y. Kong, M. Li, X. Y. Yao et al., “Template-free hydrothermal synthesis of VO_2 hollow microspheres,” *CrysEngComm*, vol. 14, no. 11, pp. 3858–3861, 2012.
- [22] H. Ham, N. H. Park, S. S. Kim, and H. W. Kim, “Evidence of ostwald ripening during evolution of micro-scale solid carbon spheres,” *Scientific Reports*, vol. 4, no. 1, article 3579, 2014.
- [23] L. Dai, C. X. Cao, Y. F. Gao, and H. J. Luo, “Synthesis and phase transition behavior of undoped VO_2 with a strong nano-size effect,” *Solar Energy Materials & Solar Cells*, vol. 95, no. 2, pp. 712–715, 2011.
- [24] M. Wang, Y. Q. Xue, Z. X. Cui, and R. Zhang, “Size-dependent crystal transition thermodynamics of nano- VO_2 (M),” *The Journal of Physical Chemistry C*, vol. 122, no. 15, pp. 8621–8627, 2018.
- [25] L. Whittaker, C. Jaye, Z. G. Fu, D. A. Fischer, and S. Banerjee, “Depressed phase transition in solution-grown VO_2 nanostructures,” *Journal of The American Chemical Society*, vol. 131, no. 25, pp. 8884–8894, 2009.
- [26] J. Jian, X. J. Wang, L. G. Li et al., “Continuous tuning of phase transition temperature in VO_2 thin films on c-cut sapphire substrates via strain variation,” *Applied Materials & Interfaces*, vol. 9, no. 6, pp. 5319–5327, 2017.
- [27] C. Z. Wu, X. D. Zhang, J. Dai et al., “Direct hydrothermal synthesis of monoclinic VO_2 (M) single-domain nanorods on large scale displaying magnetocaloric effect,” *Journal of Materials Chemistry*, vol. 21, no. 12, pp. 4509–4517, 2011.
- [28] M. Li, S. Magdassi, Y. Gao, and Y. Long, “Hydrothermal synthesis of VO_2 polymorphs: advantages, challenges and prospects for the application of energy efficient smart windows,” *Advanced Science News*, vol. 13, no. 36, article 1101147, 2017.

Research Article

Optimization of Tb^{3+}/Gd^{3+} Molar Ratio for Rapid Detection of Naja Atra Cobra Venom by Immunoglobulin G-Conjugated $GdPO_4 \cdot nH_2O:Tb^{3+}$ Nanorods

Pham Thi Lien,^{1,2} Nguyen Thanh Huong^{1,2},^{ORCID} Tran Thu Huong,^{1,2} Hoang Thi Khuyen,^{1,2} Nguyen Thi Ngoc Anh,^{1,2} Nguyen Duc Van,¹ Nguyen Ngoc Tuan,³ Vu Xuan Nghia,³ and Le Quoc Minh^{1,2,4}

¹Institute of Materials Science, Vietnam Academy of Science and Technology, Vietnam

²Graduate University of Science and Technology, Vietnam Academy of Science and Technology, 18 Hoang Quoc Viet, Cau Giay, Hanoi, Vietnam

³Vietnam Military Medical University, 160 Phung Hung, Phuc La, Ha Dong, Hanoi, Vietnam

⁴Duy Tan University, K7/25, Quang Trung, Danang, Vietnam

Correspondence should be addressed to Nguyen Thanh Huong; nthuong@ims.vast.ac.vn

Received 1 February 2019; Accepted 30 April 2019; Published 16 May 2019

Guest Editor: Zhen Yu

Copyright © 2019 Pham Thi Lien et al. This is an open access article distributed under the Creative Commons Attribution License, which permits unrestricted use, distribution, and reproduction in any medium, provided the original work is properly cited.

In this report, $GdPO_4 \cdot nH_2O$ and Tb^{3+} -doped $GdPO_4 \cdot nH_2O$ nanorods@silica- NH_2 conjugated with IgG antibody were synthesized by applying hydrothermal, sol-gel, and coprecipitation methods successively. The effects of Tb^{3+}/Gd^{3+} molar ratios of reactants on the size, morphology, and luminescence of the synthesized samples were also investigated. For the optimized $GdPO_4 \cdot nH_2O:Tb^{3+}$ sample, uniform nanorods sizing from 10 to 30 nm in diameter and from 200 to 300 nm in length were obtained with the strongest luminescence in green color with narrow bands under the UV excitation (325 nm). The results revealed that, after being coated with silica- NH_2 and conjugated with IgG antibody, all luminescence characteristic peaks of $GdPO_4 \cdot nH_2O:Tb^{3+}$ corresponding to the process of energy transfer from Gd^{3+} to Tb^{3+} and then the emission from ${}^5D_4 \rightarrow {}^7F_J$ ($J=6,5,4,3$) of Tb^{3+} were still clearly observed. The initial results of using the optimized Tb^{3+} -doped $GdPO_4 \cdot nH_2O$ nanorods@silica- NH_2 conjugated with IgG antibody for rapid selective detection of Naja atra cobra venom were also reported.

1. Introduction

Rare earth-containing luminescent nanomaterials have drawn a special interest for telecommunication, imaging, lightning, fluorescent security labelling, and biomedical applications due to their attractive physical and optical properties, biocompatibility, environmentally friendly characteristics, and nontoxicity and especially due to their high efficiency [1–18]. These materials exhibited outstanding performances such as strong, stable luminescent intensity with a large *Stock* shift, narrow peak width, and long luminescent lifetime [6]. This luminescent lifetime of these materials is significantly longer, up to milliseconds, in comparison to that of quantum dots or organic luminescent materials. That

enables to minimize intrinsic luminescent background emitted from biological samples by employing the time-resolved signal recording process. Many targeted applications such as fluorescent labelling [19], drug delivery [20], and imaging for detecting biological species like virus, bacteria, cell, DNA, RNA molecules, or proteins [15, 18, 19] of new hybrid nanophosphors containing rare-earth elements (Eu, Tb, and Er) with various host materials ($GdPO_4$, Gd_2O_3 , YVO_4 , and $NaYF_4$) have been carried out so far [20–25]. For the synthesis of these materials, numerous chemical methods of luminescent nanomaterials containing rare earth elements have been used such as coprecipitation [5], sol-gel Pechini [6], and hydrothermal/solvothermal method [26–29]. Among these hybrid nanophosphors, Tb^{3+} -doped $GdPO_4 \cdot nH_2O$

nanomaterials are found to be one of the most promising candidates for these abovementioned applications due to these nanomaterials that exhibit strong luminescent intensity, paramagnetic behavior, no toxicity, and ability to minimize photobleaching and photochemical decomposition [22, 23, 30–33]. It was reported in literature that Tb³⁺-doped GdPO₄·nH₂O nanomaterials were usually synthesized by the hydrothermal method and the effects of the doping concentration on their luminescent properties were already performed [27, 31–33]. However, it was indicated that, to obtain the highest luminescence intensity of Tb³⁺-doped GdPO₄·nH₂O, the doping Tb³⁺ concentration depended strongly on the hydrothermal synthesis parameters and no optimized procedures was provided. Furthermore, these materials have not been applied in biomedical applications to date. In details, the silica coating of Tb³⁺-doped GdPO₄·nH₂O followed by functionalization and conjugation with antibody have not been investigated.

In this paper, GdPO₄·nH₂O:Tb³⁺ nanorods were synthesized by controlling hydrothermal process and the effects of the Tb³⁺/Gd³⁺ molar ratio on the nanorod size, morphology, and luminescence of the as-prepared products were also investigated systematically. Moreover, GdPO₄·nH₂O:Tb³⁺ nanorods have been covered by silica as a shell, functionalized with NH₂ and conjugated with a specific antibody (IgG) to enable to set up a fluorescent immunoassay procedure for rapid detection and microscopic bioimaging *Naja atra cobra venom in vitro*.

2. Materials and Methods

All used chemicals were of analytical grade, including Gd(NO₃)₃·6H₂O (Sigma-Aldrich, 99.9%), Tb(NO₃)₃·6H₂O (Sigma-Aldrich, 99.9%), NH₄H₂PO₄ (Merck), and NH₄OH 28% (Merck). The deionized (DI) water was used through all the preparation steps of nanomaterials. *Naja atra cobra venom antigen* was supplied by the Immunology Department of Vietnam Military Medical University.

2.1. Synthesis of GdPO₄·nH₂O:Tb³⁺ Materials. For the synthesis of GdPO₄·nH₂O:Tb³⁺ nanorods, 20 ml of 0.1 M NH₄H₂PO₄ solution was added into a 100 ml round-bottom flask containing 0.05 M Gd(NO₃)₃ and 0.05 M Tb(NO₃)₃ with molar ratios of Tb³⁺/Gd³⁺ are 1%, 3%, 5%, 7%, and 9% during stirring. The pH value of the obtained solution was adjusted to 2 by using 1 M NH₄OH solution. After being stirred for 1 h, the mixture was transferred into a 100 ml teflon-lined stainless-steel autoclave. The autoclave was sealed and heated at 200°C for 24 hours. The white precipitate was centrifuged, washed with DI water and ethanol, and dried at 70°C for 24 hours.

2.2. GdPO₄·nH₂O:Tb³⁺ Materials Coated with Silica Layer via the Sol-Gel Process. Briefly, 0.1 g GdPO₄·nH₂O:Tb³⁺ nanorods were dispersed in 20 ml of ethanol (EtOH) by using a Vortex mixing equipment to obtain mixture A. Subsequently, 60 μl of deionized water and 60 μl of CH₃COOH were added into a 250 ml round-bottom flask containing 50 ml of EtOH and 30 μl TEOS during stirring for 15 minutes

to receive mixture B. Mixture A was then dropped into mixture B, and the final mixture was stirred for 24 hours. Finally, the resulting precipitate was centrifuged and washed with distilled water and ethanol several times. The white precipitate was dispersed in 30 ml EtOH solution for the next functionalization process.

2.3. The Surface Functionalization with -NH₂ (GdPO₄·nH₂O:Tb³⁺@Silica-NH₂). For the surface functionalization of GdPO₄·nH₂O:Tb³⁺ by the NH₂ group, 20 μl APTES (3-aminopropyltriethoxysilane) and 40 μl CH₃COOH was added into a 250 ml round-bottom flask containing 50 ml of EtOH. The solution was stirred by magnetic stirring at room temperature for 2 hours. The mixture of 0.3 g GdPO₄·nH₂O:Tb³⁺ and 30 ml EtOH was then dropped into the above solution, and the stirring was remained for 2 hours. The resulting products were collected, centrifuged, and washed with ethanol and distilled water several times. The white precipitate was kept in 30 ml deionized water for the binding process with biological elements.

2.4. Conjugation between GdPO₄·nH₂O:Tb³⁺@Silica-NH₂ with Specific IgG Antibody to Detect *Naja Atra Cobra Venom*. Glutaraldehyde (GDA) was used to form a complex between GdPO₄·nH₂O:Tb³⁺@silica-NH₂ with IgG antibody due to the fact that it is a homobifunctional cross-linker to bridge both homogenous aldehyde groups, resulting in conjugation.

The specific IgG antibody conjugation process is as follows: The GdPO₄·nH₂O:Tb³⁺@silica-NH₂ solution obtained above (in 2.3.) was centrifuged and cleaned three times with 25 mM sodium phosphate (pH 7.0). The resulting products were dissolved in 5 ml of sodium phosphate solution. Then, 10 ml of glutaraldehyde 0.5% was added and mixed by a vortex mixer for 1 hour at room temperature to form a uniform suspension. 10 μl of anti-venom rabbit antibody was mixed with 100 μl of the solution obtained above in a ratio of 1:10 then mixed well and kept at room temperature for 2 to 4 hours.

Excess glutaraldehyde linkers were blocked by adding 1.5 M ethanolamine in phosphate-buffered saline (PBS) reacting with 10% volume of GdPO₄·nH₂O:Tb³⁺@silica-NH₂-IgG solution for 2 hours at room temperature. The residual ethanolamine was then removed by washing and centrifugation three times with 0.1 mM PBS solution. The resulting products were dissolved in 5 ml of 25 mM sodium phosphate (pH 7.0) and stored at 4°C for the next steps. The final obtained product was GdPO₄·nH₂O:Tb³⁺@silica-NH₂-IgG solution.

2.5. Detection of *Cobra Venom* by the Nanorods-Antibodies (GdPO₄·nH₂O:Tb³⁺@Silica-NH₂-IgG). *Cobra venom* for detection was conducted as follows: six-well plates (polystyrene plate) were coated with 50 μl/well of *Naja atra venom* (20 μg/ml) then diluted in 0.05 M carbonate buffer at pH = 9.6. After incubation at 4°C for 12 h, the plates were washed three times with 0.15 M PBS-0.05% Tween-20 (PT) and blocked with 50 μl/well PBS, 1% BSA, 0.05% Tween-20, and 0.02% sodium azide (PBTN) for 1 hour at room

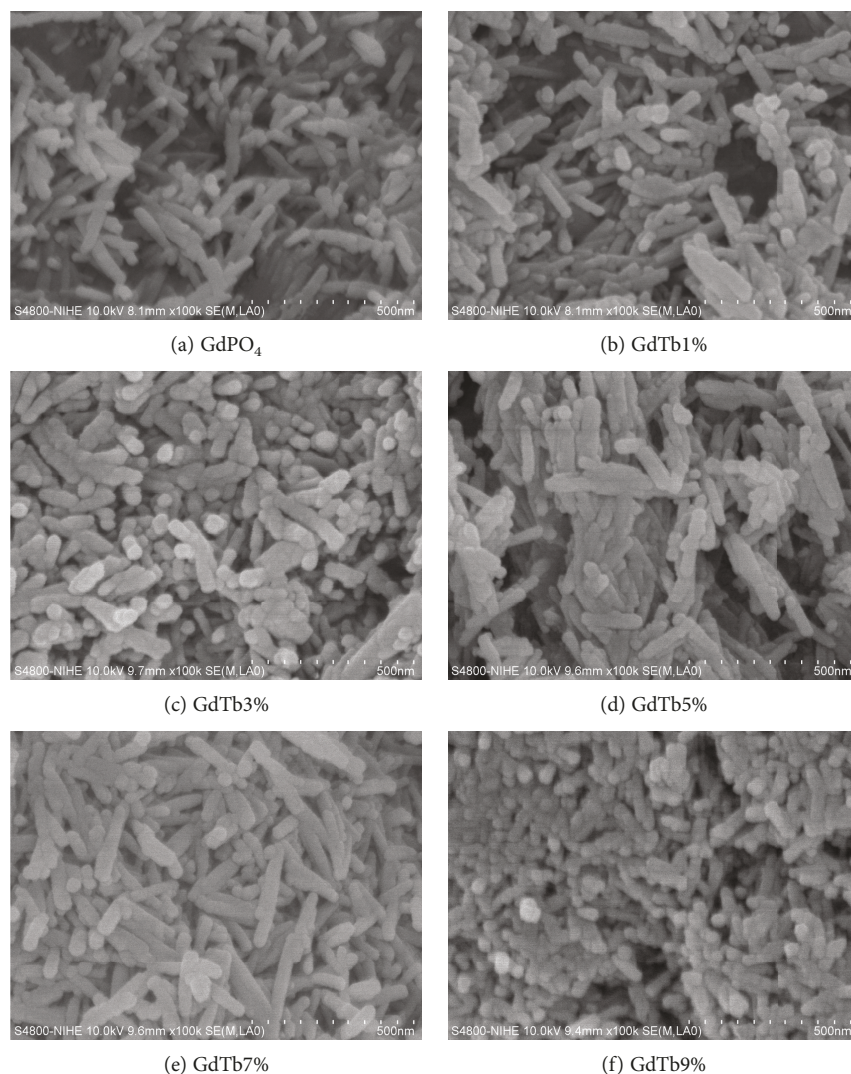


FIGURE 1: FESEM images of $\text{GdPO}_4 \cdot n\text{H}_2\text{O} : \text{Tb}^{3+}$ with molar ratios of $\text{Tb}^{3+}/\text{Gd}^{3+}$ are 0, 1, 3, 5, 7, and 9%.

temperature. After three times of washing cycle in PT, $50 \mu\text{l}$ antibody nanorods diluted in PBTN were added into each well and incubated at room temperature for 2 hours. Specific antibody-bound $\text{GdPO}_4 \cdot n\text{H}_2\text{O} : \text{Tb}^{3+} @ \text{silica-NH}_2$ nanorods were used to bind cobra venom antigens. After the plates were washed four times with PT to remove the nonsticking components, the emission color of the nanorods was used to detect the presence of specific expressed venom found under excitation UV light.

2.6. Measurements. The morphology of these nanomaterials was observed by field emission scanning electron microscopy (FESEM, Hitachi S4800). The structure of the materials was determined with the X-ray diffraction system (Siemens D5000). The fluorescence emission and excitation spectra of the materials were measured with a high-resolution microscope (FL 3-22 HORIBA). The ability to detect venom of the nanoparticles is indicated by emitting a green color under a fluorescence microscope (ZEISS Primo Star iLED).

3. Results and Discussion

3.1. The Morphology of Synthesized Samples. The FESEM images of $\text{GdPO}_4 \cdot n\text{H}_2\text{O} : \text{Tb}^{3+}$ with different molar ratios of $\text{Tb}^{3+}/\text{Gd}^{3+}$ from 1 to 9 mol % are given in Figure 1. FESEM images of $\text{GdPO}_4 \cdot n\text{H}_2\text{O} : \text{Tb}^{3+}$ show no significant change in the shape and size of the nanorods with different molar ratios.

It can be seen that $\text{GdPO}_4 \cdot n\text{H}_2\text{O} : \text{Tb}^{3+}$ nanorods with the molar ratio of 7% are the most uniform rods (average length of 300–500 nm and width of 10–30 nm).

3.2. X-Ray Diffraction Investigation of $\text{GdPO}_4 \cdot n\text{H}_2\text{O} : \text{Tb}^{3+}$. Figure 2 shows that the all diffraction peaks of $\text{GdPO}_4 \cdot n\text{H}_2\text{O}$ and $\text{GdPO}_4 \cdot n\text{H}_2\text{O} : \text{Tb}^{3+}$ have high intensity, narrow width at 2θ angles of 15.24, 20.61, 25.81, 30.00, 32.19, 38.71, 43.09, 48.1, 49.86, and 53.15 and can be distinctly indexed to a standard pattern coded 98-004-3396 of gadolinium orthophosphate hydrate.

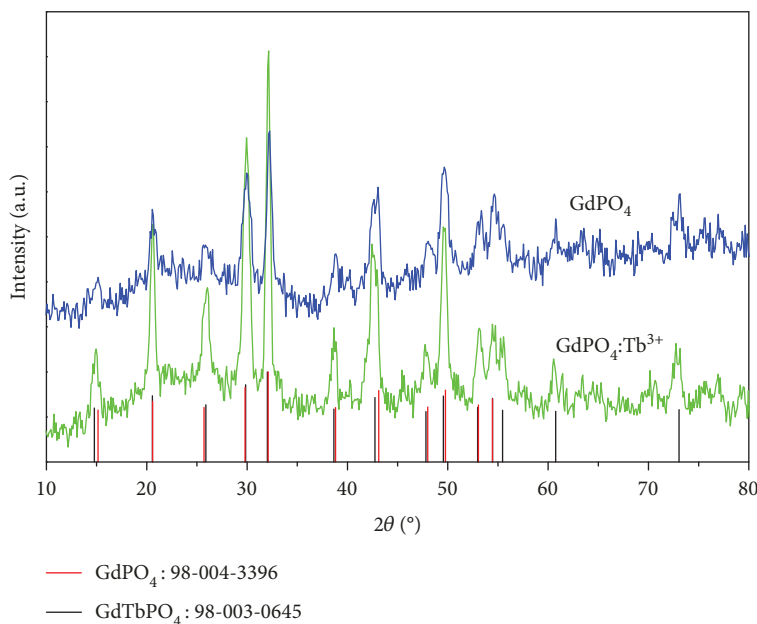


FIGURE 2: X-ray diffraction patterns of $\text{GdPO}_4 \cdot n\text{H}_2\text{O}$ and $\text{GdPO}_4 \cdot n\text{H}_2\text{O}:\text{Tb}^{3+}$.

3.3. Photoluminescence Properties. In order to investigate the luminescence intensity and determine the radiative transfer between the energy levels of the electrons in these materials, the excitation and fluorescence spectra of these samples were measured under 543 nm and 272 nm excitations, respectively (Figure 3).

In the excitation spectra of $\text{GdPO}_4 \cdot n\text{H}_2\text{O}:\text{Tb}^{3+}$ (Figure 3(a)), the characteristic transition peaks exist around 310 nm and 272 nm which belong to ${}^6\text{P}_1 \rightarrow {}^8\text{S}_{7/2}$ and ${}^8\text{S}_{7/2} \rightarrow {}^6\text{I}_1$ of Gd^{3+} , respectively [34]. The energy level between ${}^6\text{P}_1$ and ${}^8\text{S}_{7/2}$ of Gd^{3+} is similar to Tb^{3+} , so that the excitation energy of Gd^{3+} can be transferred to Tb^{3+} . Under the 272 nm excitation, the photoluminescence spectra of the $\text{GdPO}_4 \cdot n\text{H}_2\text{O}:\text{Tb}^{3+}$ (1-9%) samples emitted in the green light region with the characteristic transitions of $\text{Tb}^{3+}:$ ${}^5\text{D}_4 \rightarrow {}^7\text{F}_n$ ($n = 6, 5, 4, 3$) (shown in Figure 3(b)). The transition of ${}^5\text{D}_4 \rightarrow {}^7\text{F}_6$, ${}^5\text{D}_4 \rightarrow {}^7\text{F}_5$, ${}^5\text{D}_4 \rightarrow {}^7\text{F}_4$, and ${}^5\text{D}_4 \rightarrow {}^7\text{F}_3$ of Tb^{3+} can be observed at 488, 543, 586, and 620 nm, respectively, and the strongest emission peak was found at 543 nm. The results showed that $\text{GdPO}_4 \cdot n\text{H}_2\text{O}:\text{Tb}^{3+}$ nanorods with 7% exhibit the strongest green luminescence. It can be seen that the fluorescence of $\text{GdPO}_4 \cdot n\text{H}_2\text{O}$ doped with Tb^{3+} was greatly enhanced due to the energy transfer process from Gd^{3+} to Tb^{3+} [34, 35]. The uniform nanorods were obtained by changing the ratios of Gd^{3+} and Tb^{3+} which were functionalized and dispersed in the water and ready for biological applications.

Figure 4 presents the photoluminescence spectra of nanorod solutions: $\text{GdPO}_4 \cdot n\text{H}_2\text{O}:\text{Tb}^{3+}$ (1); $\text{GdPO}_4 \cdot n\text{H}_2\text{O}:\text{Tb}^{3+}@\text{silica}$ (2), $\text{GdPO}_4 \cdot n\text{H}_2\text{O}:\text{Tb}^{3+}@\text{silica-NH}_2$ (3), and $\text{GdPO}_4 \cdot n\text{H}_2\text{O}:\text{Tb}^{3+}@\text{silica-NH}_2\text{-IgG}$ (4) under 355 nm excitation. The green emission at 491, 544, 588, and 620 nm corresponding to ${}^5\text{D}_4 \rightarrow {}^7\text{F}_6$, ${}^5\text{D}_4 \rightarrow {}^7\text{F}_5$, ${}^5\text{D}_4 \rightarrow {}^7\text{F}_4$, and ${}^5\text{D}_4 \rightarrow {}^7\text{F}_3$ of Tb^{3+} transitions of Tb^{3+} ions, respectively. The emission intensity of these samples decreases with the

functional steps of $\text{GdPO}_4 \cdot n\text{H}_2\text{O}:\text{Tb}^{3+}$ nanorods. However, luminescent intensity is not much changed after conjugating with IgG and the maximum emission peak is found at 543 nm. This is the good condition for labelling the cobra venom antigen identification in the next steps.

3.4. IR Properties. The functionalized nanorods were analyzed by IR spectra using the Nexus 670 infrared spectrometer (Nicolet).

The infrared spectra of $\text{GdPO}_4 \cdot n\text{H}_2\text{O}:\text{Tb}^{3+}$ (a), $\text{GdPO}_4 \cdot n\text{H}_2\text{O}:\text{Tb}^{3+}@\text{silica}$ (b), $\text{GdPO}_4 \cdot n\text{H}_2\text{O}:\text{Tb}^{3+}@\text{silica-NH}_2$ (c), and $\text{GdPO}_4 \cdot n\text{H}_2\text{O}:\text{Tb}^{3+}@\text{silica-NH}_2\text{-IgG}$ (d) samples are presented in Figure 5. It can be observed that oscillations of the O-H bond were found at around 1600 cm^{-1} and near 3500 cm^{-1} in lines (a) and (b). Oscillations at 545 and 622 cm^{-1} are assigned to the stretching vibrations of $(\text{PO}_4)^{3-}$ [36]. The stretching vibrations of the C-H bond were observed at 2898 cm^{-1} , 2976 cm^{-1} and 2884 cm^{-1} , 2941 cm^{-1} corresponding to $\text{GdPO}_4 \cdot n\text{H}_2\text{O}:\text{Tb}^{3+}@\text{silica-NH}_2$ (c) and $\text{GdPO}_4 \cdot n\text{H}_2\text{O}:\text{Tb}^{3+}@\text{silica-NH}_2\text{-IgG}$ (d) samples. In these samples, the stretching vibrations of $(\text{PO}_4)^{3-}$ are still observed at 622 and 880 cm^{-1} . The peaks in the range of $3300\text{-}3500\text{ cm}^{-1}$ and $1590\text{-}1620\text{ cm}^{-1}$ appear as stretching and bending vibrations of the N-H bond. These results show that the fabricated samples were successfully surface-functionalized with the NH_2 groups as a binding agent.

3.5. Application of Nanorods Conjugated with Rabbit Antibody to Detect Naja Atra Cobra Venom Antigen

3.5.1. Evaluating the Results of Binding Nanorods with Rabbit Antibody by Infrared Spectra. The infrared spectra of the synthesized samples were used to elucidate the difference

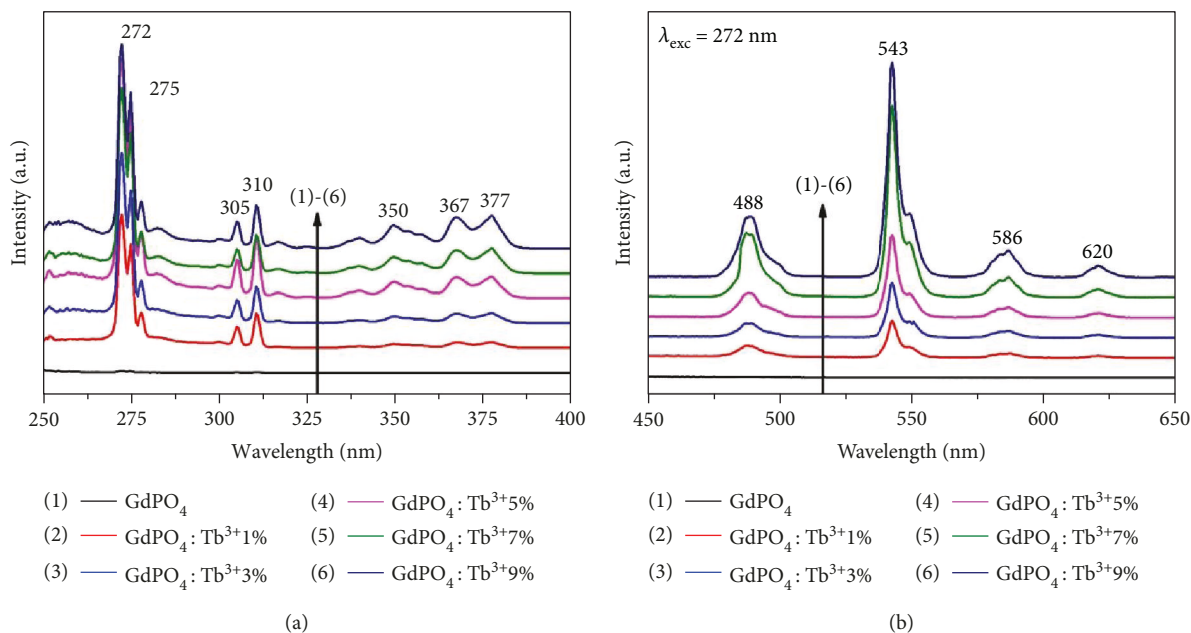


FIGURE 3: Excitation (a) and photoluminescence spectra (b) of the $\text{GdPO}_4 \cdot n\text{H}_2\text{O} : \text{Tb}^{3+}$ samples with molar ratios of $\text{Tb}^{3+}/\text{Gd}^{3+}$ are 0, 1, 3, 5, 7, and 9%.

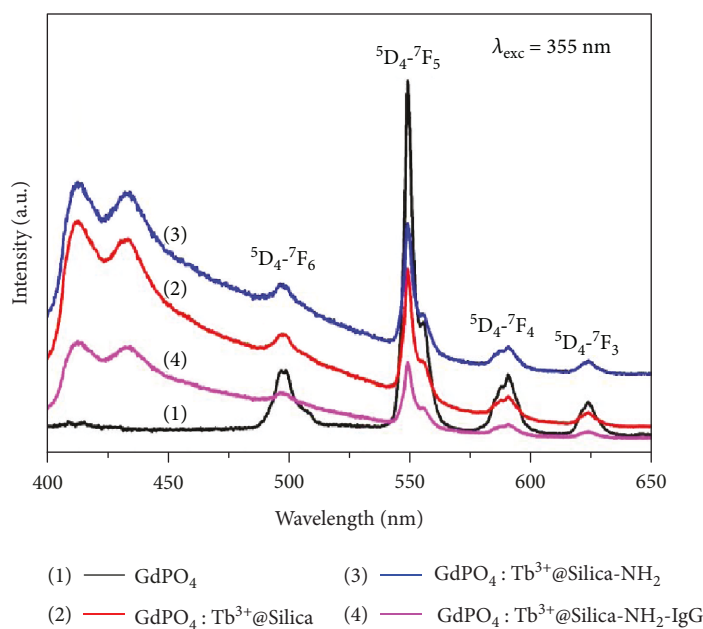


FIGURE 4: Photoluminescence spectra of $\text{GdPO}_4 \cdot n\text{H}_2\text{O} : \text{Tb}^{3+}$ with molar ratios of $\text{Tb}^{3+}/\text{Gd}^{3+} = 7\%$ conjugated with IgG.

between anti-venom antibody before and after conjugating with luminescence nanorods.

In Figure 6(a), the strong and wide peak at 3460 cm^{-1} corresponds to the O-H bond. The peak at 2079 cm^{-1} belongs to the N-H bond. The wavenumbers from 1640 cm^{-1} to 1443 cm^{-1} are the oscillating peaks of the C=O and N-H bonds in the first amine group, respectively.

Figure 6(b) shows that the peak at 1389 cm^{-1} indicates the forming the C-N bond through reaction of the aldehyde

group (O=C-H) of the GDA linker with NH_2 of IgG. Thus, it can be suggested that the conjugation (linkage) between luminescence nanorods with anti-venom antibodies was formed.

3.5.2. Evaluation the Ability of the $\text{GdPO}_4 \cdot n\text{H}_2\text{O} : \text{Tb}^{3+} @ \text{Silica} - \text{NH}_2 - \text{IgG}$ (Nanorods-Antibodies) to Detect the *Naja Atracobra* Venom. As the experimental steps described above (in Section 2.5), in order to evaluate the ability of

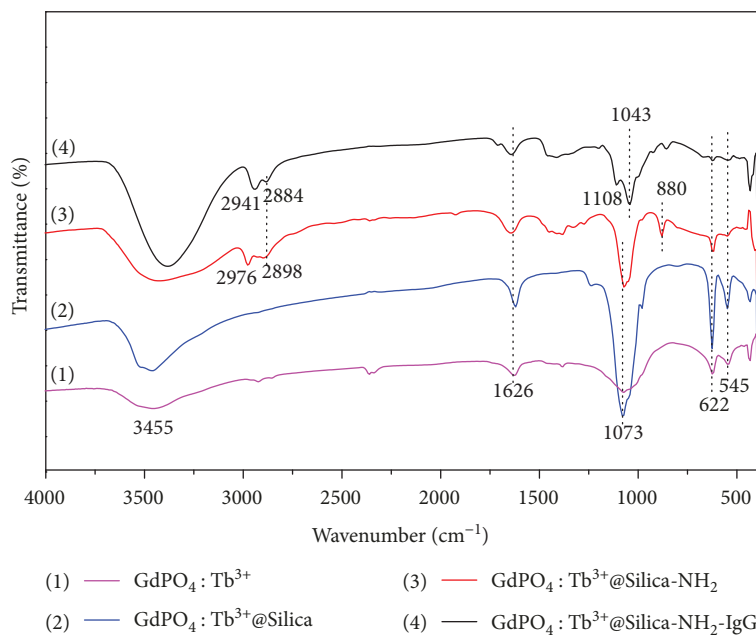


FIGURE 5: IR spectra of GdPO₄·nH₂O, GdPO₄·nH₂O:Tb³⁺, GdPO₄·nH₂O:Tb³⁺@silica-NH₂, and GdPO₄·nH₂O:Tb³⁺@silica-NH₂-IgG.

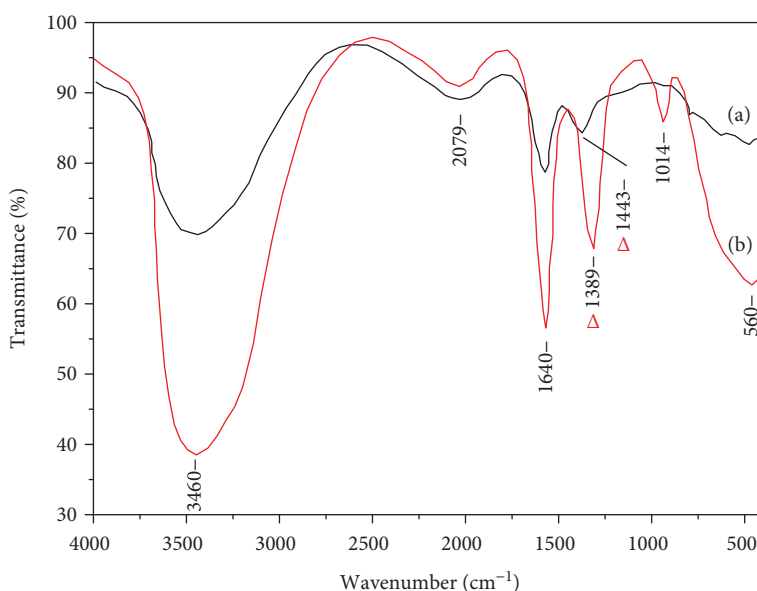


FIGURE 6: IR spectra of IgG antibody without (a) and with (b) luminescence nanorods.

detection of *Naja atra* cobra venom of nanorods, two kinds of well groups were organized. The wells coated with *Naja atra* cobra venom antigens were incubated with nanorods (1) and nanorods-antibodies (2). The image of *Naja atra* cobra venom antigens after coating on the plate under visible light of a 40x microscope is illustrated in Figure 7(a) while Figures 7(b) and 7(c) present the images of *Naja atra* cobra venom antigens conjugated with nanorods-antibodies observed without and with UV light of 40x fluorescence microscope, respectively.

The results showed that the wells incubated with nanorods-antibodies provided a green image and nanoparticles distributed uniformly throughout the field green light under a 40x fluorescence microscope (Figure 7(c)). This result shows that these wells have a specific association between the nanorods-antibodies and the *Naja atra* cobra antigen so that when it was washed, it does not wash away. Meanwhile, other emissions were not green due to the absence of a combination of antibody-coated nanoparticles and *Naja atra* cobra venom antigens so they were washed

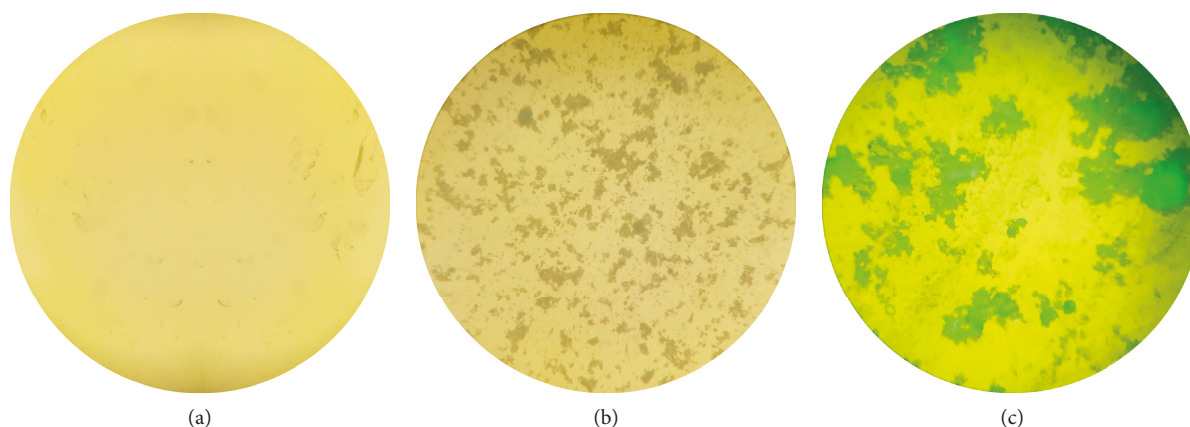


FIGURE 7: The images of *Naja atra cobra* venom antigens under visible light (a); *Naja atra cobra* venom antigens conjugated with nanorods-antibodies without UV light (b) and with UV light (c) under 40x fluorescence microscope.

away during washing. Based on these results, it could be concluded that this *Naja atra* venom detection procedure can shorten the time needed for early diagnosis and improve the efficacy of treatment and thus could facilitate early treatment of snake bite and save lives. Thus, with respect to other green-emitting luminescent materials like Yb,Er-codoped NaYF_4 or $\text{TbPO}_4 \cdot \text{H}_2\text{O}$ -based nanomaterials [19, 20], our synthesized immunoglobulin G-conjugated $\text{GdPO}_4 \cdot n\text{H}_2\text{O} : \text{Tb}^{3+}$ nanorods are compatible for detection of antigen-antibody reaction.

4. Conclusions

$\text{GdPO}_4 \cdot n\text{H}_2\text{O}$ and $\text{GdPO}_4 \cdot n\text{H}_2\text{O} : \text{Tb}^{3+}$ nanorods with a tetragonal phase were synthesized by the hydrothermal method. Optical properties of nanorod materials were optimized by varying the concentration ratio of $\text{Tb}^{3+}/\text{Gd}^{3+}$. At 7 mol % of Tb^{3+} , the nanorods exhibited the strongest luminescence because of the energy transfer from gadolinium to terbium. The most uniform nanorods have dimensions of 300–500 nm in length and 10–30 nm in width. The surface functionalization of luminescent nanorods conjugated with rabbit IgG antibodies can be used for early and rapid detecting *Naja atra cobra* venom antigen.

Data Availability

The concerning data used to support the findings of this study are available from the corresponding author upon request.

Conflicts of Interest

The authors declare that there is no conflict of interest regarding the publication of this paper.

Acknowledgments

This research is funded by Vietnam National Foundation for Science and Technology Development (NAFOSTED) under grant number 103.03-2017.53. The authors are also grateful to the Key Laboratory for Electronic and Devices,

Institute of Materials Science, Vietnam Academy of Science and Technology.

References

- [1] S. Gai, C. Li, P. Yang, and J. Lin, "Recent progress in rare earth micro/nanocrystals: soft chemical synthesis, luminescent properties, and biomedical applications," *Chemical Reviews*, vol. 114, no. 4, pp. 2343–2389, 2013.
- [2] P. Mi, N. Dewi, H. Yanagie et al., "Hybrid calcium phosphate polymeric micelles in incorporating gadolinium chelates for imaging-guided gadolinium neutron capture tumor therapy," *ACS Nano*, vol. 9, no. 6, pp. 5913–5921, 2015.
- [3] W. U. Yanli, X. U. Xianzhu, L. I. Qianlan, R. YANG, H. DING, and Q. XIAO, "Synthesis of bifunctional $\text{Gd}_2\text{O}_3 : \text{Eu}^{3+}$ nanocrystals and their applications in biomedical imaging," *Journal of Rare Earths*, vol. 33, no. 5, pp. 529–534, 2015.
- [4] V. Kumar, S. Singh, R. K. Kotnala, and S. Chawla, "GdPO₄:Eu³⁺ nanoparticles with intense orange red emission suitable for solar spectrum conversion and their multifunctionality," *Journal of Luminescence*, vol. 146, pp. 486–491, 2014.
- [5] Y. S. Vidya, K. S. Anantharaju, H. Nagabhushana, and S. C. Sharma, "Euphorbia tirucalli mediated green synthesis of rose like morphology of Gd₂O₃:Eu³⁺ red phosphor: structural, photoluminescence and photocatalytic studies," *Journal of Alloys and Compounds*, vol. 619, pp. 760–770, 2015.
- [6] H. T. Khuyen, P. T. Thu, T. T. Huong et al., "Synthesis and characterization of nanostructured europium(III) complexes containing gold nanoparticles," *Journal of Luminescence*, vol. 166, pp. 67–70, 2015.
- [7] T. Yang, C. Mocofanescu, H. G. Shen, and C. Xiao, "Nanoparticles for biomedical applications," in *Micro and Nano Manipulations for Biomedical Applications*, T. C. Yih and I. Talpasanu, Eds., pp. 43–100, Artech House Publishers, Norwood, Mass, USA, 2008.
- [8] D. Yang, P. Ma, Z. Hou, Z. Cheng, C. Li, and J. Lin, "Current advances in lanthanide ion (Ln^{3+})-based upconversion nanomaterials for drug delivery," *Chemical Society Reviews*, vol. 44, no. 6, pp. 1416–1448, 2015.
- [9] O. J. Fakayode, N. Tsolekile, S. P. Songca, and O. S. Oluwafemi, "Applications of functionalized nanomaterials in photodynamic therapy," *Biophysical Reviews*, vol. 10, no. 1, pp. 49–67, 2018.

- [10] W. Xu, Y. Chang, and G. H. Lee, "Biomedical applications of lanthanide oxide nanoparticles," *Journal of Biomaterials and Tissue Engineering*, vol. 7, no. 9, pp. 757–769, 2017.
- [11] D. Kennedy and M. G. Wilkinson, "Application of flow cytometry to the detection of pathogenic bacteria," *Current Issues in Molecular Biology*, vol. 23, pp. 21–38, 2017.
- [12] A. Escudero, A. I. Becerro, C. Carrillo-Carrión et al., "Rare earth based nanostructured materials: synthesis, functionalization, properties and bioimaging and biosensing applications," *Nano*, vol. 6, no. 5, pp. 881–921, 2017.
- [13] Z. Wang, J. G. Li, Q. Zhu et al., "EDTA-assisted phase conversion synthesis of $(\text{Gd}_{0.95}\text{RE}_{0.05})\text{PO}_4$ nanowires (RE = Eu, Tb) and investigation of photoluminescence," *Science and Technology of Advanced Materials*, vol. 18, no. 1, pp. 447–457, 2017.
- [14] J. Shen, L. D. Sun, and C. H. Yan, "Luminescent rare earth nanomaterials for bioprobe applications," *Dalton Transactions*, vol. 42, no. 42, pp. 5687–5697, 2008.
- [15] T. H. Greg, *Bioconjugate Techniques*, Pierce Biotechnology, Thermo Fisher Scientific, Rockford, IL, 3rd Edition edition, 2013.
- [16] D. Shen, B. Zhao, S. Yang et al., " $\text{NaScMo}_2\text{O}_8:\text{RE}^{3+}$ (RE = Tb, Eu, Tb/Eu, Yb/Er, Yb/Ho) phosphors: hydrothermal synthesis, energy transfer and multicolor tunable luminescence," *Journal of Materials Science*, vol. 52, no. 24, pp. 13868–13878, 2017.
- [17] J. J. H. A. van Hest, G. A. Blab, H. C. Gerritsen, C. de Mello Donega, and A. Meijerink, "Probing the influence of disorder on lanthanide luminescence using Eu-doped LaPO_4 nanoparticles," *The Journal of Physical Chemistry C*, vol. 121, no. 35, pp. 19373–19382, 2017.
- [18] B. M. Anshu, *Nanotechnology in Cancer*, Elsevier, Houston, TX, USA, 2016.
- [19] N. T. Huong, P. T. Lien, N. M. Hung et al., "Conjugation of $\text{TbPO}_4\cdot\text{H}_2\text{O}$ -based nanowires with immunoglobulin G for bioimaging," *Journal of Electronic Materials*, vol. 45, no. 5, pp. 2463–2467, 2016.
- [20] M. Wang, C. C. Mi, W. X. Wang et al., "Immunolabeling and NIR-excited fluorescent imaging of HeLa cells by using $\text{NaYF}_4:\text{Yb,Er}$ upconversion nanoparticles," *ACS Nano*, vol. 3, no. 6, pp. 1580–1586, 2009.
- [21] Q. Du, Z. Huang, Z. Wu et al., "Facile preparation and bifunctional imaging of Eu-doped GdPO_4 nanorods with MRI and cellular luminescence," *Dalton Transactions*, vol. 44, no. 9, pp. 3934–3940, 2015.
- [22] E. Pavitra and J. Su Yu, "A facile large-scale synthesis and luminescence properties of $\text{Gd}_2\text{O}_3:\text{Eu}^{3+}$ nanoflowers," *Materials Letters*, vol. 90, pp. 134–137, 2013.
- [23] L. Zhang, H. Jiu, Y. Fu et al., "Facile synthesis and luminescence of $\text{GdPO}_4:\text{Eu}$ hollow microspheres by a sacrificial template route," *Materials Letters*, vol. 101, pp. 47–50, 2013.
- [24] L. K. Bharat, Y. I. Jeon, and J. S. Yu, "Synthesis and luminescent properties of trivalent rare-earth (Eu^{3+} , Tb^{3+}) ions doped nanocrystalline $\text{AgLa}(\text{PO}_3)_4$ polyphosphates," *Journal of Alloys and Compounds*, vol. 614, pp. 443–447, 2014.
- [25] L. I. Fuhai, H. LIU, S. WEI, W. SUN, and Y. U. Lixin, "Photoluminescent properties of Eu^{3+} and Tb^{3+} codoped Gd_2O_3 nanowires and bulk materials," *Journal of Rare Earths*, vol. 31, no. 11, pp. 1063–1068, 2013.
- [26] L. Hernández-Adame, A. Méndez-Blas, J. Ruiz-García, J. R. Vega-Acosta, F. J. Medellín-Rodríguez, and G. Palestino, "Synthesis, characterization, and photoluminescence properties of Gd:Tb oxysulfide colloidal particles," *Chemical Engineering Journal*, vol. 258, pp. 136–145, 2014.
- [27] H. Song, L. Zhou, L. Li, F. Hong, and X. Luo, "Hydrothermal synthesis, characterization and luminescent properties of $\text{GdPO}_4\cdot\text{H}_2\text{O}:\text{Tb}^{3+}$ nanorods and nanobundles," *Materials Research Bulletin*, vol. 48, no. 12, pp. 5013–5018, 2013.
- [28] M. Shang, D. Geng, X. Kang, D. Yang, Y. Zhang, and J. Lin, "Hydrothermal derived $\text{LaOF}:\text{Ln}^{3+}$ (Ln = Eu, Tb, Sm, Dy, Tm, and/or Ho) nanocrystals with multicolor-tunable emission properties," *Inorganic Chemistry*, vol. 51, no. 20, pp. 11106–11116, 2012.
- [29] V. Kumar, S. Singh, and S. Chawla, "Fabrication of dual excitation, dual emission nanophosphor with broad UV and IR excitation through simultaneous doping of triple rare earth ions Er^{3+} , Yb^{3+} , Eu^{3+} in GdPO_4 ," *Superlattices and Microstructures*, vol. 79, pp. 86–95, 2015.
- [30] N. T. Huong, N. M. Hung, P. T. Lien et al., "Fabrication and characterization of luminescent magnetic bifunctional nanocomposite based on $\text{TbPO}_4\cdot\text{H}_2\text{O}$ nanowires and Fe_3O_4 nanoparticles," *Journal of Electronic Materials*, vol. 45, no. 7, pp. 3646–3650, 2016.
- [31] F. Hu, X. Wei, Y. Qin et al., " $\text{Yb}^{3+}/\text{Tb}^{3+}$ co-doped GdPO_4 transparent magnetic glass-ceramics for spectral conversion," *Journal of Alloys and Compounds*, vol. 674, pp. 162–167, 2016.
- [32] H. Lai, X. Yang, and H. Yang, "Luminescent properties of $\text{GdPO}_4:\text{Eu}$ nanorods," *Journal of Materials Science: Materials in Electronics*, vol. 23, no. 1, pp. 285–289, 2012.
- [33] X.-y. Kuang, H. Liu, W.-y. Hu, and Y.-z. Shao, "Hydrothermal synthesis of core-shell structured $\text{TbPO}_4:\text{Ce}^{3+}/\text{TbPO}_4:\text{Gd}^{3+}$ nanocomposites for magnetic resonance and optical imaging," *Dalton Transactions*, vol. 43, no. 32, pp. 12321–12328, 2014.
- [34] L. Li, G. Li, D. Wang, Y. Tao, and X. Zhang, "Energy transfer mechanism of $\text{GdPO}_4:\text{RE}^{3+}$ (RE = Tb, Tm) under VUV-UV excitation," *Science in China Series E: Technological Sciences*, vol. 49, no. 4, pp. 408–413, 2006.
- [35] C. R. Kesavulu, H. J. Kim, S. W. Lee, J. Kaewkhao, E. Kaewnuam, and N. Wantana, "Luminescence properties and energy transfer from Gd^{3+} to Tb^{3+} ions in gadolinium calcium silicoborate glasses for green laser application," *Journal of Alloys and Compounds*, vol. 704, pp. 557–564, 2017.
- [36] N. Yaiphaba, R. S. Ningthoujam, N. R. Singh, and R. K. Vatsa, "Luminescence properties of redispersible Tb^{3+} -doped GdPO_4 nanoparticles prepared by an ethylene glycol route," *European Journal of Inorganic Chemistry*, vol. 2010, no. 18, pp. 2682–2687, 2010.

Research Article

Synthesis and Photocatalytic Properties of Co-Doped $\text{Zn}_{1-x}\text{Co}_x\text{Mn}_2\text{O}$ Hollow Nanospheres

Long Ma,^{1,2} Zhiqiang Wei ,^{1,2} Xueliang Zhu,² Jiahao Liang,² and Xudong Zhang²

¹State Key Laboratory of Advanced Processing and Recycling of Non-Ferrous Metals, Lanzhou University of Technology, Lanzhou 730050, China

²School of Science, Lanzhou University of Technology, Lanzhou 730050, China

Correspondence should be addressed to Zhiqiang Wei; qianweizuo@163.com

Received 20 December 2018; Accepted 21 March 2019; Published 9 May 2019

Guest Editor: Zhen Yu

Copyright © 2019 Long Ma et al. This is an open access article distributed under the Creative Commons Attribution License, which permits unrestricted use, distribution, and reproduction in any medium, provided the original work is properly cited.

A series of Co-doped $\text{Zn}_{1-x}\text{Co}_x\text{Mn}_2\text{O}$ nanocrystals with a spinel structure were successfully prepared by hydrothermal method, and the influence of Co doping concentration on the microstructure, morphology, elemental composition, and optical and photocatalytic properties of the samples was characterized. The experimental results show that all samples exhibit a tetragonal structure, Co^{2+} ions are successfully substituted for the lattice site of Zn^{2+} to generate ZnMn_2O_4 nanocrystals, and the crystalline size decreases as Co-doped concentration increase. The morphologies are loose hollow microsphere structures. The band gap of $\text{Zn}_{1-x}\text{Co}_x\text{Mn}_2\text{O}$ samples is smaller than that of pure ZnMn_2O_4 and has been red shifted. The photocatalytic activity of doped $\text{Zn}_{1-x}\text{Co}_x\text{Mn}_2\text{O}_4$ samples is obviously higher than that of pure ZnMn_2O_4 samples for the photodegradation of MO under visible light irradiation. All these results demonstrate that Co-doped spinel ZnMn_2O_4 nanocrystals are a meaningful choice for photocatalytic degradation of the pollutants.

1. Introduction

In recent decades, with the development of modern industry, the growth of population, and the acceleration of urbanization, the increased pollution of natural water and air has become one of the major challenges that the modern human society and the ecological system are facing and the main pollution sources are nondegradable and toxic artificial dyes [1–4]. The toxic compounds in water media cause serious harm to human health. Nanoscale semiconductor photocatalysts have attracted extensive research interest in the field of environmental restoration owing to their potential value, such as nontoxic, inexpensive, strong oxidizing activity, and chemical stability [5–8].

Spinel structure ZnMn_2O_4 belongs to I41/amd space group, and with a narrow band gap of 1.86 eV [9, 10]. ZnMn_2O_4 nanocrystals possess unique properties that are quite different from those of the bulk solid state due to their surface effect, quantum size effect, small size effect, and quantum tunnelling effect [11, 12]. Spinel structure ZnMn_2O_4

nanocrystals have attracted considerable attention due to their novel properties and broad application prospect in the gas sensor [13], photocatalyst [14], supercapacitor electrode [15, 16], lithium ion battery anode [17], energy storage [18], nonvolatile memory [19], etc. In recent years, some researchers have studied transition metal ion-doped ZnMn_2O_4 nanocrystals to obtain the desired crystal structure and energy band structure by providing extra positive carriers in the host material [20]. The crystal structure and energy band structure of semiconductor materials can be modified to improve their physical properties by controlling the preparation process, changing the type and amount of doped elements [21, 22]. In addition, transition metal ion configuration doping can significantly improve the separation rate of photoinduced carriers in semiconductor photocatalysts, inhibit the recombination of photoinduced electron hole pairs, and greatly improve photocatalytic activity [23]. Unfortunately, as far as we know, there are few reports about the influence of doping concentration on the photocatalytic performance of the transition

metal-ion doped ZnMn₂O₄ nanostructure. Therefore, the main purpose of this study is to study the effect of doping concentration on the microstructure and photocatalytic activity.

In this work, Co-doped Zn_{1-x}Co_xMn₂O nanocrystals with different ratios ($x = 0, 0.1, 0.3, \text{ and } 0.5$) were successfully synthesized by hydrothermal method. The influence of Co doping concentration on the microstructure, morphology, elemental composition, and optical properties of the samples was investigated by X-ray diffraction (XRD), field emission scanning electron microscopy (FESEM), X-ray energy dispersive spectrometry (XEDS), ultraviolet-visible spectroscopy (UV-Vis), and Fourier transform infrared spectroscopy (FT-IR), and the photocatalytic activity of Zn_{1-x}Co_xMn₂O nanocrystals was evaluated by the photodegradation of MO dye in aqueous solution under UV light irradiation.

2. Material and Methods

2.1. Synthesis. A facile hydrothermal method was used to synthesize Zn_{1-x}Co_xMn₂O₄ ($x = 0, 0.1, 0.3, \text{ and } 0.5$) nanocrystals. In a typical experiment, zinc nitrate (Zn(NO₃)₂·6H₂O, AR, Tianjin Kaixin Chemical Industry Co. Ltd.), manganese nitrate (Mn(NO₃)₂·6H₂O, AR, Tianjin Kemeiou Reagent Co. Ltd.), cobalt nitrate (Co(NO₃)₂·6H₂O, AR, Shanghai Zhongqin Reagent Co. Ltd.), polyethylene glycol-400 (PEG-400, AR, Shandong West Asia Chemical Reagent Co. Ltd.), absolute ethyl alcohol (AR, China Pharmaceutical Group Reagent Co. Ltd), and citric acid (AR, Tianjin Kemeiou Reagent Co. Ltd.) were used in this study without any further purification. According to the chemical formula of Zn_{1-x}Co_xMn₂O₄ ($x = 0, 0.1, 0.3, \text{ and } 0.5$) and the molar ratio of metal cations, the stoichiometric quantities of zinc nitrate, cobalt nitrate, and manganese nitrate as precursors were weighed. Zn(NO₃)₂, Mn(NO₃)₂, and Co(NO₃)₂ were mixed in distilled water and magnetically stirred at room temperature for 30 min. Meanwhile, appropriate amounts of citric acid and PEG-400 were dripped into the above-mixed solution under magnetic stirring for 3 hours. Subsequently, the resulting solution was transferred to a 100 mL Teflon-lined stainless steel autoclave. The hydrothermal reaction process was conducted at 180°C for 24 h in an oven and then cooled to room temperature naturally. Finally, the resultant precipitate was separated centrifugally, washed several times with distilled water and absolute alcohol, respectively, and then dried at 60°C in a vacuum oven for 10 h. Thus, Zn_{1-x}Co_xMn₂O₄ nanocrystals were collected and used for further study. By comparison, Zn_{1-x}Co_xMn₂O₄ nanoparticles with different ratios ($x = 0, 0.1, 0.3, \text{ and } 0.5$) were also prepared using the abovementioned procedure.

2.2. Characterization. The crystal structure of the as-obtained samples was examined by X-ray diffractometer (XRD) using the CuK α source ($\lambda = 1.54056 \text{ \AA}$), the scanning rate 0.005°/s, and step size 0.02°. The morphology of the samples was investigated using a field emission scanning electron microscope (SEM) (JEOL JSM-6701F) equipped with an X-ray energy dispersive spectroscopy (XEDS). The ultraviolet-visible (UV-Vis) diffuse reflectance spectra (DRS) of the

products were recorded on a UV-Vis spectrophotometer (PERSEE TU-1901) using BaSO₄ as reference. Fourier transform infrared spectroscopy (FT-IR) studies were measured by a Nexus 670 FT-IR spectrometer in the range of 4000–400 cm⁻¹.

2.3. Photocatalytic Activity Test. The photocatalytic property of the samples was evaluated by measuring the degradation of methyl orange (MO) aqueous solution in a cylindrical glass vessel under simulated sunlight, and the reaction vessel was kept at a constant temperature using a circulating cooling system. The reaction solution was irradiated with the light source of a 300 W xenon lamp, and the distance between the solution surface and the light source was kept at 30 cm to avoid thermal effect. In this work, 20 mg of the as-synthesized samples was dispersed into a 100 mL MO aqueous solution (the initial MO aqueous solution concentration was 10 mg/L). The mixed suspensions were magnetically stirred for 30 min in the dark to reach the adsorption-desorption equilibrium between the photocatalyst and organic dye MO. During the photocatalytic process, about 2.5 mL of the reaction solution was collected from the container at predetermined intervals (30, 60, 90, 120, and 150 min) and the solid catalyst powder was separated and recovered by external magnetism field method. Then, the concentration of residual MO in the solution was determined by detecting the adsorption and degradation performance using an UV-visible spectrophotometer.

3. Results and Discussion

3.1. Structural Characterization. Figure 1 depicts the XRD patterns of pure ZnMn₂O₄ and Co-doped Zn_{1-x}Co_xMn₂O₄ samples. The diffraction peaks of all samples can be well indexed to single-phase ZnMn₂O₄ tetragonal structures (space group: 141/amd, $a = b = 0.5722 \text{ nm}$, and $c = 0.9326 \text{ nm}$), which are in agreement with the reported values of JCPDS card no. 71-2499 [24]. No extra diffraction peaks of other impurity phases such as metal oxides or metal clusters are detected when the doping atomic percentage ranges from 10% to 50% from the XRD patterns, indicating that all Co ions are assumed to be successfully incorporated into Zn²⁺ ion sites without changing the parent ZnMn₂O₄ structure. The crystallite size of the samples is calculated from the full width at half maximum (FWHM) and the peak position using the most intense diffraction peak (211) by the following Scherrer formula: $D = K\lambda/B \cos \theta$, where D represents the crystallite size, $K = 0.9$ is the Scherrer constant, λ is the wavelength of X-ray (CuK α , 1.54056 Å), θ is the Bragg diffraction angle, and B is FWHM in radians of the (211) plane. The crystallite sizes for Zn_{1-x}Co_xMn₂O₄ ($x = 0, 0.1, 0.3, \text{ and } 0.5$) are 36, 33, 31, and 29 nm; it is clear that the crystallite size gradually decreases with the increase of the Co doping amount.

3.2. Morphological Studies. The SEM image of the pure ZnMn₂O₄ sample is showed in Figure 2(a). It is clearly visible that the morphology of pure ZnMn₂O₄ is a regular porous microspheres architecture mainly composed of many

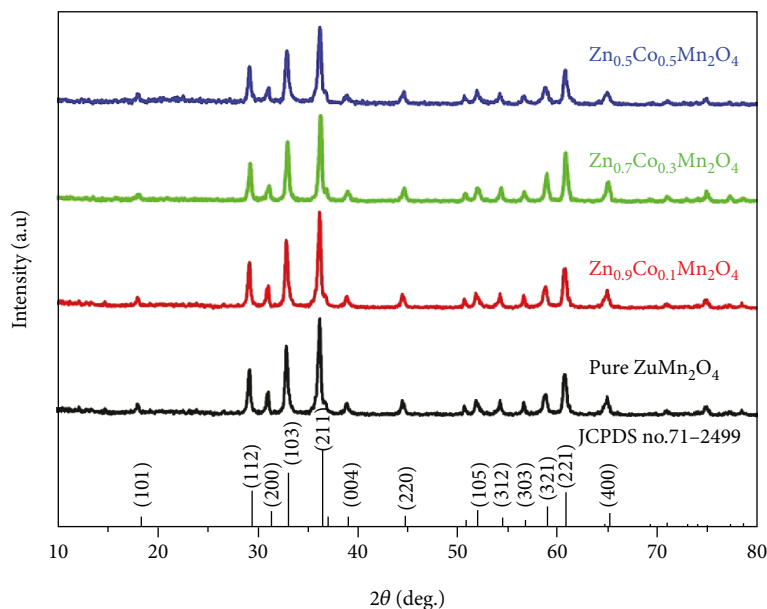


FIGURE 1: XRD patterns of $Zn_{1-x}Co_xMn_2O_4$ samples.

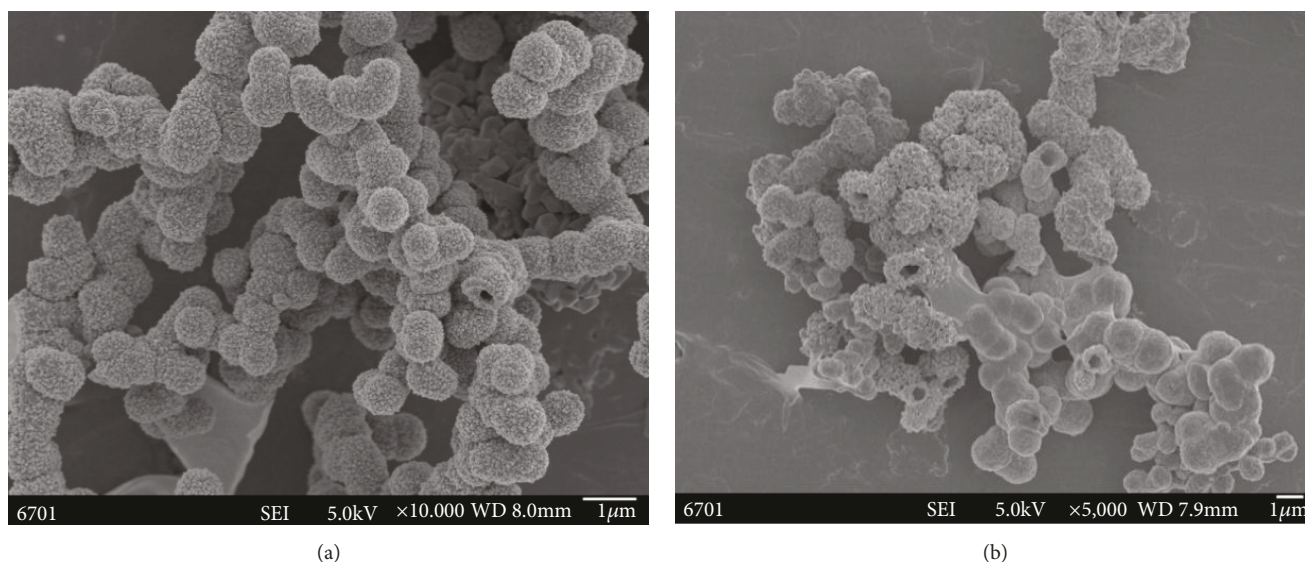


FIGURE 2: SEM images of (a) pure $ZnMn_2O_4$ and (b) $Zn_{0.7}Co_{0.3}Mn_2O_4$ samples.

nanoparticles, with the diameter of the rough and porous microspheres ranging from 300 to 500 nm, with the average diameter of about 400 nm. Figure 2(b) presents the SEM image of the $Zn_{0.7}Co_{0.3}Mn_2O_4$ sample, showing a loose and irregular microsphere morphology composed of massive nanoparticles. With the increase of the Co doping content, the edges of the microsphere become looser and hollow and some stacked microspheres appear in breakage and exhibit hollow microspheres. The hollow microspheres grow bigger in size and rougher and irregular in morphology. This loose hollow microsphere structure contributes to improving the electrochemical performance.

Figure 3(a) shows the XEDS patterns of the pure $ZnMn_2O_4$ sample to further clarify the chemical components of the as-prepared samples. It is easily found that pure $ZnMn_2O_4$ mainly exhibits the peak characteristic of Zn, Mn, and O elements. Figure 3(b) obviously confirms the presence of Co elements besides Zn, Mn, and O elements for the $Zn_{0.7}Co_{0.3}Mn_2O_4$ sample, whereas the spectrum of pure $ZnMn_2O_4$ does not find the presence of Co elements. The XEDS results further verify XRD, which indicates that Co-doped $ZnMn_2O_4$ nanocrystals were successfully synthesized by hydrothermal method and Co^{2+} is successfully substituted as dopant in the $ZnMn_2O_4$ matrix. It is evident

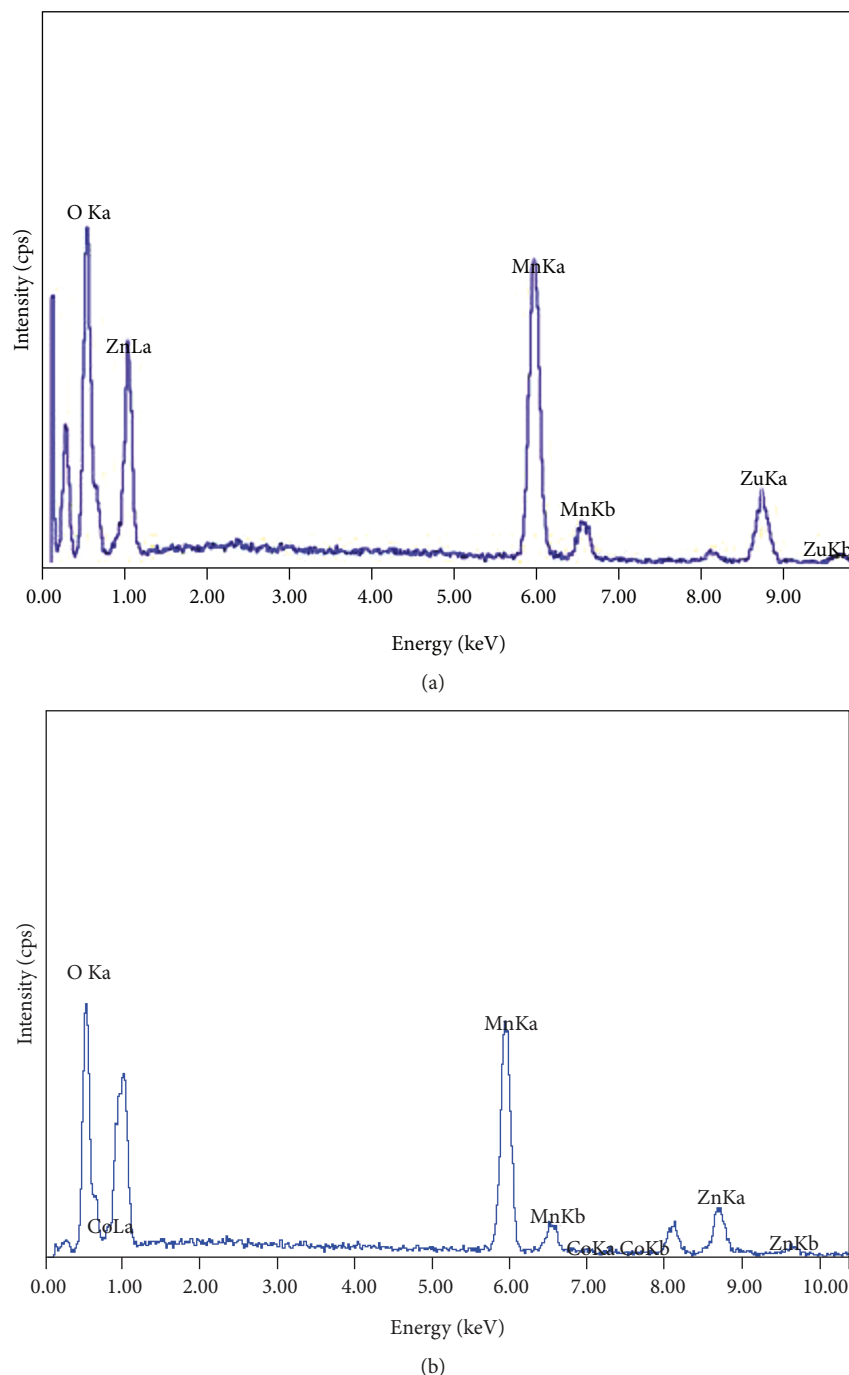


FIGURE 3: XEDS patterns of (a) pure ZnMn_2O_4 and (b) $\text{Zn}_{0.7}\text{Co}_{0.3}\text{Mn}_2\text{O}_4$ samples.

that the synthesis condition helps to further study the influence of Co doping concentration on the properties of $\text{Zn}_{1-x}\text{Co}_x\text{Mn}_2\text{O}_4$ nanocrystals.

3.3. UV-Vis DRS Results. The optical properties of the samples are investigated by UV-Vis DRS. Figure 4(a) shows the absorption spectra of $\text{Zn}_{1-x}\text{Co}_x\text{Mn}_2\text{O}_4$ samples. From Figure 4(a), Co-doped $\text{Zn}_{1-x}\text{Co}_x\text{Mn}_2\text{O}_4$ samples show the similar absorption property as that of the pure ZnMn_2O_4 except that the absorption edge slightly shifts to a short

wavelength with increasing Co content. The drift of the absorption edge revealed the interaction between Co ions and ZnMn_2O_4 . For $\text{Zn}_{1-x}\text{Co}_x\text{Mn}_2\text{O}_4$ nanocrystals with a direct band structure, according to the Tauc rule [25]: $[\alpha h\nu]^2 = A(h\nu - E_g)$, the optical band gap E_g is evaluated from the linear intercept of the $(\alpha h\nu)^2$ versus $h\nu$ plots as displayed in Figure 4(b). Consequently, the band gaps for $\text{Zn}_{1-x}\text{Co}_x\text{Mn}_2\text{O}_4$ ($x = 0, 0.1, 0.3, \text{ and } 0.5$) are calculated to be 2.21, 2.07, 2.02, and 1.98 eV, respectively. Furthermore, the band gap of the Co-doped ZnMn_2O_4 samples smaller than

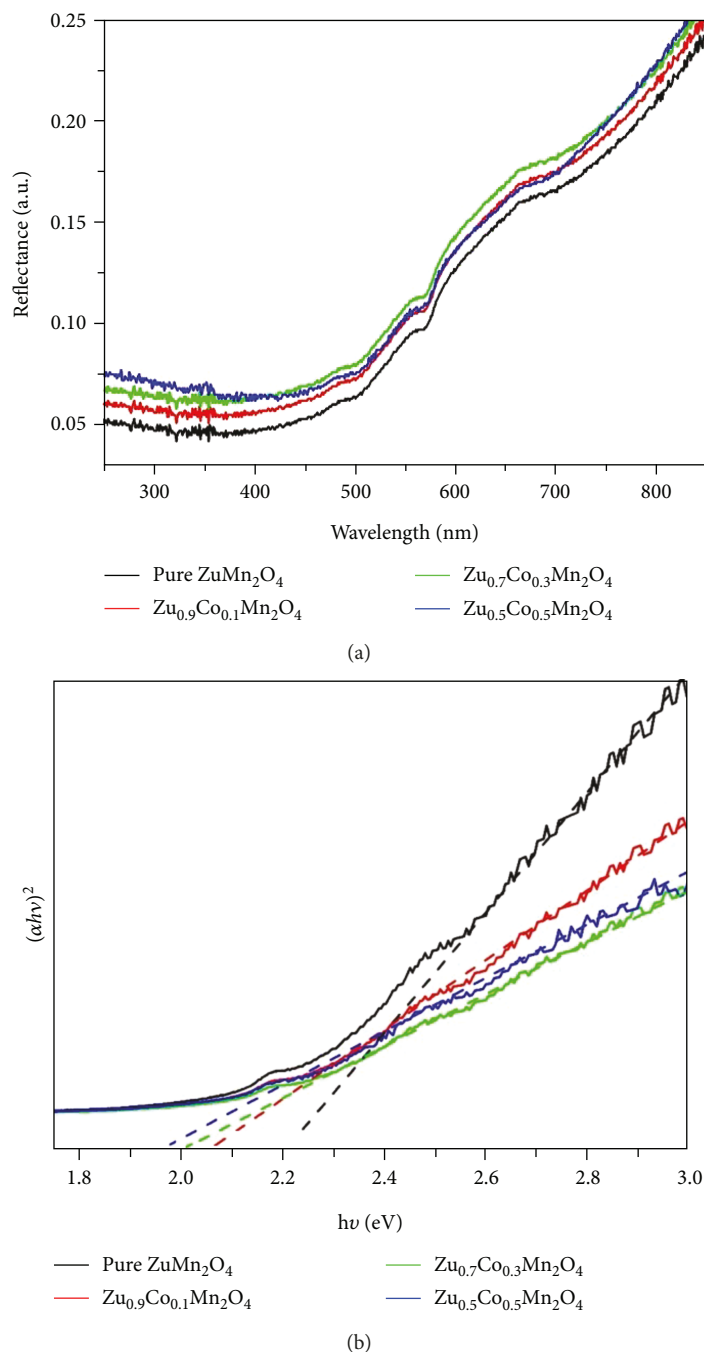


FIGURE 4: (a) UV-Vis diffuse reflectance spectra and (b) $(\alpha h\nu)^2$ versus $h\nu$ curves of $\text{Zn}_{1-x}\text{Co}_x\text{Mn}_2\text{O}_4$ samples.

that of pure ZnMn_2O_4 and the band gap energy gradually decrease with the increase of Co concentration. This is manifested by the presence of a redshift in the band gap energy for Co-doped $\text{Zn}_{1-x}\text{Co}_x\text{Mn}_2\text{O}_4$ nanocrystals.

3.4. FT-IR Spectra. The chemical structure of $\text{Zn}_{1-x}\text{Co}_x\text{Mn}_2\text{O}_4$ samples was investigated using FT-IR, and the results were shown in Figure 5, wherein all of the samples exhibit very similar FT-IR absorption bands. A broad absorption band at 3410 cm^{-1} in the spectrum of $\text{Zn}_{1-x}\text{Co}_x\text{Mn}_2\text{O}_4$ nanocrystals corresponds to O-H stretching vibrations of

chemically bonded hydroxyl groups. The peak that appeared at 2923 cm^{-1} attributed to the vibrational absorption peaks corresponding to the C-H bonds [26], and the peak at 1542 cm^{-1} was caused by the C=O stretching vibrations of the remaining carbonyl groups in the compound [27]; the band at 1367 cm^{-1} can be assigned to the organic compounds of PEG-400 or alcohol induced in the process of preparation and test, and the presence of the peak at 1084 cm^{-1} is owing to C-O stretching vibrations [26]. It is noteworthy that two distinct peaks that appear at 505 and 622 cm^{-1} are dependent on the formation of metal-oxygen bonds of tetrahedral and

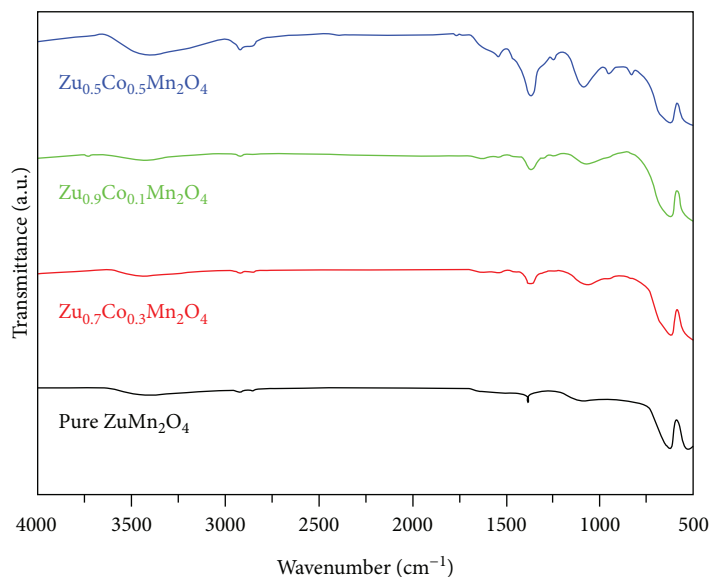


FIGURE 5: FT-IR spectra of $Zn_{1-x}Co_xMn_2O_4$ samples.

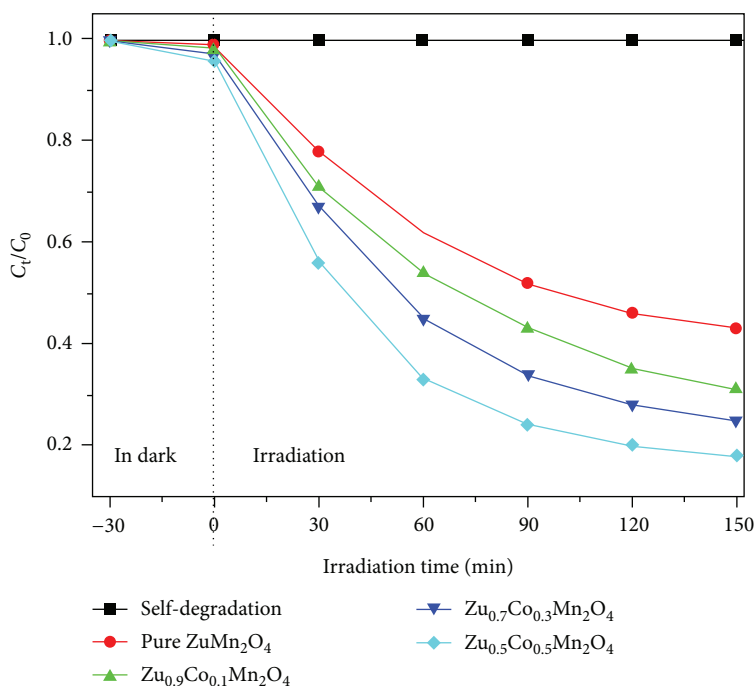
octahedral sites, i.e., Zn–O and Mn–O bonds [28]; these bands confirm the formation of spinel compounds for $Zn_{1-x}Co_xMn_2O_4$ nanocrystals. The corresponding peak position of the Fourier infrared spectrum of the sample did not change with the increase of the Co doping concentration, which is also consistent with the XRD data, indicating that Co^{2+} was successfully doped into the $ZnMn_2O_4$ lattice.

3.5. Photocatalytic Performance. In order to study the influence of Co doping concentration on the degradation efficiency, MO dye was selected as target pollutant for evaluating the photocatalytic activity of $Zn_{1-x}Co_xMn_2O_4$ nanocrystals. Figure 6(a) depicts the MO degradation of $Zn_{1-x}Co_xMn_2O_4$ samples with different doping ratios versus time (t) under simulated sunlight irradiation. Blank experiment was performed without any catalyst, it was found that there was no obvious self-degradation in the MO dye aqueous solution under visible light irradiation for 180 min, the blank experiment suggested that MO has good stability without catalyst, and the spontaneous photolysis can be negligible under visible light illumination. It is worth noting that the concentration of the MO dye slightly decreased when the reaction mixture is stirred for 30 min without light illumination, because $Zn_{1-x}Co_xMn_2O_4$ nanocrystals possess a larger specific surface area and can adsorb the MO dye well. The degradation rate of pure $ZnMn_2O_4$ is about 57% after xenon lamp irradiation for 150 mins, while the photocatalytic activity of $Zn_{1-x}Co_xMn_2O_4$ samples is obviously higher than that of pure $ZnMn_2O_4$ samples, and the decolorization rates are 69%, 75%, and 82%. It is obvious that the photocatalytic performance increases with the increase of Co doping amount and Co^{2+} ions replaced the lattice site of Zn^{2+} to generate single-phase $ZnMn_2O_4$ nanocrystal results in the effective separation of photoinduced electron-hole pairs to improve the photocatalytic activity.

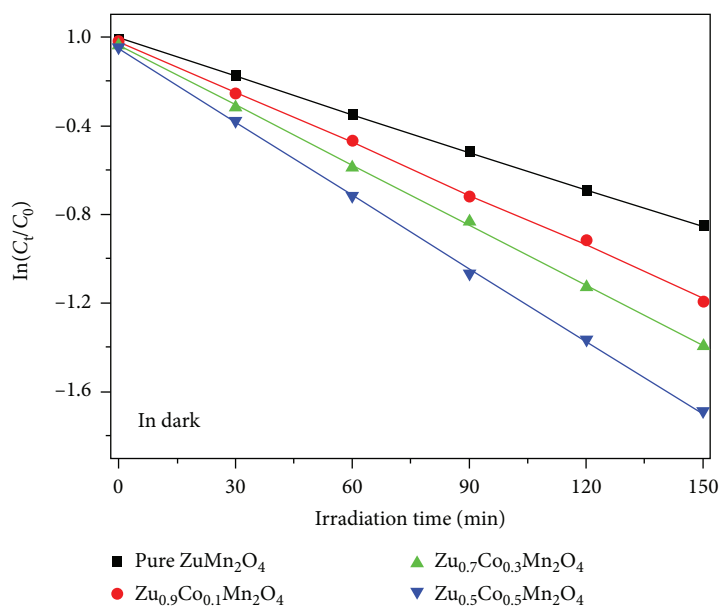
To better compare the photocatalytic efficiency for $Zn_{1-x}Co_xMn_2O_4$ nanocrystals of MO decolorization, the kinetic study was performed using a first-order kinetic equation: $\ln(C_t/C_0) = -kt$, where k represents reaction rate constant (h^{-1}), t is the irradiation time, and C_t and C_0 denote the initial concentration and the reaction concentration, respectively, of MO after light irradiation. The first-order kinetics of $Zn_{1-x}Co_xMn_2O_4$ nanocrystals for photocatalytic decolorization of MO as shown in Figure 6(b) and the k values for $Zn_{1-x}Co_xMn_2O_4$ ($x = 0.1, 0.3, \text{ and } 0.5$) are 0.470, 0.545, and 0.658 h^{-1} , respectively; these values demonstrate that doped $Zn_{1-x}Co_xMn_2O_4$ nanocrystals have a higher efficiency than that of pure samples ($k = 0.336 h^{-1}$). The improvement of photocatalytic efficiency is mainly due to the fact that Co-doped $Zn_{1-x}Co_xMn_2O_4$ nanocrystals possess smaller particle size and larger specific surface area and Co^{2+} can adjust the crystal structure and energy band structure, which accelerate the migration of the photogenerated electron-hole pairs toward its surface and prevent the electron-hole pairs from recombination.

The stability and reusability for the $Zn_{0.5}Co_{0.5}Mn_2O_4$ sample were evaluated by cyclic experiments of photocatalytic degradation of MO under the same conditions. As shown in Figure 7, the degradation efficiency of the $Zn_{0.5}Co_{0.5}Mn_2O_4$ sample exhibits a minor decrease from 82% to 79.5% after five consecutive cycles of photocatalytic experiments and the repetition rate is still maintained at 80%. The little decreases may relate to the particle aggregation of the sample after a long time reaction. Hence, $Zn_{1-x}Co_xMn_2O_4$ nanocrystals possess excellent photocatalytic active and good stability; these results demonstrate that Co-doped $ZnMn_2O_4$ nanocrystals possess good application prospects in photocatalytic degradation of pollutants.

Under simulated sunlight irradiation, the electrons (e^-) in the valence band (VB) of $ZnMn_2O_4$ can be excited to its



(a)



(b)

FIGURE 6: (a) Photocatalytic degradation of MO over time and (b) first-order kinetic curves of Zn_{1-x}Co_xMn₂O₄ samples.

conduction band (CB), while the holes (h^+) is generated in VB of ZnMn₂O₄. Zn_{1-x}Co_xMn₂O₄ nanocrystals can effectively promote the generation of photoinduced electron-hole pairs owing to the reduction of average grain size and the band gap for Co-doped Zn_{1-x}Co_xMn₂O₄ nanocrystals. The electrons at VB are excited to transition to CB, thus forming a hole in VB and generated an electron-hole pair (equation (1)). Electrons react with dissolved oxygen in the solution to form superoxide radicals

($\cdot\text{O}_2^-$). At the same time, photoinduced holes react with water to generate $\cdot\text{OH}$, H^+ (equation (2)). Meanwhile, H^+ further reacts with oxygen to form H_2O_2 (equation (3)). Obviously, hydrogen peroxide reacts with O_2^- to produce $\cdot\text{OH}$, OH^- , and O_2 (equation (4)). As strong oxidants, $\cdot\text{OH}$ reacts strongly with organic pollutants and promote the decomposition of organic pollutants. Finally, $\cdot\text{OH}$ and O_2^- oxidize MO to CO_2 , H_2O , and other small molecule compounds (equation (5)) [3].

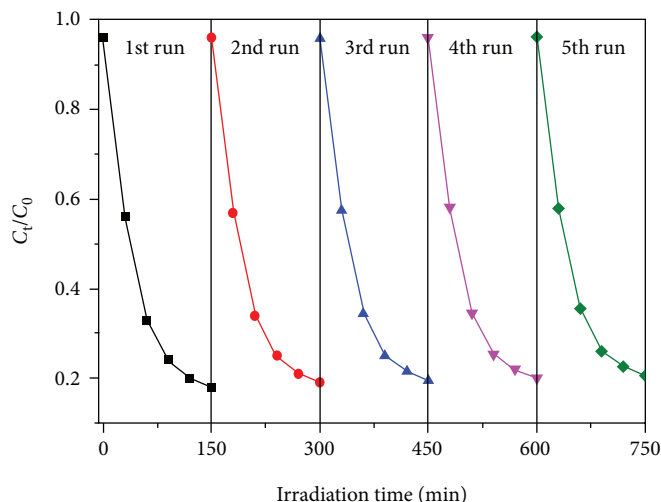
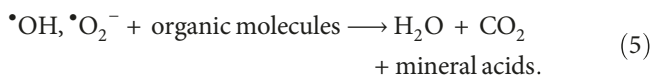
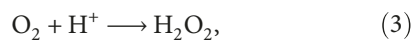
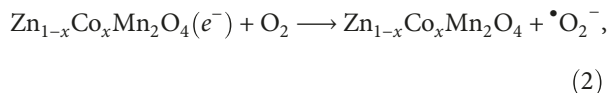
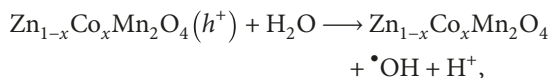
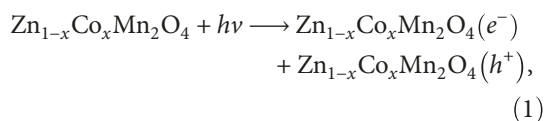


FIGURE 7: Photocatalytic cycle stability of $\text{Zn}_{0.7}\text{Co}_{0.3}\text{Mn}_2\text{O}_4$ samples.

Under simulated sunlight irradiation, the photocatalytic decolorization reaction of the photoinduced electron-hole transport for $\text{Zn}_{1-x}\text{Co}_x\text{Mn}_2\text{O}_4$ nanocrystals is as follows [29]:



4. Conclusion

- (1) Co-doped $\text{Zn}_{1-x}\text{Co}_x\text{Mn}_2\text{O}_4$ nanocrystals with different ratios ($x = 0, 0.1, 0.3, \text{ and } 0.5$) were successfully synthesized via a facile hydrothermal method. All samples exhibit single-phase spinel tetragonal with good crystallization. Co^{2+} ions are successfully substituted for the lattice site of Zn^{2+} to generate single-phase ZnMn_2O_4 nanocrystals
- (2) The morphologies of all the samples are loose hollow microsphere structures. The crystalline size decreases as Co-doped concentration increase. The energy band gap of Co-doped $\text{Zn}_{1-x}\text{Co}_x\text{Mn}_2\text{O}_4$ nanocrystalline is smaller than that of pure ZnMn_2O_4 has been red shifted

- (3) The photocatalytic activity of doped $\text{Zn}_{1-x}\text{Co}_x\text{Mn}_2\text{O}_4$ samples is obviously higher than that of pure ZnMn_2O_4 samples for the photodegradation of MO under visible light irradiation. Co-doped ZnMn_2O_4 nanocrystals can act as a potential photocatalyst for photocatalytic degradation of the pollutants

Data Availability

The figure data used to support the findings of this study are included within the article.

Conflicts of Interest

The authors declare that they have no conflicts of interest.

Acknowledgments

This work was supported by the National Natural Science Foundation of China (no. 51261015) and the Natural Science Foundation of Gansu Province, China (no. 1308RJZA238).

References

- [1] A. Fujishima, X. Zhang, and D. Tryk, "Heterogeneous photocatalysis: from water photolysis to applications in environmental cleanup," *International Journal of Hydrogen Energy*, vol. 32, no. 14, pp. 2664–2672, 2007.
- [2] H. Zhai, J. Qi, X. Zhang et al., "Preparation and photocatalytic performance of hollow structure LiNb_3O_8 photocatalysts," *Nanoscale Research Letters*, vol. 12, no. 1, p. 519, 2017.
- [3] W. Zhao, Z. Wei, L. Zhang, X. Wu, and X. Wang, "Cr doped SnS_2 nanoflowers: preparation, characterization and photocatalytic decolorization," *Materials Science in Semiconductor Processing*, vol. 88, pp. 173–180, 2018.
- [4] K. Maeda and K. Domen, "New non-oxide photocatalysts designed for overall water splitting under visible light," *The Journal of Physical Chemistry C*, vol. 111, no. 22, pp. 7851–7861, 2007.

- [5] C. Zheng, H. Yang, Z. Cui, H. Zhang, and X. Wang, "A novel $\text{Bi}_4\text{Ti}_3\text{O}_{12}/\text{Ag}_3\text{PO}_4$ heterojunction photocatalyst with enhanced photocatalytic performance," *Nanoscale Research Letters*, vol. 12, no. 1, p. 608, 2017.
- [6] S. Thaweesak, M. Lyu, P. Peerakiatkhajohn et al., "Two-dimensional $\text{g-C}_3\text{N}_4/\text{Ca}_2\text{Nb}_2\text{TaO}_{10}$ nanosheet composites for efficient visible light photocatalytic hydrogen evolution," *Applied Catalysis B: Environmental*, vol. 202, pp. 184–190, 2017.
- [7] F. Wang, H. Yang, H. Zhang, and J. Jiang, "Growth process and enhanced photocatalytic performance of CuBi_2O_4 hierarchical microcuboids decorated with AuAg alloy nanoparticles," *Journal of Materials Science: Materials in Electronics*, vol. 29, no. 2, pp. 1304–1316, 2018.
- [8] Z. Li, J. Zhang, J. Lv, L. Lu, C. Liang, and K. Dai, "Sustainable synthesis of CeO_2/CdS -diethylenetriamine composites for enhanced photocatalytic hydrogen evolution under visible light," *Journal of Alloys and Compounds*, vol. 758, pp. 162–170, 2018.
- [9] J. Zou, B. Liu, H. Liu, Y. Ding, T. Xin, and Y. Wang, "Facile synthesis of interconnected mesoporous ZnMn_2O_4 nanopeanuts for Li-storage via distinct structure design," *Materials Research Bulletin*, vol. 107, pp. 468–476, 2018.
- [10] M. Abdollahifar, S.-S. Huang, Y.-H. Lin et al., "High-performance carbon-coated ZnMn_2O_4 nanocrystallite supercapacitors with tailored microstructures enabled by a novel solution combustion method," *Journal of Power Sources*, vol. 378, pp. 90–97, 2018.
- [11] B. Ameri, S. S. H. Davarani, H. R. Moazami, and H. Darjazi, "Cathodic electrosynthesis of $\text{ZnMn}_2\text{O}_4/\text{Mn}_3\text{O}_4$ composite nanostructures for high performance supercapacitor applications," *Journal of Alloys and Compounds*, vol. 720, pp. 408–416, 2017.
- [12] H. Wang, Z. Li, J. Xu, Y. Zhang, L. Yang, and W. Qiu, "Resistance switching properties of $\text{Ag}/\text{ZnMn}_2\text{O}_4/\text{p-Si}$ fabricated by magnetron sputtering for resistance random access memory," *Journal of Wuhan University of Technology-Materials Science Edition*, vol. 30, no. 6, pp. 1159–1162, 2015.
- [13] J. Morán-Lázaro, E. Guillen-López, F. López-Urías et al., "Synthesis of ZnMn_2O_4 nanoparticles by a microwave-assisted colloidal method and their evaluation as a gas sensor of propane and carbon monoxide," *Sensors*, vol. 18, no. 3, p. 701, 2018.
- [14] L. Zhao, X. Li, and J. Zhao, "Fabrication, characterization and photocatalytic activity of cubic-like ZnMn_2O_4 ," *Applied Surface Science*, vol. 268, pp. 274–277, 2013.
- [15] P. E. Saranya and S. Selladurai, "Efficient electrochemical performance of ZnMn_2O_4 nanoparticles with rGO nanosheets for electrodes in supercapacitor applications," *Journal of Materials Science: Materials in Electronics*, vol. 29, no. 4, pp. 3326–3339, 2018.
- [16] X. Zhu, Z. Wei, W. Zhao, X. Zhang, L. Zhang, and X. Wang, "Microstructure and electrochemical properties of ZnMn_2O_4 nanopowder synthesized using different surfactants," *Journal of Electronic Materials*, vol. 47, no. 11, pp. 6428–6436, 2018.
- [17] W. Zhou, D. Wang, L. Zhao et al., "Template-free fabrication of graphene-wrapped mesoporous ZnMn_2O_4 nanorings as anode materials for lithium-ion batteries," *Nanotechnology*, vol. 28, no. 24, article 245401, 2017.
- [18] J. Bhagwan, N. Kumar, K. L. Yadav, and Y. Sharma, "Probing the electrical properties and energy storage performance of electrospun ZnMn_2O_4 nanofibers," *Solid State Ionics*, vol. 321, pp. 75–82, 2018.
- [19] C. Wei, H. Wang, J. Xu, Y. Zhang, X. Zhang, and L. Yang, "Resistive switching behavior of $\text{Ag}/\text{Mg}_{0.2}\text{Zn}_{0.8}\text{O}/\text{ZnMn}_2\text{O}_4/\text{p}^+-\text{Si}$ heterostructure devices for nonvolatile memory applications," *Journal of Wuhan University of Technology-Materials Science Edition*, vol. 32, no. 1, pp. 29–32, 2017.
- [20] Q. Liu, Z. Zhang, B. Liu, and H. Xia, "Rare earth oxide doping and synthesis of spinel $\text{ZnMn}_2\text{O}_4/\text{KIT-1}$ with double gyroidal mesopores for desulfurization nature of hot coal gas," *Applied Catalysis B: Environmental*, vol. 237, pp. 855–865, 2018.
- [21] R. Gherbi, Y. Bessekhoud, and M. Trari, "Optical and transport properties of Sn-doped ZnMn_2O_4 prepared by sol-gel method," *Journal of Physics and Chemistry of Solids*, vol. 89, pp. 69–77, 2016.
- [22] W. H. Zhao, Z. Q. Wei, X. L. Zhu, X. D. Zhang, and J. L. Jiang, "Optical and magnetic properties of diluted magnetic semiconductor $\text{Zn}_{0.95}\text{Mn}_{0.05}\text{S}$ nanorods prepared by a hydrothermal method," *International Journal of Materials Research*, vol. 109, no. 5, pp. 405–412, 2018.
- [23] R. Gherbi, Y. Bessekhoud, and M. Trari, "Structure, optical and transport properties of Mg-doped ZnMn_2O_4 ," *Journal of Alloys and Compounds*, vol. 655, pp. 188–197, 2016.
- [24] C. Feng, W. Wang, X. Chen, S. Wang, and Z. Guo, "Synthesis and electrochemical properties of ZnMn_2O_4 anode for lithium-ion batteries," *Electrochimica Acta*, vol. 178, pp. 847–855, 2015.
- [25] Y. Yan, H. Yang, X. Zhao, R. Li, and X. Wang, "Enhanced photocatalytic activity of surface disorder-engineered CaTiO_3 ," *Materials Research Bulletin*, vol. 105, pp. 286–290, 2018.
- [26] C. P. Neto, J. Rocha, A. Gil et al., " ^{13}C solid-state nuclear magnetic resonance and Fourier transform infrared studies of the thermal decomposition of cork," *Solid State Nuclear Magnetic Resonance*, vol. 4, no. 3, pp. 143–151, 1995.
- [27] Y. S. Feng, S. M. Zhou, Y. Li, C. C. Li, and L. D. Zhang, "Synthesis and characterization of tin oxide nanoparticles dispersed in monolithic mesoporous silica," *Solid State Sciences*, vol. 5, no. 5, pp. 729–733, 2003.
- [28] S. Naz, S. K. Durrani, M. Mehmood, and M. Nadeem, "Hydrothermal synthesis, structural and impedance studies of nanocrystalline zinc chromite spinel oxide material," *Journal of Saudi Chemical Society*, vol. 20, no. 5, pp. 585–593, 2016.
- [29] F. Achouri, S. Corbel, L. Balan et al., "Porous Mn-doped ZnO nanoparticles for enhanced solar and visible light photocatalysis," *Materials & Design*, vol. 101, pp. 309–316, 2016.

Research Article

Template-Free Preparation and Photocatalytic and Photoluminescent Properties of Brookite TiO₂ Hollow Spheres

Yunjian Wang  and Yuchan Li

Anhui Key Laboratory of Energetic Materials, College of Chemistry and Materials Science, Huaibei Normal University, Huaibei, 235000 Anhui, China

Correspondence should be addressed to Yunjian Wang; wangyunjianmail@163.com

Received 24 December 2018; Accepted 19 February 2019; Published 25 March 2019

Guest Editor: Zhen Yu

Copyright © 2019 Yunjian Wang and Yuchan Li. This is an open access article distributed under the Creative Commons Attribution License, which permits unrestricted use, distribution, and reproduction in any medium, provided the original work is properly cited.

The preparation of high-purity brookite TiO₂ with a unique morphology is rare and difficult. Herein, high-purity brookite TiO₂ hollow spheres were hydrothermally synthesized by employing titanium sulfate as the titanium source and chloroacetic acid and sodium hydroxide as the pH regulator. The structure, morphology, and optical properties were characterized by X-ray diffraction (XRD), scanning electron microscopy (SEM), transmission electron microscopy (TEM), X-ray photoelectron spectroscopy (XPS), and UV-Vis diffuse reflectance spectroscopy (UV-Vis DRS). The results showed that the as-prepared brookite TiO₂ exhibited a hollow-sphere morphology with a size of about 1.0 micrometer and showed a direct band gap of 3.13 eV. Additionally, thermal analysis in combination with infrared spectroscopy showed that the as-prepared brookite TiO₂ was surface capped by water and organic molecules. Finally, the photocatalytic and photoluminescent properties of brookite TiO₂ were studied.

1. Introduction

The control of TiO₂ polymorphs and morphology has attracted enormous interest due to its fascinating structure and shape-dependent physicochemical properties [1–3]. As a popular photocatalyst, TiO₂ contains three common polymorphs: anatase, rutile, and brookite [4, 5]. All three polymorphs are constructed by the different connections of the distorted TiO₆ octahedra. Among these polymorphs, the preparation and properties of both anatase and rutile are intensively studied [6, 7]. Alternatively, the report on TiO₂ in the brookite form is rare for a lack of understanding of its properties and synthetic approach [8]. In this regard, Lin et al. report the first breakthrough in the synthesis of a brookite TiO₂ nanosheet with an excellent photocatalytic performance through a spatial charge transfer control with specific crystal surface exposure [9]. Since then, a growing number of methods are emerging to explore the unique morphology-dependent property of brookite TiO₂. For

example, Choi and Yong report the facile hydrothermal preparation of brookite nanoarrays using an environmentally benign one-step reaction [10]. Just like nitrogen-doped anatase or rutile, nitrogen-doped brookite TiO₂ with enhanced visible-light photoactivity is also reported by Pan and Jiang [11]. Although numerous synthetic strategies have been developed for the fabrication of the brookite phase, the phase-formation mechanism of a brookite polymorph is still under controversy, and it still remains the least studied TiO₂ photocatalyst due to the difficulties usually encountered in obtaining it as a pure phase [12]. Although it is exceedingly difficult to explore a novel approach, it is still of great interest to synthesize pure brookite with a unique morphology for its great potential in applications ranging from solar cells and sensors to photocatalysis [13–15]. Herein, we report the first fabrication of pure brookite hollow spheres through the self-assembly of nanoblocks under a facile hydrothermal condition, and we report brookite's structure, surface, and photocatalytic properties as well.

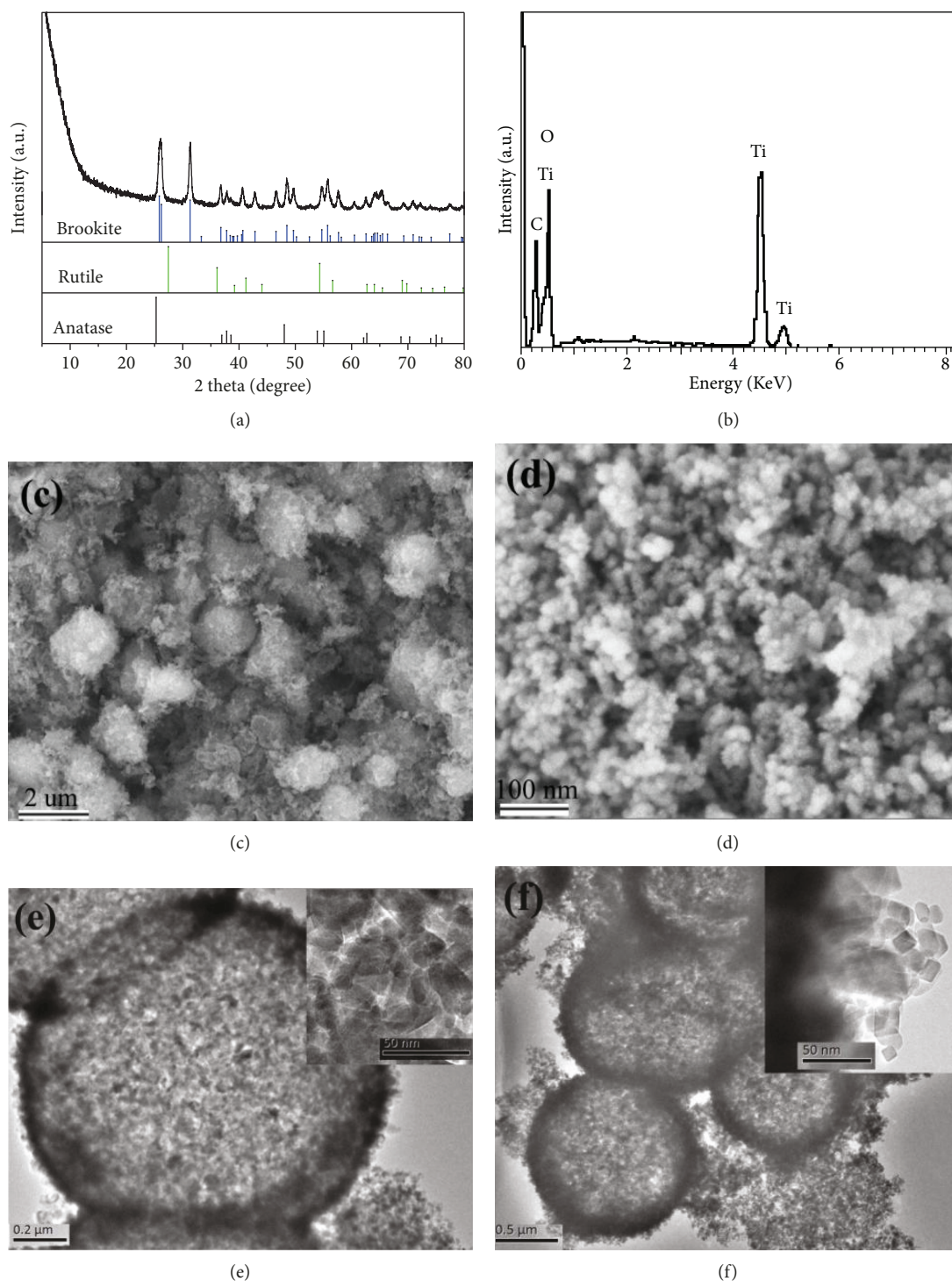


FIGURE 1: (a) XRD pattern, (b) EDS spectrum, and (c, d) SEM and (e, f) TEM images of the sample.

2. Experimental

2.1. Materials. All reagents were purchased from Sinopharm Chemical Reagent Co. Ltd., Shanghai, China. All reagents were of analytical purity and used without further purification.

2.2. Sample Preparation. The brookite TiO_2 sample was prepared under a typical hydrothermal condition as follows: 2.6301 g titanium sulfate was dissolved in 30 mL distilled

water under constant stirring; then, 5.0 g chloroacetic acid, 2.125 g NaOH, and 15.012 g carbamide were added into the above solution and stirred for 2 h until the solution became a translucent yellow; then, the solution was transferred to a 100 mL Teflon-lined stainless steel autoclave that was allowed to react at 200°C for 9 h. The product was centrifuged and washed with deionized water for three times and then dried at 80°C for 12 h.

2.3. Sample Characterization. XRD analysis was performed on a Bruker D8 ADVANCE X-ray powder diffractometer equipped with Cu K α radiation. The morphology of the sample was observed by FE-SEM (JEOL JSM-6700) and TEM (JEM-2010). The infrared spectrum of the sample was measured on a PerkinElmer IR spectrophotometer using a KBr pellet technique. TG-DTA was measured on a NETZSCH STA 449C apparatus. Optical diffuse reflectance spectra of the samples were measured using a Lambda 900 UV-Vis spectrometer. The valence states were studied by XPS employing an ESCALAB MKII spectrometer from VG Scientific Co., with an Al K α (1486.6 eV) line at 150 W. The photocatalytic activities were evaluated by the degradation of 10 ppm methyl orange (MO) in an aqueous solution under ultraviolet radiation. The photoluminescence spectrum was measured on a Cray Eclipse fluorescence spectrophotometer with a Xe lamp excited at 310 nm and recorded at a scan rate of 120 nm \cdot min $^{-1}$.

3. Results and Discussion

Figure 1(a) shows the XRD pattern of the hydrothermally prepared TiO $_2$ sample at 200°C for 9 h. It is seen that the peak which appeared at $2\theta = 30.8^\circ$ is the diffraction peak from the (121) crystal plane of brookite, which is a characteristic of a brookite polymorph. The diffraction peak of rutile was not observed. It should be noted that anatase has almost the same diffraction peaks of brookite except for the diffraction peaks of the (121) crystal plane. For the mixture of rutile and brookite, the phase content of brookite can be estimated from the relative intensity of their diffraction peak. Based on previous literature, the phase purity of brookite was evaluated up to 99.8% by the intensity ratio of diffraction peaks using the following formula: $I_{121}^{\text{brookite}} / (I_{120}^{\text{brookite}} + I_{101}^{\text{anatase}})$ [16]. EDS analysis in Figure 1(b) shows that the sample is composed of Ti and O elements with a small amount of carbon, which might come from the surface-adsorbed organics. The surface morphology and size of the sample was investigated by SEM, as displayed in Figures 1(c) and 1(d). The brookite TiO $_2$ presents irregular spheres with sizes ranging from 1 to 2 μm . The internal structure of the spheres was further examined by TEM, as shown in Figures 1(e) and 1(f). The brookite sphere has a hollow structure, assembled by nanoblocks of 20 nm in size. The inserts in Figures 1(e) and 1(f) show the surface structure of the hollow sphere. Figure 2 shows the XRD patterns of the samples prepared for different periods of hydrothermal reaction time. It is observed that the sample formed at the early stage of 1 h is the mixture of anatase and a small amount of brookite. It is interesting to find that anatase gradually transformed into brookite form with the increase of reaction time, and high-purity brookite was obtained by extending the reaction time to 9 hours. The anatase-to-brookite phase transition can be seen from the change of diffraction peak intensity from brookite, as indicated by the arrows in Figure 2. The crystalline size increased during the phase-transition process, which conforms with the popular opinion that anatase TiO $_2$ is stable in small sizes while brookite is more stable in big sizes [17].

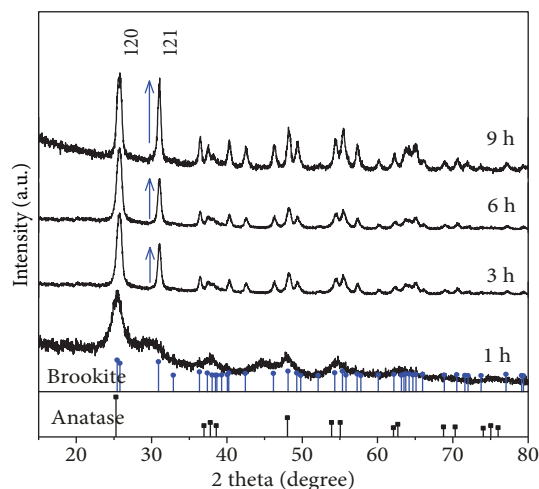


FIGURE 2: XRD patterns of the samples prepared at given periods of time. (The arrow points out the intensity of the (121) diffraction peak from brookite which increases with time.)

The thermal stability of the as-prepared brookite TiO $_2$ was investigated by TG-DTA, as shown in Figure 3(a). Apparently, about 3.5 wt.% weight loss below 400°C was attributed to the vaporization of the water molecules that existed on the surface of the sample [18], which was further suggested by the wide endothermic peak in this temperature range. In the temperature range from 400 to 800°C, an obvious 16.8 wt.% weight loss in the TGA curve accompanied with a sharp exothermic peak in the DTA curve was observed, which may be attributed to the combustion of surface-adsorbed organic matter in an air atmosphere [19]. It is noted that the DTA curve exhibits another strong endothermic peak at around 900°C despite that no significant weight loss was observed on the TGA curve in this temperature range, corresponding to the polymorph transition from metastable brookite to stable rutile. In previous literature reported by Xu et al. [20], brookite-to-rutile phase-transition temperature was fixed at 850°C as detected by in situ high-temperature XRD. By comparison, this phase-transition temperature observed in our work is a little higher, and it may be related to the hollow structure of brookite. To further investigate the surface-adsorbed species, the FT-IR spectrum of the brookite sample was measured in the wavenumber range 400-4000 cm^{-1} . The strongest band located at 3458 cm^{-1} is attributed to the vibration of H-O bonds for surface adsorption, and the weak absorption centered at 1645 cm^{-1} is associated with the deformation vibration of H-O bonds from the surface adsorption layers [21]. Several bands at 422, 484, 560, and 728 cm^{-1} in the low wavenumber range are the characteristic absorption peaks of brookite TiO $_2$ [22]. From the UV-Vis absorption spectrum in Figure 3(c), the absorption edge was found to be around 387.2 nm for the hollow-structure brookite. It is generally believed that the brookite-structure TiO $_2$ belongs to an indirect-type semiconductor [9, 23]. The corresponding bandgap energy is estimated as follows:

$$\alpha = \frac{K(h\nu - E_g)^{1/n}}{h\nu}, \quad (1)$$

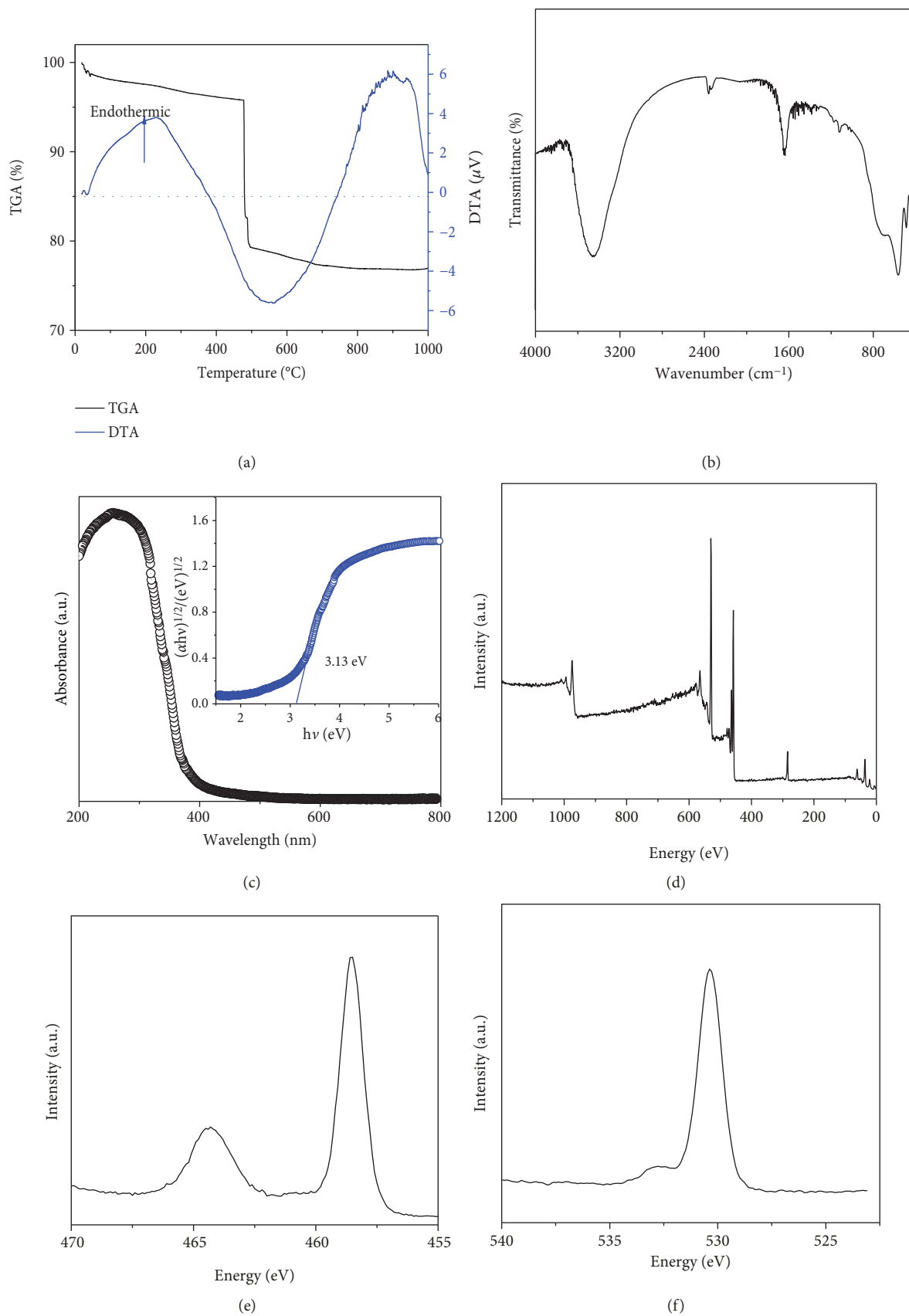


FIGURE 3: (a) TG-DTA curves, (b) FT-IR spectrum, and (c) UV-visible diffusion reflectance spectrum. Insert shows the energy dependence of $(\alpha h\nu)^2$ for the sample. (d) XPS survey spectrum and high-resolution XPS spectrum for O 1s (e) and Ti 2p (f) of the sample.

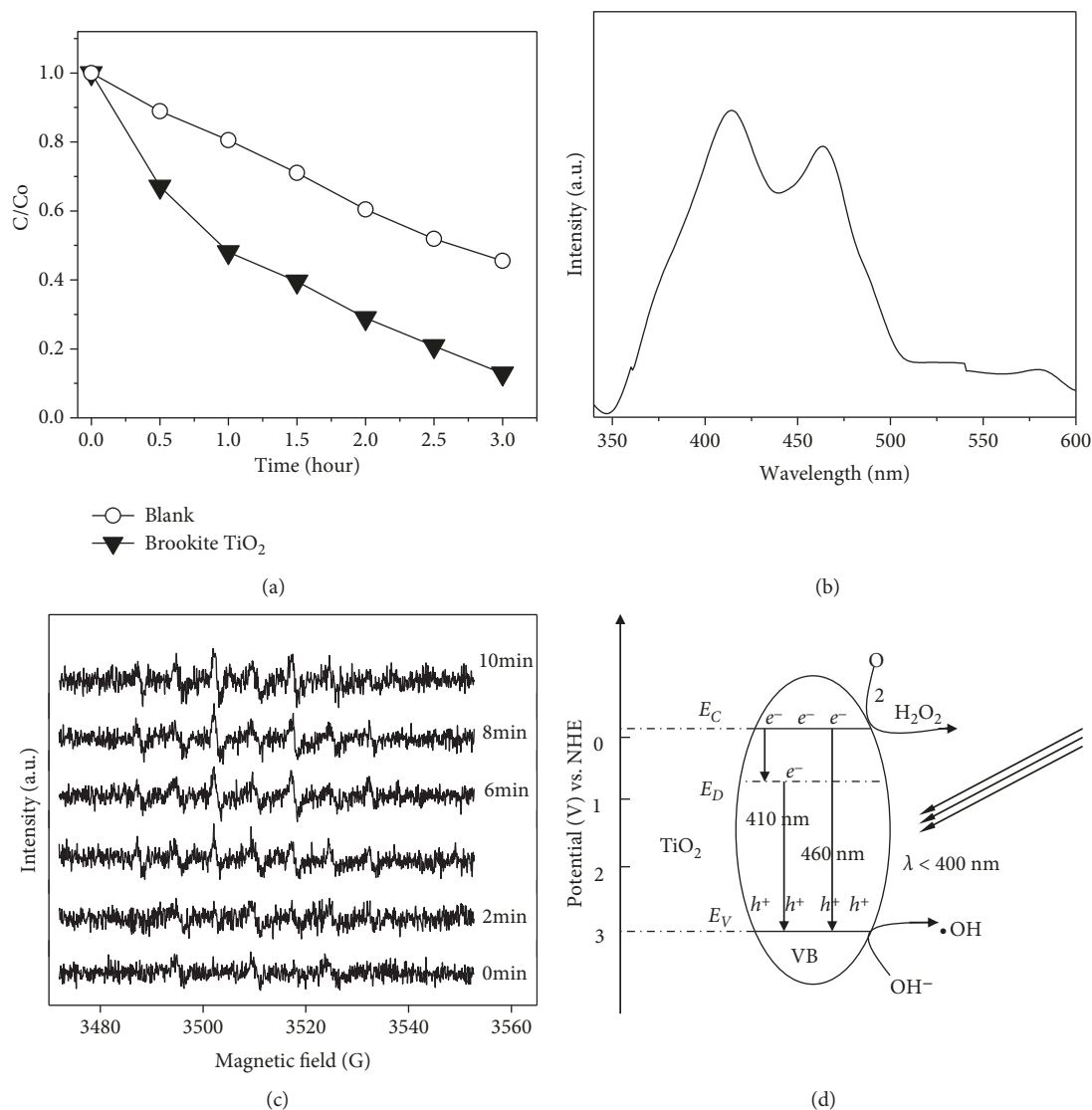


FIGURE 4: (a) Photocatalytic performance of MO degradation, (b) photoluminescence emission spectrum excited at 310 nm, (c) time-varied ESR spectra for DMPO-OH, and (d) schematic diagram for the photochemical process for TiO₂ hollow spheres.

where α is absorbance, $h\nu$ represents the energy of incident photons, K is a constant, and n equals to 2 for direct transition and 1/2 for indirect transition [24]. As displayed in the insert of Figure 3(c), the bandgap energy E_g was 3.13 eV for the prepared hollow-structure brookite TiO₂, in good agreement with previously reported results [25]. The surface chemical property of the sample was determined by the XPS technique. The survey and core level spectra for Ti 2p and O 1s are given in Figures 3(d)–3(f). Ti 2p signals consist of the well distinct Ti 2p_{1/2} and Ti 2p_{3/2} peaks located at 464.5 and 458.5 eV, respectively. In the O 1s spectrum, there appears a strong signal at around 530.2 eV accompanied by a shoulder at 531.7 eV which originates from the crystalline oxygen (O²⁻) and the surface-adsorbed oxygen, respectively [26].

The photocatalytic property of the as-prepared brookite TiO₂ was evaluated by the degradation of an MO solution under UV light. Figure 4(a) shows the degradation rate of MO with and without the sample under UV light. As we

can see, brookite TiO₂ exhibits photocatalytic activity with an efficiency of nearly 85% in 3 h, which is relatively lower than previously reported [9, 27]. Photocatalysis and photoluminescence are two competitive processes of photoinduced carriers, and low photocatalytic activity often results from high band-to-band photoluminescent efficiency [28]. Figure 4(b) shows the photoluminescence spectrum excited at 310 nm. Two main emission peaks appear at about 410 and 464 nm wavelengths, respectively. The former is attributed to band-band photoluminescence, and the latter is attributed to the transition between impurity and valence energy levels [28]. Moreover, ESR spin-trapping analysis was employed to probe the active species. As shown in Figure 4(c), it is observed that four characteristic 1:2:2:1 quadruple peaks of DMPO-OH show a slow augmentation with UV-light irradiation. According to the above investigations, the photocatalytic and photoluminescent mechanisms of brookite TiO₂ are proposed in Figure 4(d). When TiO₂ is

irradiated with light with an energy higher or equal to the band gap energy, electrons are excited to the conduction band with the simultaneous generation of holes (h^+) in the valence band. The separation and recombination of photoinduced charge carriers are competitive processes, which produce the photocatalytic reaction and photoluminescent process, respectively.

4. Conclusions

In summary, high-purity brookite-type TiO₂ nanomaterials were prepared by regulating the reaction time using titanium sulfate as the titanium source and chloroacetic acid as the surface active agent under hydrothermal conditions. With the prolongation of the hydrothermal reaction time, the originally formed anatase-phase TiO₂ gradually transformed into the brookite phase, and a high-purity brookite sample was obtained when the hydrothermal reaction time was prolonged to 9 h. TEM characterization found that the as-prepared brookite TiO₂ exhibited a hollow-sphere morphology self-assembled by nanoblocks. The surface of the brookite TiO₂ sample was capped by water and other organic molecules, as indicated by FT-IR and TG-DTA results. The photocatalytic and photoluminescent properties of the brookite TiO₂ hollow spheres were investigated for the first time. The reported findings will be greatly useful in phase and morphology regulation of titanium dioxide.

Data Availability

The findings of this study are available from the corresponding author upon request. The public database is not used in this article.

Conflicts of Interest

The authors declare that there is no conflict of interests regarding the publication of this paper.

Acknowledgments

This work was financially supported by the Educational Committee of the Natural Science Foundation of Anhui Province (No. KJ2017A386) and the Anhui Provincial Innovation Team of Design and Application of Advanced Energetic Materials (KJ2015TD003).

References

- [1] L. B. Xiong, J. L. Li, B. Yang, and Y. Yu, "Ti³⁺ in the surface of titanium dioxide: generation, properties and photocatalytic application," *Journal of Nanomaterials*, vol. 2012, Article ID 831524, 13 pages, 2012.
- [2] Y. Zou, X. Tan, T. Yu, Y. Li, Q. Shang, and W. Wang, "Synthesis and photocatalytic activity of chrysanthemum-like brookite TiO₂ nanostructures," *Materials Letters*, vol. 132, pp. 182–185, 2014.
- [3] G. Li, L. Li, J. Boerio-Goates, and B. F. Woodfield, "High purity anatase TiO₂ nanocrystals: near room-temperature synthesis, grain growth kinetics, and surface hydration chemistry," *Journal of the American Chemical Society*, vol. 127, no. 24, pp. 8659–8666, 2005.
- [4] J. M. Johnson, N. Kinsinger, C. Sun, D. Li, and D. Kisailus, "Urease-mediated room-temperature synthesis of nanocrystalline titanium dioxide," *Journal of the American Chemical Society*, vol. 134, no. 34, pp. 13974–13977, 2012.
- [5] D. Machon, M. Daniel, V. Pischedda, S. Daniele, P. Bouvier, and S. LeFloch, "Pressure-induced polyamorphism in TiO₂ nanoparticles," *Physical Review B*, vol. 82, no. 14, article 140102, 2010.
- [6] J. Yu, J. Low, W. Xiao, P. Zhou, and M. Jaroniec, "Enhanced photocatalytic CO₂-reduction activity of anatase TiO₂ by coexposed {001} and {101} facets," *Journal of the American Chemical Society*, vol. 136, no. 25, pp. 8839–8842, 2014.
- [7] H. Chen, C. E. Nanayakkara, and V. H. Grassian, "Titanium dioxide photocatalysis in atmospheric chemistry," *Chemical Reviews*, vol. 112, no. 11, pp. 5919–5948, 2012.
- [8] S. Selcuk and A. Selloni, "Facet-dependent trapping and dynamics of excess electrons at anatase TiO₂ surfaces and aqueous interfaces," *Nature Materials*, vol. 15, no. 10, pp. 1107–1112, 2016.
- [9] H. Lin, L. Li, M. Zhao et al., "Synthesis of high-quality brookite TiO₂ single-crystalline nanosheets with specific facets exposed: tuning catalysts from inert to highly reactive," *Journal of the American Chemical Society*, vol. 134, no. 20, pp. 8328–8331, 2012.
- [10] M. Choi and K. Yong, "A facile strategy to fabricate high-quality single crystalline brookite TiO₂ nanoarrays and their photoelectrochemical properties," *Nanoscale*, vol. 6, no. 22, pp. 13900–13909, 2014.
- [11] J. Pan and S. P. Jiang, "Synthesis of nitrogen doped faceted titanium dioxide in pure brookite phase with enhanced visible light photoactivity," *Journal of Colloid and Interface Science*, vol. 469, pp. 25–30, 2016.
- [12] D. Dambournet, I. Belharouak, and K. Amine, "Tailored preparation methods of TiO₂ anatase, rutile, brookite: mechanism of formation and electrochemical properties," *Chemistry of Materials*, vol. 22, no. 3, pp. 1173–1179, 2010.
- [13] R. Kaplan, B. Erjavec, G. Dražić, J. Grdadolnik, and A. Pintar, "Simple synthesis of anatase/rutile/brookite TiO₂ nanocomposite with superior mineralization potential for photocatalytic degradation of water pollutants," *Applied Catalysis B: Environmental*, vol. 181, pp. 465–474, 2016.
- [14] M. Altomare, M. V. Dozzi, G. L. Chiarello, A. di Paola, L. Palmisano, and E. Selli, "High activity of brookite TiO₂ nanoparticles in the photocatalytic abatement of ammonia in water," *Catalysis Today*, vol. 252, pp. 184–189, 2015.
- [15] X. Zhao, B. M. Sánchez, P. J. Dobson, and P. S. Grant, "The role of nanomaterials in redox-based supercapacitors for next generation energy storage devices," *Nanoscale*, vol. 3, no. 3, pp. 839–855, 2011.
- [16] J. G. Li, T. Ishigaki, and X. Sun, "Anatase, brookite, and rutile nanocrystals via redox reactions under mild hydrothermal conditions: phase-selective synthesis and physicochemical properties," *Journal of Physical Chemistry C*, vol. 111, no. 13, pp. 4969–4976, 2007.
- [17] K. Sabyrov, N. D. Burrows, and R. L. Penn, "Size-dependent anatase to rutile phase transformation and particle growth," *Chemistry of Materials*, vol. 25, no. 8, pp. 1408–1415, 2013.
- [18] H. Yan, P. Song, S. Zhang, Z. Yang, and Q. Wang, "Facile fabrication and enhanced gas sensing properties of hierarchical

- MoO₃ nanostructures,” *RSC Advances*, vol. 5, no. 89, pp. 72728–72735, 2015.
- [19] R. Bleta, P. Alphonse, and L. Lorenzato, “Nanoparticle route for the preparation in aqueous medium of mesoporous TiO₂ with controlled porosity and crystalline framework,” *Journal of Physical Chemistry C*, vol. 114, no. 5, pp. 2039–2048, 2010.
- [20] Q. Xu, J. Zhang, Z. Feng, Y. Ma, X. Wang, and C. Li, “Surface structural transformation and the phase transition kinetics of brookite TiO₂,” *Chemistry - An Asian Journal*, vol. 5, no. 10, pp. 2158–2161, 2010.
- [21] W. Tong, L. Li, W. Hu, T. Yan, and G. Li, “Systematic control of monoclinic CdWO₄ nanophase for optimum photocatalytic activity,” *Journal of Physical Chemistry C*, vol. 114, no. 3, pp. 1512–1519, 2010.
- [22] W. Hu, L. Li, G. Li, C. Tang, and L. Sun, “High-quality brookite TiO₂ flowers: synthesis, characterization, and dielectric performance,” *Crystal Growth & Design*, vol. 9, no. 8, pp. 3676–3682, 2009.
- [23] J. C. Yu, L. Zhang, and J. Yu, “Direct sonochemical preparation and characterization of highly active mesoporous TiO₂ with a bicrystalline framework,” *Chemistry of Materials*, vol. 14, no. 11, pp. 4647–4653, 2002.
- [24] V. M. Huxter, T. Mirkovic, P. S. Nair, and G. D. Scholes, “Demonstration of bulk semiconductor optical properties in processable Ag₂S and EuS nanocrystalline systems,” *Advanced Materials*, vol. 20, no. 12, pp. 2439–2443, 2008.
- [25] M. Monai, T. Montini, and P. Fornasiero, “Brookite: nothing new under the sun?,” *Catalysts*, vol. 7, no. 10, p. 304, 2017.
- [26] K. S. Kim and N. Winograd, “X-ray photoelectron spectroscopic studies of nickel-oxygen surfaces using oxygen and argon ion-bombardment,” *Surface Science*, vol. 43, no. 2, pp. 625–643, 1974.
- [27] J. Zhang, P. Zhou, J. Liu, and J. Yu, “New understanding of the difference of photocatalytic activity among anatase, rutile and brookite TiO₂,” *Physical Chemistry Chemical Physics*, vol. 16, no. 38, pp. 20382–20386, 2014.
- [28] J. Liqiang, Q. Yichun, W. Baiqi et al., “Review of photoluminescence performance of nano-sized semiconductor materials and its relationships with photocatalytic activity,” *Solar Energy Materials and Solar Cells*, vol. 90, no. 12, pp. 1773–1787, 2006.

Research Article

One-Pot Synthesis of Titanate Nanotubes Decorated with Anatase Nanoparticles Using a Microwave-Assisted Hydrothermal Reaction

Suziete B. S. Gusmão,¹ Anupama Ghosh ,² Thalles M. F. Marques,³ Odair P. Ferreira ,⁴ Anderson O. Lobo,^{1,5} Josy A. O. Osajima,¹ Cleanio Luz-Lima,² Romulo R. M. Sousa,¹ Jose M. E. Matos,⁶ and Bartolomeu C. Viana ^{1,2}

¹Interdisciplinary Laboratory of Advanced Materials, Materials Science and Engineering Graduate Program, Federal University of Piauí, Teresina, PI CEP 64049-550, Brazil

²FisMat, Department of Physics, Federal University of Piauí, Teresina, PI CEP 64049-550, Brazil

³Federal Institute of Technology, Ciência e Tecnologia do Piauí, São João do Piauí, PI 64760-000, Brazil

⁴Laboratory of Advanced Functional Materials, Department of Physics, Federal University of Ceará, Fortaleza, CE CEP 60455-900, Brazil

⁵Department of Chemistry, Massachusetts Institute of Technology, Cambridge, MA 02139, USA

⁶Department of Chemistry, Federal University of Piauí, Teresina, PI CEP 64049-550, Brazil

Correspondence should be addressed to Anupama Ghosh; anupama1984@gmail.com and Bartolomeu C. Viana; bartolomeu@ufpi.edu.br

Received 27 November 2018; Accepted 20 January 2019; Published 14 March 2019

Guest Editor: Zhen Yu

Copyright © 2019 Suziete B. S. Gusmão et al. This is an open access article distributed under the Creative Commons Attribution License, which permits unrestricted use, distribution, and reproduction in any medium, provided the original work is properly cited.

A nanoheterostructure of titanate nanotubes decorated with anatase nanoparticles (TiNT@AnNP) was synthesized for the first time by a microwave-assisted hydrothermal one-pot reaction. Characterization by X-ray diffraction, Raman spectroscopy, scanning electron microscopy, energy-dispersive X-ray spectroscopy, high-resolution transmission electron microscopy, selected-area electron diffraction, and X-ray photoelectron spectroscopy showed highly crystalline and nanometer-sized TiNT@AnNP. The synthesized TiNT@AnNP degraded an anionic dye (Remazol blue) more efficiently under UV-visible light (380–780 nm) than a commercial anatase-TiO₂ precursor. We correlated this increased efficiency of photodegradation to the large surface area and the efficient separation of photoinduced electron-hole pairs. Finally, we propose a mechanism to highlight the influence of a microwave-assisted hydrothermal synthesis in the production of TiNT@AnNP for environmental applications.

1. Introduction

Nanostructured titanium oxide- (TiO₂-) based compounds are one of the most intensely studied families of inorganic oxides in the literature [1]. Their fascinating structural, electronic, and biological properties make them useful for various environmental, energy, and biomedical applications, such as adsorption, photochemical degradation, Li-ion batteries, photovoltaic cells, oil-water separation, and antibacterial activity [1]. A layered titanate nanostructure has strong

structural similarity to the anatase phase of TiO₂, with similar building blocks of TiO₆ octahedrons, connected by corner- and edge-sharing oxygen atoms forming negatively charged two-dimensional sheets, which facilitates fast ion diffusion, leading to exchange and intercalation, and the increased surface area facilitates photocatalytic application [2]. Different synthetic techniques, such as template-based methods, sol-gel process, anodic oxidation, and hydrothermal treatment have been used to generate titanate nanostructures with different morphologies and properties [3]. A vast

number of structure-property relationship studies led scientists not only to apply these materials in various fields but also to understand the basic mechanism of the phase transformation between crystalline phases of titania and titanates, as well as to the possibility to generate new functional materials with tailored properties [4]. Formation of a TiO_2 - (anatase-) trititanate heterostructure is one example, which has been a hot topic recently because of its increased efficiency in photocatalysis and photodegradation [5]. These properties have been associated with different structural and electronic properties, such as the band gap and the surface area [5, 6]. TiO_2 - (anatase-) trititanate heterostructures are easily interconverted by low-energy-requiring pathways as predicted by calculations because of the structural similarity between trititanate and TiO_2 (anatase) [7]. These behaviors are associated with either a topochemical reaction involving dehydration of the titanate layers, followed by an in situ rearrangement of the structural units leading to titanate-to-anatase phase transformation [8], or a gradual decomposition and dissolution of the titanate surface, causing the production of $\text{Ti}(\text{OH})_4$ fragments, which undergo dehydration resulting in Ti-O-Ti bridge formation, thereby starting the nucleation of the anatase phase [9]. Synthesis of a titanate-anatase heterostructure was achieved by controlled thermal annealing, causing a two-step dehydration, the first step being at the layers, leading to a decrease in interlayer distance, and the second step resulting in partial destruction of the tube, forming anatase particles on titanate nanotubes at 350–400°C [10]. Milder postsynthetic treatment of titanate nanotubes (48 h stirring in 0.05 M HNO_3 at 70°C) generated titanate nanotubes decorated with anatase nanocrystals of 5–20 nm in diameter [11, 12]. Postsynthetic hydrothermal treatment of titanate tubes at 150°C for 24 h yielded phase transformation of trititanate to anatase, which exhibited an increased surface area as well as a decreased band gap, which is ideal for photocatalysis reactions [13].

In recent years, another great advance in the synthetic strategy has been achieved by using microwave heating in place of conventional heating as it is a faster and more efficient heating method [14]. The first microwave adaptation of the Kasuga-introduced conventional alkaline hydrothermal synthesis of titanate nanotubes from anatase TiO_2 [15] was in 2005 by Wang et al. [16]; the reaction time was reduced to 6 h. Recently, detailed analysis was performed on microwave synthesis of titanate nanostructures to understand and evaluate the advantage of microwave irradiation compared to conventional heat treatment, and it was found that it not only decreases the reaction time manyfold but also helps to obtain nanostructures with a greater surface area compared to the conventional method, which, in turn, can help the nanostructures act as a better catalyst [17, 18]. The careful selection of the reaction time and temperature can lead to a trititanate-anatase mixed phase final product because of incomplete conversion to titanate nanotubes and partial retention of the starting structure (anatase), which can give rise to better photoactivity than either a pure anatase phase or a pure trititanate phase [19, 20]. Additionally, a microwave-assisted hydrothermal synthesis can give rise to the formation of anatase nanostructures under conditions

similar to those that result in titanate nanotubes in conventional hydrothermal synthesis, possibly due to the rapid molecular rearrangement caused by uniform microwave irradiation [21].

Herein, a very simple one-pot synthesis of a titanate-anatase nanostructure has been realized for the first time using a microwave-assisted alkaline hydrothermal method starting from pure anatase powder. Long, thin titanate nanotubes decorated with anatase nanocrystals of average diameter 3.3 nm (TiNT@AnNP) were obtained. This unique nanoheterostructure was thoroughly characterized by high-resolution transmission electron microscopy (HRTEM) and was found to contain anatase and titanate nanostructures, corroborating the findings of X-ray diffraction (XRD), Raman spectroscopy, and selected-area electron diffraction (SAED) analysis. The synthesized TiNT@AnNP photocatalytically degraded the dye Remazol blue more efficiently than a commercial anatase- TiO_2 precursor did. We propose and discuss a mechanism to explain the influence of the microwave-assisted hydrothermal route to produce TiNT@AnNP . Our method is an alternative and economic one-pot synthetic route to achieve a better catalyst.

2. Experimental Part

2.1. Synthesis of the Nanoheterostructure. TiNT@AnNP was synthesized by a microwave-assisted alkaline hydrothermal method. For this, 3.00 g of anatase TiO_2 (Sigma-Aldrich, 99.8% purity, free from other metal ions, 60–80 nm average particle size) was dispersed in 90 mL of NaOH solution (10 mol L^{-1}) under magnetic stirring for 30 min and then transferred to a Teflon reactor, which was sealed and subjected to microwave irradiation (domestic micro-oven model Panasonic, 2.45 MHz, maximum power of 700 W) at 140°C for 3 h. The solid product obtained was washed with deionized water and vacuum dried for 24 h.

2.2. Characterization. XRD patterns were obtained with a Shimadzu XRD 6000 powder diffractometer with the use of $\text{Cu K}\alpha$ radiation ($\lambda = 1.5406 \text{ \AA}$). Raman spectra were obtained with a Raman spectrometer (Senterra, Bruker) with a 2.33 eV laser excitation source. Scanning electron microscopy (SEM), energy-dispersive X-ray spectroscopy (EDS), and scanning transmission electron microscopy (STEM) were performed with a scanning electron microscope (FEI Quanta 250 FEG with an EDAX Genesis-Apollo X SDD detector attached). HRTEM and SAED were performed with an FEI Tecnai $\text{G}^2 \text{ F20}$ instrument. N_2 adsorption-desorption analysis was conducted with a Belsorp mini II at 77 K up to 760 Torr. UV-visible diffuse reflectance spectroscopy of the samples was performed in absorbance mode with a Shimadzu UV-2600 spectrophotometer. For the optical bandwidth energy for an indirect transition, the Kubelka-Munk function was used [22]. The X-ray photoelectron spectra (XPS) were obtained with a Scienta Omicron ESCA+ spectrometer system equipped with an EA 125 hemispherical analyzer and an Xm 1000 monochromatic X-ray source (Al $\text{K}\alpha$, 1486.7 eV). The X-ray source was used with a power of 280 W as the spectrometer worked in a constant-pass energy

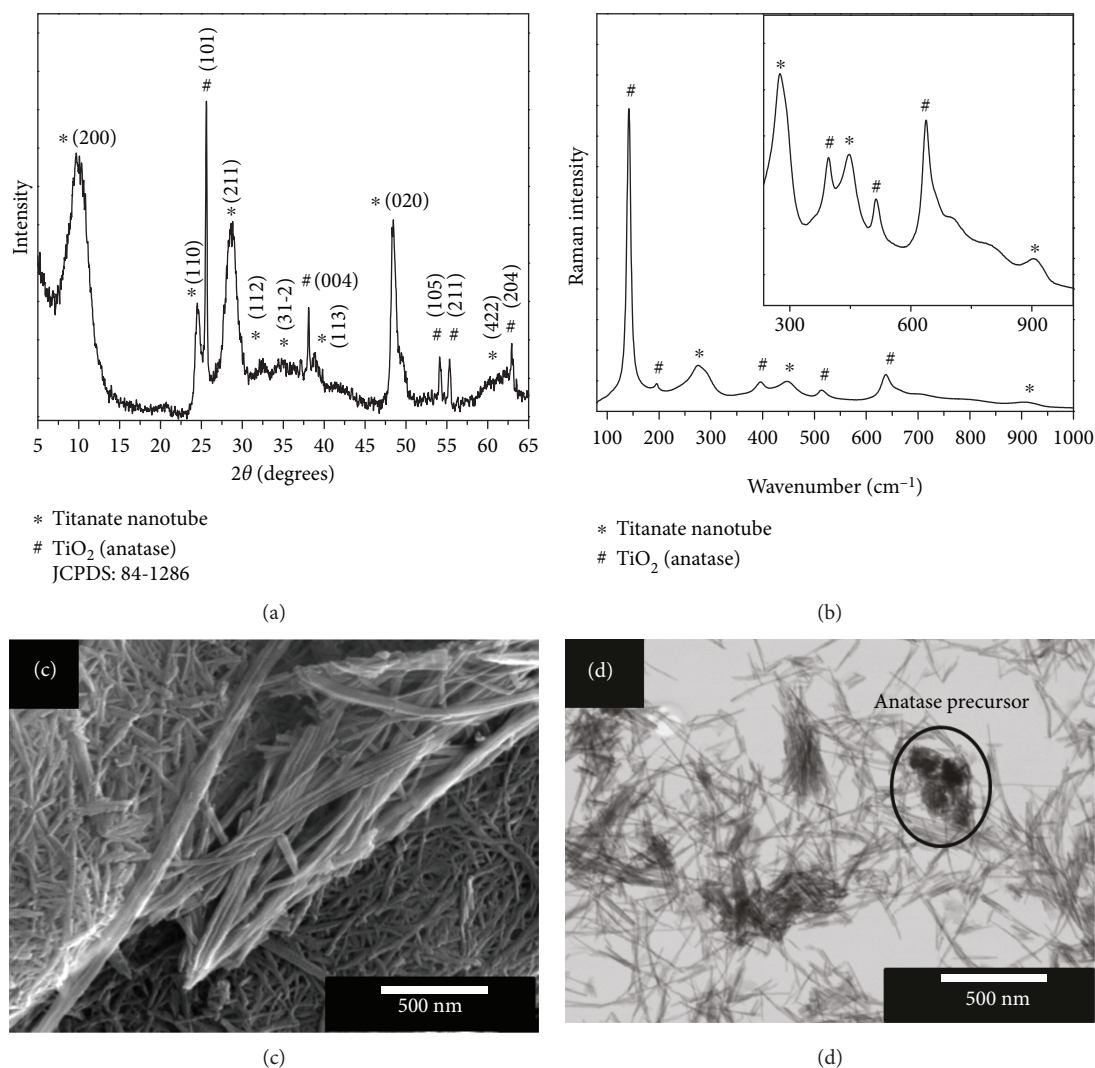
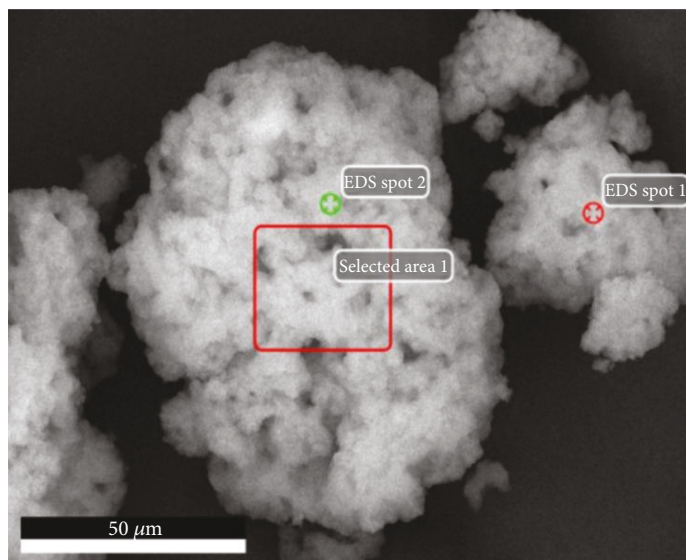


FIGURE 1: (a) X-ray diffraction and (b) Raman spectra of titanate nanotubes decorated with anatase nanoparticles (TiNT@AnNP); the inset shows the zoom in of the spectra in the $230\text{-}1000\text{ cm}^{-1}$ region to facilitate the visualization of the titanate-related bands. (c) Scanning electron micrograph and (d) scanning transmission electron micrograph of TiNT@AnNP; the existence of unreacted precursor anatase clusters is shown in the circle.

mode of 50 eV. A Scienta Omicron CN10 charge neutralizer with a beam energy of 1.6 eV charge was used to compensate the charge effect while the spectra were obtained. For corrections of peak shifts due to the remaining charge effect, the binding energies of all spectra were scaled with the use of the main peak of C 1s at 284.8 eV as a reference. Wide-scan spectra, for peak identification, were recorded with a step of 0.5 eV, and high-resolution spectra for core levels were obtained with the step of 0.03 eV. All the X-ray photoelectron spectra were analyzed with the software program CasaXPS, where the background in high-resolution spectra is computed by the Shirley method. Peak fitting of core levels was done with an asymmetric Gaussian-Lorentzian product function for the peak shape.

2.3. Photocatalytic Activity Test. In a typical photodegradation experiment with the anionic dye Remazol blue (RB),

350 mL of aqueous dye solution with a concentration of 50 mg L^{-1} was taken in a beaker and 200 mg of the catalyst added. The system was kept in a closed box and first stirred in the dark for 30 minutes with the aid of a magnetic stirrer to establish the adsorption-desorption equilibrium. It was observed that the absorbance bands of the RB dye did not decrease over time, which leads us to infer that the adsorption process does not occur or negligible. After the adsorption test, the actual photodegradation was carried out by immersing a mercury lamp (80 W, Philips, with emission at UV-visible range 380 nm-780 nm) inserted into a quartz tube. The solution was continued to be stirred under magnetic stirring, the temperature was maintained at $25 \pm 5^\circ\text{C}$ with a thermostatic bath, and excess oxygen was bubbled with an air pump. The rate of dye degradation was observed for 60 min, during which, aliquots were withdrawn at 0, 5, 10, 15, 20, 25, 30, 45, and 60 min,



Elements (atomic %)	EDS spot 1	EDS spot 2	EDS area 1
O	66.34	65.53	61.41
Na	11.72	16.75	12.70
Ti	19.85	17.69	25.30

FIGURE 2: Elemental composition (Na, Ti, and O) of TiNT@AnNP probed by EDS in different parts of the sample, as shown in the attached SEM diagram.

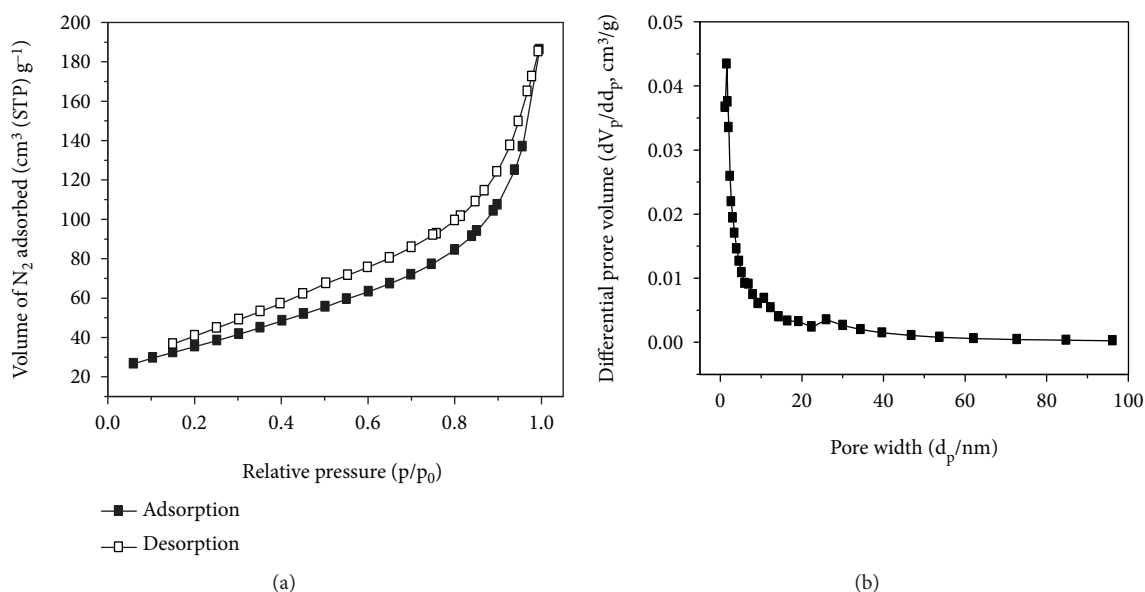


FIGURE 3: (a) N_2 adsorption-desorption isotherms and (b) pore size distribution of TiNT@AnNP.

centrifuged, and analyzed with a Shimadzu UV-3600 spectrophotometer (in absorbance mode). The dye concentration was determined by the corresponding value of the absorbance at $\lambda_{\max} = 591$ nm. All photocatalysis experiments were performed in triplicate.

In order to study the influence of light on the degradation of the RB dye, in the absence of the catalyst, a photolysis study was carried out. The methodology was very similar to the typical photocatalysis experiment, described above, but without the catalyst. The results for photolysis (Supplementary Figure 1) indicated 49.5% degradation of the RB dye at the end of 60 minutes of irradiation in our reactor.

3. Results and Discussion

The XRD diffractograms (Figure 1(a)) show the characteristic diffraction peaks of the anatase phase of TiO_2 around $2\theta = 25^\circ$, 38° , 54° , 55° , and 63° , corresponding to the crystallographic planes (101), (004), (105), (211), and (204), respectively (JCPDS card no. 84-1286), and wider peaks characteristic of titanate nanotubes at $2\theta = 9.8^\circ$, 24° , 28° , and 48° , corresponding to the crystallographic planes (200), (110), (211), and (020), respectively, of titanate nanotubes [19, 23, 24]. After careful scrutiny, some other wider peaks with low intensities were assigned to the titanate nanotube structures centered around $2\theta = 32^\circ$, 34.8° , 38.8° , and 61.5° , corresponding to

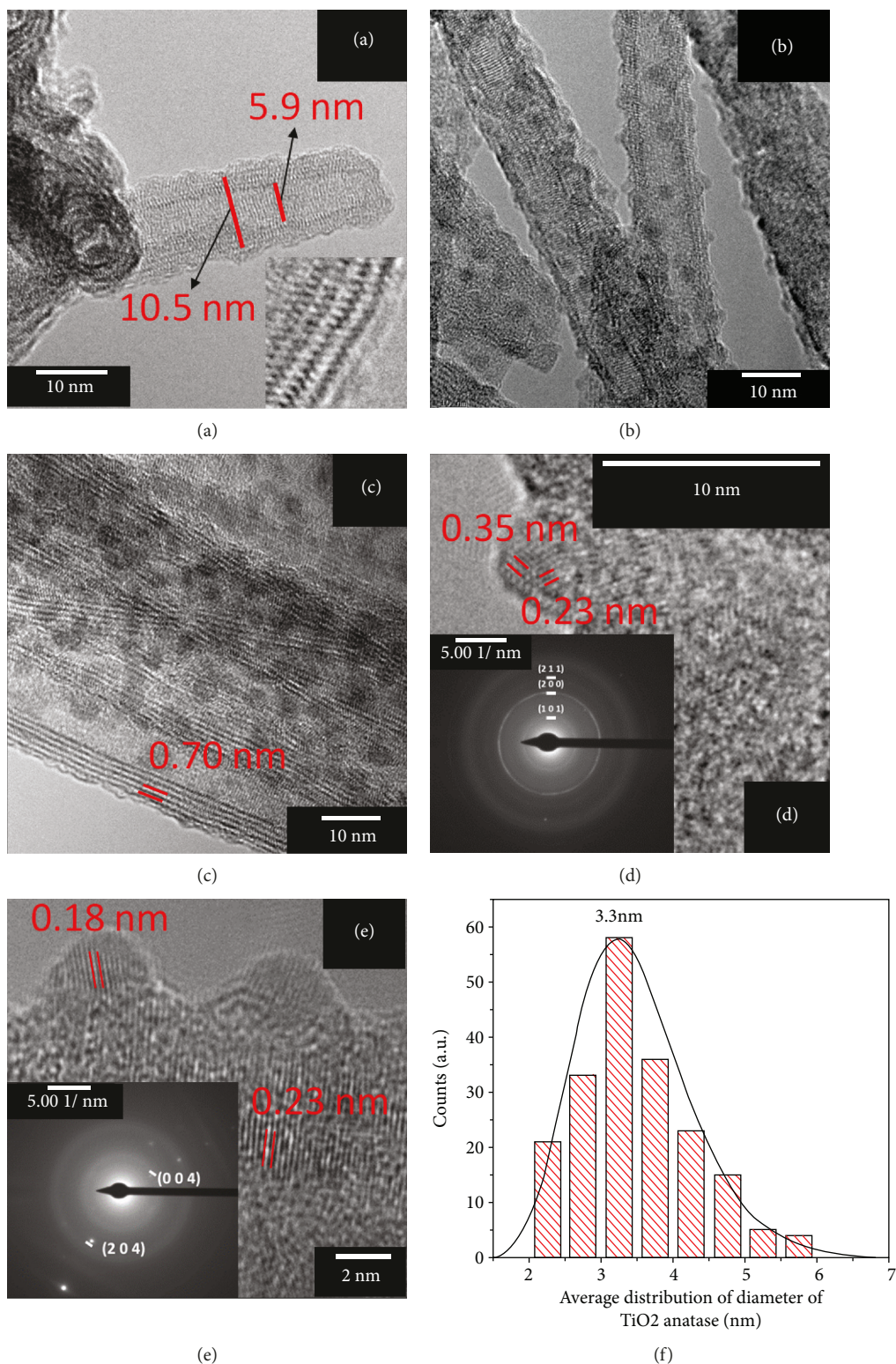


FIGURE 4: High-resolution transmission electron microscopy images of the titanate nanotubes decorated with anatase nanoparticles showing (a) the internal and external diameter of titanate nanotubes; the inset shows the TiO_6 octahedra, arranged in a zig-zag fashion, forming the walls of the titanate nanotubes. (b) Titanate nanotubes decorated with anatase nanocrystals, (c) interlamellar distance of the nanotubes, and (d, e) crystallite planes with corresponding d-spacings of the anatase nanoparticles decorating nanotubes; the insets in (d, e) show selected-area electron diffraction patterns showing a bright spot as well as concentric circles corresponding to these planes. (f) Diameter distribution of anatase nanoparticles, showing an average particle diameter of 3.3 nm.

the crystallographic planes (112), (31-2), (113), and (422), respectively, characteristic of titanate nanotubes [25].

The interlamellar distance of the nanotubes (d_{200}) was calculated with Bragg's law and was 0.87 nm, which matches with a structure similar to sodium trititanate, $\text{Na}_2\text{Ti}_3\text{O}_7$, according to previous literature [26, 27]. The interplanar distances of the planes of the anatase phase were also calculated with Bragg's law and were $d_{101} = 0.35$ nm, $d_{004} = 0.24$ nm, $d_{200} = 0.18$ nm, $d_{105} = 0.17$ nm, $d_{211} = 0.16$ nm, and $d_{204} = 0.15$ nm. The mean crystallite size of the anatase particle was calculated to be approximately 65 nm from the sharpest anatase peak at $2\theta \approx 25^\circ$, which corresponds to the unreacted precursor, also identified in the STEM image (Figure 1(d)). The Raman spectrum (Figure 1(b)) shows vibrational modes corresponding to the anatase phase at 142, 196, 395, 515, and 638 cm^{-1} , as well as vibrational modes of titanate nanotubes at 280, 448, and 908 cm^{-1} , emphasized in the inset of Figure 1(b) [28, 29]. It was possible to confirm the formation of titanate nanotubes starting from the anatase precursor with the structural information obtained from the XRD patterns and Raman spectra and the morphological data obtained by scanning electron microscopy and STEM (Figures 1(c) and 1(d)).

The chemical composition of the titanate nanotubes was investigated by energy-dispersive X-ray spectroscopy (EDS). The atomic percentages of the elements were shown in Figure 2, which leads to the Na/Ti and Ti/O atomic ratios to be 0.66 and 0.32, respectively. These values suggest a $\text{Na}_2\text{Ti}_3\text{O}_7$ phase structure [30] with a small excess of oxygen, probably due to the presence of water in the structure.

The N_2 adsorption-desorption isotherms at 77 K of TiNT@AnNP were shown in Figure 3(a), which shows a mixed II-type IV nature with a small H4 hysteresis loop, characteristic to the titanate nanotubes, reflective of its mesoporous nature [31]. The specific surface area was calculated using the Brunauer-Emmett-Teller (BET) method which showed a drastic increase of the BET surface area of TiNT@AnNP ($127\text{ m}^2/\text{g}$) compared to that of the anatase- TiO_2 precursor material ($15\text{ m}^2/\text{g}$). The pore size distribution of TiNT@AnNP was shown in Figure 3(b), and the average pore diameter as well as the total pore volume was calculated using Brunauer-Joyner-Halenda (BJH) method and was found to be 8.7 nm and $0.26\text{ cm}^3/\text{g}$, respectively, confirming the mesoporous nature.

To carefully study TiNT@AnNP, HRTEM was performed rigorously, and surprisingly the titanate nanotubes were found to be homogeneously and intensively decorated with anatase nanoparticles. Representative HRTEM images are shown in Figures 4(a)–4(e). The internal and external diameters of the titanate nanotubes were 5.9 and 10.5 nm, respectively (Figure 4(a)). A close zoom in of the wall structure of the titanate nanotube shows the TiO_6 octahedra, connected in zig-zag fashion, depicted in the inset of the Figure 1. However, a previously unreported feature was observed: titanate nanotubes appear to be uniformly decorated with anatase nanocrystals after the microwave hydrothermal reaction (Figure 4(b)), giving rise to a nanoheterostructure. The interlamellar spacing between the multilayers of the

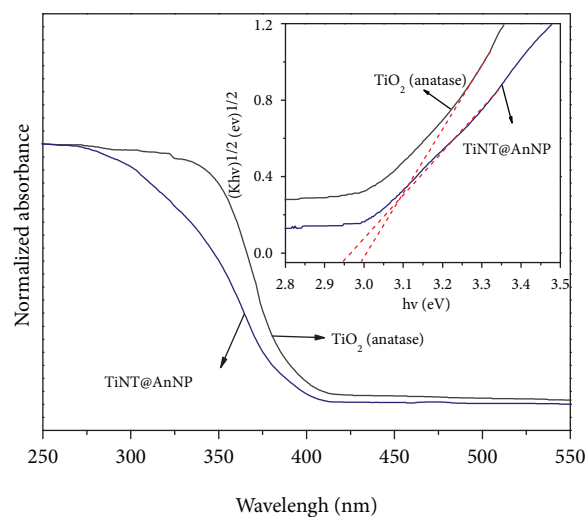


FIGURE 5: UV-visible diffuse reflectance spectra of TiO_2 (anatase) and titanate nanotubes decorated with anatase nanoparticles (TiNT@AnNP) and band gap obtained by the Kubelka-Munk method (inset).

nanotubes measured by HRTEM was 0.70 nm (Figure 4(c)). The reduction of the interlayer distance (compared with the value obtained by XRD) could be rationalized by the fact that for HRTEM analysis, the sample was subjected to a high vacuum, which resulted in the release of water from the titanate layers, promoting a shortening of the distance between the layers [32].

The SAED patterns of TiNT@AnNP shown in the insets in Figures 4(d) and 4(e) indicate the predominance of diffuse concentric rings [25], but because of the low crystallinity of the titanate tubes, it was difficult to assign the planes of this phase. However, concentric rings associated with the more crystalline phase related to anatase nanocrystals were seen in the SAED images, corresponding to the different Bragg planes, especially (101), (004), (200), (211), and (204). The interplanar distances of the anatase nanocrystals of the heterostructure were measured from the HRTEM images (Figures 4(d) and 4(e)) directly and were found to be $d_{101} = 0.35$ nm, $d_{004} = 0.23$ nm, and $d_{200} = 0.18$ nm, which corroborates the values found by XRD as well as SAED. If carefully observed, an amorphous interface can be seen between these two crystalline phases, titanate nanotubes and anatase nanoparticles, which can be clearly seen in Figure 4(e). This is a site with structural defects, which could be responsible for the electron trapping, stopping the electron-hole pair recombination and therefore leading to better photooxidation of the dyes. The average diameter distribution of the anatase nanoparticles of TiNT@AnNP is shown in Figure 4(f) and was 3.3 nm.

The UV-visible (solid) absorption spectra of TiNT@AnNP and the anatase precursor are shown in Figure 5. The band gaps of the corresponding spectra were evaluated by the Kubelka-Munk method [22] and are shown in the inset in Figure 5. The results indicate that the formation of TiNT@AnNP resulted in a change in the electronic levels of

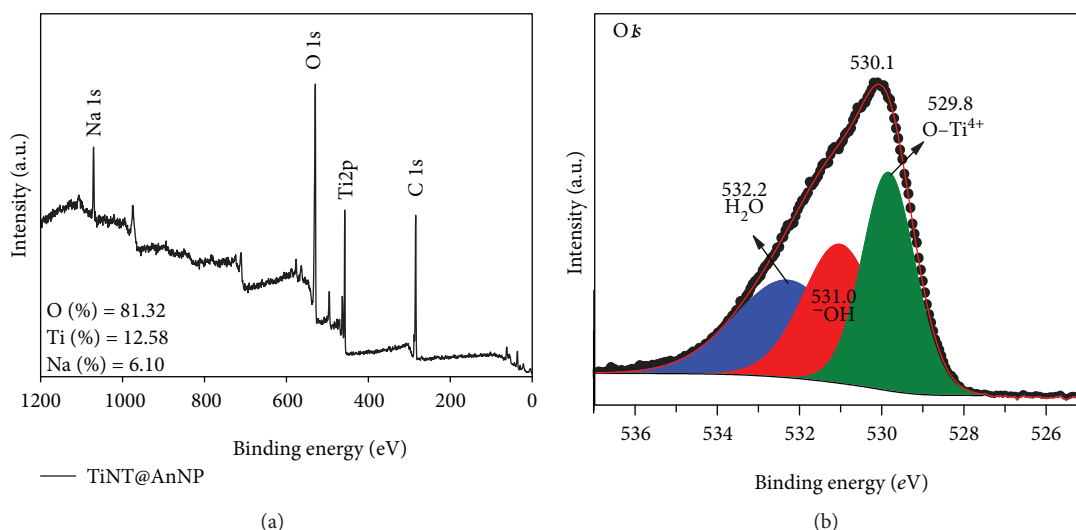


FIGURE 6: (a) Full scan X-ray photoelectron spectroscopy of TiNT@AnNP; (b) O 1s spectra deconvoluted into subpeaks.

the anatase precursor as the band gap decreased to 2.94 eV (nanoheterostructure) from 2.99 eV (anatase). Although the change is small, the enhanced photocatalytic activity of TiNT@AnNP in the degradation of Remazol blue can be attributed to the synergism associated with the mixed phase and defect-rich phase boundaries, which increases the efficiency of generating electron-hole pairs.

The XPS (Figure 6(a)), the maximum energy for C 1s (284.8 eV) was used as the reference binding energy) reveals the surface compositional information of the TiNT@AnNP. The surface elemental composition of the TiNT@AnNP was found to be Na₂Ti_{4.12}O_{26.68} (Figure 6(a)), with a higher compositional value of both Ti and O compared to that found from EDS, mentioned earlier. This may be attributed to the surface sensitivity of the XPS method, as it takes up the additional signals of Ti and O from the anatase-TiO₂ nanoparticles, decorated on the surface of the tubes. Further excess of O can be accounted for the structural water as O 1s spectrum of TiNT@AnNP (Figure 6(b)) shows that the O 1s peak at 530.1 eV can be deconvoluted into subpeaks at 532, 531, and 529.8 eV, which are attributed to H₂O, -OH, and Ti-O, respectively. Similar results were reported by Kim et al. [33], who found that the O 1s peak is formed from Ti-O in TiO₂ and OH in Ti-OH. The higher intensity of the Ti-OH groups in TiNT@AnNP indicates the presence of a large amount of surface hydroxyl groups [6].

Although the stepwise formation of TiNT@AnNP from anatase particles was investigated thoroughly in this work, two possible mechanisms are suggested from a study of the literature and indirect evidence and are shown in the schemes in Figure 7. Because trititanate nanotubes have building blocks similar to those of anatase TiO₂, the former can be converted to the latter by simple chemical routes. In acidic conditions, this transformation follows a topochemical reaction mechanism, whereas in alkaline conditions it proceeds through a dissolution and nucleation mechanism [34]. There has been much controversy about the exact mechanism of the formation of titanate nanotubes from

anatase TiO₂ via an alkaline hydrothermal synthesis route, but there is agreement in that to begin with the surface of the starting material, anatase particles, which is delaminated in an alkaline medium, giving rise to smaller entities such as Ti(OH)₄, and then recrystallizes to form trititanate nanosheets, which roll up to form nanotubes [35]. In our first proposed mechanism (path 1 in Figure 7), it is surmised that because of the superefficient, rapid, and less selective internal heating by microwaves, all the aforementioned processes probably happen simultaneously and at an elevated rate in the reactor. As the precursor anatase particles is dissolved in NaOH, generating Ti(OH)₄, they crystallize not only as trititanate sheets, which then roll up to form titanate nanotubes, but also as anatase nanocrystals of smaller diameter (3-4 nm), which can precipitate on the surface of the nanotube, formed at the same time, and are attached with the help of dangling hydroxyl groups on the titanate nanotube surface, thereby generating the observed TiNT@AnNP heterostructure. As an alternative, we propose another two-step mechanism, depicted in Figure 7 as path 2, where the titanate nanotube is first generated by the dissolution-recrystallization pathway from the anatase particles, followed in the second step by corrosion of the wall of the tubes in alkaline solution to generate Ti(OH)₄, which recrystallizes as anatase nanocrystals over the nanotubes. A similar mechanism was observed in conventional alkaline hydrothermal posttreatment of sodium trititanate nanotubes, where the surface of the sodium trititanate tube slowly decomposes to produce Ti(OH)₄ fragments, which rearrange themselves through dehydration, giving rise to a Ti-O-Ti linkage, eventually seeding to form a tetragonal faceted single crystal of anatase TiO₂ [9]. Because of the fast kinetics and the stochastic nature of the reaction happening in the microwave reactor, it is impossible at this stage to choose between these two pathways, but careful observation of the HRTEM images of the reaction conducted for 1 and 4 h in conditions similar to those described above shows that the nanocrystals obtained in the latter case are larger than those obtained in the former case (shown in Supplementary

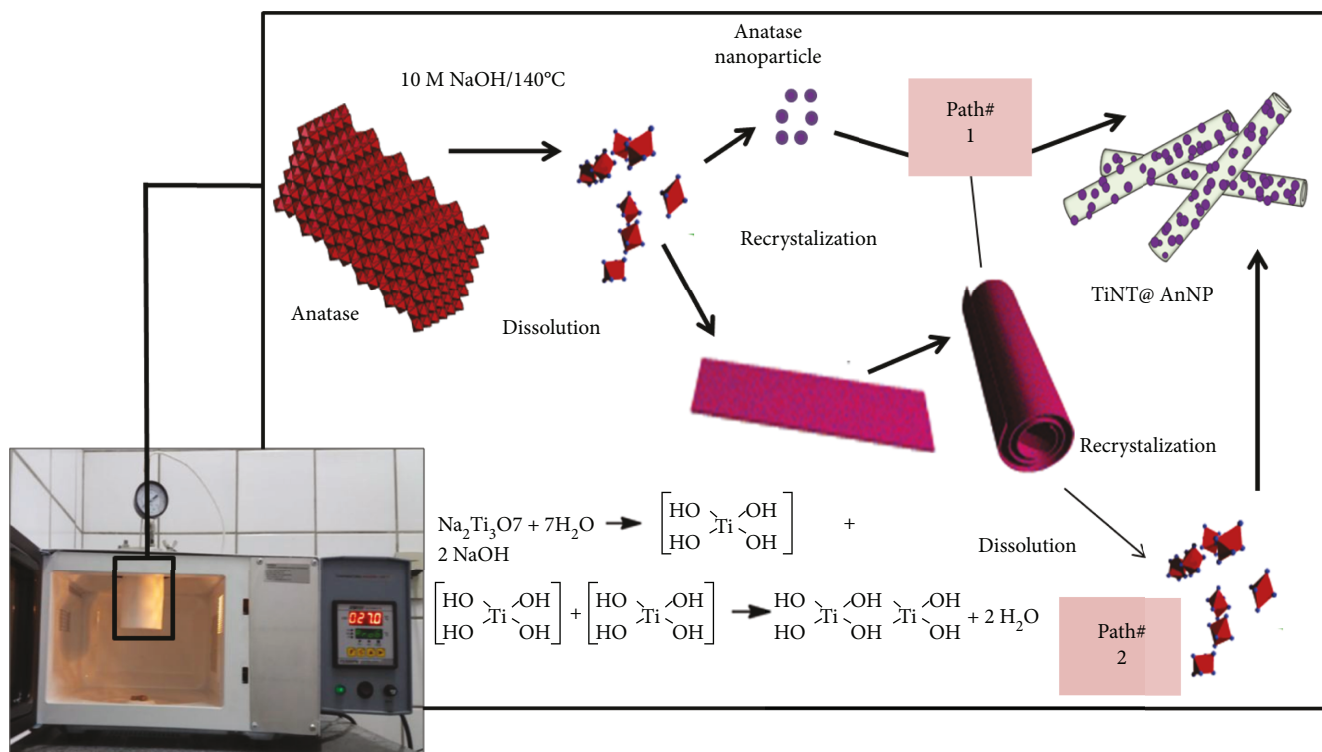


FIGURE 7: Two possible mechanisms for the formation of titanate nanotubes decorated with anatase nanoparticles (TiNT@AnNP) by microwave-assisted hydrothermal synthesis (the figure was created based on the observation of reference [33]).

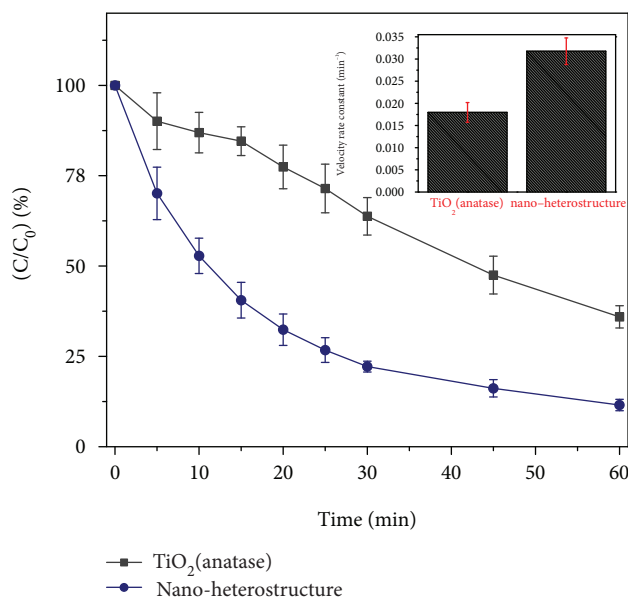


FIGURE 8: Photocatalytic degradation of Remazol blue as a function of the irradiation time under visible light for the anatase precursor and the titanate nanotubes decorated with the anatase nanoparticles obtained, triplicated; the inset shows the rate constants of the degradation experiment, triplicated, considering the Langmuir-Hinshelwood pseudo-first-order kinetic pathway.

Figure 2), which suggests that the second possibility (path 2 in Figure 7) is more likely, which is promoting the ripening of anatase nanoparticles.

Experiments investigating the photocatalytic degradation of the anionic dye Remazol blue by TiNT@AnNP as well as the precursor were performed under UV-visible light irradiation (Figure 8). At the beginning of the photocatalysis experiment, the photocatalysts were added to the solution (50 mg/L) of the dye Remazol blue and agitated for 30 minutes in the dark. Then the concentration of the solution was measured by means of UV-Vis spectroscopy, and it was found unchanged, i.e., no significant adsorption of the dye was observed by the catalyst under the experimental conditions. In both cases, degradation followed the Langmuir-Hinshelwood pseudo-first-order kinetics model, as shown by the best fit with a correlation coefficient (R^2) = 0.953 and 0.977, respectively. The degradation rate constant was 0.0317 min^{-1} for TiNT@AnNP, whereas for the anatase precursor, it was 0.017 min^{-1} . The rate constant and the degradation capacity, as shown in Figure 8, for the hybrid system compared with the precursor material were much greater, indicating that a microwave-assisted hydrothermal synthesis is an alternative option for fast and efficient one-pot production of a catalyst, which can be used for complete degradation of the dye Remazol blue.

4. Conclusion

A nanoheterostructure of a titanate nanotube decorated with anatase nanoparticles was generated by a one-pot microwave-assisted hydrothermal method with anatase as the precursor; this had not been reported previously.

Morphological and structural characterization showed that these anatase nanoparticles are anchored on the titanate nanotubes with a homogeneous distribution and have an average diameter of 3.3 nm. Two possible mechanisms for the formation of the heterostructure were proposed, and the mechanism involving the formation of titanate nanotubes followed by corrosion of the walls by NaOH and recrystallization of anatase nanocrystals over the nanotube surface was argued to be more likely because the longer synthesis produces larger anatase nanoparticles on nanotubes. Finally, TiNT@AnNP was investigated for its ability to degrade the anionic dye Remazol blue photocatalytically, and it was found to be more efficient than the precursor TiO₂ (anatase), probably because of its greater surface area and efficiency of separation of photoinduced electron-hole pairs. Thus, the microwave-assisted hydrothermal route can be used as an alternative efficient and one-pot method to generate TiNT@AnNP with increased efficiency for photodegradation of dyes.

Data Availability

The data used to support the findings of this study are available from the corresponding author upon request.

Conflicts of Interest

The authors declare no conflict of interest.

Authors' Contributions

The manuscript was written through the contribution of all authors, specifically: conceptualization, B.C.V., A.O.L., A.G., J.A.O.O., R.R.M.S, C.L., and O.P.F.; methodology, S.B.S.G., A.G., J.A.O.O., T.M.F.M., and B.C.V.; investigation, S.B.S.G., A.G., A.O.L., J.A.O.O., T.M.F.M, O.P.F., and B.C.V.; resources, B.C.V.; supervision, B.C.V. and A.G.; project administration, B.C.V.; funding acquisition, B.C.V., O.P.F, and A.O.L. All authors have given their approval to the final version of the manuscript.

Acknowledgments

The authors gratefully acknowledge the financial support from the Brazilian funding agencies FAPEPI (grant 001/2018), CAPES (Procad 2013 grant 183995), and CNPq (grants 305632/2016-7 and PVE 400397/2014-5). A.O.L. would like to thank CNPq (grant 303752/2017-3) for the financial support.

Supplementary Materials

The Supplementary Material contains information about the photolysis experiment of the Remazol blue (RB) dye solution using HG lamp for 60 min (without the photocatalyst), showing the low degradation of RB without the photocatalyst. Also, it presents HRTEM images of the titanate nanotubes decorated with anatase nanoparticles synthesized at 1 h and 4 h, showing larger anatase nanoparticles in the sample treated at 4 h than 1 h. (*Supplementary Materials*)

References

- [1] Y. Zhang, Z. Jiang, J. Huang et al., "Titanate and titania nanostructured materials for environmental and energy applications: a review," *RSC Advances*, vol. 5, no. 97, pp. 79479–79510, 2015.
- [2] Y. L. Pang, S. Lim, H. C. Ong, and W. T. Chong, "A critical review on the recent progress of synthesizing techniques and fabrication of TiO₂-based nanotubes photocatalysts," *Applied Catalysis A: General*, vol. 481, pp. 127–142, 2014.
- [3] H.-H. Ou and S.-L. Lo, "Review of titania nanotubes synthesized via the hydrothermal treatment: fabrication, modification, and application," *Separation and Purification Technology*, vol. 58, no. 1, pp. 179–191, 2007.
- [4] D. S. Xu, J. M. Li, Y. X. Yu, and J. J. Li, "From titanates to TiO₂ nanostructures: controllable synthesis, growth mechanism, and applications," *Science China Chemistry*, vol. 55, no. 11, pp. 2334–2345, 2012.
- [5] R. Doong and C. Tsai, "Synergistic effect of Cu adsorption on the enhanced photocatalytic degradation of bisphenol A by TiO₂/titanate nanotubes composites," *Journal of the Taiwan Institute of Chemical Engineers*, vol. 57, pp. 69–76, 2015.
- [6] F. Chen, Y. Li, Z. Liu, and P. Fang, "Facile synthesis of TiO₂/tritanate heterostructure with enhanced photoelectric efficiency for an improved photocatalysis," *Applied Surface Science*, vol. 341, pp. 55–60, 2015.
- [7] F. Alvarez-Ramirez and Y. Ruiz-Morales, "Ab initio molecular dynamics calculations of the phase transformation mechanism for the formation of TiO₂ titanate-type nanosheets from anatase," *Chemistry of Materials*, vol. 19, no. 12, pp. 2947–2959, 2007.
- [8] H. Y. Zhu, Y. Lan, X. P. Gao et al., "Phase transition between nanostructures of titanate and titanium dioxides via simple wet-chemical reactions," *Journal of the American Chemical Society*, vol. 127, no. 18, pp. 6730–6736, 2005.
- [9] J. Li and D. Xu, "Tetragonal faceted-nanorods of anatase TiO₂ single crystals with a large percentage of active {100} facets," *Chemical Communications*, vol. 46, no. 13, pp. 2301–2303, 2010.
- [10] L. Zhang, H. Lin, N. Wang, C. Lin, and J. Li, "The evolution of morphology and crystal form of titanate nanotubes under calcination and its mechanism," *Journal of Alloys and Compounds*, vol. 431, no. 1-2, pp. 230–235, 2007.
- [11] A. Sandoval, R. Zanella, and T. E. Klimova, "Titania nanotubes decorated with anatase nanocrystals as support for active and stable gold catalysts for CO oxidation," *Catalysis Today*, vol. 282, pp. 140–150, 2017.
- [12] H. Zhu, X. Gao, Y. Lan, D. Song, Y. Xi, and J. Zhao, "Hydrogen titanate nanofibers covered with anatase nanocrystals: a delicate structure achieved by the wet chemistry reaction of the titanate nanofibers," *Journal of the American Chemical Society*, vol. 126, no. 27, pp. 8380–8381, 2004.
- [13] H. Yu, J. Yu, B. Cheng, and M. Zhou, "Effects of hydrothermal post-treatment on microstructures and morphology of titanate nanoribbons," *Journal of Solid State Chemistry*, vol. 179, no. 2, pp. 349–354, 2006.
- [14] D. M. P. Mingos and D. R. Baghurst, "Tilden lecture. Applications of microwave dielectric heating effects to synthetic problems in chemistry," *Chemical Society Reviews*, vol. 20, pp. 1–47, 1991.

- [15] T. Kasuga, M. Hiramatsu, A. Hoson, T. Sekino, and K. Niihara, "Formation of titanium oxide nanotube," *Langmuir*, vol. 14, no. 12, pp. 3160–3163, 1998.
- [16] Y.-a. Wang, J. Yang, J. Zhang, H. Liu, and Z. Zhang, "Microwave-assisted preparation of titanate nanotubes," *Chemistry Letters*, vol. 34, no. 8, pp. 1168–1169, 2005.
- [17] S. H. Cho, N. H. Hao, and T. Yamaguchi, "Comparative analysis and characterization of TiO₂ nanotubes produced by microwave assisted hydrothermal method and normal hydrothermal," *Journal of Ceramic Processing Research*, vol. 17, no. 1, pp. 41–45, 2016.
- [18] M. C. Manique, A. P. Silva, A. K. Alves, and C. P. Bergmann, "Titanate nanotubes produced from microwave-assisted hydrothermal synthesis: characterization, adsorption and photocatalytic activity," *Brazilian Journal of Chemical Engineering*, vol. 34, no. 1, pp. 331–339, 2017.
- [19] D. C. Manfro, A. dos Anjos, A. A. Cavalheiro, L. A. Perazolli, J. A. Varela, and M. A. Zaghete, "Titanate nanotubes produced from microwave-assisted hydrothermal synthesis: photocatalytic and structural properties," *Ceramics International*, vol. 40, no. 9, Part A, pp. 14483–14491, 2014.
- [20] S. Preda, M. Rutar, P. Umek, and M. Zaharescu, "A study of thermal properties of sodium titanate nanotubes synthesized by microwave-assisted hydrothermal method," *Materials Research Bulletin*, vol. 71, pp. 98–105, 2015.
- [21] S. Ribbens, V. Meynen, G. V. Tendeloo et al., "Development of photocatalytic efficient Ti-based nanotubes and nanoribbons by conventional and microwave assisted synthesis strategies," *Microporous and Mesoporous Materials*, vol. 114, no. 1–3, pp. 401–409, 2008.
- [22] S. Valencia, J. M. Marin, and G. Restrepo, "Study of the bandgap of synthesized titanium dioxide nanoparticles using the sol-gel method and a hydrothermal treatment," *The Open Materials Science Journal*, vol. 4, no. 1, pp. 9–14, 2010.
- [23] B. C. Viana, O. P. Ferreira, A. G. Souza Filho, A. A. Hidalgo, J. Mendes Filho, and O. L. Alves, "Highlighting the mechanisms of the titanate nanotubes to titanate nanoribbons transformation," *Journal of Nanoparticle Research*, vol. 13, no. 8, pp. 3259–3265, 2011.
- [24] C.-K. Lee, C.-C. Wang, M.-D. Lyu, L.-C. Juang, S.-S. Liu, and S.-H. Hung, "Effects of sodium content and calcination temperature on the morphology, structure and photocatalytic activity of nanotubular titanates," *Journal of Colloid and Interface Science*, vol. 316, no. 2, pp. 562–569, 2007.
- [25] Q. Chen, G. H. Du, S. Zhang, and L.-M. Peng, "The structure of trititanate nanotubes," *Acta Crystallographica Section B Structural Science*, vol. 58, no. 4, pp. 587–593, 2002.
- [26] E. Morgado, M. A. S. de Abreu, G. T. Moure, B. A. Marinkovic, P. M. Jardim, and A. S. Araujo, "Characterization of nanostructured titanates obtained by alkali treatment of TiO₂-anatases with distinct crystal sizes," *Chemistry of Materials*, vol. 19, no. 4, pp. 665–676, 2007.
- [27] V. C. Ferreira and O. C. Monteiro, "New hybrid titanate elongated nanostructures through organic dye molecules sensitization," *Journal of Nanoparticle Research*, vol. 15, 2013.
- [28] B. C. Viana, O. P. Ferreira, A. G. S. Filho, A. A. Hidalgo, J. M. Filho, and O. L. Alves, "Alkali metal intercalated titanate nanotubes: a vibrational spectroscopy study," *Vibrational Spectroscopy*, vol. 55, no. 2, pp. 183–187, 2011.
- [29] M. A. Cortés-Jácome, G. Ferrat-Torres, L. F. F. Ortiz et al., "In situ thermo-Raman study of titanium oxide nanotubes," *Catalysis Today*, vol. 126, no. 1–2, pp. 248–255, 2007.
- [30] O. P. Ferreira, A. G. Souza Filho, J. Mendes Filho, and O. L. Alves, "Unveiling the structure and composition of titanium oxide nanotubes through ion exchange chemical reactions and thermal decomposition processes," *Journal of the Brazilian Chemical Society*, vol. 17, no. 2, pp. 393–402, 2006.
- [31] M. Thommes, K. Kaneko, A. V. Neimark et al., "Physisorption of gases, with special reference to the evaluation of surface area and pore size distribution (IUPAC Technical Report)," *Pure and Applied Chemistry*, vol. 87, no. 9–10, 2015.
- [32] T. M. F. Marques, C. Luz-Lima, M. Sacilloti et al., "Photoluminescence enhancement of titanate nanotubes by insertion of rare earth ions in their interlayer spaces," *Journal of Nanomaterials*, vol. 2017, Article ID 3809807, 9 pages, 2017.
- [33] G. S. Kim, S. G. Ansari, H. K. Seo, Y. S. Kim, and H. S. Shin, "Effect of annealing temperature on structural and bonded states of titanate nanotube films," *Journal of Applied Physics*, vol. 101, no. 2, article 024314, 2007.
- [34] J. Li, H. Yang, Q. Li, and D. Xu, "Enlarging the application of potassium titanate nanowires as titanium source for preparation of TiO₂ nanostructures with tunable phases," *CrystEngComm*, vol. 14, no. 9, 2012.
- [35] Á. Kukovecz, M. Hodos, E. Horváth, G. Radnóczy, Z. Kónya, and I. Kiricsi, "Oriented crystal growth model explains the formation of titania nanotubes," *The Journal of Physical Chemistry B*, vol. 109, no. 38, pp. 17781–17783, 2005.

Research Article

Synthesis and Characterization of ZnO-ZrO₂ Nanocomposites for Photocatalytic Degradation and Mineralization of Phenol

M. C. Uribe López,¹ M. A. Alvarez Lemus ¹, M. C. Hidalgo,² R. López González ¹,
P. Quintana Owen,³ S. Oros-Ruiz,⁴ S. A. Uribe López,⁵ and J. Acosta¹

¹Juárez Autonomous University of Tabasco, Nanotechnology for Biomedicine and Environmental Applications, Academic Division of Engineering and Architecture, Carr. Cunduacán Jalpa de Méndez Km 1, Col. La Esmeralda, CP 86690 Cunduacán, Tabasco, Mexico

²Instituto de Ciencia de Materiales de Sevilla (ICMS), Consejo Superior de Investigaciones Científicas (CSIC)-Universidad de Sevilla, Américo Vespucio 49, 41092 Sevilla, Spain

³CINVESTAV Unidad Mérida, Departamento de Física Aplicada, AP. 73 Cordemex, 97310 Mérida, Yucatán, Mexico

⁴Autonomous Metropolitan University-Iztapalapa, CONACYT-Research Fellow-Department of Chemistry, ECOCATAL Group, Av. San Rafael Atlixco No. 186, Col. Vicentina, Iztapalapa 09340, Mexico

⁵Juárez Autonomous University of Tabasco, CONACYT-Research Fellow, Academic Division of Engineering and Architecture, Carr. Cunduacán Jalpa de Méndez Km 1, Col. La Esmeralda, CP 86690 Cunduacán, Tabasco, Mexico

Correspondence should be addressed to M. A. Alvarez Lemus; mayra.alvarez@ujat.mx

Received 18 June 2018; Revised 8 October 2018; Accepted 1 November 2018; Published 10 January 2019

Guest Editor: Zhen Yu

Copyright © 2019 M. C. Uribe López et al. This is an open access article distributed under the Creative Commons Attribution License, which permits unrestricted use, distribution, and reproduction in any medium, provided the original work is properly cited.

ZnO-ZrO₂ nanocomposites using zinc (II) acetylacetonate and different ZnO contents (13, 25, 50, and 75% mol) were synthesized through sol-gel method. The synthesis process was strongly related to nanocomposite properties especially on their structural composition. The obtained ZnO-ZrO₂ nanomaterials presented tetragonal crystalline structure for zirconia whereas hexagonal one was formed in ZnO. Raman spectroscopy and XRD patterns confirmed the formation of tetragonal zirconia whereas inhibition of monoclinic structure was observed. Addition of ZnO affected the pore size distribution of the composite, and the measured specific surface areas were from 10 m²/g (for pure ZnO) to 46 m²/g (pristine ZrO₂). Eg values of ZrO₂ were modified by ZnO addition, since calculated values using Kubelka-Munk's function varied from 4.73 to 3.76 eV. The morphology and size of the nanomaterials investigated by electron microscopy showed formation of nanorods for ZnO with sizes ranging from 50 nm to 300 nm while zirconia was formed by smaller particles (less than 50 nm). The main advantage of using the nanocomposite for photocatalytic degradation of phenol was the mineralization degree, since 75ZnO-ZrO₂ nanocomposite surpassed mineralization reached by pure ZnO and also inhibited formation of undesirable intermediates.

1. Introduction

Zirconium oxide (ZrO₂) known as zirconia is an interesting material due to its application in various photochemical heterogeneous reactions. ZrO₂ is an n-type semiconductor with a wide band gap energy between 5.0 and 5.5 eV [1]. Because of this, ZrO₂ requires UV-C light (<280 nm) to be excited and generate electron-hole pairs [2]. A strategy to overcome this is by doping ZrO₂ with different transition metal ions or coupling with other metal oxides with dissimilar band edge [3]. Composites made of two metal oxides have attracted much attention in different researches because they possess

improved physicochemical properties than the pure oxides. Usually, composites enhance photocatalytic activity [4, 5], produce new crystallographic phases with quite different properties than the original oxides, create defect energy levels in the band gap region [6], change the surface characteristics of the individual oxides due to the formation of new sites in the interface between the components [7], and also increase the stability of a photoactive crystalline phase [8]. In order to enhance optical properties of ZrO₂ several semiconductors like SiO₂, TiO₂, ZnO, WO₃, and NiO have been coupled to ZrO₂. Together with TiO₂, zinc oxide is one of the most investigated n-type semiconductor materials due to its low-cost,

easy fabrication, wide band-gap, and photocatalytic activity for degrading several organic pollutants into less harmful products [9]. The main advantage of ZnO is that it absorbs a larger fraction of the solar spectrum than TiO₂ [10]. The band gap of ZnO is ~3.37 eV, and its exciton-binding energy is about 60 meV [11]. Many reports have been published about the good physicochemical properties given by the use of ZnO in composites. For instance, a composite made by nanostructures transparent conducting metal-oxides (TCMOs) as ZnO/NiO resulted in an excellent candidate for acetone sensing [12]. Nanocomposites of Zn(1-x)MgxO/graphene showed an excellent performance to remove methylene blue dye under natural sunlight illumination [13]. TiO₂/ZnO nanocomposites with different contents of ZnO showed an improvement in the degradation of the organic dyes brilliant green and methylene blue under solar light irradiation [14]. ZnO/TiO₂ photocatalyst exhibited much higher photocatalytic activity than pure TiO₂, ZnO, and P-25 in the degradation of 4-chlorophenol under low UV irradiation [15]. The composites of ZnO/Ag₂CO₃/Ag₂O demonstrated a potential effect in the photodegradation of phenol under visible light irradiation due to the facilitate charge transfer and suppress recombination of photogenerated electrons and holes [16].

Recently, composites of ZrO₂ with ZnO have attracted much attention because of their excellent properties as a semiconductor material, especially for the degradation reactions of recalcitrant organic pollutants. The enhancement in photocatalytic activity of ZnO-ZrO₂ composites has been associated with the changes in their structural, textural, and optical properties, such as surface area, particle size, formation of a specific crystalline phase, and low band gap energy [4, 17, 18]. In addition, the improved electron-hole pair enhances the photocatalytic efficiency. Under illumination, both the semiconductors of nanocomposite are simultaneously excited, and the electrons slip to the low-lying conduction band of one semiconductor, while holes move to the less anodic valence band. Sherly et al. [19] attributed the efficiency of Zn₂Zr (ZnO and ZrO₂ in 2:1 ratio) photocatalyst in the degradation of 2,4-dichlorophenol to the good stability and the efficient separation of photogenerated electron-hole pairs. Aghabeygi and Khademi-Shamami [4] stated that the good properties of 1:2 molar ratio of ZrO₂:ZnO as photocatalyst in the degradation of Congo Red dye could be by the decrease in the rate of the hole-electron pairs recombination when the excitation takes place with energy lower than E_g. Besides, they proposed that ZnO could increase the concentration of free electrons in the CB of ZrO₂ by reducing the charge recombination in the process of electron transport. Gurushantha et al. [20] demonstrated a photocatalytic enhancement in the ZrO₂/ZnO (1:2) nanocomposite for the degradation of acid orange 8 dye under UV light irradiation (254 nm). They observed that the reduction of energy gap, the increase of the density states, and the stability of the composite increased the photocatalyst efficiency.

In this work, we investigated the effect of ZnO on the photocatalytic properties of ZnO-ZrO₂ nanocomposites obtained by sol-gel method in the photodegradation of phenol in water under UV-A irradiation.

2. Materials and Methods

2.1. Reagents. Zirconium (IV) butoxide (80 wt. % in 1-butanol), phenol (ReagentPlus ≥99%), and Zinc Acetylacetonate hydrate were purchased from Sigma-Aldrich; hydrochloric acid (36.5–38%) was obtained from Civeq (México). In all cases, deionized water was used.

2.2. Synthesis of ZrO₂. 81.2 mmol of de Zirconium (IV) butoxide were added dropwise to 48.9 mL of deionized water and ethanol mixture (1:8) preheated at 70°C. Before addition of the alkoxide, pH was adjusted at pH 3 with hydrochloric acid (2.5 M). The white suspension was kept under temperature at 70°C, with continuous stirring and reflux for 24 h. The gel was dried at 70°C for 8 h afterwards. Finally, the obtained powder was ground and then calcined at 500°C for 4 h.

2.3. Synthesis of ZnO. 11.38 mmol of Zinc Acetylacetonate hydrate (powder, Sigma-Aldrich) were added into 50 mL of ethanol (96%, Civeq) previously heated at 70°C and adjusted at pH 3 with chlorhydric acid (2.5 M) (36.5–38%, Civeq) during 30 min. The suspension was stirred for 4 h at 70°C and then being aged for 24 h under continuous agitation. Later, the resulting gel was washed several times with ethanol and deionized water. Finally, the white powders were dried at 70°C during 6 h, ground, and then calcined at 500°C for 4 h.

2.4. Synthesis of ZnO-ZrO₂ Nanocomposites. Different molar percentages (13%, 25%, 50%, and 75%) of ZnO were incorporated into ZrO₂ and named as 13ZnO-ZrO₂, 25ZnO-ZrO₂, 50ZnO-ZrO₂, and 75ZnO-ZrO₂. The photocatalysts were prepared as follows: the appropriated amount of Zinc Acetylacetonate hydrate was dissolved into 50 mL of ethanol previously heated at 70°C and adjusted at pH 3 (HCl, 2.5 M). ZrO₂ sols were prepared separately as previously described but just before the addition of the half of the total amount of alkoxide was completed, the corresponding ZnO sol was incorporated into the mixture, followed by the dropwise of the rest of the zirconium alkoxide. The mixture was kept under vigorous stirring and reflux at 70°C during 24 h. The obtained gels were washed several times with ethanol and deionized water, then they were, dried, ground, and calcined at 500°C during 4 h. The proposed reactions are presented in Supplementary Materials (Figures S1, S2, and S3).

2.5. Characterization of the Nanocomposites. X-ray diffraction (XRD) patterns were obtained on a Bruker D8 Advance diffractometer using CuKα radiation (1.5418 Å) in the 2θ scan range of 10–90°. The average crystallite size of the samples was estimated using the Debye-Scherrer equation (equation (1)).

$$D = \frac{0.89\lambda}{\beta \cos \theta}, \quad (1)$$

where λ is the wavelength of CuKα radiation, β is the peak width at half maximum, and θ is the diffraction angle.

To calculate the percentage of monoclinic and tetragonal phases of pure ZrO_2 , we used the monoclinic phase fraction X_m and the following equation described by Garvie and Nicholson [21]:

$$X_m = \frac{I_{m(-111)} + I_{m(111)}}{I_{m(-111)} + I_{m(111)} + I_{t(101)}} \times 100, \quad (2)$$

where I_m and I_t represent the integral intensities of monoclinic (111) and (-111) and tetragonal (101) peaks.

Raman spectroscopy was performed with an XploRA PLUS Raman system equipment (HORIBA) with a CCD detector, an optical microscope (Olympus BX), and solid-state laser (532 nm/25 mW). Fourier transformed infrared spectra (FT-IR) were collected in a Shimadzu IRAffinity-1 spectrophotometer. The powders (<5%wt) were pressed into 100 mg wafers together with KBr (J.T.Baker, Infrared grade).

Diffuse reflectance UV-Vis spectroscopy (UV-Vis/DRS) was carried out on Shimadzu UV-2600 spectrophotometer equipped with an integrating sphere accessory and $BaSO_4$ as reference (99% reflectance). The band-gap (E_g) values were calculated using Kubelka-Munk function, $F(R)$, by the construction of a Tauc's plot: $(F(R) \cdot hv)^2$ or $(F(R) \cdot hv)^{1/2}$ versus energy (eV), for a direct and indirect allowed transition, respectively. The BET specific surface areas (S_{BET}) and pore volume (BJH method) of the samples were determined by N_2 adsorption-desorption isotherms at 77°K using a Quantachrome Autosorb 3B instrument. Degasification of the samples was performed at 100°C during 12 h. Surface morphology of the materials was analyzed by field emission scanning electron microscopy (FESEM) using a Hitachi S-4800 microscope, whereas high-resolution transmission electron microscopy (HRTEM) was performed in a JEOL JSM-2100 electron microscope operated at 200 kV, with a 0.19 nm resolution.

2.6. Photocatalytic Activity. Synthesized particles were tested in the photodegradation of phenol. The photocatalytic study was carried out in a 250 mL pyrex reactor covered with a UV-transparent Plexiglas (absorption at 250 nm); the intensity of the radiation over the suspension was 90 W/m². For each test, 200 mg of photocatalyst were suspended into 200 mL of phenol solution (50 ppm). The suspension was magnetically stirred in the dark with oxygen flow of 20 L/h until adsorption-desorption equilibrium was reached (ca. 20 min). Then the suspension was illuminated with an Osram Ultra-Vitalux lamp (300 W, UV-A, $\lambda = 365$ nm). Aliquots of 3 mL were taken and filtered (Millipore Millex-HV 0.45 μ m) for further analysis. Variations in phenol concentration were tracked by high-performance liquid chromatography (HPLC) using an Agilent Technologies 1200 chromatograph equipped with a UV-Vis detector and Eclipse XDB-C18 column 5 μ m, 4.6 mm \times 150 mm. The mobile phase was water/methanol (65:35) at a flow rate of 0.8 mL/min. Mineralization of phenol was measured by the total organic content (TOC) in a Shimadzu 5000 TOC analyzer. The percentage of mineralization was estimated using the equation (equation (2)):

$$\% \text{ Mineralization} = 1 - \frac{TOC_{\text{final}}}{TOC_{\text{initial}}} * 100, \quad (3)$$

where TOC_{initial} and TOC_{final} are the total organic carbon concentrations in the media before and after the photocatalytic reaction, respectively.

3. Results

3.1. X-Ray Diffraction Analysis. X-ray patterns of the photocatalysts are depicted in Figure 1(a). All the diffractograms of the samples containing ZnO exhibited sharp and strong peaks at 31.70°, 34.30° y 36.20 (2θ) which correspond to (100), (002), and (101) reflections, respectively, and agree with the characteristic peaks of ZnO wurtzite-type hexagonal crystalline structure (JCPDS 36-1451). The high intensity of the (101) peak suggests anisotropic growth and orientation of the crystals [22, 23].

On the other hand, pristine ZrO_2 showed broad peaks located at 28.20°, 30.20°, and 31.50° (2θ). The peak centered at 30.20°(101) is characteristic of tetragonal crystalline phase (t- ZrO_2) according to JCPDS 79-1771 card, whereas those at 28.20°(-111) and 31.5°(111) are representative of monoclinic phase (m- ZrO_2 , JCPDS 37-1484). These results suggest a mixture of both tetragonal and monoclinic crystalline phases, which is commonly observed on ZrO_2 materials when calcined at similar temperatures [24, 25].

When ZnO was added to ZrO_2 , the corresponding peaks to monoclinic phase were not observed, indicating inhibition of monoclinic phase. As the content of ZnO increases, the reflection (101) observed at 30.20° (2θ) appeared slightly shifted towards 30.38° except for the 50ZnO- ZrO_2 sample; therefore, the peaks observed for all the ZnO- ZrO_2 materials are assigned to the presence of tetragonal phase. To distinguish between the diffraction patterns of cubic and tetragonal phases of ZrO_2 , the 2θ region at 71–77° was carefully examined. The asymmetric doublets at ~74° indicated the formation of tetragonal ZrO_2 [26–28]. Figure 1(b) shows the tetragonal doublets for all ZnO- ZrO_2 materials. Crystallite size and percentage of phases for pure ZnO and ZrO_2 and ZnO- ZrO_2 nanocomposites were determined using Debye-Scherrer equation and Garvie and Nicholson method. Because monoclinic phase was not observed in ZnO- ZrO_2 composites, we considered only the integral intensities of tetragonal and wurtzite peaks of ZrO_2 and ZnO, respectively. The obtained values are presented in Table 1.

3.2. Raman Spectroscopy. The theory of groups predicts six Raman-active modes of vibrations for tetragonal ($A_{1g} + 2B_{1g} + 3E_g$) and 18 for monoclinic ($9A_g + 9B_g$) of ZrO_2 , whereas for ZnO there are 4 Raman-active modes, although splitting of E_2 modes into longitudinal optical (LO) and transversal optical (TO) gives place to 6 active modes. In Figure 2, Raman spectra of the photocatalysts are presented. For ZnO, two peaks can be clearly observed, the first one at 99 cm^{-1} and the second at 434 cm^{-1} , corresponding to E_2 mode characteristic of wurtzite-type structure; two additional weak bands at 326 and 380 cm^{-1} were also observed which are related to 2-phonon and A_1 (TO) mode,

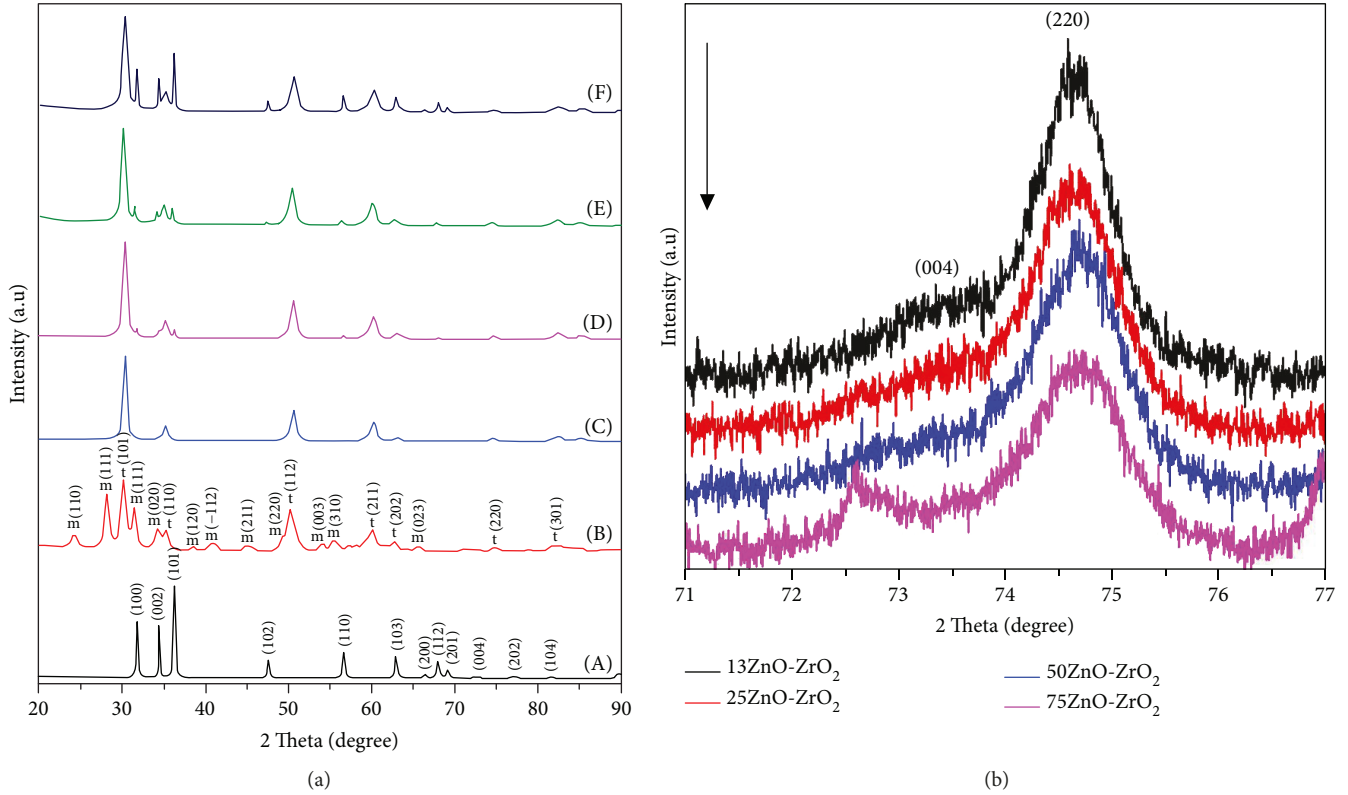


FIGURE 1: (a) XRD pattern of (A) ZnO, (B) ZrO₂, (C) 13ZnO-ZrO₂, (D) 25ZnO-ZrO₂, (E) 50ZnO-ZrO₂, and (E) 75ZnO-ZrO₂ calcined at 500°C. t = tetragonal and m = monoclinic of ZrO₂; w = wurtzite for ZnO. (b) XRD pattern of the samples evaluated in the region of 71–77° to identify the tetragonal doublets of ZrO₂.

TABLE 1: Crystallite size and percentage of phase content of nanocomposites obtained from Debye-Scherrer equation and Garvie and Nicholson method, respectively. m represents monoclinic and t tetragonal phase of ZrO₂. w indicates the wurtzite structure of ZnO.

Sample	Crystallite size (nm)	hkl	Phase content (%)
ZnO	33.2	(101)	100%
ZrO ₂	14.3	(101) _m	59.7%
	15.4	(-111) _t	40.3%
13ZnO-ZrO ₂	18.2	(101) _t	100%
25ZnO-ZrO ₂	14.5	(101) _t	88.0%
	44.7	(101) _w	12.0%
50ZnO-ZrO ₂	14.4	(101) _t	82.0%
	48.3	(101) _w	18.0%
75ZnO-ZrO ₂	13.8	(101) _t	60.9%
	44.6	(101) _w	39.1%

respectively [29]. The ZrO₂ spectrum showed several peaks located at 100, 176, 217, 306, 333, 380, 474, 501, 534, 553, 613, and 638 cm⁻¹, which are very close to those reported for monoclinic phase. The peaks attributed to tetragonal structure were located at 142 and 265 cm⁻¹ whereas two additional bands reported for this structure around 318 and 461 cm⁻¹ seemed to be overlapped with monoclinic signals;

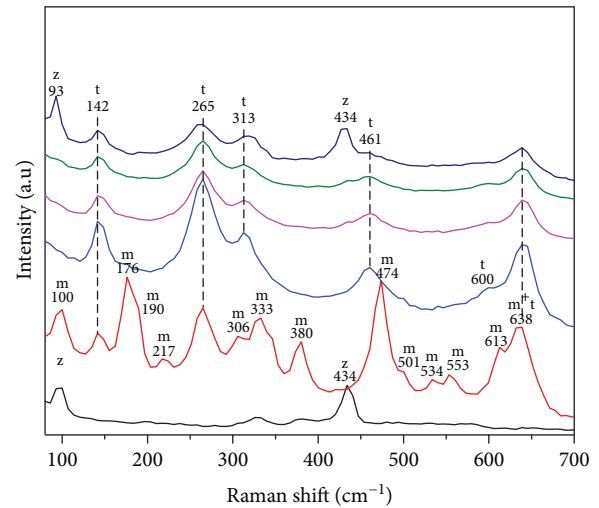


FIGURE 2: Raman spectra of ZnO-ZrO₂ nanocomposites. (A) ZnO, (B) ZrO₂, (C) 13ZnO-ZrO₂, (D) 25ZnO-ZrO₂, (E) 50ZnO-ZrO₂, and (F) 75ZnO-ZrO₂. m indicates monoclinic and t tetragonal structures for ZrO₂ whereas z indicates wurtzite crystalline structure of ZnO.

the peaks between 640 and 641 cm⁻¹ are shared by monoclinic and tetragonal structures [30, 31]. Since cubic structure of zirconia usually exhibits one strong peak around 617 cm⁻¹, the absence of this signal indicates the presence of a mixture of only two structures (monoclinic and tetragonal) in pristine

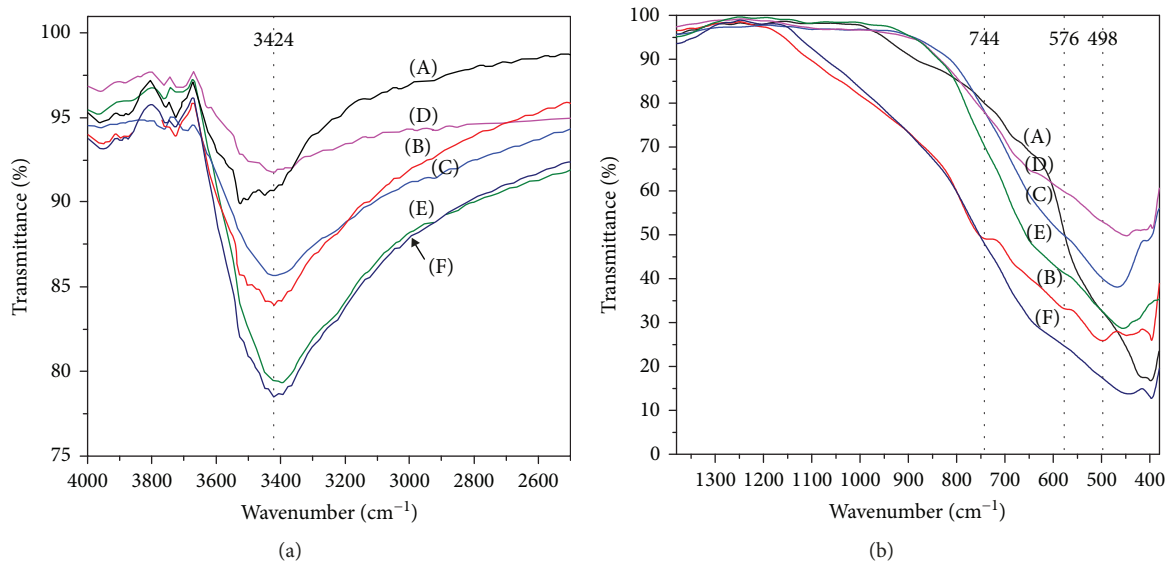


FIGURE 3: (a) FT-IR full spectra of (A) ZnO, (B) ZrO₂, (C) 13ZnO-ZrO₂, (D) 25ZnO-ZrO₂, (E) 50ZnO-ZrO₂, and (F) 75ZnO-ZrO₂ composites with different content of ZnO. (b) FTIR region from 1300 to 400 cm⁻¹.

ZrO₂. For the ZnO-ZrO₂ composites, Raman spectra did not show sharp peaks. As the content of ZnO increased, we observed the broadening of the peaks that correspond to tetragonal structure modes; this broadening is related to the decrease in the crystallite size of this crystalline phase, usually due to phonons associated with the nanosized particles. On the other hand, the absence of representative signals for monoclinic structure in both Raman spectra and XRD patterns leads us to conclude that ZnO inhibited the formation of this structure in ZnO-ZrO₂ composites. Additionally, Rietveld refinement of 13ZnO-ZrO₂ was performed (Supplementary Materials, Figure S4 and Table S1). This analysis confirmed the absence of both solid solution and cubic crystalline phase formation; the estimated percentages of each crystalline structure are shown in Table 1.

3.3. FTIR Analysis. Figure 3 shows the spectra of pure ZnO, ZrO₂, and ZnO-ZrO₂ composites with different content of ZnO. FTIR spectra of all materials presented wide bands at 3410–3450 cm⁻¹ which correspond to O-H stretching vibrations of physical adsorbed water on the catalyst surface [32]. Compared to the ZrO₂ band, a shift of the O-H band to lower frequencies occurs as the percentage of ZnO increases in the ZnO-ZrO₂ composites. Pure ZnO spectrum showed an intense band centered at 423 cm⁻¹. This band is characteristic for Zn-O vibrations [23, 32]. Two intense bands appeared at 744 cm⁻¹ and 576 cm⁻¹ have been associated with vibrations of Zr-O in monoclinic structure. An additional band located at 498 cm⁻¹ was also present in ZrO₂ spectrum; this signal corresponds to Zr-O-Zr vibrations in tetragonal structure [33–35], which appears slightly shifted for all ZnO-ZrO₂ nanocomposites. This behavior can be attributed to the addition of divalent oxides like ZnO (Zn⁺²) to ZrO₂. Also, the incorporation of these oxides may produce a lattice deformation on the crystalline structure, with subsequent modification on the force constants of Zr-O and related bonds [33].

3.4. Specific Surface Area. Figure 4 shows the N₂ adsorption-desorption isotherms of the nanocomposites as well as their corresponding pore size distribution (insets). The isotherms for all the samples presented type IV(a) shape according to IUPAC classification [36] which corresponds to mesoporous structures where capillary condensation takes place and is accompanied by hysteresis. The adsorbed volume in all cases is relatively low which explains the observed values for specific surface area. It has been reported that ZnO usually exhibits poor BET surface areas ranging from 1 to 15 m²/g when no additives are used to improve this property. In our samples, pure ZnO showed a S_{BET} = 10 m²/g while ZrO₂ exhibited 46 m²/g.

The isotherms of both ZnO and ZrO₂ pure oxides showed a narrow hysteresis loop, which for ZrO₂ starts at 0.4 (P/P₀) and for ZnO this occurs at higher relative pressures (0.8) (Figure 4(a)). When composites were analyzed, hysteresis loop for all the composition was slightly broader than pure oxides, indicating changes in porosity (Figure 4(b)). ZnO showed H3-type hysteresis loop at high relative pressure. However, ZrO₂ and all ZnO-ZrO₂ composites exhibited H2-type hysteresis which is associated with the presence of bottle-shaped mesopores that can be explained as a consequence of the interconnectivity of pores [1]. The specific surface area decreased from 46 to 8 m²/g when 25% of ZnO was incorporated, and for 75ZnO-ZrO₂, S_{BET} value was 36 m²/g, and its N₂ isotherm showed a broader hysteresis loop than the observed pure oxides. Additional effect of ZnO incorporation was observed in BJH pore size distribution: pristine ZrO₂ showed a wide pore size distribution from meso- to macropores, whereas ZnO presented pores around 30 nm and also macroporosity; when both oxides were coupled, pore size distribution for all composites showed unimodal distribution with very close pore size average.

3.5. Diffuse Reflectance UV-Vis Spectroscopy. The absorption spectra of the oxides are depicted in Figure 5(a). The UV-Vis

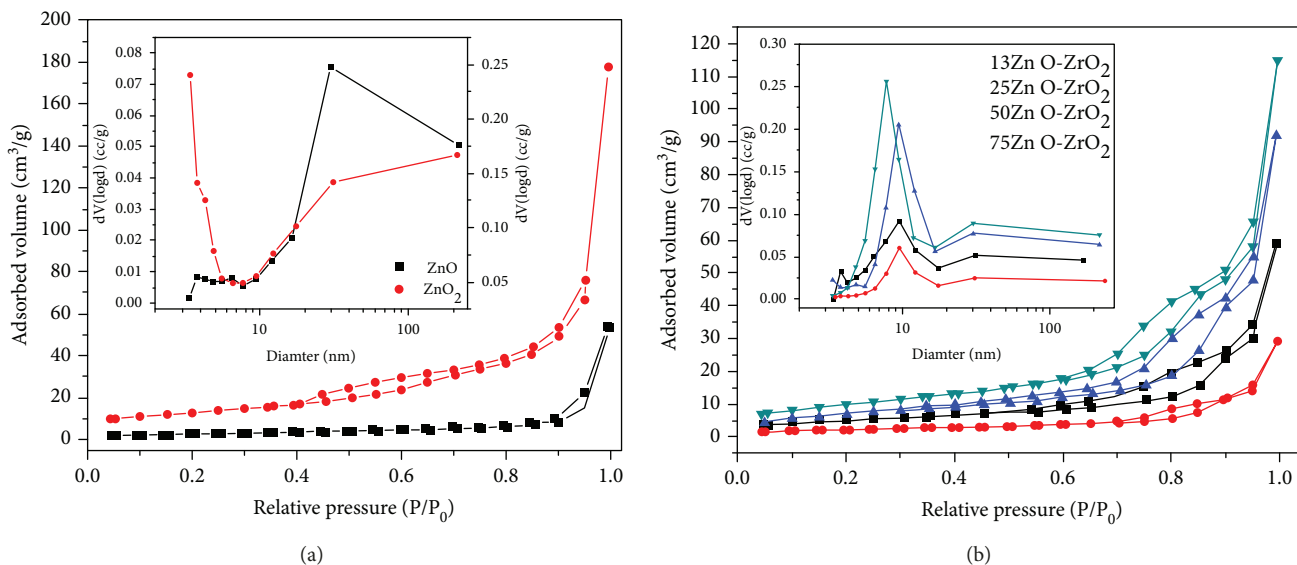


FIGURE 4: N_2 adsorption-desorption BET isotherms of (a) pure oxides and (b) different ZnO-ZrO₂ composites; the insets represent BJH pore size distribution from desorption branches.

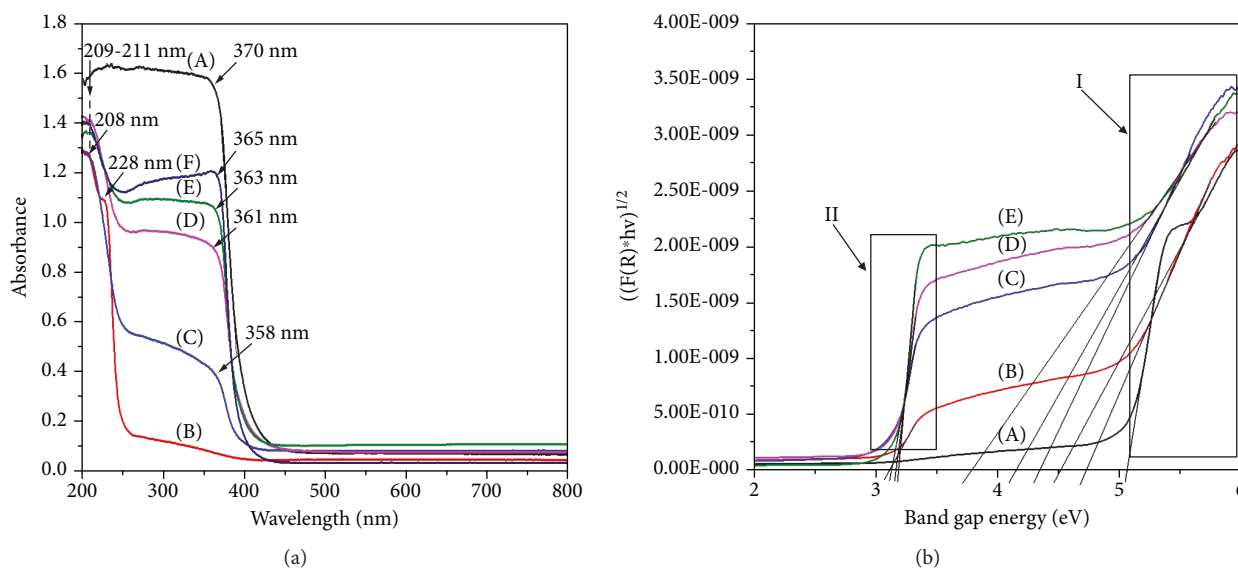


FIGURE 5: (a) UV-Vis/DR absorption spectra of (A) ZnO, (B) ZrO₂, (C) 13ZnO-ZrO₂, (D) 25ZnO-ZrO₂, (E) 50ZnO-ZrO₂, and (F) 75ZnO-ZrO₂ composites; (b) Kubelka-Munk function of (A) ZrO₂, (B) 13ZnO-ZrO₂, (C) 25ZnO-ZrO₂, (D) 50ZnO-ZrO₂, and (E) 75ZnO-ZrO₂ composites. (I) represents the first and (II) the second edge of the samples considered for Eg estimations.

spectrum of ZnO shows an absorption edge at 370 nm, which is in good agreement with literature [37]. This characteristic band can be assigned to the intrinsic band-gap absorption of ZnO due to the electron transitions from the valence band to the conduction band ($O2p \rightarrow Zn3d$) [38]. ZrO₂ spectrum showed a small absorption band at 208 nm and another large band at 228 nm, which appeared at lower wavelengths than the characteristic bands reported for ZrO₂, usually observed ~ 240 nm [39]. These bands correspond to the presence of Zr species as the tetrahedral Zr^{+4} , and it is electronically produced by the charge transfer transition of the valence band $O2p$ electron to the conduction band $Zr4d$ ($O_2 \rightarrow Zr^{4+}$) level

upon UV light excitation [40]. There was no other absorption band observed in the UV-Vis region. It has been reported that the identification of ZrO₂ phases can be possible by using UV range of DRS. The two bands observed in pure ZrO₂ are typically observed since ZrO₂ has two band-to-band transitions. According to Sahu and Rao [41], the first transition corresponds to values around 5.17–5.2 eV that can be associated with m-ZrO₂. In the ZrO₂ here prepared, we observed by DRX that monoclinic and tetragonal phases are presented in pure oxide. The band at high energy cannot be observed when the content of ZnO increases, not only due to the disappearance of monoclinic phase but also for the

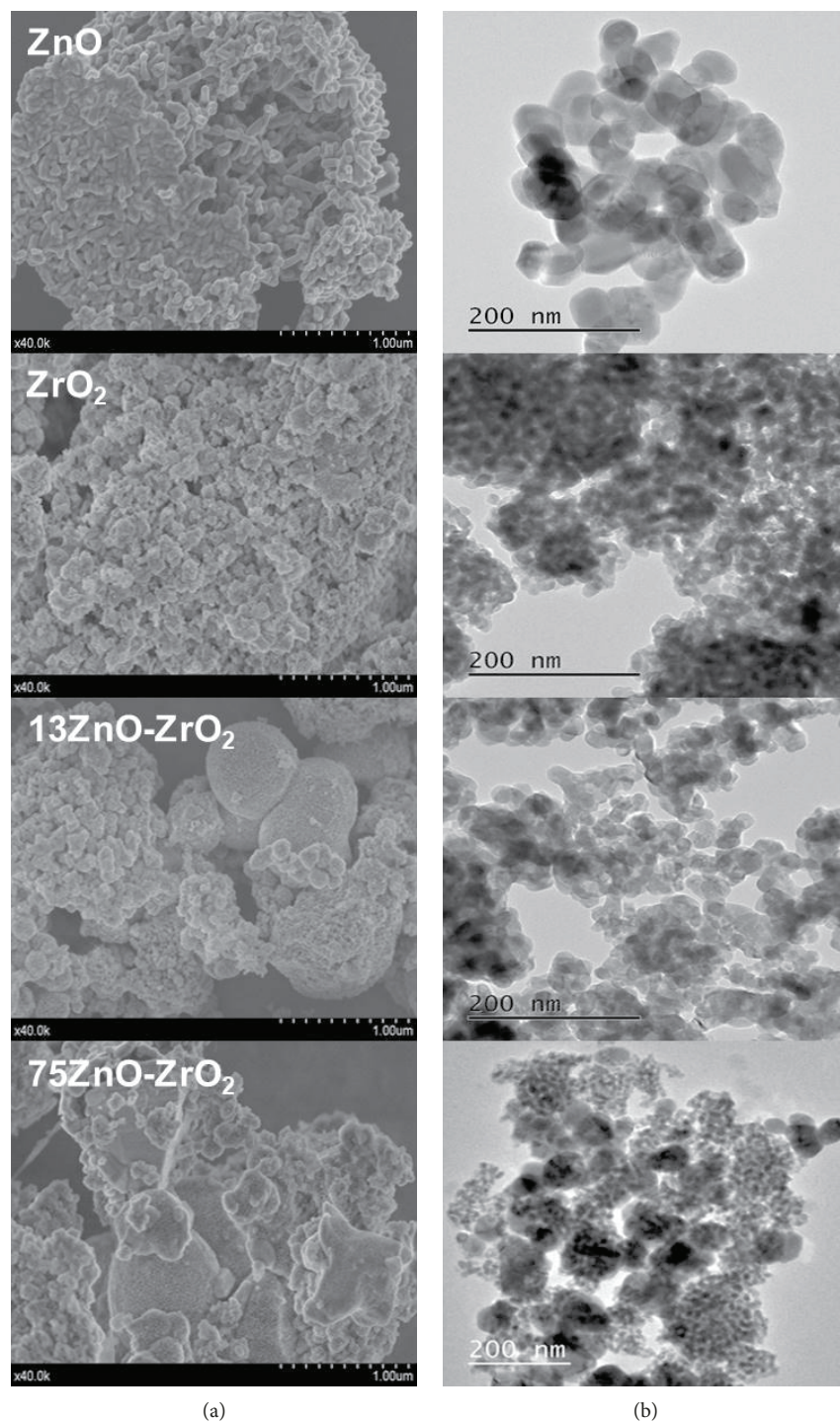


FIGURE 6: FESEM (a) and the corresponding HRTEM (b) micrographs of pure oxides and ZnO-ZrO₂ composites.

incorporation of ZnO affecting the shape of the spectrum. The spectrum of pure ZrO₂ also depicts a small shoulder with an onset at 310 nm that can be attributed to t-ZrO₂ crystalline structure [42]. The shape as well as the intensity of this band changes as the content of ZnO increases and slightly shifts towards lower energy region, due to the effect of ZnO.

The addition of ZnO modified the absorption edge of ZrO₂ towards lower values. A red shift was observed in the last band of all ZnO-ZrO₂ materials towards longer

wavelength region, due to the introduction of energy levels in the interband gap [17]. Kubelka-Munk function was used to estimate the band gap of the nanocomposites (Figure 5(b)). The band gap values of pure ZnO and ZrO₂ were evaluated by using $n = 2$ (direct transitions) and $n = 1/2$ (indirect transitions), respectively, and their values are summarized in Table S2 (Supplementary Materials).

For ZnO-ZrO₂ materials, it can be noticed the presence of two edges instead of only one; the bandgap was estimated

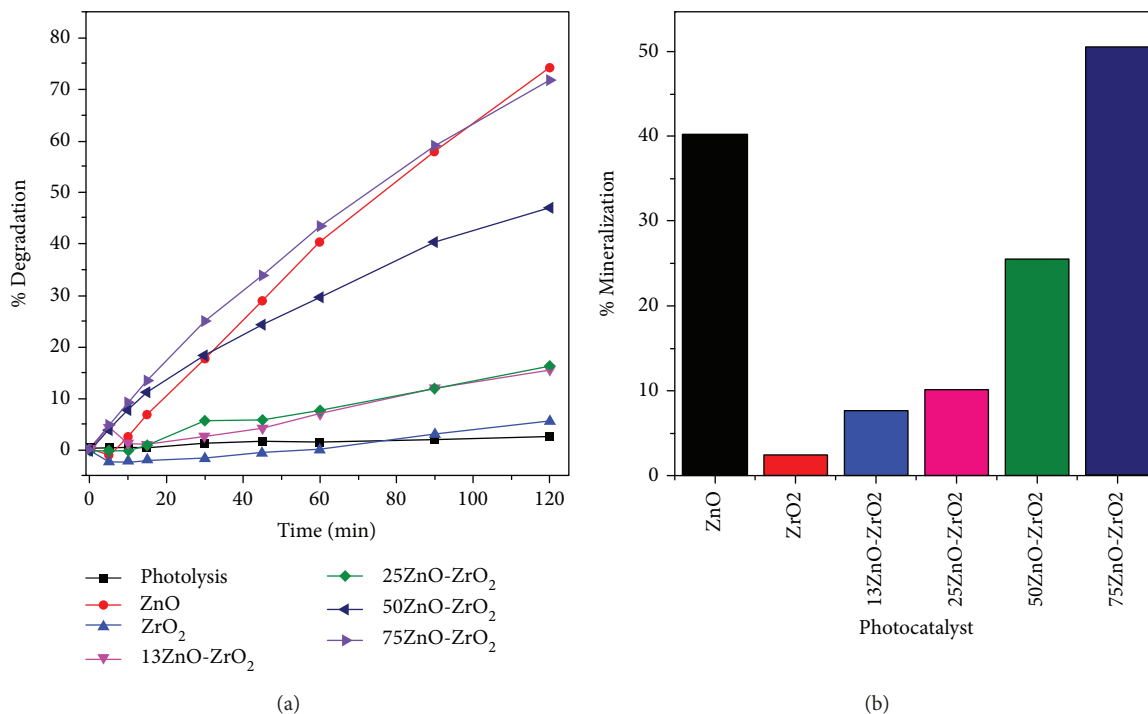


FIGURE 7: (a) Degradation curves of phenol by ZnO, ZrO₂, and different ZnO-ZrO₂ composites (experimental conditions: phenol = 50 ppm, volume of phenol = 200 mL, and catalyst dosage = 200 mg). (b) TOC results obtained after 120 min of illumination in the UV.

using $n = 1/2$. The obtained value for ZnO was 3.26 eV (Supplementary Materials, Figure S5) whereas 4.53 and 5.06 eV were calculated for ZrO₂ (for the two edges observed in the corresponding spectrum), these values changed to 4.73, 4.35, 3.76, and 4.16 eV by the addition of different contents of ZnO (indicated as I in Figure 5(b)), being 50ZnO-ZrO₂ the one with the lowest value. With regard to the low-energy shoulder observed in ZnO-ZrO₂ spectra (indicated as II in Figure 5(b)), the calculated values were 3.07, 3.10, 3.15, and 3.16 eV for the composites with 13, 25, 50, and 75% of ZnO, respectively, allowing nanocomposites to be excited at lower energy.

3.6. Electron Microscopy. Morphology of the nanocomposites was investigated using electron microscopy, and the images are shown in Figure 6. We observed that ZnO nanoparticles are rod-like shaped with sizes ranging from 100 to 300 nm producing agglomerates. On the other hand, ZrO₂ is made of smaller particles nonuniform in shape and size. In 13ZnO-ZrO₂ nanocomposite, we observed that ZnO particles change in shape whereas some ZrO₂ agglomerates grew up to 1 μ m but also smaller quasispherical particles around 300 nm were observed. The most significant change was exhibited by 75ZnO-ZrO₂ nanocomposite, since agglomerates of particles with smaller sizes were obtained.

3.7. Photocatalytic Test. Previous to the test, adsorption-desorption equilibrium was reached after stirring the suspensions for 20 minutes in the dark, of which in general all the composites presented low adsorption of the pollutant. The results of photocatalytic degradation are shown in

TABLE 2: Kinetic parameters estimated from pseudofirst order kinetics.

Photocatalyst	k (min ⁻¹)	R ²	$t_{1/2}$ (min)
ZrO ₂	0.7×10^{-3}	0.9585	1155
13ZnO-ZrO ₂	1.3×10^{-3}	0.9193	533
25ZnO-ZrO ₂	1.5×10^{-3}	0.9808	462
50ZnO-ZrO ₂	5.3×10^{-3}	0.9939	130
75ZnO-ZrO ₂	10.3×10^{-3}	0.9964	67
ZnO	11.2×10^{-3}	0.9810	62

Figure 7(a). Here, we observed that pure ZrO₂ degraded only 5% of phenol even after 120 min; when ZnO was incorporated, a slight increase in photodegradation with 13 and 25% of ZnO was observed, but they barely degraded around 15% of the pollutant. By increasing the ZnO content up to 50% mol, 47% of phenol was degraded, whereas 71% of degradation was achieved using 75ZnO-ZrO₂ composite. For the prepared ZnO, 74% of degradation was obtained during the same time. The kinetic parameters were also calculated assuming pseudofirst order kinetics (Table 2) where we observed that $t_{1/2}$ for 75ZnO-ZrO₂ composite was very close to that calculated for ZnO.

It is well known that ZnO can be activated under UV-A light and generally exhibits good photodegradation rates, but it is also needed to assess the mineralization of the pollutant. For this purpose, TOC analysis was performed and the results are tabulated in Figure 7(b). Pure ZrO₂

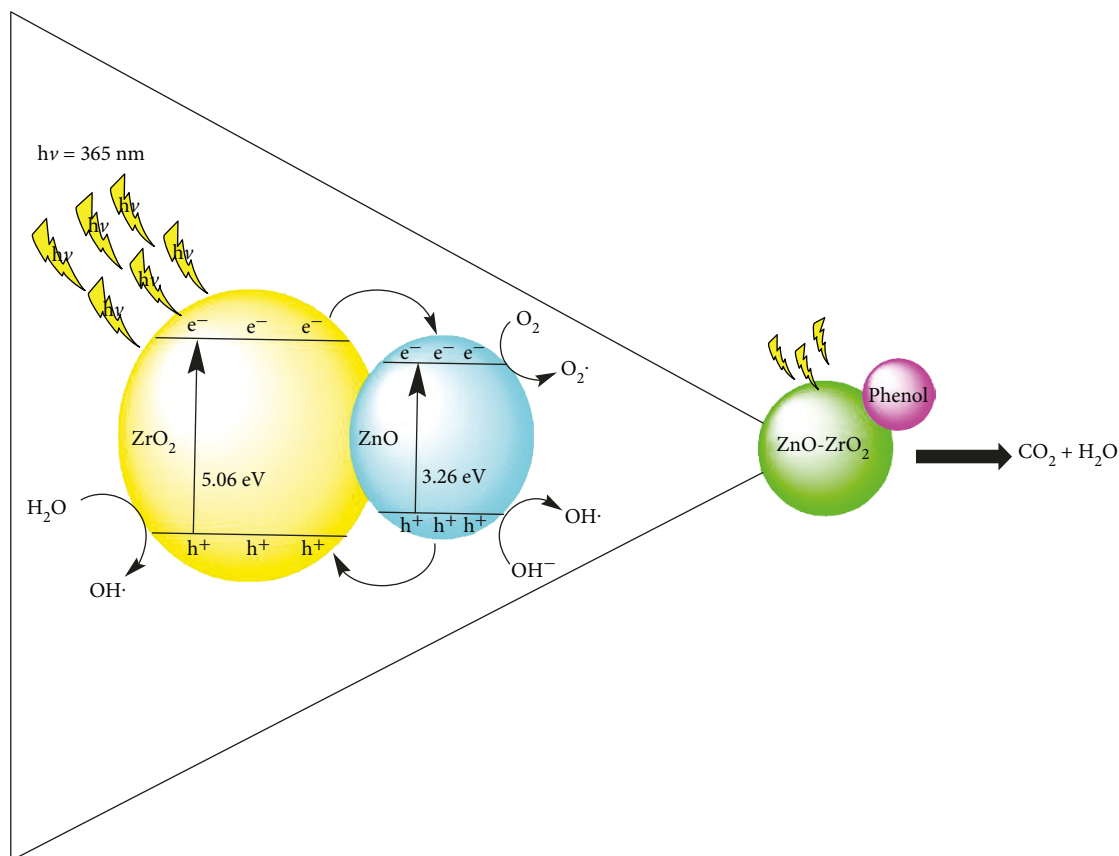


FIGURE 8: Schematic representation of photocatalytic mechanism of electron-hole pair separation of ZnO-ZrO₂ composites for the degradation of phenol.

mineralized 2.5% of phenol, but the mineralization increases with increasing ZnO content, which stabilizes tetragonal crystalline phases of ZrO₂. Although ZnO reached 74% degradation, the mineralization of the pollutant was 40%, while 51% of mineralization was achieved with 75ZnO-ZrO₂. Tetragonal ZrO₂ has been reported as the most active polymorph of ZrO₂ which also shows high selectivity in catalytic reactions. These results showed that at this concentration, ZnO-ZrO₂ composite improved the mineralization of phenol when compared to pure ZnO. Besides, it was also confirmed that intermediaries like catechol, resorcinol, and hydroquinone were not generated during the photodegradation with 75ZnO-ZrO₂.

According to the obtained results, a schematic representation of phenol degradation is shown in Figure 8. When the ZnO-ZrO₂ composites were excited by UV-A irradiation (365 nm), electrons migrate from the valence band (VB) to the conduction band (CB) of ZnO, leading to the formation of electron/hole (e^-/h^+) pairs. Since the energy levels of ZnO fit well into the band gap of ZrO₂, the electrons from the CB of ZrO₂ can easily be transferred to the CB of ZnO; conversely, the holes migrate from the VB of ZnO to the VB of ZrO₂, and thereby the electron-hole pair recombination may be decreased in ZnO-ZrO₂ composites. These e^- and h^+ react with water and oxygen to produce hydroxyl (OH \cdot) radicals which are very reactive and can easily oxidize

the phenol until obtaining CO₂ and water. As a result, we obtained an enhancement in photocatalytic performance of phenol degradation by the composite with the highest ZnO percentage [8, 19, 20, 43].

4. Discussion

It is well known that the catalytic and photocatalytic performance of ZrO₂ can be affected by crystalline phases. Although there are some reports on the catalytic activity of ZnO-ZrO₂ materials, deep structural studies have not been performed so far. The fact that both tetragonal and cubic phases exhibit similar XRD patterns makes it difficult to discern these structures based only on X-ray diffraction analysis, and Rietveld refinement or Raman spectroscopy are good tools for elucidating this ambiguity. In this work, we observed that by adding ZnO, only the t-ZrO₂ phase was obtained, and this phenomenon could also be suspected by analyzing Raman results. In all composites, t-ZrO₂ was detected as well as zincite (wurtzite-type) structure for ZnO. Formation of the nanocomposite influenced the crystallite size of both ZnO and ZrO₂, increasing for ZnO but decreasing for t-ZrO₂ as a function of the ZnO-ZrO₂ ratio. The absence of solid solution could be explained not only due to the differences in valence between ions, which depends on the amount of Zn²⁺ species [44], but also due to the synthesis procedure

here reported. Lattice parameters of the 13ZnOZrO_2 nanocomposite are provided in Supplementary Materials. We observed small changes when compared to pure zirconia; this can be attributed to the presence of the divalent oxide, since incorporation of these type of oxides causes lattice deformation on the crystalline structure of ZrO_2 , with subsequent modification on the force constants of Zr-O and related bonds [33].

Since band gap is one important feature to consider in photoactivity, many attempts to improve this property have been made. By coupling ZnO and ZrO_2 , radiation of low energy can be absorbed by the ZnO-ZrO_2 composites. From the calculated E_g values, it can be assumed that the energy levels for both the valence band (VB) and conduction band (CB) in ZnO fit in with the bandgap of ZrO_2 . When the electrons are excited, most of the electrons from the conduction band of ZrO_2 can be easily transferred to the conduction band of ZnO , and thus, the band gap may be decreased, indicating that ZnO-ZrO_2 nanoparticles have a suitable band gap to generate excited electron/hole pairs [17] allowing the use of simulated solar radiation.

Both oxides, ZnO and ZrO_2 , are well known for their photocatalytic properties, but one of their limitations is the need of UV light for its activation, especially ZrO_2 that usually requires UV radiation due to its wide band gap. Here, we investigated the effect of ZnO in the photocatalytic performance of ZrO_2 under simulated solar light. Since the use of pure ZnO leads to the formation of several compounds during the photoreaction, it is remarkable that 75ZnO-ZrO_2 nanocomposite conducted to a reaction without formation of any intermediaries, which represents the main advantage of using ZnO-ZrO_2 .

5. Conclusions

So far, ZnO-ZrO_2 materials have been reported for several catalytic reactions with an enhanced performance compared to their pristine moieties. Recently, this type of composites has been studied also as photocatalysts with promising results, but full understanding of their properties related to their composition are needed. In this work, we prepared ZnO-ZrO_2 composites using zinc (II) acetylacetonate and zirconium n-butoxide as raw materials. We observed that synthesis procedure strongly affected the stabilization of zirconia polymorphs, where ZnO plays an important role in inhibiting ZrO_2 monoclinic structure and stabilizing tetragonal phase. By coupling ZnO to ZrO_2 , we observed significant changes in the absorption behavior of ZrO_2 shifting its absorption edges in the UV region toward lower energies. The pore distribution of the composite was intensely changed by the interaction of both oxides, directing to a larger amount of mesopores than the observed for uncoupled oxides. Test revealed that 75ZnO-ZrO_2 composite exhibited good performance in the degradation of phenol using simulated solar radiation, improved the mineralization reached by pure ZnO and ZrO_2 , and inhibited the formation of undesirable intermediates usually obtained as a result of photocatalytic degradation of phenol.

Data Availability

All data obtained from characterizations technics used to support this study are available from the corresponding author upon request.

Conflicts of Interest

The authors declare that they have no conflicts of interest.

Acknowledgments

We are grateful to D.H. Aguilar and A. Marín for their technical assistance, and acknowledge the financial support of the projects UJAT-IB-43, CONACYT-INFR-269701, SEP-CONACYT-CB-183196, FOMIX-Yucatán 2008-108160, and CONACYT LAB-2009-01 (No. 123913). In addition, we would like to thank CONACYT for the fellowship given to M. Uribe, and to ICMS-CSIC, LANNBIO CINVESTAV-Mérida, UAM-I, and UJAT for the facilities.

Supplementary Materials

In the supplementary information, the authors provided the details on the mechanism of formation for ZnO-ZrO_2 materials, as well as the crystalline data obtained through the Rietveld refinement and HRTEM of the 13ZnOZrO_2 . (*Supplementary Materials*)

References

- [1] B. Sathyaseelan, E. Manikandan, I. Baskaran et al., "Studies on structural and optical properties of ZrO_2 nanopowder for opto-electronic applications," *Journal of Alloys and Compounds*, vol. 694, pp. 556–559, 2017.
- [2] C. Karunakaran, R. Dhanalakshmi, and P. Gomathisankar, "Phenol-photodegradation on ZrO_2 . Enhancement by semiconductors," *Spectrochimica Acta Part A: Molecular and Biomolecular Spectroscopy*, vol. 92, pp. 201–206, 2012.
- [3] A. M. Hussein and R. V. Shende, "Enhanced hydrogen generation using ZrO_2 -modified coupled ZnO/TiO_2 nanocomposites in the absence of noble metal co-catalyst," *International Journal of Hydrogen Energy*, vol. 39, no. 11, pp. 5557–5568, 2014.
- [4] S. Aghabeygi and M. Khademi-Shamami, " ZnO/ZrO_2 nanocomposite: sonosynthesis, characterization and its application for wastewater treatment," *Ultrasonics Sonochemistry*, vol. 41, pp. 458–465, 2018.
- [5] C. Karunakaran, R. Dhanalakshmi, P. Gomathisankar, and G. Manikandan, "Enhanced phenol-photodegradation by particulate semiconductor mixtures: interparticle electron-jump," *Journal of Hazardous Materials*, vol. 176, no. 1-3, pp. 799–806, 2010.
- [6] A. Shirmardi, M. A. M. Teridi, H. R. Azimi, W. J. Basirun, F. Jamali-Sheini, and R. Yousefi, "Enhanced photocatalytic performance of ZnSe/PANI nanocomposites for degradation of organic and inorganic pollutants," *Applied Surface Science*, vol. 462, pp. 730–738, 2018.
- [7] L. J. Tomar and B. S. Chakrabarty, "Synthesis, structural and optical properties of $\text{TiO}_2\text{-ZrO}_2$ nanocomposite by

- hydrothermal method," *Advanced Materials Letters*, vol. 4, no. 1, pp. 64–67, 2013.
- [8] B. M. Pirzada, N. A. Mir, N. Qutub, O. Mehraj, S. Sabir, and M. Muneer, "Synthesis, characterization and optimization of photocatalytic activity of $\text{TiO}_2/\text{ZrO}_2$ nanocomposite heterostructures," *Materials Science and Engineering: B*, vol. 193, pp. 137–145, 2015.
- [9] R. Yousefi, J. Beheshtian, S. M. Seyed-Talebi, H. R. Azimi, and F. Jamali-Sheini, "Experimental and theoretical study of enhanced photocatalytic activity of Mg-doped ZnO NPs and ZnO/rGO nanocomposites," *Chemistry - An Asian Journal*, vol. 13, no. 2, pp. 194–203, 2018.
- [10] C. Jaramillo-Páez, J. A. Navío, M. C. Hidalgo, and M. Macías, "High UV-photocatalytic activity of ZnO and Ag/ZnO synthesized by a facile method," *Catalysis Today*, vol. 284, pp. 121–128, 2017.
- [11] A. C. Mohan and B. Renjanadevi, "Preparation of zinc oxide nanoparticles and its characterization using scanning electron microscopy (SEM) and X-ray diffraction(XRD)," *Procedia Technology*, vol. 24, pp. 761–766, 2016.
- [12] G. Kavitha, K. T. Arul, and P. Babu, "Enhanced acetone gas sensing behavior of n-ZnO/p-NiO nanostructures," *Journal of Materials Science: Materials in Electronics*, vol. 29, no. 8, pp. 6666–6671, 2018.
- [13] A. Kharatzadeh, F. Jamali-Sheini, and R. Yousefi, "Excellent photocatalytic performance of $\text{Zn}(1-x)\text{Mg}x\text{O}/\text{rGO}$ nanocomposites under natural sunlight irradiation and their photovoltaic and UV detector applications," *Materials & Design*, vol. 107, pp. 47–55, 2016.
- [14] P. Prasannalakshmi and N. Shanmugam, "Fabrication of TiO_2/ZnO nanocomposites for solar energy driven photocatalysis," *Materials Science in Semiconductor Processing*, vol. 61, pp. 114–124, 2017.
- [15] G. S. Pozan and A. Kambur, "Significant enhancement of photocatalytic activity over bifunctional ZnO– TiO_2 catalysts for 4-chlorophenol degradation," *Chemosphere*, vol. 105, pp. 152–159, 2014.
- [16] N. Rosman, W. N. W. Salleh, A. F. Ismail et al., "Photocatalytic degradation of phenol over visible light active $\text{ZnO}/\text{Ag}_2\text{CO}_3/\text{Ag}_2\text{O}$ nanocomposites heterojunction," *Journal of Photochemistry and Photobiology A: Chemistry*, vol. 364, pp. 602–612, 2018.
- [17] M. M. Ibrahim, "Photocatalytic activity of nanostructured ZnO– ZrO_2 binary oxide using fluorometric method," *Spectrochimica Acta Part A: Molecular and Biomolecular Spectroscopy*, vol. 145, pp. 487–492, 2015.
- [18] G. C. Lakshmi, S. Ananda, R. Somashekar, and C. Ranganathaiah, "Synthesis of ZnO/ZrO_2 nanocomposites by electrochemical method and photocatalytic degradation of fast green dye, paper dyeing and printing press effluent," *International Journal of Advanced Materials Science*, vol. 3, no. 3, pp. 221–237, 2012.
- [19] E. D. Sherly, J. J. Vijaya, N. C. S. Selvam, and L. J. Kennedy, "Microwave assisted combustion synthesis of coupled ZnO– ZrO_2 nanoparticles and their role in the photocatalytic degradation of 2,4-dichlorophenol," *Ceramics International*, vol. 40, no. 4, pp. 5681–5691, 2014.
- [20] K. Gurushantha, L. Renuka, K. S. Anantharaju et al., "Photocatalytic and photoluminescence studies of ZrO_2/ZnO nanocomposite for LED and waste water treatment applications," *Materials Today: Proceedings*, vol. 4, no. 11, Part 3, pp. 11747–11755, 2017.
- [21] R. C. Garvie and P. S. Nicholson, "Phase analysis in zirconia systems," *Journal of the American Ceramic Society*, vol. 55, no. 6, pp. 303–305, 1972.
- [22] Y. Peng, J. Ji, X. Zhao, H. Wan, and D. Chen, "Preparation of ZnO nanopowder by a novel ultrasound assisted non-hydrolytic sol-gel process and its application in photocatalytic degradation of C.I. Acid Red 249," *Powder Technology*, vol. 233, pp. 325–330, 2013.
- [23] M. M. Ba-Abbad, A. A. H. Kadhum, A. Bakar Mohamad, M. S. Takriff, and K. Sopian, "The effect of process parameters on the size of ZnO nanoparticles synthesized via the sol-gel technique," *Journal of Alloys and Compounds*, vol. 550, pp. 63–70, 2013.
- [24] F. Heshmatpour and R. B. Aghakhanpour, "Synthesis and characterization of nanocrystalline zirconia powder by simple sol-gel method with glucose and fructose as organic additives," *Powder Technology*, vol. 205, no. 1-3, pp. 193–200, 2011.
- [25] A. K. Singh and U. T. Nakate, "Microwave synthesis, characterization, and photoluminescence properties of nanocrystalline zirconia," *The Scientific World Journal*, vol. 2014, Article ID 349457, 7 pages, 2014.
- [26] C. Wang, M. Boucher, M. Yang, H. Saltsburg, and M. Flytzani-Stephanopoulos, "ZnO-modified zirconia as gold catalyst support for the low-temperature methanol steam reforming reaction," *Applied Catalysis B: Environmental*, vol. 154-155, pp. 142–152, 2014.
- [27] R. Srinivasan, R. J. de Angelis, G. Ice, and B. H. Davis, "Identification of tetragonal and cubic structures of zirconia using synchrotron x-radiation source," *Journal of Materials Research*, vol. 6, no. 6, pp. 1287–1292, 1991.
- [28] R. C. Garvie, R. H. Hannink, and R. T. Pascoe, "Ceramic steel?," *Nature*, vol. 258, no. 5537, pp. 703–704, 1975.
- [29] S. K. Sharma and G. J. Exarhos, "Raman spectroscopic investigation of ZnO and doped ZnO films, nanoparticles and bulk material at ambient and high pressures," *Solid State Phenomena*, vol. 55, pp. 32–37, 1997.
- [30] D. Gazzoli, G. Mattei, and M. Valigi, "Raman and X-ray investigations of the incorporation of Ca^{2+} and Cd^{2+} in the ZrO_2 structure," *Journal of Raman Spectroscopy*, vol. 38, no. 7, pp. 824–831, 2007.
- [31] V. G. Keramidis and W. B. White, "Raman scattering study of the crystallization and phase transformations of ZrO_2 ," *Journal of the American Ceramic Society*, vol. 57, no. 1, pp. 22–24, 1974.
- [32] T. Ivanova, A. Harizanova, T. Koutzarova, and B. Vertruyen, "Effect of annealing temperatures on properties of sol-gel grown ZnO– ZrO_2 films," *Crystal Research and Technology*, vol. 45, no. 11, pp. 1154–1160, 2010.
- [33] J. Chandradass, K.-S. Han, and D. Bae, "Synthesis and characterization of zirconia- and silica-doped zirconia nanopowders by oxalate processing," *Journal of Materials Processing Technology*, vol. 206, no. 1–3, pp. 315–321, 2008.
- [34] E. S. Agorku, A. T. Kuvarega, B. B. Mamba, A. C. Pandey, and A. K. Mishra, "Enhanced visible-light photocatalytic activity of multi-elements-doped ZrO_2 for degradation of indigo carmine," *Journal of Rare Earths*, vol. 33, no. 5, pp. 498–506, 2015.
- [35] H. Sudrajat, S. Babel, H. Sakai, and S. Takizawa, "Rapid enhanced photocatalytic degradation of dyes using novel N-doped ZrO_2 ," *Journal of Environmental Management*, vol. 165, pp. 224–234, 2016.

- [36] M. Thommes, K. Kaneko, A. V. Neimark et al., "Physisorption of gases, with special reference to the evaluation of surface area and pore size distribution (IUPAC Technical Report)," *Pure and Applied Chemistry*, vol. 87, no. 9-10, pp. 1051–1069, 2015.
- [37] X. Zhao, M. Li, and X. Lou, "Sol-gel assisted hydrothermal synthesis of ZnO microstructures: morphology control and photocatalytic activity," *Advanced Powder Technology*, vol. 25, no. 1, pp. 372–378, 2014.
- [38] A. K. Zak, M. E. Abrishami, W. H. A. Majid, R. Yousefi, and S. M. Hosseini, "Effects of annealing temperature on some structural and optical properties of ZnO nanoparticles prepared by a modified sol-gel combustion method," *Ceramics International*, vol. 37, no. 1, pp. 393–398, 2011.
- [39] K. G. Kanade, J. O. Baeg, S. K. Apte, T. L. Prakash, and B. B. Kale, "Synthesis and characterization of nanocrystalline zirconia by hydrothermal method," *Materials Research Bulletin*, vol. 43, no. 3, pp. 723–729, 2008.
- [40] T. Sreethawong, S. Ngamsinlapasathian, and S. Yoshikawa, "Synthesis of crystalline mesoporous-assembled ZrO₂ nanoparticles via a facile surfactant-aided sol-gel process and their photocatalytic dye degradation activity," *Chemical Engineering Journal*, vol. 228, pp. 256–262, 2013.
- [41] H. Ranjan Sahu and G. Ranga Rao, "Characterization of combustion synthesized zirconia powder by UV-Vis, IR and other techniques," *Bulletin of Materials Science*, vol. 23, no. 5, pp. 349–354, 2000.
- [42] S. N. Basahel, T. T. Ali, M. Mokhtar, and K. Narasimharao, "Influence of crystal structure of nanosized ZrO₂ on photocatalytic degradation of methyl orange," *Nanoscale Research Letters*, vol. 10, no. 1, p. 73, 2015.
- [43] S. Sultana, Rafiuddin, M. Z. Khan, and M. Shahadat, "Development of ZnO and ZrO₂ nanoparticles: their photocatalytic and bactericidal activity," *Journal of Environmental Chemical Engineering*, vol. 3, no. 2, pp. 886–891, 2015.
- [44] G. Štefanić, S. Musić, and M. Ivanda, "Phase development of the ZrO₂-ZnO system during the thermal treatments of amorphous precursors," *Journal of Molecular Structure*, vol. 924-926, pp. 225–234, 2009.